Characterization and Monitoring of XENONnT Photosensors and Search for New Physics with the First XENONnT Science Data

Dissertation

zur

Erlangung der naturwissenschaftlichen Doktorwürde
(Dr. sc. nat.)

vorgelegt der
Mathematisch-naturwissenschaftlichen Fakultät
der
Universität Zürich

von
Giovanni Volta
aus
Italien

Promotionskommission
Prof. Dr. Laura Baudis (Vorsitz)
Prof. Dr. Nicola Serra
Dr. Michelle Galloway

Zürich, 2023

A Elena
alla mia famiglia
e a miei amici

"Quando tutto questo finirà
Sarò una nazione da ricostruire
Una città messa in ginocchio dalla fame
Una parola sola
E tutto questo finirà"

Quando finirà - Elephant Brain

ABSTRACT

The Standard Model of particle physics is arguably one of the most outstanding achievements of human intellect. Even though in the last 50 years, it has demonstrated considerable successes in providing experimental predictions, there are still unexplained phenomena. Galactic and extra-galactic observations point to a Universe in which the mass content is dominated by a hypothetical form of non-luminous matter, called dark matter, that cannot be explained by the Standard Model of particle physics. Moreover, astrophysical observations and everyday experience suggest that anti-baryons are essentially absent in the Universe. This matter-antimatter asymmetry could be resolved if the number of baryons and leptons were not a true symmetry of nature, implying the decay of bound protons and neutrons in nuclei.

Mainly motivated by the search for dark matter in the form of weakly interactive massive particles (WIMPs), the XENON collaboration started a multistage experiment based on a dual-phase (liquid and gas) xenon time projection chamber, aiming to enhance the sensitivity of elastic scattering of WIMPs with xenon nuclei by increasing the target mass and decreasing the background level. The first part of this manuscript motivates the use of liquid xenon for these searches and describes the dual-phase TPC detection principle. The current phase, XENONnT, was assembled and commissioned during 2020 and early 2021. The main detector of the experiment is a 8.6 t xenon dual-phase time projection chamber with an instrumented liquid xenon mass of 5.9 t, constantly monitored by 494 VUV-sensitive photomultiplier tubes. WIMPs interaction in the xenon is expected to primarily produce nuclear recoils (NRs) while the background is dominated by electron recoils (ERs) interactions.

The photosensors are essential for the operation of the experiment. Out of the 494 PMTs, 386 were purchased new, and the rest were inherited from the previous experiment phase, XENON1T. The new PMTs were selected after a rigorous testing campaign outlined in this manuscript. Next, the XENONnT TPC assembly is presented, focusing mainly on the PMTs. The characterization of the PMTs conducted during the commissioning of the experiment and the working conditions adopted to improve the performances are then described in detail. Ultimately, the PMT performances and their evolution during the first physics search data taking are discussed. As a result of the meticulous testing procedure, the quality of XENONnT photosensors has improved significantly over that of XENON1T PMTs. This is further demonstrated by the performance of the PMTs obtained during the first acquisition of physics data. XENONnT PMTs have demonstrated reliability at cryogenic temperatures with a uniform and consistent response over time: Only 3 $\%$ of PMTs were excluded from the analysis, a factor $\sim$ 5 smaller than in XENON1T.

From May to December 2021, XENONnT collected the first physics search data (SR0). Motivated by an excess over the expected background observed by XENON1T at low energies in the ER region, possibly due to signs of new physics, XENONnT performed for the first time a simultaneous blind analysis of the ER and NR events. The second part of this manuscript is devoted to presenting the results of the leading physics channels of XENONnT experiment. The analysis pipeline and the detector response characterization are presented. The development of two data quality criteria based on scintillation signals is discussed. Next, the derivation of the optical properties implemented in the XENONnT simulation framework is illustrated. Lastly, the impact on the total ER background budget of radioactive nuclei from detector materials is shown.

In this first science run, XENONnT achieved an unprecedented ER background index at low energies, thanks to the reduction of the ^{85}Kr and ^{222}Rn concentrations. Within the $(1, 30)$ keV energy range and in a 4.37 t fiducial mass, a rate of (15.8 ± 1.3) $(\mathrm{t} \times \mathrm{yr} \times \mathrm{keV})^{-1}$ was observed, roughly $\sim$ 5 times lower than its predecessor, XENON1T. No significant excess above the background was observed in the low-energy ER and WIMP searches. Therefore, upper limits on WIMP-nucleon elastic scattering for a wide range of WIMP masses were derived, leading to a minimal upper limit of 2.58×10^{-47} cm^2 at 90 % confidence level for the spin-independent case at a WIMP mass of 28 GeV/c^2. Similarly, the analysis of low-energy ER data has placed stringent new limits on solar axions, neutrino-enhanced magnetic moment, and bosonic dark matter.

The last part of this manuscript is devoted to the nucleon disappearance analysis in ^{129}Xe performed with the XENONnT SR0 data. This process is a baryon or lepton - or a combination of them - violation process which, if it exists, could be connected to the matter-antimatter asymmetry of the Universe. A radiogenic technique is used in the analysis, in which one searches for the radioactive decay of nuclei resulting from the invisible nucleon decay in some favorable and abundant isotope within the detector. Using the total exposure of XENONnT, the p, nn, and pp disappearances in ^{129}Xe were investigated by searching for the decay of ^{128}I, ^{127}Xe, and ^{127}Te, respectively. No sign of the radioactive decay of these nuclei was observed, and therefore, lower limits at 90 % C.L. were set on the decay lifetimes of nucleons and di-nucleons, leading to a factor $\mathcal{O}(10)$ improvement with respect to the current limits derived via the ^{129}Xe radiogenic search: $\tau_p > 6.09 \times 10^{25}$ yr, $\tau_{nn} > 1.96 \times 10^{25}$ yr, and $\tau_{pp} > 4.76 \times 10^{24}$ yr.

Contents

1 THE QUEST FOR DARK MATTER 1
1.1 Evidence of Dark Matter 1
1.1.1 Galactic and extragalactic scales 1
1.1.2 The cosmological scale 3
1.1.3 Dark Matter in the Milky Way 4
1.2 The anthology of dark matter 7
1.2.1 Dark matter properties 8
1.2.2 Dark matter candidates 8
1.3 Dark Matter detection experiments 13
1.3.1 Direct detection of WIMP-nucleus scattering 14
1.3.2 State of the art in direct detection 17

2 INVISIBLE NUCLEON DECAY 20
2.1 The baryon asymmetry of the Universe 20
2.2 State of the art of baryon number violation process 22
2.2.1 Exclusive and inclusive searches 22
2.2.2 Xenon-based nucleon disappearance searches 23

3 THE XENON PROJECT 26
3.1 Xenon as a detector medium 26
3.2 Dual-phase time projection chamber 31
3.3 The XENONnT experiment 34
3.3.1 The XENONnT TPC 35
3.3.2 The vetos and auxiliary systems of XENONnT 36
3.3.3 XENONnT challenges 37
3.3.4 Main physics goals of the XENONnT experiment 41

4 XENONNT PHOTOSENSORS: *FROM TESTING TO ASSEMBLY IN THE TPC* 43
4.1 Design and operating principle of XENONnT PMT 43
4.1.1 PMT operating principle 44
4.1.2 Design of R11410-21 PMT 47
4.2 The XENONnT PMT testing campaign 49
4.2.1 MarmotX facility 50

4.2.2 Testing campaign result 50
4.2.3 Conclusion 55
4.3 Installation of XENONnT PMTs 55
4.3.1 The XENONnT PMT cables 56
4.3.2 The XENONnT PMT connectors 57
4.3.3 Cables and bases production, assembly and cleaning 59
4.3.4 The PMT array assembly 60
4.3.5 The XENONnT TPC installation 61

5 CHARACTERIZATION AND PERFORMANCE OPTIMIZATION OF XENONNT PMTS: *FROM COMMISSIONING TO SCIENCE DATA TAKING* **66**
5.1 The PMT calibration 67
5.1.1 The PMT calibration system 67
5.1.2 The PMT calibration processing 68
5.1.3 The gain calculation 70
5.1.4 The SPE acceptance calculation 72
5.1.5 Important remarks 73
5.2 PMT commissioning phase 75
5.2.1 Outgassing and nitrogen phase 75
5.2.2 Cooling and xenon filling phase 76
5.2.3 Performances optimization for science run 0 80
5.3 Performance of the PMTs during the first science run 84
5.3.1 Time monitoring of PMT performances 84
5.3.2 SPE shape 86

6 FIRST SCIENCE RUN OF XENONNT **91**
6.1 A brief summary of the first XENONnT science run 92
6.2 Data processing pipeline 93
6.2.1 Event building 93
6.2.2 Event corrections 94
6.3 Data quality criteria 100
6.3.1 Cuts overview 102
6.3.2 The S1 area fraction top cut 102
6.3.3 The S1 pattern likelihood cuts 106
6.3.4 Total selection efficiency 110
6.4 Energy calibration 111
6.5 Optical Monte Carlo-data matching in XENONnT 113
6.5.1 XENONnT MC framework 113
6.5.2 Optical simulation 114
6.5.3 Optical parameters 116
6.5.4 Data-MC matching procedure 117
6.6 Signal and background modeling 119

6.6.1 Low-energy ER and WIMP analysis techniques and the sought-after signals 120
6.6.2 Backgrounds sources 121
6.6.3 Review of radiogenic ER material background prediction 122
6.7 Results 124
6.7.1 Low-energy ER analysis results 125
6.7.2 WIMP search results 125
6.8 Conclusions 128

7 SEARCH FOR NUCLEON DISAPPEARANCE IN ^{129}XE WITH THE FIRST XENONNT SCIENCE DATA **131**
7.1 Preliminary studies before the analysis 131
7.1.1 Validation of full chain simulation 132
7.1.2 The effective simulator: FastSimulator 138
7.1.3 Updates on the radiogenic background from detector materials 142
7.2 Analysis of nucleon disappearance in XENONnT 143
7.2.1 Expected signals 143
7.2.2 Data selection 145
7.2.3 Total selection efficiency 149
7.2.4 Background model 153
7.2.5 Statistical framework 165
7.2.6 Results 167
7.2.7 Conclusion 177

8 CONCLUSION **179**

APPENDIX A H1 HYPOTHESIS FITTING RESULTS **183**

Listing of figures

1.1 Rotation velocity profile of M31 2
1.2 MACS J0416.1–2403 2
1.3 CMB temperature anisotropies 4
1.4 CMB temperature power spectrum 5
1.5 Rotational velocity profile of the Milky Way 6
1.6 Dark matter halo models 6
1.7 Time evolution of measured Dark matter density 6
1.8 Dark Matter velocity distribution 7
1.9 Dark Matter candidates 8
1.10 WIMP comoving density evolution 12
1.11 Spin-independent form factors 15
1.12 Spin-independent differential rate in terrestrial detector 17
1.13 Up-to-date upper limits on the spin-independent DM-nucleon cross-section 19

3.1 Particles mean free path in xenon 27
3.2 Schematic of xenon scintillation 29
3.3 Signal yields for ER and NR 31
3.4 Dual-phase TPC detection principle 32
3.5 Energy calibration from light and charge anti-correlation 33
3.6 NR and ER discrimination in XENON1T 34
3.7 Schematic view of XENONnT 35
3.8 XENONnT TPC 37
3.9 The XENONnT experiment 38

4.1 Schematic of R11410 photomultiplier tube 45
4.2 PMT spatial and angular uniformity responses 47
4.3 3-inch Hamamatsu R11410-21 PMT 48
4.4 Voltage divider circuit 48
4.5 Resistor chain adopted in the PMTs of XENONnT's TPC 49
4.6 Render of the MarmotX testing facility 51
4.7 Render of the MarmotX support structure 51
4.8 HV-scan during the PMT testing campaign 52
4.9 PMT afterpulses spectrum 53

4.10 Event rate monitoring and light emission test 54
4.11 XENONnT vacuum breakdown chamber 57
4.12 XENONnT cabling scheme 57
4.13 PMTs connectors 58
4.14 PMT sectors 58
4.15 Cleaning of PMT cables 60
4.16 PMT arrays details 60
4.17 PMT array assembly 61
4.18 XENONnT PMT array 61
4.19 Details of TPC electrodes stack and bottom PMT array 63
4.20 Above ground TPC assembly 63
4.21 Underground TPC assembly 65

5.1 PMT calibration system 67
5.2 LED arrival time 69
5.3 Waveforms of PMT calibration 69
5.4 PMT charge spectra 71
5.5 Occupancy estimation 72
5.6 SPE acceptance 74
5.7 Highlights during the first part of the commissioning 76
5.8 Gain monitoring during xenon cooling 77
5.9 Light levels for PMT calibration 79
5.10 Gain characteristic curves of PMTs 80
5.11 Gain parameters of PMTs 80
5.12 SPE acceptance dependence on PMT gain 80
5.13 SPE resolution dependence on PMT gain 80
5.14 PMT noise RMS in SR0 82
5.15 PMT voltage setting in SR0 82
5.16 PMT SPE acceptance at 15 ADC in SR0 83
5.17 PMT gain in SR0 83
5.18 Time evolution of PMT gains in SR0 85
5.19 SPE acceptance evolution in SR0 85
5.20 True SPE acceptance at DAQ threshold 86
5.21 PMT charge spectrum fit 87
5.22 SPE charge spectrum 88
5.23 SPE charge spectrum fit 89
5.24 Average SPE charge *pdf* 89

6.1 XENONnT SR0 livetime accumulation 93
6.2 XENONnT event building 94
6.3 (S1; S2) waveform 95
6.4 Field distortion correction 96

6.5 Relative light yield 97
6.6 Electron lifetime from one $^{83\mathrm{m}}$Kr calibration campaign 98
6.7 S2 correction map 100
6.8 Lone hits correction 101
6.9 Single electron gain and extraction efficiency correction 101
6.10 Continuous counterpart of binomial distribution 103
6.11 Binomial test in XENONnT 104
6.12 Data-driven AFT probability map from $^{83\mathrm{m}}$Kr 105
6.13 Data-driven acceptance of S1 AFT cut with ^{220}Rn calibration data 106
6.14 S1 AFT cut on ^{220}Rn calibration data 107
6.15 Total S1 pattern likelihood cut on ^{220}Rn calibration data 109
6.16 Top and bottom S1 patter likelihood cuts on ^{220}Rn calibration data 109
6.17 Data-driven acceptance of S1 PL cuts with ^{220}Rn calibration data 110
6.18 Total efficiencies of low-energy ER and WIMP analyses 111
6.19 Energy reconstruction in XENONnT 112
6.20 XENONnT full chain simulation flowchart 115
6.21 Data-MC optical matching 119
6.22 XENONnT SR0 ER and NR models 125
6.23 Low-energy ER background only fit result 126
6.24 WIMP search data 127
6.25 XENONnT SR0 WIMP-nucleons spin-independent elastic scattering result 129

7.1 Data-driven S1 AFT acceptance as a function of the energy 133
7.2 S2 single scatter selection in XENONnT SR0 134
7.3 Data- and simulation-driven SS-MS spatial resolution 135
7.4 Ratio of multiple-site to single-site from ^{212}Pb simulation and calibration data 137
7.5 ^{212}Pb single-site energy spectrum comparison from simulation and calibration data 138
7.6 Effective XENONnT detector response flowcharts 140
7.7 ^{212}Pb simulated driven total selection efficiency 141
7.8 FastSimulator ^{212}Pb energy spectrum validation 142
7.9 Updated examples of XENONnT radiogenic background from the detector materials 143
7.10 Expected XENONnT material energy spectrum in 4.37 t fiducial volume 144
7.11 Expected single-site energy spectra for nucleon and di-nucleon disappearance in ^{129}Xe . . . 146
7.12 Fit of full absorption peak spectra of ^{214}Bi, ^{60}Co, and ^{40}K 147
7.13 XENONnT SR0 energy bias 148
7.14 Predicted spatial distribution of the background 149
7.15 Pseudo-significance scan 151
7.16 Total efficiency for β, ^{212}Pb, and ^{214}Pb 152
7.17 Expected radiogenic background from detector materials 154
7.18 ^{238}U and ^{232}Th decay chains 155
7.19 Backgrounds expected for ^{212}Pb and ^{214}Pb in the nucleon disappearance analysis 157
7.20 ^{nat}Kr concentration in SR0 158

7.21 Backgrounds expected for ^{85}Kr and solar ν in the nucleon disappearance analysis 158
7.22 Backgrounds expected for ^{136}Xe and ^{124}Xe in the nucleon disappearance analysis 159
7.23 Rate evolution of neutron-induced background in SR0 161
7.24 Neutron activation backgrounds and ^{83m}Kr leftover 162
7.25 Example of $\Delta\chi^2_\lambda$ scan 167
7.26 Schematic diagram of the inference pipeline 168
7.27 Background-only fit 169
7.28 Background-only fit residuals 169
7.29 Background-only parameter correlations 171
7.30 ^{128}I hypothesis fit 172
7.31 $\Delta\chi^2_\lambda$ scan for ^{128}I hypothesis fit 173
7.32 ^{127}Xe hypothesis fit 174
7.33 Correlation between ^{127}Xe and ^{129m}Xe 174
7.34 $\Delta\chi^2_\lambda$ scan for ^{127}Xe hypothesis fit 175
7.35 ^{127}Te hypothesis fit 176
7.36 $\Delta\chi^2_\lambda$ scan for ^{127}Te hypothesis fit 176
7.37 Livetime upper limits at 90 % CL for the nucleon and di-nucleon disappearance in XENONnT SR0 178

A.1 Parameter correlations for ^{128}I hypothesis 184
A.2 Parameter correlations for ^{127}Xe hypothesis 185
A.3 Parameter correlations for ^{127}Te hypothesis 186

PREFACE

The work I will illustrate in this manuscript is the result of the work of many people. The XENON collaboration counts more than 170 scientists, and everybody contributes to running the experiment and performing the analysis. Thus, not everything I am going to show is my own work. My contributions are listed, divided by chapter and with a brief description.

- Chapter 4, XENONnT photosensors - The PMT testing campaign at the University of Zurich (section 4.2) was mainly performed by Dr. Adam Brown. At the beginning of my Ph.D. project, $\sim$ 40 PMTs to test were left. Therefore my contribution was partial. Together with Dr. Adam Brown, we were responsible for preparing the voltage dividers and cables for XENONnT's PMTs. Lastly, as part of the XENONnT PMT working group, I participated in all assembly phases of the PMT arrays at LNGS. In addition, I participated in the operations of the TPC assembly, both above- and under-ground. These operations are summarized in section 4.3.
- Chapter 5, Characterization and performance optimization of XENONnT PMTs - I have been deeply involved in the calibration of XENONnT's PMTs. Data processing, as well as gain and SPE acceptance analyses, were developed by Dr. Chiara Capelli, Dr. Shingo Kazama and myself (section 5.1). I have followed all stages of PMT commissioning, from closing the cryostats to starting SR0. With Dr. Chiara Capelli and a few other physicists and technicians, I spend $\sim$ 3 months during the 2020 COVID outbreak at LNGS to provide people power to the XENON collaboration and proceed with the experiment timeline (section 5.2). I was responsible for delivering the PMT gains from the weekly calibration to Alexander Bismark, which developed the gain evolution time model. I monitored the SPE acceptance over the entire science data taking, providing the inputs to evaluate the XENONnT detection efficiency (section 5.3). Lastly, I developed the PMT single photoelectron spectra used in the simulation software for realistic simulation of S1 and S2 signals. (section 5.3.2).
- Chapter 6, First science run of XENONnT - the entire XENON collaboration contributed to low-energy ER analysis and WIMP search. I was responsible for several aspects, from the development of two data quality criteria (section 6.3.2 and 6.3.3) to the estimation of radiogenic background from detector materials (section 7.2.4). A special mention to Valentino Aerne, who helped develop the S1 pattern likelihood cuts during his bachelor thesis. In addition, I provided the optical parameter settings (section 6.5) for the XENONnT simulation framework. The re-weight approach was proposed by Dr. Andrii Terliuk, and together we developed the analysis framework and derived the optimal settings that best reproduced the ^{83m}Kr calibration data.
- Chapter 7, Search for nucleon disappearance in ^{129}Xe with the first XENONnT science data - the search for the nucleon and di-nucleon disappearance in ^{129}Xe was initially proposed by Prof. Dr. Laura Baudis. The analysis described in this manuscript is my own work. Nevertheless, other collaboration members' contributed to it. The SS-MS spatial resolution map, essential for the FastSimulator software, was developed by Jaron Grigat (section 7.1.2). Particular recognition goes to Dr.

Diego Ramirez, who supervised the development of FastSimulator. Cecilia Ferrari made an important contribution to the simulation-driven cut acceptances (section 7.2.3). Paloma Cimental was responsible for characterizing neutron activation backgrounds (section 7.2.4). Last, Dr. Christian Wittweg and Yannik Müller helped me develop the inference framework and guided me in interpreting the results.

1

The quest for Dark Matter

From the cosmological to sub-galactic scales, a wide range of evidence concur with the existence of a non-luminous substance. Commonly referred to as Dark Matter (DM), this component dominates the density of cosmological matter at the expense of regular baryonic matter. The search for this elusive component, whose nature is yet unknown, is one of the most fascinating quests in contemporary physics. This chapter introduces the evidence for DM, possible candidates, and the experimental approaches to reveal its true nature.

1.1 Evidence of Dark Matter

The following sections contain some of the evidence for DM, from the galactic to the cosmological scale. Not all the evidence in the literature will be presented in this manuscript. To look deeper into these topics, refer to [1].

1.1.1 Galactic and extragalactic scales

The origin of the name Dark Matter is attributed to the Swiss physicist Fritz Zwicky, who in 1933 showed that the velocity dispersion of the Coma Cluster was too high for its galaxies to be gravitationally bounded without the addition of a non-luminous matter component [2]. Only starting from the early 70s, the scientific community became convinced that most of the matter in the Universe is *dark*. Among all the contributions, the Andromeda galaxy (M31) rotation curve analysis published by Rubin and Ford represents a milestone [3]. Combining observations of the 21 cm hydrogen line with optical surface photometry, Rubin and Ford measured the galaxy rotation velocity as a function of the radius, affirming that an additional mass was needed in the outer part to justify the observed dynamics.

At very large galaxy radii, where the luminous matter contribution becomes negligible, Newtonian gravity, as well as General Relativity, predicts that the rotational velocity should fall as $v(r) = \sqrt{GM(r)/r} \sim 1/\sqrt{r}$, where G is the gravitational constant, r is the distance from the center of the galaxy, and $M(r)$ is the mass profile. Approaching the optical edge of the galaxy, where stars and interstellar gas begin to be sparser, the observable mass decreases. Therefore, the velocity should drop as well. On the contrary, the observations show that it approaches a plateau. The dark matter hypothesis interprets this plateau as evidence of additional non-luminous matter contributing to the total mass profile such that $M(r) \sim r$, and thus $v(r) \sim$ constant [4].

A competing hypothesis - Modified Newtonian Dynamics (MOND) – is that Newton's law, and hence General Relativity, is incorrect at small accelerations [5, 6]. In the MOND framework, a new constant with the dimension of acceleration is introduced, which dominates the dynamics for values $\leq \mathcal{O}(10^{-8}\ \text{cm s}^{-2})$. MOND can solve various problems at the galactic scale, e.g., galaxy rotation curve, without introducing any new matter component. However, it applies to few observables and has problems dealing with galaxy clusters and cosmological observations [7].

Fig1.1 shows the M31 rotation velocity data over imposed with the rotation curve model as described in [8, 9]. Still today, after more than 50 years, the conclusions are the same: the gravitational field of the galaxy is larger than what one expects if only the observable matter would imply. The galaxy velocity profile is an excellent example of introducing dark matter, but not the most appealing. The DM description is very model dependent, and their accuracy is still unsatisfactory, as shown by the mismatch in Fig1.1 for small radii.

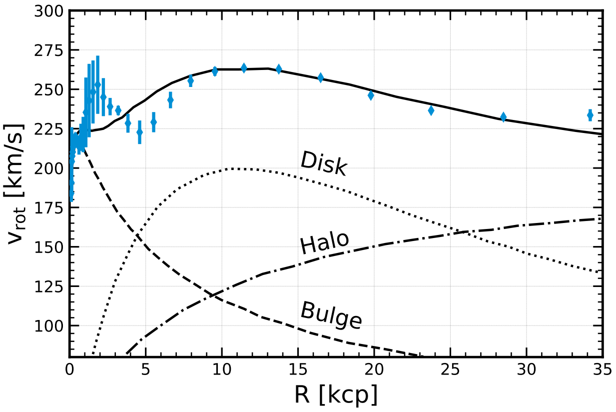

Figure 1.1: Rotation velocity profile of M31 (Andromeda Galaxy). The rotation curve model, with black lines, is reproduced following [9]. The measurement in blue is from [8].

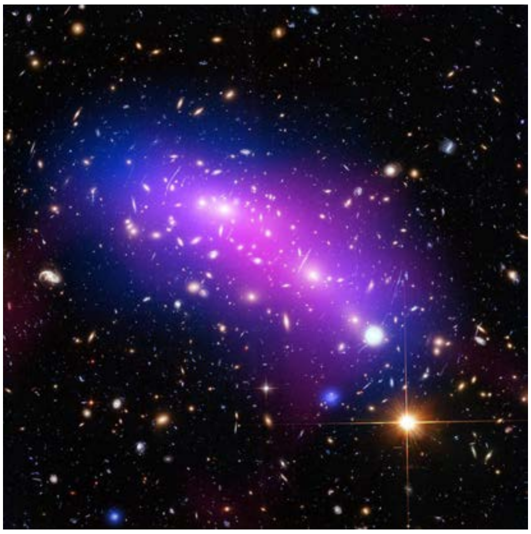

Figure 1.2: MACS J0416.1–2403: example of the collision of two galaxies clusters, known as *bullet cluster*, from [10, 11].

Evidence of DM on an extra-galactic scale comes from comparing gravitational lensing measurement [12] and X-ray observation [13] in a galaxies cluster merging. Through gravitational lensing, the gravitation fields of the clusters can be mapped and their mass distribution derived. Similarly, from X-ray observation, the density profiles of the gas can be inferred. Given the non-luminous features of DM, the X-ray observation describe the baryonic content of the cluster. Numerous observations show that the gravitational potential, derived by the lensing technique, does not coincide with the distribution of ordinary matter inferred by X-ray telescopes. This can be appreciated on the merging galaxy clusters in MACS J0416.1–2403 [10, 11] as shown in Fig.1.2. The position of the gas is shown in red, and it is accumulated at the center of the structure where the clusters collide. Whereas the map of the gravitational field, in blue, suggests that most of the mass is in the outer regions of the structure. Assuming a collisionless DM, these observations are consistent with the dark matter paradigm.

1.1.2 The cosmological scale

An enormous step forward in DM understating comes from studying the cosmic microwave background (CMB). Modern cosmology assumes an expanding Universe originating from a hot and dense region with tiny anisotropies. In the early stage of the Universe, until $\sim 370,000$ years after the Big Bang, the temperature and the density were high enough that any attempt to form neutral atoms, even the lightweight hydrogen, was impossible because of the presence of photons sufficiently energetic to ionize atoms and destroy any bonds between electrons and nuclei. During this period, the Compton scattering between photons and free electrons ensured the kinetic equilibrium between the radiation and ordinary matter. Hence, almost perfect black-body radiation was filling the entire Universe. As soon as the temperature of the Universe was lower than $\sim$ eV, the Compton scattering became ineffective. Then, the recombination epoch began. The photons decoupled from ordinary matter and started to travel freely through space. These photons constitute the most powerful probe of the early Universe [1, 14]. The CMB appears today as a black body spectrum with a temperature of (2.722 ± 0.027) K, characterized by tiny anisotropies of the order of $\mathcal{O}(10^{-5})$ K. The latest temperature anisotropies map from Planck collaboration [15, 16] is shown in Fig.1.3. All the structures in the Universe formed via gravitational clustering, starting from small initial fluctuations in the matter-photon fluid density. These primordial fluctuations remained imprinted in the temperature fluctuations of the CMB. From their analysis, the energy and matter budget of the Universe and its expansion rate is computed with great precision.

The anisotropies in the CMB are described by acoustic oscillations in the photon-baryon plasma originating from the counteraction of gravitation and pressure forces. Both baryonic and dark matter interact gravitationally. However, only baryonic matter interacts electromagnetically. Therefore, while collapsing under the effect of the gravitation field, the baryonic matter can counteract the increase of overdensity region more effectively due to the radiation pressure from interaction with photons, while dark matter does not [1, 14]. Hence they affect the CMB differently. Indeed, the energy density (ρ) of baryonic and dark matter can be derived from the CMB power spectrum peaks, shown in Fig.1.4. Often, the *density parameter* Ω, obtained by dividing ρ by the critical density ρ_{cr}[1], is reported to compare more easily the different constituents of the Universe. The current best-fit, from the Planck collaboration [15, 16], suggests a flat Universe with the following energy budget[2]:

$$\mathrm{H_0} \sim 67.32 \ \mathrm{km\ s^{-1} Mpc^{-1}} \ ; \ \Omega_\mathrm{b} \sim 0.049 \ ; \ \Omega_\mathrm{c} \sim 0.264 \ ; \ \Omega_\Lambda \sim 0.684,$$

---

[1] The critical density $\rho_{cr} = 3H^2/8\pi G$, where H is the Hubble constant, and G is Newton's gravitational constant, is the parameter that defines the geometry of the Universe [1].

[2] Planck collaboration provides different sets of cosmological parameters, depending on the model and data used. These values come from table 7 in [15]

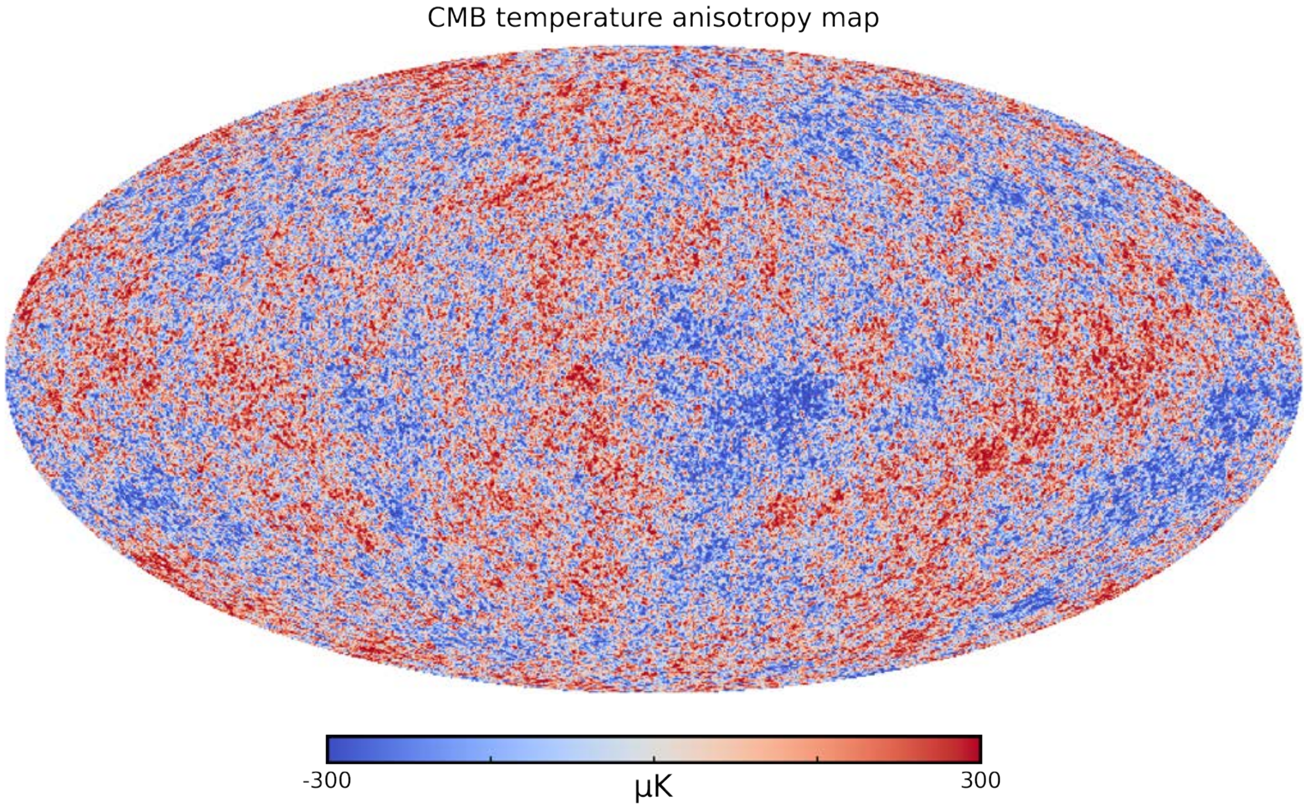

Figure 1.3: CMB temperature anisotropies map in Mollweide projection, Galactic coordinates, and Kelvin temperatures. Plot reproduced using [17]. The data for the map is available in [18].

where H_0 is the Hubble constant, Ω_b is the baryonic density parameter, Ω_c is the DM density parameter and Ω_Λ is dark energy contribution to the total energy budget, by far the most dominant term.

In favor of the Planck results, there is the baryon density estimation derived from Big Bang Nucleosynthesis (BBN). The amount of light elements, like helium and deuterium, are correlated with Ω_b. These elements started to form when the Universe temperature was around 1 MeV. Before that, any atom or nucleus produced would have been immediately destroyed by high-energy photons. Knowing the conditions of the early Universe and the relevant nuclear cross-sections, the initial abundance of all the elements can be calculated [1]. In addition, these abundances can be measured, e.g., absorption features in the spectrum of distant quasars [19]. Then, the baryon density can be derived by combining these measurements with BBN calculations. The agreement with the CMB results is remarkable, although tensions with the measures exist, which have not yet been resolved, such as the abundance of ^{7}Li [20].

1.1.3 Dark Matter in the Milky Way

The evidence of DM in the Milky Way is manifested through the inconsistencies in the velocity curve if only the baryonic contribution is considered. In Fig.1.5, the Milky Way rotation profile is shown according to [21, 8]. Our position inside the disk of the Milky Way poses additional challenges in measuring its kinematics. Different experimental approaches need to be used to derive the Milky Way rotation curve for a wide range of radii. Combining the outcomes is not straightforward, and this lead to an increase in the uncertainties of the galaxy description [21, 8, 22, 23].

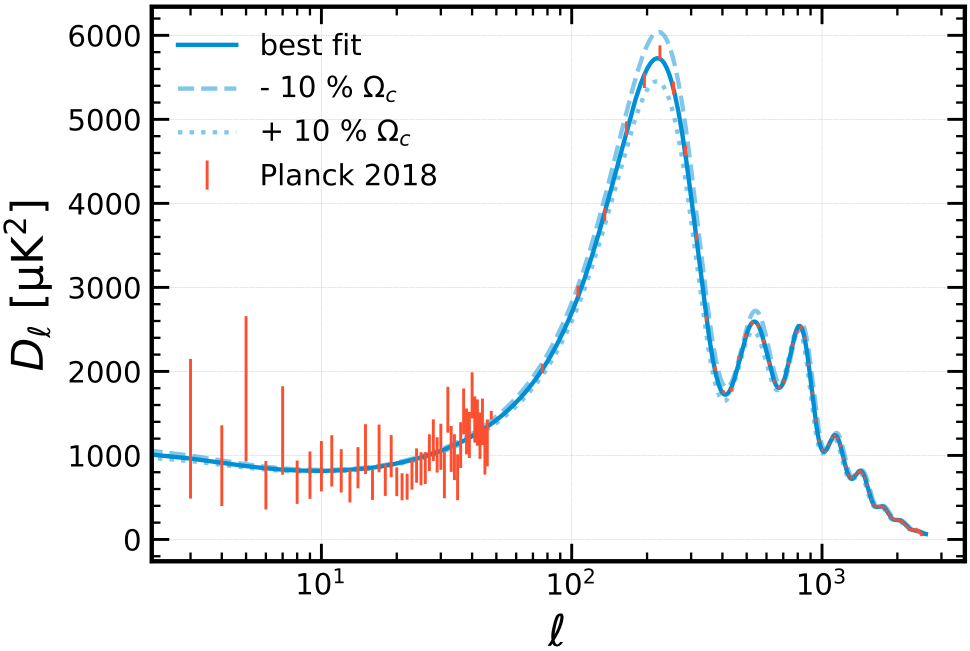

Figure 1.4: CMB temperature power spectrum. The effect of adding or removing dark matter from the total energy budget of the Universe is shown with the dashed and dotted curves, respectively. Plot reproduced using [17]. The best fit is shown in with the solid line, and it has been taken from [15].

The Milky Way DM density profile and its velocity distribution at the radius of the Earth are key ingredients for interpreting the results of laboratory experiments. These depend on the model used to describe the DM halo. In the literature, several descriptions are available. Some of them are collected in Fig.1.6. Here the different halo profiles, normalized to be equal at 20 kpc, are shown. Two categories can be appreciated: cored halo models, which are a modification of the isothermal model ($\rho_{\text{isothermal}} \sim r^{-2}$ [24]) with a steeper decrease of density at large radii, and central cusp models, which are based on extensive N-body numerical simulations which predict an infinitely increasing central peak [21]. Different models lead to a different description of the Milky Way; consequently, the local density of dark matter can change.

The different models lead to different values for the local DM density, which vary significantly between 0.2 to 0.6 GeV/cm^3. The recommended value to interpret laboratory experiments is derived using a simplified smooth, isothermal, and spherical dark matter halo called *standard halo model* (SHM) [26], where the local DM density is assumed to be 0.3 GeV/cm^3 [27]. In Fig.1.7, the latest local DM density estimations and, with a dashed horizontal line, the recommended value are shown.

As it will be shown in section 1.3.1, the other fundamental ingredient for laboratory experiments is the flux of dark matter passing through the Earth. The DM velocity distribution is usually described by an isotropic truncated Maxwell–Boltzmann distribution. The distribution, in the galactic rest frame, can be written as:

$$f(\vec{v}) = \frac{1}{N(v_0)} e^{\left(-\vec{v}^2/v_0^2\right)} \Theta(v_{esc} - |\vec{v}|) \tag{1.1}$$

where the most probable velocity v_0 is $\sim$ 238 km/s. Even if it is not physical, a hard cut-off Θ, which is zero for velocity greater than the escape velocity v_{esc} and one otherwise, is introduced to account for the limit

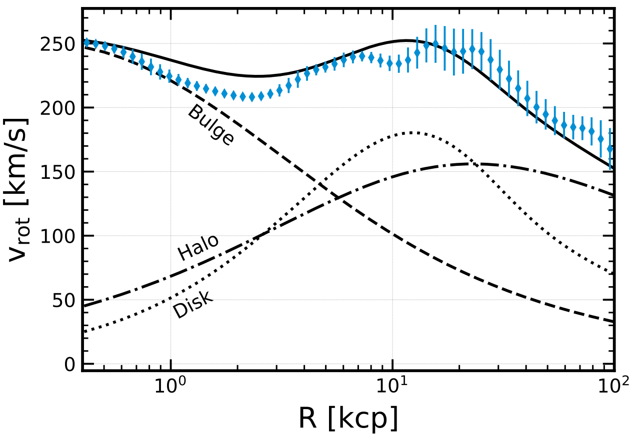

Figure 1.5: Rotational velocity profile of the Milky Way deconvolved in the three main components. The Navarro-Frenk-White (NFW) [25] is adopted for the dark matter density profile. The curves are reproduced using the data (blue points) and models (black lines) from [21, 8].

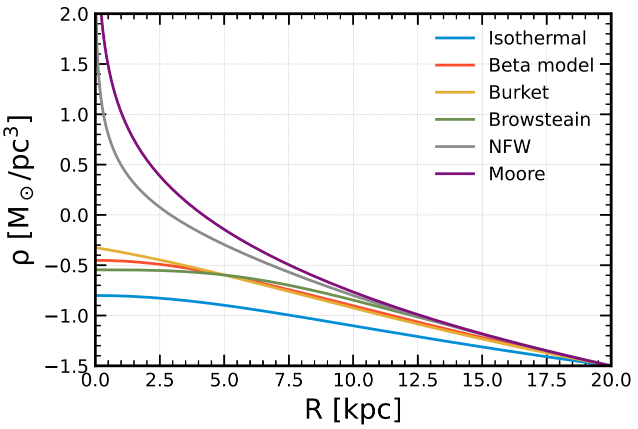

Figure 1.6: The different theoretical DM density profiles normalized at R = 20 kpc following [21]. Different models lead to different values for the local DM density. The plot is reproduced using the information in [21], where the models represented here are discussed.

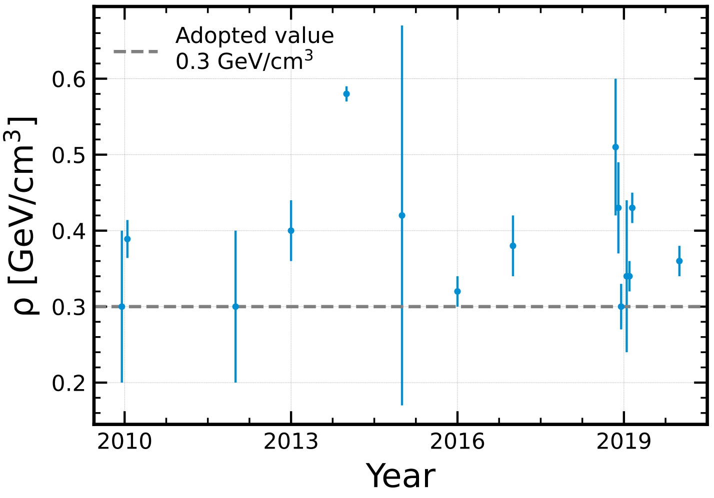

Figure 1.7: Measured dark matter density evolution in the last years. Reproduced using data from [21]. The dashed gray line represents the recommended value from [27].

the gravitation bound does not hold anymore. The v_{esc} is estimated to be around 500 to 600 km/s. $N(v_0)$ is a normalization factor such that the integral of $f(\vec{v})$ over all the velocities is 1. Earth-based experiments prefer to express the velocity distribution in the laboratory frame. This requires a Galilean boost, as shown in Eq.1.2, considering the motion $\vec{v}_\odot$ of the Sun to the Galaxy, which is characterized by the canonical value for the disk rotation speed $v_{\mathrm{rot}} \sim 220$ km/s [28, 29]. The motion $\vec{V}(t)_\oplus$ of the Earth around the Sun must also be considered. This changes throughout the year with an average value of $V_\oplus \sim 29.8$ km/s, leading to an annual modulation in the velocity distribution. An exhaustive discussion on the velocity distribution to the laboratory frame can be found in [30].

$$f(\vec{v})^{Lab} = f(\vec{v} + \vec{v}_\odot + \vec{V}(t)_\oplus) \tag{1.2}$$

Even though the SHM is commonly used, it has some tensions with the prediction from dark matter-only halo simulation, e.g., Via Lactea II [31]. These frictions arise from different initial assumptions, which can lead to very different results. In the case of Via Lactea II, the simulation reveals a fractal nature of dark matter clustering. Therefore, the isotropy hypothesis may not be valid, which may lead to the presence of substructures in the local distribution of DM. Including baryons in the simulation of disk galaxy formation, like the MW, significantly change the DM density profile and the expected velocity distribution, diminishing the difference with SHM [32]. Moreover, a recent measurement of metal-poor stellar halo velocity distribution tends to agree that a significant DM halo component is not virilized [33]. In conclusion, the understanding of our galaxy is still far from being fully grasped.

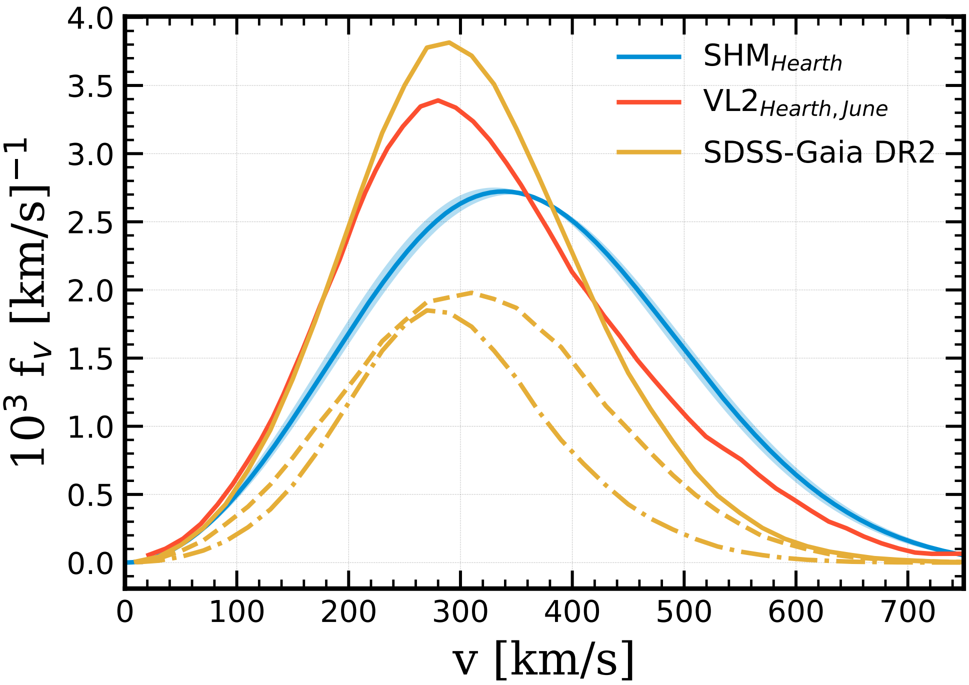

Figure 1.8: Dark Matter velocity distribution in the Earth rest frame. SHM computed using [34]. The shaded blue band represents the effect of yearly Earth rotation. Via Lactea II curve extracted from [35], while SDSS-GAIA curve is from [33]. The latter counts two components: the dashed line for the halo and the dashed-dot lines for the substructure. The SDSS-GAIA data were fetched from [36].

1.2 The anthology of dark matter

The following sections outline some dark matter candidates and their features. Astrophysical observations place boundaries on the properties that a DM candidate needs to satisfy. These properties are discussed in the following section. Then, an overview of the DM candidates is given. Only a few candidates are discussed extensively in this thesis.

1.2.1 Dark matter properties

The modern Universe picture is based on the ΛCDM model [1]. In a nutshell, we live in a zero-curvature Universe dominated today by non-baryonic dark matter and dark energy, associated with the cosmological constant Λ, with initial perturbations generated by inflation in the very early Universe. The DM is responsible for the gravitational collapse of ordinary matter and eventually for forming the large-scale structures in the Universe observed today. Instead, dark energy is responsible for the Universe's accelerated expansion. The ΛCDM model is widely accepted for its ability to make predictions for two important observables: the power spectrum for the CMB, discussed in section 1.1.2, and the matter power spectrum, namely the spectrum of density fluctuations in the matter. The latter one has not been discussed in this manuscript. More information can be found in [1].

Regardless of the particle nature of a dark matter candidate, ΛCDM and cosmological/astrophysical observations require certain ingredients for the candidate to be met. Here the main ones are listed.

Dark in the sense that it should not have an electric charge, thus without electromagnetic interaction, or at least extremely weak.

Cold or more generally non-relativistic at the decoupling epoch, otherwise the large-scale structure of the Universe would be more difficult to explain[3]. This is a less strict property since there are relativistic candidates that can explain DM.

Collisionless or at least much less collisional than baryons. This is motivated, for instance, by the bullet cluster structure shown in Fig.1.2, which otherwise could not be explainable with the DM paradigm.

Stable or at least with a lifetime longer than the age of the Universe.

1.2.2 Dark matter candidates

There are several potential candidates that make up the DM. The mass range of interest, or equivalently the energy, is shown in Fig.1.9.

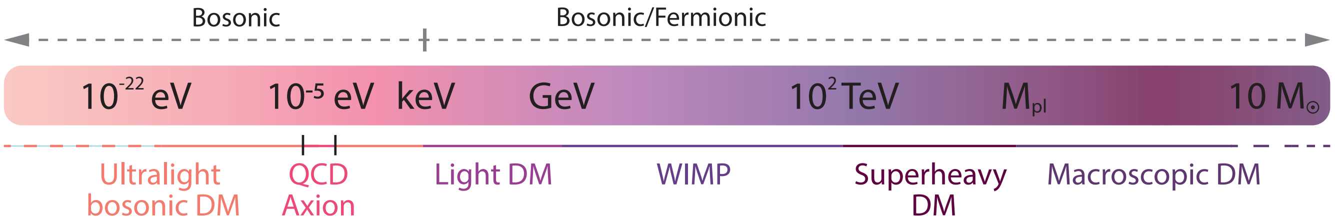

Figure 1.9: Dark Matter candidates. Sketch inspired by [37]

It can be a single fermion or a single boson. In the case of fermion, the Fermi Dirac statistics, plus the measured DM density, constraints the mass to be larger than $\mathcal{O}(\text{keV})$ [38]. Whereas for boson, either

---

[3] the C in ΛCDM stands for cold, namely cold dark matter

scalar or vector, the limit is $\sim 10^{-22}$ eV by imposing that the de Broglie wavelength has to be smaller than $\mathcal{O}(\text{kpc})$ to be able to form the dwarf galaxies [39]. The entire span of candidates below keV is usually called ultralight bosonic dark matter. In this mass range, there is a rather small but important sliver around 10^{-5} eV, which correspond to the classic QCD axions [40].

The transition from particle to composite object is around 10^{19} GeV, namely the Planck scale, at which an elementary particle with mass greater than this bound would be smaller than Schwarzschild radius $2M/M_{\text{Pl}}^2$. In this region, the most appealing candidates are *massive astrophysical compact halo objects* (MACHOs), which are large and non-luminous objects made from baryonic matter [41], and Primordial Black Holes which might have been formed in the first stages of the Universe from the collapse of density perturbations during the radiation domination epoch [42].

The region more explored is from keV up to ~ 100 TeV, populated by thermal DM candidates. These candidates are postulated to be in equilibrium with the SM bath at the decoupling epoch. Here is possible to distinguish two ranges. The first one is for sub-GeV mass candidates, called light DM, which are generally connected to *dark* or hidden extension of the SM [43, 44]. Whereas, the GeV-TeV mass range corresponds to weakly interacting massive particles (WIMPs), motivated, for instance, by supersymmetric extension of SM [45, 46] and Universal Extra Dimensions extension [47]. The equilibrium feature is not necessary for this mass range. Indeed, there are interesting candidates, such as sterile neutrino models [48] or Freeze-in DM models [49], that do not rely on this bound.

It is possible to show that DM candidates, once in thermal equilibrium with the SM bath, cannot have a mass greater than ~ 100 TeV. This is known as unitary bound [50]. In between the $\mathcal{O}(10\text{ TeV})$ scale and M_{Pl}, a particle explanation for the dark matter conundrum is still conceivable, such as WIMPzillas [51].

For an in-depth discussion of each possible DM candidate, refer to [46, 52, 45]. Only neutrinos, WIMPs, and axions will be further discussed.

Neutrinos

Neutrinos have been for long considered a valid candidate for DM. However, to account for all the DM they need to have a mass of the order of $\mathcal{O}(10\text{ keV})$. This does not agree with the current laboratory constraint on the neutrino mass, which is < 0.8 eV at 90% CL [53]. The upper bound on the total neutrino density is then $\Omega_\nu h^2 \leq 0.008$[4]. This bound is even tighter when it is derived from the analysis of CMB anisotropies combined with large-scale structure ($\Omega_\nu h^2 \leq 0.00067$ at 95% CL)[5] [15]. Therefore, neutrinos do not contribute sufficiently to the total energy budget to be the dominant dark matter component. To bypass the mass problem, in 1993, Dodelson and Widrow proposed an additional more massive right-handed, or sterile, neutrino without Standard Model weak interactions, apart from mixing with the left-handed, or active, SM neutrinos. With the right production mechanism, a sterile neutrino with a mass of 92 eV could solve the DM problem [54]. A minimal SM extension with three sterile neutrinos has been proposed. One is at the keV scale to account for DM, and two heavier sterile neutrinos, in the range of 150 MeV to 100 GeV, to explain the neutrino oscillation and the baryon asymmetry in the Universe [55].

---

[4] Following [15], $\Omega_\nu h^2 \simeq \sum m_\nu/93.04\text{eV} \sim 0.8\text{eV}/93.04\text{eV} \sim 0.008$

[5] this implies $m_\nu < 0.23$ eV

Axions and axion-like particles

The strong interaction in the SM allows for the violation of the combination of charge conjugation symmetry (C) and parity symmetry (P). However, no violation of the CP-symmetry has ever been observed in experiments testing the strong interaction. This problem is known as *strong CP problem*. In the context of, Peccei and Quinn [56], Weinberg and Wilczek [57] identified a new pseudo Nambu-Goldeston boson connected to global chiral U(1) spontaneously broken symmetry as a possible solution. This new particle, known as QCD axions (A), would solve the strong CP problem as long as the following relation is valid:

$$m_A = 5.70(7)\mu\text{eV}\left(\frac{10^{12}\text{ GeV}}{f_A}\right), \tag{1.3}$$

where m_A is the mass of the QCD axion and f_A is the scale at which the new symmetry breaks. As described by Peccei and Quinn, the phenomenology of the axions foresees the mixing with SM particles, e.g., photons, nucleons, and electrons, such that the couplings are proportional to the axion mass m_A. Even though QCD axions are supposed to be light, they are excellent DM candidates. Vacuum realignment and topological defects are two well-justified mechanisms within the Peccei-Quinn framework that provides a non-thermal mechanism of a large non-relativistic (cold) population [58]. Considering the current astrophysical and cosmological mass constraints, traditional particle physics experiments cannot observe axions produced in the early Universe. Their search requires different techniques, based on high-precision sensors of continuous wave signals [44]. However, thanks to the mixing with SM particles, they might be produced abundantly in other dense regions, like the Sun, and they can be detected by particle physics experiments that look for energy depositions in a ground base detector.

Other extensions of SM predict the existence of a more general light boson also linked to a spontaneously broken symmetry at a high energy scale, f_a, which shares with QCD axions the phenomenology [58]. The axion-like particles, or in short ALPs (a), are not connected to the Peccei-Quinn mechanism, and, therefore, the relation between m_a and the interaction couplings is not guaranteed. These more general axion particles can also be produced not-thermally through a vacuum realignment mechanism and contribute to the dark matter. The m_a mass and coupling with photons are independent, making the parameter space available for ALPs significantly broad and, therefore, their search attractive.

Weakly interacting massive particles

A class of DM candidates that satisfy all the properties discussed in section 1.2.1 are the weakly interacting massive particles, or WIMPs [59].

The thermally produced WIMPs have received great attention from the scientific community since the thermal decoupling framework provides a successful production mechanism known as freeze-out. This mechanism is based on the competition between the rate Γ of a certain number density-changing interaction process and the expansion of the Universe, governed by the Hubble factor H, both time-dependent.

Considering Γ as the annihilation and pair productions rate, when $\Gamma \gg$ H, the interactions are very efficient, and the number density is in equilibrium, more precisely, chemical equilibrium. However, due to the expansion of the Universe, there is a temperature/energy epoch at which the Γ becomes smaller than

H. At this point, any number density changing interaction, besides the dilution due to the expansion, will become inefficient. Decoupling will then take place, and no interaction will occur. The freeze-out condition will be satisfied, and the number density will no longer change, besides getting more and more diluted due to the Universe's expansion.

An exhaustive description of the freeze-out mechanism can be found in [60]. It is assumed that in the very early and hot Universe, SM species and DM were in thermal equilibrium thanks to the following process:

$$\chi + \chi \leftrightarrow \mathrm{SM} + \mathrm{SM} \tag{1.4}$$

$$\chi + \mathrm{SM} \leftrightarrow \chi + \mathrm{SM} \tag{1.5}$$

where with the letter χ is represented a generic WIMP. The annihilation and production processes in Eq.1.4 guarantee the chemical equilibrium for temperatures above the WIMP particle mass. The elastic scattering process with SM particles in Eq.1.5 guarantees the kinematic equilibrium. The kinematic decoupling will not be discussed here, but the epoch at which this happens is important for the formation of structures in the Universe [61, 62]. For $T_{\text{Universe}} \sim \mathrm{M}_\chi$, the balance between annihilation and production is destroyed: There is not enough energy for the lighter species to produce WIMP. As a consequence, the total number of WIMP particles decreases. The number density decreasing is determined by the Boltzmann equation for the non-relativistic case. The Eq.1.6 shows the relation between number density n and temperature T in the relativistic case and not.

$$\begin{aligned} n_{\text{rel}} &\propto T^{\,3} \text{ for } m \ll T \\ n_{\text{non-rel}} &\propto (mT)^{3/2} e^{-m/T} \text{ for } m \gg T \end{aligned} \tag{1.6}$$

The exponential suppression keeps going until the expansion of the Universe overcomes the annihilation rate: $\Gamma_{\text{annihaltion}} \lesssim H$. When the density becomes too low, the annihilation reaction becomes inefficient, and the number density starts to depart from equilibrium. The epoch at which this happens is called freeze-out.

Introducing the comoving number density as $\mathrm{Y} \sim n/s^3$, where n is a number density and $s \sim T^3$ is the entropy density, it is possible to show that if no entropy is produced $\mathrm{Y}_{\text{today}} = \mathrm{Y}_{\text{freeze-out}}$. This means that for epochs in which the Universe temperature is smaller than the freeze-out temperature, the WIMPs are a sort of *isolate system*, and its comoving number density is a constant. In Fig.1.10 is sketched the time evolution of Y [63].

Given this result, it is possible to write today's WIMP relic abundance $\Omega_\chi(T_0)$ as a function of thermally averaged annihilation cross-section σ_{ann} times velocity v [60]:

$$\Omega_\chi(T_0)h^2 \simeq \frac{m_\chi n_\chi(T_0)}{\rho_{cr}} h^2 = \frac{T_0{}^3}{\rho_{cr}} \frac{x_{\text{freeze-out}}}{\overline{M}_{Pl}} \frac{1}{\langle \sigma_{ann} v \rangle} h^2 \tag{1.7}$$

where $T_0 \approx 2.35 \times 10^{-13}$ GeV [63] is the today temperature of the Universe, $\rho_{cr} \approx 8 \times 10^{-47}\, h^2$ GeV^4 is the critical energy density, $\overline{M}_{Pl} \approx 2.4 \times 10^{18}$ GeV [63] is the reduced Planck mass and x is equal to $\mathrm{m}_\chi/\mathrm{T}$. For

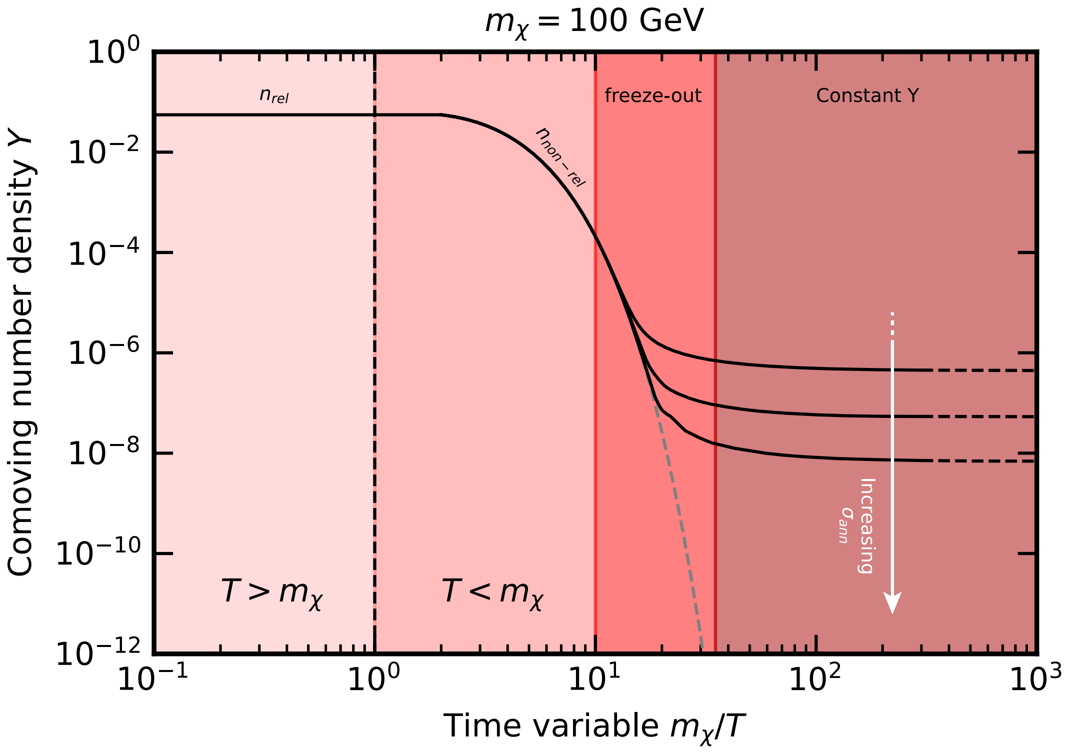

Figure 1.10: Comoving density evolution. The gray dashed line shows the number density if the annihilation reactions are in equilibrium with the cosmic plasma. The x-axis m_χ/T can be interpreted as a time variable. Hence, at early times ($T > m_\chi$), the reaction rate is much greater than the Universe's expansion rate. However, as soon as the temperature of the Universe falls to m_χ, the chemical equilibrium breaks and dark matter number density n starts to decrease. When the Universe expands far enough, annihilation becomes ineffective, and the n deviates from the equilibrium curve. From here on, no density-changing processes are acting anymore besides the dilution due to the Universe's expansion. Hence, the comoving density freezes out and approaches a constant value. The higher the annihilation cross-section, the smaller the constant comoving density.

convenience, all quantities are expressed in natural units[6]. The value of $x_{\text{freeze-out}}$ can be estimated by the Boltzmann equation, assuming that around freeze-out, the number density of WIMP DM is equal to $n_{\text{nor-rel}}$ in Eq.1.6. The full derivation of the Boltzmann equation can be found in [64, 65]. The rigorous calculation shows that $x = 25$ is an appropriate value for masses from 100 GeV to 10 TeV [66]. Finally, considering $\langle \sigma_{ann} v \rangle \approx 3 \times 10^{-26}$ cm^3/s, the right DM relic density $\Omega_\chi \approx 0.3$ is obtained. For typical velocities, $v \approx 0.1$ c one obtains a cross-section of weak strength for WIMP with a mass around the electroweak scale [67]. This coincidence is so remarkable to the point that it is known as the WIMP miracle.

Many beyond SM models contain well-motivated WIMP candidates. Among these, there is the supersymmetry (SUSY) model, which was initially proposed as a solution to the hierarchy problem in the SM [45]. SUSY postulates the existence of *superpartners* counterpart of SM particles with spin different by one half. Another essential ingredient in SUSY extension is the conservation of *R-parity*: a multiplicative quantum number defined by the combination of baryon number, lepton number, and spin. Standard

---

[6] From the PDG[63]: $\rho_{cr} \sim 1.053 \times 10^5\, h^2$ GeV cm^{-3} and 1 $cm^{-1} \sim 1.98 \times 10^{-14}$ GeV. In addition, 1 GeV = 1.16×10^{13} K.

Model particles have R-parity $R = 1$, and the superpartners have $R = -1$. Thus, R-parity conservation implies that SUSY particles are only produced or destroyed in pairs. Therefore, the lightest SUSY particle (LSP) is stable and can only be destroyed via pair annihilation. The LSP is an electrically neutral particle, for example, the lightest neutralino $\tilde{x}_1^0$, constituting a very well-motivated WIMP candidate [45].

1.3 Dark Matter detection experiments

Astrophysical and cosmological observation provides an indirect way to observe dark matter. However, a more direct approach is needed to measure its physics properties, such as mass, coupling, and interaction cross-section with ordinary matter. In the experimental physics landscape, three different techniques are pursued: the production of dark matter candidates at particles accelerators such as the LHC, the detection of the dark matter annihilation products in high-density regions (indirect searches), and the direct detection of the scattering process of dark matter particles and ordinary matter in ultrasensitive low background experiments. A quick summary of these methods follows. A dedicated section is reserved for the direct detection method applied to WIMP searches, in which the expected signal for WIMP candidates in a terrestrial detector will be derived. The section concludes with a state-of-the-art summary of direct detection.

Collider experiments

Dark matter particles could be produced directly in high-energy proton-proton collisions through the reverse process of DM annihilation. As described in section 1.2.2, the thermal WIMP solution would suggest new physics around the electroweak scale, which can already be probed by current colliders as LHC. Although complementary, this makes colliders a precious tool for probing WIMP dark matter physics. Dark matter produced at colliders would pass undisturbed through the detector, given the tiny coupling expected with the SM sector. This would lead to an apparent violation of energy-momentum conservation. Two analysis techniques are exploited to detect the presence of DM: search for events containing one SM particle with an imbalance in the transverse momentum due to the presence of DM particles, or search for an excess of events in the invariant mass spectrum or in a specifically chosen angular distributions due to the decay of DM particles [68]. Observing a new particle species would not automatically solve the dark matter problem. It could be unstable on cosmological time scales, or its production in the early Universe could be suppressed. For a review of the field, refer to [69].

Indirect searches

The particle solution of dark matter can be indirectly probed by looking for an anomalous flux of standard model particles, such as photons, neutrinos, or cosmic rays, produced by the annihilation or decays of dark matter candidates in dense cosmological/astrophysical objects, such as galaxies, the Sun or even the Earth. Among all the regions in the Universe, dwarf spheroid galaxies are good candidates because they are expected to be dark-matter dominated [70]. Given the several types of messenger, the detection method relies on gamma-ray telescopes, X-ray telescopes, cosmic-ray detectors, and neutrino telescopes. However, any excess measured above the background requires a good understanding of the background, which is extremely model-dependent, e.g., the dark matter halo described in section 1.1.2. A comprehensive review of the field can be found in [71].

Direct searches

This methodology consists of searching for signals induced in terrestrial detectors due to the passage of dark matter particles, called direct detection. An ultra-low background level is mandatory for this rare event search. Indeed, these experiments are carried out in deep underground laboratories to shield against cosmic rays. They also require careful selection of each detector component to minimize radioactive residual in the detector materials. The detection principle is based on reconstructing the energy deposited by elastic, or even inelastic, scattering of dark matter particles with the atomic nuclei and electrons in the detecting material. The deposited energy can be transformed into heat, light, or charge, and the detectors are designed to be sensitive to one or two of these signals. Several experimental approaches exist, summarized by [72] and in the following section.

1.3.1 Direct detection of WIMP-nucleus scattering

The expected WIMP signal is usually derived in the SHM context, as described in section 1.1.3. The local dark matter density ρ_χ is assumed to be 0.3 GeV/cm^3, with the velocity distribution described by a Maxwellian distribution with the most probable velocity v_0 equal to 238 km/s and truncated at the escape velocity $v_{esc} \sim 544$ km/s. Given the chargeless nature of WIMPs, they are expected to scatter mainly with the atomic nucleus, originating a nuclear recoil (NR) that might be detectable. Being far from relativistic velocity, the WIMP-nucleus scattering can be described through classical mechanics. The momentum transferred involved is such that the scattering is coherent; namely, the WIMP sees the nucleons as a unicum, and the scattering can be treated from the nucleus point of view.

The recoil energy $\mathrm{E_{nr}}$ of a nucleus of mass m_N after elastic collision of a WIMP χ of mass m_χ and velocity v_χ, with respect to the nucleus, is equal to:

$$E_{\mathrm{nr}} = \frac{\mu^2 v_\chi^2}{m_N}(1 - cos\theta) = \frac{q^2}{2m_N}, \tag{1.8}$$

where $\mu \equiv m_\chi m_N/(m_\chi + m_N)$ is the reduced mass of the WIMP-nucleus system, θ is the scattering angle in the center of mass frame, and q is the momentum transferred in the scatter. Combining $\mathrm{E_{nr}}$ with the interaction rate, defined as $R = \phi\,\sigma\,N$, where ϕ is the flux of incident particles (that is the number density n_χ multiply by WIMP velocity v), σ is the interaction cross-section, and N is the number of targets in the detector, the differential rate as a function of energy recoil can be written as [30]:

$$\frac{dR}{dE_{\mathrm{nr}}} = \frac{\rho_\chi}{m_x}\frac{1}{m_N}\left\langle v\frac{d\sigma}{dE_{nr}}\right\rangle = \frac{\rho_\chi}{m_\chi}\frac{1}{m_N}\int_{v_{min}}^{\infty}\vec{v}f(\vec{v})\frac{d\sigma}{dE_{nr}}d\vec{v} \tag{1.9}$$

Where $v_{min} = \sqrt{m_n E_{nr}/2\mu^2}$ is the minimum WIMP velocity that can result in a recoil energy $E_{\rm nr}$. The differential rate is a featureless falling exponential: $\exp(-E_{\rm nr}/(E_0 r))$, where E_0 is the most probable kinetic energy of the incident WIMP ($1/2\ m_\chi v_0^2$) and r is the kinetic factor defined as $4m_\chi m_N/(m_\chi + m_N)^2$ (see for instance Fig.1.12).

The velocity distribution for SHM has already been discussed in section 1.1.3, the effect of Galilean boost from the galactic frame to the detector frame, and Earth's motion around the Sun are discussed in depth in [30]. The motion of the Earth produces an annual variation on the event rate of $\mathcal{O}(5\,\%)$ from June to December. Hence, the expected number of dark matter events will modulate over the year.

As was anticipated before, in the limit of low momentum transfer $\vec{q}$, the nucleus can be treated as a point-like object where the WIMP scatters coherently with all the nucleons. However, this is lost when the de Broglie wavelength associated with $\vec{q}$ is comparable, or smaller, to the size of the nucleus, which is described by the empirical relation between the radius and the number of nucleons ($r \sim 1.2\ A^{1/3}$). The nuclear form factor F, which is the Fourier transform of the spatial charge distribution, takes into account the finite size of the nucleus and corrects for coherence loss such that the cross-section can be expressed as $\sigma(E_{\rm nr}) \propto \sigma_0 \times F^2(E_{\rm nr})$, where σ_0 is the cross-section at zero momentum transfer. The nuclear form factor depends on the nature of the interaction, e.g., spin-dependent [73, 74] or spin-independent [75]. Fig.1.11 shows the spin-independent form factors for 4 different detector materials. The effect is significant for target media with large atomic mass, as shown for the xenon line in Fig.1.11.

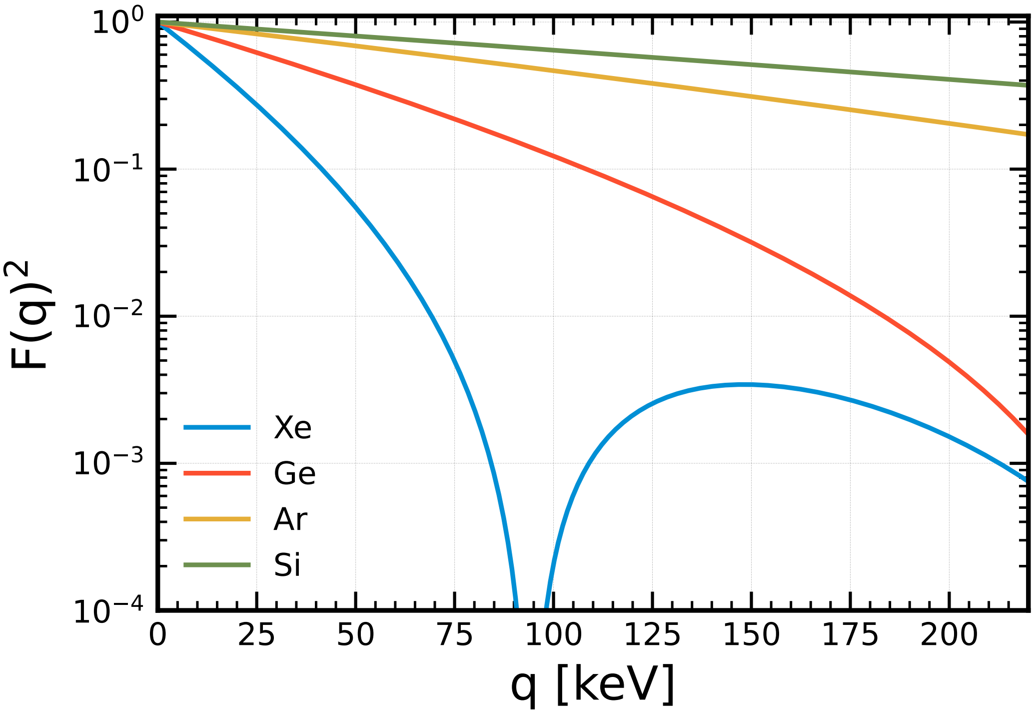

Figure 1.11: Spin independent form factors for 4 different detector materials. Plot reproduced using [34] and references within.

The interaction of WIMPs with ordinary matter is a priori unknown; it depends on the nature of WIMP couplings to quarks which are calculated through an effective Lagrangian describing the interaction of the particular WIMP candidate with quarks and gluons. Given the coherence of the interaction, the resulting cross-section is promoted to a WIMP-nucleon cross-section. It can be assumed to be the sum of spin-independent (SI) and spin-dependent (SD) contributions originating from a scalar and/or vector interaction and a spin-spin interaction, respectively [76, 77]. Other effective lagrangians, in addition to the standard SI and SD models (which are described by effective lagrangians as well), have been proposed in the literature to explore alternative nuclear coupling and responses [78].

In general, the WIMP-nucleon cross section can be written as:

$$\frac{d\sigma}{dE_{\text{nr}}} = \frac{m_N}{2\mu^2 v^2}\left(\sigma_0^{SI} F_{SI}^2(E_{\text{nr}}) + \sigma_0^{SD} F_{SD}^2(E_{nr})\right) \tag{1.10}$$

where each cross-section at zero momentum transfer is multiplied by the relative form factor. The SI cross-section can be expressed as:

$$\sigma_0^{SI} = \sigma_N \frac{\mu^2}{\mu_N^2}\left[Zf_p + (A-Z)f_n\right]^2 \tag{1.11}$$

where $f_{p,n}$ are the contributions of protons and neutrons to the total coupling strength, respectively, and μ_N is the WIMP-nucleon reduced mass. With the assumption of equal coupling strength, the SI cross-section grows quadratically with the number of nucleons A. In addition, if $m_\chi \gg m_N$ would imply $\mu^2/\mu_N^2 \approx A^2$, so the cross-section scales as $\sigma_0^{SI} \propto \mu^2 \times A^2 \approx A^4$. However, the form-factor suppression becomes more significant as the size of the nucleus increases, although it still rises rapidly with A. As a result, heavy nuclei are preferable for direct detection, such as to increase the sensitivity to WIMP scattering.

The SD cross-section is more informative if the interaction with protons and with neutrons is disentangled:

$$\sigma_0^{SD} = \frac{32}{\pi}\mu_N^2 G_F^2\left[a_p\langle S_p\rangle + a_n\langle S_n\rangle\right]^2 \frac{J+1}{J} \tag{1.12}$$

In Eq.1.12, G_F^2 is the Fermi coupling constant, J the total nuclear spin, and $a_{p,n}$ are the proton and neutron couplings. The average spin contributions from proton and neutron are denoted with $\langle S_{p,n}\rangle$. SD scattering is often subdominant compared to SI scattering in direct detection experiments for two main reasons: absence of A^2 enhancement and suppression from spin-zero isotopes. Indeed, only nuclei with non-zero J can contribute.

Finally, the expected number of events in a detector is derived by integrating Eq.1.9, as shown in Eq.1.13.

$$N_{\text{events}} = T\int_{E_{\text{low}}}^{E_{\text{high}}} dE_{\text{nr}}\, \epsilon(E_{\text{nr}})\frac{d\sigma}{dE_{\text{nr}}} \tag{1.13}$$

T is the data taking time of the experiment, E_{low} and E_{high} are the detector energy threshold and the upper boundary, respectively, and ϵ contains the detector response effects and analysis efficiency. The differential rate as a function of recoil energy for four different detector materials is shown in Fig.1.12. The solid line is for $m_\chi \sim 1$ TeV/c^2, while the dashed line is for $m_\chi \sim 100$ GeV/c^2. Going to high E_R, the form factor effect in the xenon curves is evident. However, in the low recoil energy range, it is the material with the highest events yield. Assuming the SHM, a $\sigma_n \sim 10^{-47}$ cm^2, and $m_\chi \sim 100$ GeV/c^2, the spin independent rate is $\sim \mathcal{O}(1)$ events/(t × yr) for recoil energies below ~ 10 keV. High exposure, low energy threshold, and ultra-low backgrounds are required to be sensitive to such a small signal. At last, these searches also rely on distinguishing between (nuclear recoil) signal and (electronic recoil) background events. This will be further discussed in section 3.1.

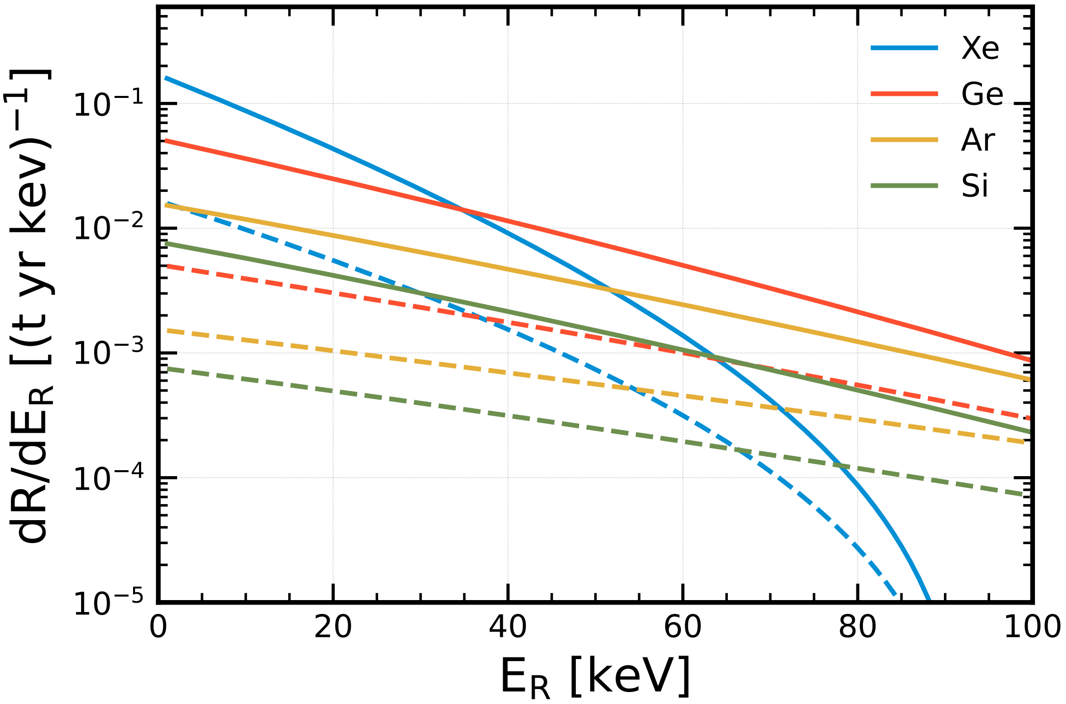

Figure 1.12: Spin-independent differential rate in the terrestrial detector for four different detector materials. Two WIMP masses are shown: 1 TeV/c^2 with solid lines and 100 GeV/c^2 with dashed lines. The spin-independent cross-section assumed is 10^{-47} cm^2. Plot reproduced using [34].

1.3.2 State of the art in direct detection

The direct detection landscape is wide and embraces several different types of experiments. A detailed review of their current status and future plans can be found in [79]. Here, the leading technologies are briefly summarized, and the current status of the spin-independent searches is presented.

The first technology presented here goes under the category of bolometers, also called cryogenic detectors, given their working temperature of around 10 ÷ 20 mK. They are based on collecting the deposited energy following a particle interaction as heat signals in the form of phonons by measuring the temperature increase. Adding the scintillation readout, scintillation bolometers like CRESST [80], or the charge readout, semiconductor bolometers like SuperCDMS [81] or CDMSLite [82], it is possible to perform particle discrimination. Due to the low energy, $\mathcal{O}(10$ meV$)$, needed to produce elementary excitations, namely the phonon, this technology can achieve eV-scale energy resolution and energy thresholds. Thus, bolometers are indispensable for probing the GeV and sub-GeV WIMP mass range where the recoil energy is $\leq \mathcal{O}(\text{keV})$. The main limitation is the exposure of the order of kg × day, which is not comparable with the ton × yr scale of the others technologies, such as noble liquid based detectors.

Detector technologies based on noble liquid or gas offer several advantages. The most used are xenon and argon. They are excellent scintillators, and they require $\mathcal{O}(\mathrm{eV})$ for electron-ion pair production. This allows to use them in scintillation mode, such as DEAP-3600 [83], or combining light and charge readout, such as Dark-Side [84, 85, 86], LUX [87, 88], LZ [89, 90], PandaX-II[91], PandaX-4T [92], and the XENON experiments [93, 94, 95, 96]. The target purity is, in general, worse compared to bolometer detectors. However, distillation and purification techniques reduce the impact of radioactive contaminants and electronegative impurities. The background from the surrounding is efficiently suppressed thanks to the high density ($\rho_{\mathrm{Xe}} \sim 2.94$ g/cm^3, $\rho_{\mathrm{Ar}} \sim 1.40$ g/cm^3 at their boiling points temperature [72]) and, hence, thanks to the self-shielding feature. Charge-to-light ratio provides an effective tool for particle identification, further enhanced in the argon-based detectors by the pulse shape analysis of the scintillation signals. In addition, the $\mathcal{O}(\mathrm{keV})$ energy threshold and resolution and the ton-scale size make this technology on of the best methods to look at WIMP scattering. An in-depth discussion of the xenon-based detector is presented in chapter 3.

Together with experiments described previously, other technologies help to explore the dark matter parameter space. These include scintillating crystals, ionization detectors, and bubble chambers [79]. The last experiment which will be discussed is DAMA/LIBRA experiment. The detector is based on 25 ultra-pure scintillator crystals of thallium-doped sodium iodide (NaI(Tl)), each with a 9.70 kg mass. Photomultipliers, coupled to crystals, record the scintillation light originating after the interaction of a particle in the crystal [97]. DAMA/LIBRA collaboration claims 12.9σ evidence of a modulating dark matter signal over 20 independent annual cycles and in various experimental configurations [98, 99], which is in tension with the other results. The suggested mass and cross-section have been widely probed by several experiments without finding any evidence. These results are still debated in the community.

Besides DAMA/LIBRA, no experiment observed any signal which can be interpreted as due to dark matter particle interaction. Fig.1.13 shows the spin-independent parameter space currently excluded. It can be seen that the current detector generation is approaching the so-called neutrino fog [100], while the following experiments DARWIN [101] and ARGO [102] are expected to probe it. This region will limit the WIMP sensitivity due to neutrino-induced background events via coherent scattering of neutrinos with the nucleus, called CEνNS. This $\nu + A_N^Z \to \nu + A_N^{\prime Z}$ processes due to astrophysical neutrinos, e.g., from the Sun, will resemble the WIMP signature posing additional challenges on WIMP searches [103, 104].

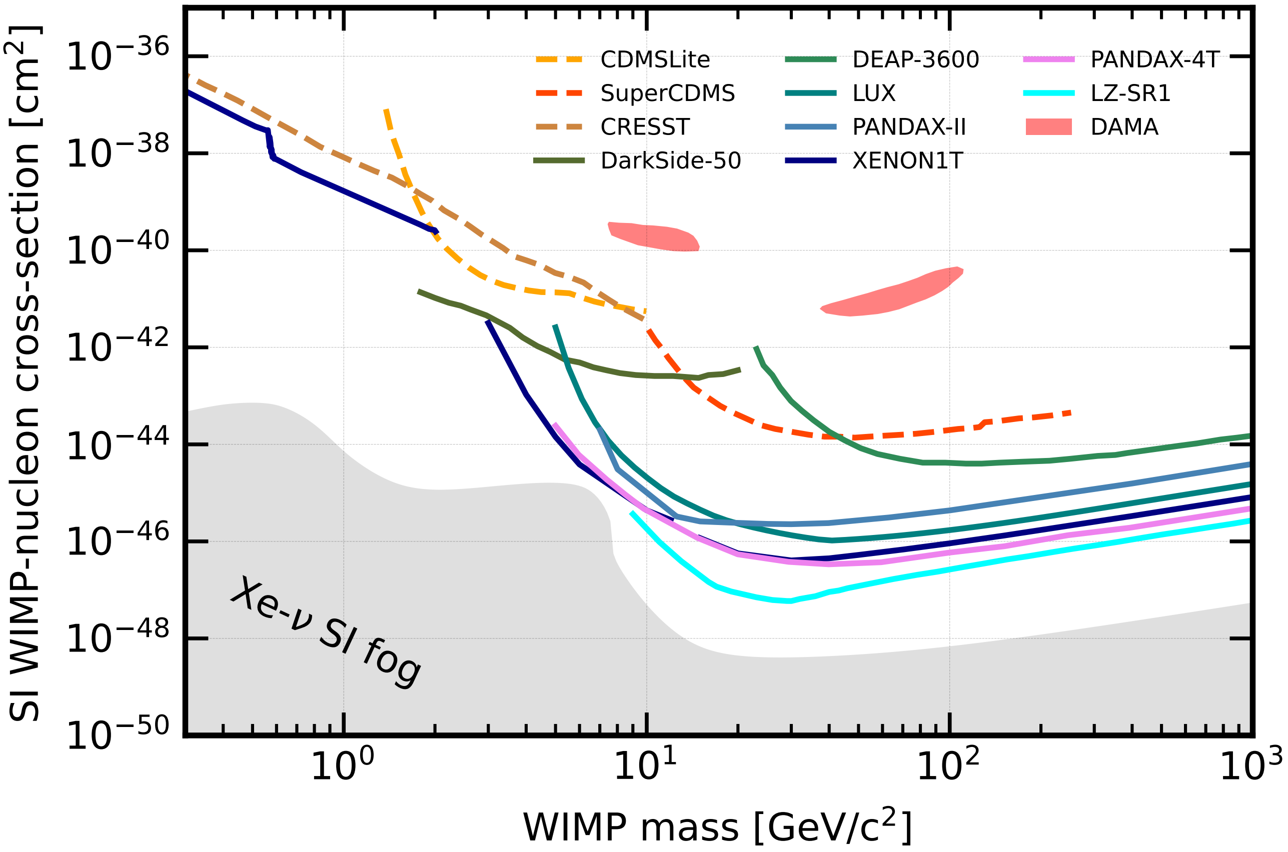

Figure 1.13: Up-to-date upper limits on the spin-independent DM-nucleon cross-section as a function of DM mass. Dashed lines represent the limits from bolometers detectors, while solid lines show the noble gas-based detectors. The red contour regions are from the DAMA/LIBRA experiment. The grey region represents the neutrino fog, considering xenon as the detector medium. The references are in the text.

2

Invisible nucleon decay

Within the Standard Model of particle physics, the baryon number (B) is a conserved quantity. This implies that the proton, which is the lightest baryon, must be stable. However, there are several reasons to expect that B is not a true symmetry of nature. One is the asymmetry between matter and antimatter observed in the Universe. This imbalance could be explained if there were a mechanism of baryon number violation, which would eventually lead to the decay of the proton.

This chapter introduces the matter-antimatter asymmetry problem and discusses the proton, or more generally, the nucleon decay search programs, focusing on the invisible decay searches carried out with xenon-based detectors.

2.1 The baryon asymmetry of the Universe

Antimatter was first postulated by Paul Dirac while trying to combine the theory of special relativity with the concept of quantum mechanics [105]. Dirac's theory foresees that fermions can manifest themselves in two forms with identical mass but opposite quantum numbers, e.g., electric charge. With the discovery of the positron by Carl Anderson [106, 107], Dirac's hypothesis was accepted by the scientific community and laid the foundation for quantum field theory, which forms the foundation of the Standard Model (SM) of particle physics.

Everyday experience indicates that antimatter is not present in large quantities in the nearby vicinity. At the time of Dirac, the concept of the Big Bang was not yet formulated; hence, the matter-antimatter asymmetry was explained by assuming that the Universe was set up like this [108]. As discussed in section 1.1.2, the Universe was hot at the early stages, and the antimatter should have been present when pair-creation and annihilation reactions were in thermal equilibrium. With the Universe expansion and the consequent cooling, the pair-creation stopped, and almost all particles and antiparticles annihilated with each other, with a small amount of matter surviving. The difference between the number of baryons N_B and anti-baryons $N_{\bar{B}}$ divided by their sum just before antiprotons disappeared from the primordial plasma is used to quantify the baryon asymmetry of the Universe, or in short, BAU (η)[1]. The parameter η is related to the remnant density of baryons ρ_B, which can be determined independently by the Big Bang Nucleosynthesis argument and CMB power spectrum [109]. Both consistently give values of $\eta \sim 10^{-10}$ at the time of the disappearance of antiprotons from the primordial plasma. Then, for 10^{10} quarks, there were $(10^{10} - 1)$ antiquarks. The symmetric part annihilated into photons and neutrinos, while the asymmetric part survived and gave rise to galaxies, stars, and planets. Therefore, the BAU ($\eta \simeq 1$) that is observed today was generated from a tiny initial asymmetry.

Most of the theoretical efforts are directed towards developing dynamic asymmetry from a matter-antimatter symmetric initial state, either directly in the baryon sector, called baryogenesis, or in the lepton sector, called leptogenesis, which is then transferred to the baryon sector. To have successful dynamic asymmetry, three ingredients need to be satisfied. These ingredients, called Sakharov conditions [110, 111], are violations of baryon number conservation, violation of charge conjugation (C) symmetry and charge conjugation parity (CP) symmetry, and departure from thermal equilibrium. The first one ensures that there are processes that produce more baryons than anti-baryons. The second one predicts that processes producing baryons and anti-baryons are unbalanced towards the first species. Last, the departure from thermal equilibrium avoids washing out the generated baryon asymmetry. The Standard Model of particle physics and the modern cosmology model (ΛCDM) fulfill all three Sakharov conditions. Baryon number is violated by sphaleron processes [112, 113, 114], a non-perturbative weak process that violates baryon and lepton number conservation while preserving their difference. Moreover, C and CP are violated by the weak interaction [115], and the departure from thermal equilibrium is fulfilled thanks to the expansion of the Universe. However, these processes are insufficient to explain the $\eta \sim 10^{-10}$. Therefore, to explain the BAU, additional sources of violation of baryon number conservation and violation of C and CP symmetries are needed.

BAU is not the only reason that the exact conservation of baryon number B is in question. The B conservation in the Lagrangian of the Standard Model arises accidentally. Namely, all the terms that could violate B have dimensions larger than 4, and they do not enter in the description. In quantum field theory, the action describes the evolution of a state, namely, the integral over spacetime of the Lagrangian. Among other requirements, the Lagrangian must be renormalizable, which implies that it must contain only terms of dimension less than or equal to four in the fields and their derivatives [116]. However, explicit B-violation is a prediction of Grand Unified Theories (GUTs) [63] where the proton is allowed to decay. The idea of GUT is that the symmetry groups in the Standard Model, namely $U(1)$ for the electromagnetic force, $SU(2)$ for the weak interaction, and $SU(3)$ for the strong interaction, are a subgroup of a larger symmetry which manifests itself at energies above $\Lambda \sim 10^{14\div16}$ GeV. Below this energy, the symmetry is spontaneously broken and the SM interactions require individual descriptions. Above that, the coupling constants converge to a single value. In the GUT frameworks, quarks and leptons belong to one family, and B and L violation processes are allowed. In this extension of the SM, the proton can decay with a lifetime proportional to the GUT energy scale with $\tau \sim O(\Lambda^4/m_\mathrm{p}^5)$, where $m_\mathrm{p} = 0.938$ GeV is the proton

---

[1] Baryons and anti-baryons production and annihilation were in thermal equilibrium until the Universe temperature dropped below 1 GeV, namely the mass of the proton. This happened $\sim 10^{-6}$ seconds after the Big Bang.

mass [117]. The GUTs which predict unification scales near the lower limit of Λ, such as the $SU(5)$ proposed by Georgi and Glashow [118], have already been ruled out by the experiments. Higher dimension groups as $SO(10)$ [119] or GUT models based on supersymmetry (SUSY) have not yet been disproven. Moreover, several mechanisms within GUT have been proposed in recent years that can violate B and L, or even a combination of these, by one unit or more [120, 121, 122]. Therefore, these frameworks remain viable as BAU solutions.

Theories based on extra dimensions, such as brane worlds, also predict the decay or disappearance of massive fermions through the passage into dimensions not directly accessible to experiment [123, 124]. In these models, the electric charge is also violated. These types of decays, in which the products of the process cannot be observed, are called invisible decays. Although different in nature compared to the extra-dimension decays, invisible decays also collect those channels with neutrinos in the final state, such as $\mathrm{n} \rightarrow 3\nu$ or $\mathrm{n} \rightarrow 5\nu$ [125, 126] or into more exotic particles like majorons [127, 128]. In invisible decays, the decay products leave no traces in a detector. The search for these channels differs from the classical analyses that look for traces of the final states of nucleon decay.

2.2 State of the art of baryon number violation process

An extensive baryon number violation search program has been carried out since the mid-1970s when the first GUT was formulated. None of the experimental efforts found a significant signal. This section briefly summarizes the state-of-the-art nucleon decay research focused on invisible channels similar to that pursued in this thesis.

2.2.1 Exclusive and inclusive searches

Nucleon decay searches can be separated into two families: exclusive and inclusive [120]. Exclusive searches focus on some specific and dynamically allowed nucleon decay channels, assuming that the final state of the decay contains electromagnetically and strongly interacting particles. Experiments that look for exclusive nucleon decays require a high mass of detector material ($O(10^3)$ kton) and a sub-MeV energy threshold. The most sensitive searches come from Super-Kamiokande [129]. With $\sim$ 50 kton of water, the Super-Kamiokande experiment has been operating for over 25 years since 1996. The analysis technique relies on Cherenkov radiation from a particle passing through the detector. Hence, it is sensitive to decay modes with electromagnetically interacting particles in the final state. The Super-Kamiokande experiment holds the best limits on most of the two-body and three-body exclusive nucleon decay search, exceeding a lifetime of 10^{34} yr (at 90% confidence level) for $p \rightarrow \mathrm{e}^+\pi^0$ [130]. This experimental limit ruled out the minimal $SU(5)$ GUT. In any case, other GUTs expect the proton lifetime to be higher. Hence, this channel is still the main channel for GUTs testing. Models like SUSY SU(5) GUT, important for Dark Matter as well, predict the decay of protons into $\bar{\nu}K^+$ or μ^+K^0. The Super-Kamiokande collaboration recently published the result for the later decay mode: No evidence was observed, and a lower limit of $\tau > 3.6 \times 10^{33}$ yr at 90% confidence level has been placed for $p \rightarrow \mu^+K^0$ [131].

Even if exclusive searches constitute the strongest probes, searching for all the kinematically allowed channels is getting increasingly complicated due to the growing complexity of the final states. In this regard, inclusive nucleon decay searches are essential: A model-independent approach focusing less on the number and nature of final state particles, allowing to probe several decay channels simultaneously. Invisible nucleon decay searches belong to this category. Generally, inclusive searches have less sensitivity than exclusive ones, with nucleon(s) lifetime lower limits that span from 10^{24} yr to 10^{30} yr. Nevertheless, these searches are fundamental to cover otherwise not considered signals, such as those with neutrinos in the final states or extra-dimension decays.

Nuclear de-excitation searches are the primary technique for invisible searches. The residual nucleus and its excited energy states are known if one or more nucleons disappear in an inner shell with energy below the nucleon-emission threshold. Therefore, one can look for the subsequent γ-rays from the nuclear de-excitation to infer the nucleon decay [132, 133]. Up to date, the most stringent decay limits come from nuclear de-excitation studies of the ^{16}O and ^{12}C nuclei from the SNO+ [134] and KamLAND [135, 136] experiments, respectively. The lower lifetime limits at 90$\%$ CL for the nucleon (n and p) and di-nucleon (nn, np, and pp) invisible decays from SNO+ [137] and KamLAND [138] are collected in Tab.2.1.

Decay mode	lower lifetime limit	Reference
$n \longrightarrow inv$	$> 9.0 \times 10^{29}$ yr	[137]
$p \longrightarrow inv$	$> 9.6 \times 10^{29}$ yr	[137]
$nn \longrightarrow inv$	$> 1.4 \times 10^{30}$ yr	[138]
$np \longrightarrow inv$	$> 6.0 \times 10^{28}$ yr	[137]
$pp \longrightarrow inv$	$> 1.1 \times 10^{29}$ yr	[137]

Table 2.1: Lower lifetime limits at 90% C.L. for the nucleon and di-nucleon invisible decay modes.

Like the de-excitation searches, the radiogenic approach allows for an additional method for looking at invisible nucleon decay. Instead of looking for the γ-ray from the nuclear de-excitation, this method focuses on the radioactive decay of the daughter nuclei created by the decay of nucleons in the parent nuclei within the detector, ignoring any potential signature from the initial disappearance of the nucleons. This analysis technique is common in ultra-low-background experiments, such as the Majorana Demonstrator [139]. The disappearance of one or more nucleons in the atomic shell will create a daughter nucleus in an excited state – unless the disappeared nucleons were in the outermost shell. If the subsequent nuclear de-excitation proceeds through a γ-emission, the nature of the daughter nucleus will be defined by the number of decayed nucleons. As opposed to that, nothing can be said about the resulting nucleus if the de-excitation happens with some heavier particles (p, n, or α-particle). Given a de-excitation through a γ-ray, it is possible to look for the radioactive decay of the daughter nucleus and use it as evidence for the nucleon disappearance process [140].The application of this technique in xenon-based detectors will be discussed in the following section.

2.2.2 Xenon-based nucleon disappearance searches

Xenon-based detectors for rare events, such as DAMA/LXe [141] or EXO-200 [142], are efficient detectors for nucleon disappearance analysis thanks to their low background level, good energy resolution, and often keV energy threshold[2]. The radiogenic analysis strategy used for nucleon disappearance searches was first used by DAMA/LXe to look for baryon violation processes in ^{129}Xe [143] and subsequently in ^{136}Xe [144]. The EXO collaboration recently used this strategy to investigate tri-nucleon disappearance in ^{136}Xe [145]. The work in this thesis consists of the search for the nucleon and di-nucleon disappearance in ^{129}Xe, one of the most abundant isotopes (26.4%) in the XENONnT xenon inventory.

DAMA/LXe search for the nucleons decay into invisible channels using ^{129}Xe

The DAMA collaboration investigated the nucleon and di-nucleon disappearance in ^{129}Xe, using a xenon-based single phase TPC with a mass of ~ 9.5 kg, 99.5 % enriched in ^{129}Xe [143]. With a Poisson counting approach, utilizing an exposure of 2257.7 kg × day, they looked for a trace of p, pp, and nn disappearance. No evidence for these decays was found, and 90% C.L. lower lifetime limits were placed.

The resulting daughter nuclei assuming nucleon and di-nucleon disappearance in ^{129}Xe are collected in Tab.2.2. The radioactive decay features of the daughter nuclei are also reported. Looking at the half-lives of the daughter nuclei, only p, pp, and nn decay can be searched for with this method and this xenon isotope since the disappearance of n and np leads to stable nuclei.

Decay	Daughter nucleus	Half-life	Decay mode
n	$^{128}_{54}$Xe	stable	
p	$^{128}_{53}$I	24.99 min	β^- 94% (Q = 2.127 MeV); β^+, EC 6% (Q = 1.258 MeV)
nn	$^{127}_{54}$Xe	36.41 days	EC (Q = 0.664 MeV)
np	$^{127}_{53}$I	stable	
pp	$^{127}_{52}$Te	9.4 hours	β^- (Q = 0.694 MeV)

Table 2.2: The daughter nuclei originating from nucleon and di-nucleon disappearances in ^{129}Xe. The radioactive decay modes and $T_{1/2}$ of the daughter nuclei are taken from [146].

The following equation was used in the DAMA/LXe search to estimate the lifetime limits reported in Tab.2.3 [143]:

$$\tau_{\text{lim}} = \epsilon_{\text{det}} \times \epsilon_{\Delta E} \times N_{\text{nucl}} \times N_{\text{obj}} \times \lambda_{\text{obj}} \times \frac{t}{S_{\Delta E}} \tag{2.1}$$

where ϵ_{det} is the detection efficiency, $\epsilon_{\Delta E}$ is the amount of signal that falls in the energy range of interest, N_{nucl} is the number of parent nuclei, N_{obj} is the number of nucleons or nucleon pairs (n, pp or nn pairs) inside the parent nucleus, whose decay could produce the specific daughter nucleus, λ_{obj} is the average decay probability of N_{obj}, t is the lifetime of the data acquisition, and $S_{\Delta E}$ is the number of events due to the effect, which can be excluded at a given confidence level based on the experimental data.

The parameters N_{obj} and λ_{obj} are the only ones not straightforward to obtain. N_{obj} is computed as in [147], and it is based on the following argument: Given the disappearance of one nucleon or more, it

---

[2] This is not the case for EXO-200 which had an energy threshold of ~ 500 keV

will be more energetically convenient for the excited daughter nucleus to emit a γ-ray if its excited energy is lower than the binding energy of the least bound nucleon. Through this argument, one can write a series of inequalities that return which nucleons would produce the desired daughter nucleon if they decayed. These inequalities require calculating the binding energy of nucleons before and after decay. More information can be found in [143, 140].

Traditionally λ_{obj} is taken equal to 1 for protons and neutrons, whereas, for di-nucleons, two methods are used in the literature. The more conservative one assumes λ_{obj} equal to 1, while the other approach, like DAMA/LXe [143], takes into account the pairing effect[3]: The decay of a pair of nucleons with zero total spin is more likely [143, 140]. The ingredients for Eq.2.1 for the three decay channels investigated, as well as the lower lifetime limits obtained by DAMA/LXe, are reported in Tab.2.3.

Decay	$N_{\text{obj}} \times \lambda_{\text{obj}}$	ΔE [keV]	ϵ_{det}	$\epsilon_{\Delta\text{E}}$	$\text{S}_{\Delta\text{E}}$	τ_{lim} [yr]
p	24	(350, 500)	98.6 %	10.2 %	35.9	$> 1.9 \times 10^{24}$
nn	9	(150, 315)	94.4 %	51.6 %	11.5	$> 1.2 \times 10^{25}$
pp	4	(350, 500)	99.2 %	17.6 %	35.9	$> 5.5 \times 10^{23}$

Table 2.3: DAMA/LXe results of ^{129}Xe nucleon and di-nucleon disappearance analysis. To retrieve the limit using the values listed here and Eq.2.1, the total number of ^{129}Xe nuclei is needed. In DAMA/LXe, this is equal to $3{\times}10^{25}$.

Despite the low exposure, DAMA/LXe experiment demonstrated that DM experiments are efficient detectors for radiogenic nucleon decay searches. Therefore, invisible decay searches remain appealing new physics channels for large-scale xenon experiments, such as XENONnT. Thanks to its low energy threshold, the well-understood background, and the high xenon active mass[4] the XENONnT experiment is expected to improve sensitivity by several orders of magnitude with respect to DAMA/LXe experiment.

---

[3] Under the influence of the short-range nucleon–nucleon force nucleons preferentially form neutron and proton pairs whose total angular momentum is zero.

[4] Considering the 26.4 % ^{129}Xe concentration in the XENONnT xenon inventory, in every tonne of xenon there is 264 kg of ^{129}Xe.

3

The XENON project

Dual-phase liquid and gas Xe time projection chambers (TPCs) are the world-leading technology for the direct detection of WIMPs in the GeV-TeV mass range [63]. The XENON project is one among several scientific programs based on this technology. The experiment, which involves about 200 scientists from over 25 institutions across the world, aims to detect DM particles with an ultra-sensitive and low background detector based on xenon. It is a phased program that aims to gradually improve the sensitivity by increasing the mass of the active xenon target and reducing the background index. Located at Laboratori Nazionali del Gran Sasso National (LNGS) at a depth of 3600-meter water equivalent, it started in 2006 with the prototype XENON10 [148] (instrumented mass $\sim$ 14 kg), followed by XENON100 [149] (instrumented mass $\sim$ 62 kg). Between 2013 and 2016, the first ton-scale detector was built: XENON1T [150] (instrumented mass $\sim$ 2 tons). XENON1T reached an upper limit, at 90% confidence level, on the cross-section of SI elastic WIMP scattering off nucleons equal to $4.1{\times}10^{-47}$ cm^2 for 30 GeV/c^2 WIMPs [93]. With the new experiment XENONnT [151] (instrumented mass $\sim$ 5.9 tons), the collaboration aims to improve the sensitivity to WIMP-nucleon scattering by a factor $\sim$ 10 compared to its predecessor.

In this chapter, the xenon properties as detector material are discussed, and the dual-phase xenon TPC detection principle is presented in the context of XENONnT. Then, the design and the operation principle of the XENONnT experiment are introduced. The XENONnT dual-phase TPC is detailed, as well as the other infrastructures required for the operation of the experiment. The chapter concludes with an overview of the XENONnT physics goals relevant to this manuscript.

3.1 Xenon as a detector medium

Liquid xenon proves to be an excellent particle detector medium. Among the noble liquids, it is the most efficient at stopping penetrating radiation, thanks to its high atomic number (Z=54) and density (2.86 $\mathrm{g/cm^{-3}}$

at 177 K). In Fig.3.1, the mean free path for different incident particles is shown as a function of the energy. Xenon has the property of self-shielding from external radiation, as shown by its small penetration length for different particles. Like other noble liquids, it responds to energy depositions with ionization electrons and scintillation photons while having the highest charge and light yields with a fast time response. Its relatively high condensation temperature (~ 163 K at 1 atm) requires a modest cryogenic system for gas liquefaction and thermodynamic stability. Thanks to its high atomic mass (A = 131), the SI cross-section is more enhanced than for the other noble liquids used for DM searches, as seen in Eq.1.11. Moreover, DM SD searches are possible thanks to the presence of isotopes in natural Xe with non-zero nuclear spin: ^{129}Xe with a nuclear spin which equals to 1/2 and ^{131}Xe equals to 3/2. Additionally, the large energy difference between the valence and the conduction bands (9.28 eV at 135 K [153]) makes xenon an efficient insulator. A summary of the physical properties of xenon can be found in Tab.3.1.

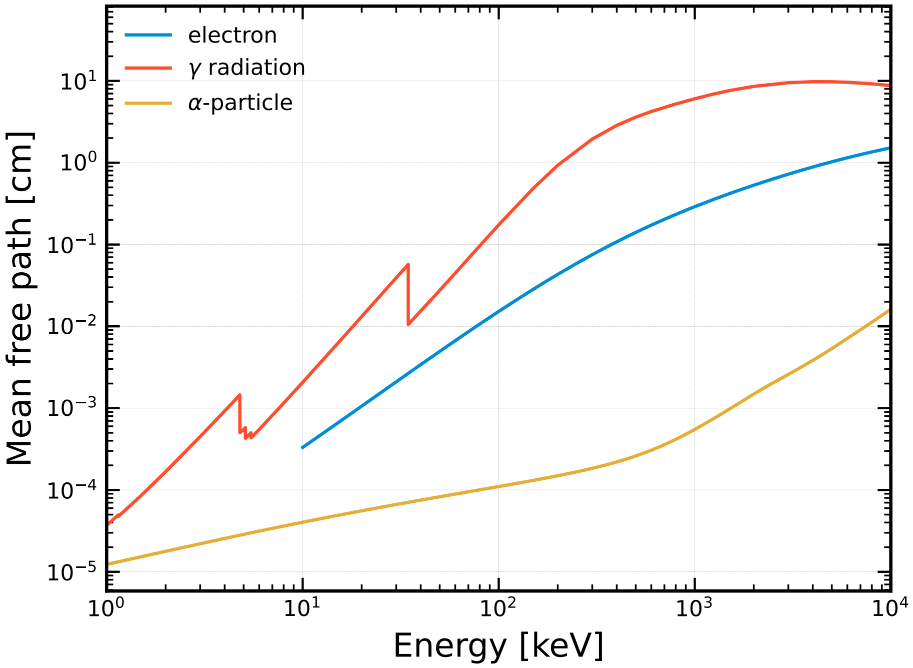

Figure 3.1: Mean free path, as a function of the energy, for different incident particles in liquid xenon. Curves valid for liquid xenon density equal to 2.86 g/cm^{-3}. Electron is shown in blue, γ radiation in orange, and α particle in yellow. The data are taken from [152].

Charged particles in liquid Xe continuously interact via the Coulomb force with the atomic electrons present in the medium they pass through, depositing some energy at every interaction. Additionally, the interactions with the nuclei might occur, drastically changing the incoming particle's trajectory. The energy deposited may be sufficient to excite the atom or remove an electron, producing an electron-ion pair. X-rays and γ-rays will partially, or even fully, transfer their energy to the electrons of the medium via photoelectric absorption, Compton scattering, or pair production. The energetic electrons, and positrons in the case of pair production, produced will then undergo Coulomb interaction with electrons and nuclei in the medium [157]. If the carriers of the deposited energy are the electrons, the scattering process is called electronic recoil (ER). Unlike photons, the other chargeless particles, like neutrons or WIMPs, prefer to interact with the constituents of the nucleus or with the nucleus itself. The result of the elastic scattering is the recoiling nuclei of xenon. The recoiling nuclei lose their energy by colliding with electrons and other

Atomic number	54			
Atomic mass	131.293	g mol^{-1}		[154]
Boiling point	165.11	K	at 1 atm	
Pressure	1.92	bar	at 177 K	[155]
Density	2.86	g cm^{-3}	at 177 K	
Natural composition	^{124}Xe(0.095%), ^{126}Xe(0.089%), ^{128}Xe(1.910%), ^{129}Xe(26.4%), ^{130}Xe(4.071%), ^{131}Xe(21.23%), ^{132}Xe(26.91%), ^{134}Xe(10.44%), ^{136}Xe(8.86%)			[156]

Table 3.1: Physical properties of xenon. The Atomic mass is valid for the natural composition of xenon.

nuclei within the detector [158], exciting or even ionizing them. These processes are called nuclear recoil (NR). WIMPs also interact with the atomic electrons, but for typical masses above 10 GeV/c^2, the energy deposited is below the usual detector energy threshold. While elastic scattering is the dominant process for low-energy for these particles, approaching $\mathcal{O}$(MeV), they can also scatter inelastically with the nuclei, leaving the initial Xe in an exited nuclear state [159, 160]. A nucleus can absorb neutrons, leading the former to a different isotope [161]. In ER and NR processes, some energy deposited by the incoming particle is undetected. Energy depositions that do not produce excitation or ionization are commonly referred to as heat [162].

The process of partitioning the deposited energy into the ionization and the scintillation channels is sketched in Fig.3.2. The excited xenon atoms (Xe*) quickly interact with neighboring atoms to form excited dimers (Xe$_2^*$). From the decay of the latter, vacuum ultraviolet scintillation light ($\lambda = 174.8 \pm 0.1_{\text{stat}} \pm 0.1_{\text{syst}}$ nm [163]) is produced. The xenon scintillation light is characterized by two components resulting from the de-excitation of the singlet and the triplet states of the excited dimer. The decay constants, (4.3 ± 0.6) ns for the singlet state and (22.0 ± 2.0) ns for the triplet state, make liquid Xe a very fast scintillator [164]. However, the $\mathcal{O}$(ns) time difference makes it difficult to discriminate NR from ER based on the pulse shape [165]. As a direct consequence of scintillation light from dimers de-excitation, the xenon atoms are transparent to their scintillation light. This ensures low light attenuation [162].

The amount of photons emitted depends on the nature of the interacting particle. For instance, a quenching for high ionizing particles has been observed, such as α particles and recoiling nuclei, which both have high stopping power, leading to denser tracks when passing through the interacting medium [166]. As a result of the quenching, smaller signals will be generated. A possible explanation of this quenching comes from biexcitonic collision, also known as Penning ionization, proposed in [167]. In this process, two Xe* atoms combine, leading to an electron-ion pair that can recombine and get undetected. Therefore, up to two scintillation photons can be lost[1]. Finally, the heat produced by ER is negligible, whereas the recoiling nuclei, produced after NR events, likely undergo sub-threshold scattering, e.g., atomic motion, and therefore heat dissipation is the dominant factor. The fraction of energy lost in heat is energy dependent. It increases with recoil energy, and it is modeled using the descriptions given by Lindhard et al. [168, 169].

The electron-ion recombination leads to the formation of excited dimers as well. Only partial recombination would occur since some thermalized electrons, too far from their parent ion, would escape [170]. The recombination contribution can be further reduced with an external electric field that removes free electrons from the interaction point.

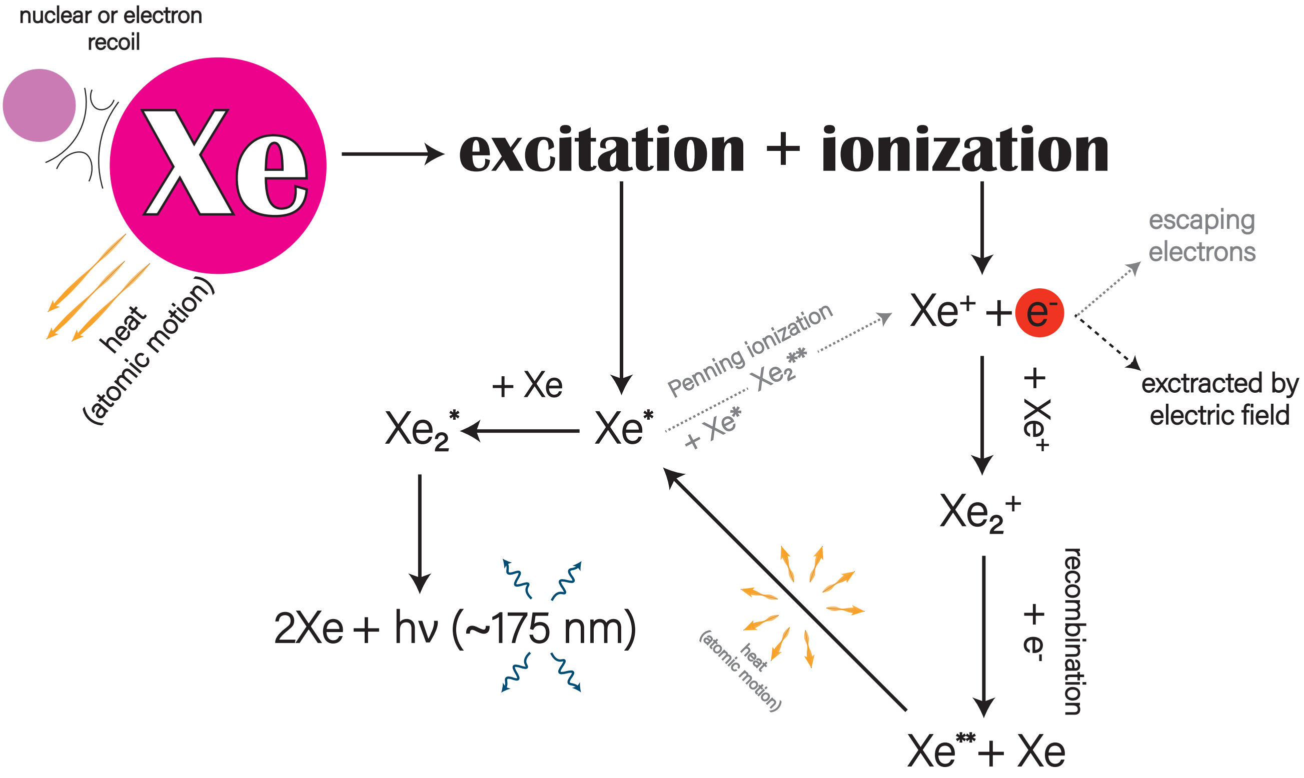

Figure 3.2: Schematic of the xenon energy partitioning after a particle interaction. The main steps involved in the conversion from deposited energy into detectable signals for a TPC are shown. Schematic inspired by [160].

The free electrons produced in the ionization channel can be measured separately if an electric field is applied to the detector medium. In this way, electrons that do not recombine can be extracted from the interaction vertex. During the ionization, Xe^+ ions are also produced, but they move several orders of magnitude slower under the effect of the same electric field [171]. The recombination probability is a key point for understanding excitation and ionization partitioning. It depends on the intensity of the electric field and the structure of the ionization track [172]. Recombination is inversely proportional to electric

---

[1] Even though similar quenchings are present for α particles and recoiling nuclei, the mechanism is different. They both generate dense tracks but with different shapes. The former leads to long tracks, while the recoiling nucleus produces smaller ones. The electron-ion recombination is then different [166].

field strength and increases with denser tracks. Particles with high energy loss per unit distance dE/dx have higher recombination rates, e.g., α particles or, more importantly, neutrons [166], producing smaller charge signals. On the contrary, particle interactions leading to ER events create sparse ionization tracks. Therefore, extracting the free electrons from the interaction point is less difficult.

The different recombination probabilities and the heat losses result in a different light and charge yields for nuclear and electron recoils. The light and the charge yields are quantified by the number of fundamental quanta, which are the scintillation photons n_γ and the ionized electrons $\mathrm{n}_{\mathrm{e}^-}$, respectively, produced from a particle interaction in xenon. The different yields allow for particle discrimination in a detector with separate charge and light signal readouts. Electronic recoil events lose almost all their energy through electronic excitation, whereas NR events also lose energy through elastic collisions with other atoms. While some of these interactions create further electron-ion pairs, most have energies below the ionization threshold. A full review of xenon micro-physics can be found in Refs. [167, 172, 173]. The variations in yield can be understood in terms of recoil energy, as shown in Fig.3.3. The light and the charge yields are represented in blue and red, respectively. The ER yields are shown in light colors, whereas the NR ones are represented in dark colors. The electric field intensity spans from 20 V/cm, represented by the dashed lines, to 200 V/cm, represented by the solid lines. The region contained by the two lines is meant to show how the light and charge yields change as a function of the applied electric field. ER events are greatly affected by the electric field, while NRs are not. This is due to the track structure, where the recombination in the dense NR track is almost inevitable. The curves have been computed using NEST (Noble Element Simulation Technique) [174]. Given the distinct signatures in the light and the charge yields, the event discrimination is performed in the charge-to-light ratio parameter space, where ER events lead to a higher ratio than NR events (see section 3.2 for more details).

Other advantages exist using the scintillation and the ionization signals simultaneously. As mentioned earlier, a portion of ionization electron contributes to the scintillation light through recombination, but since those electrons lost in the recombination cannot contribute to the ionization signal, and the ones which are extracted from the interaction cannot contribute to the scintillation signal, the light and charge yields are complementary and anti-correlated. Hence, the deposited energy $\mathrm{E}_{\mathrm{dep}}$ can be reconstructed as: $E_{\mathrm{dep}} = W \times (n_\gamma + n_{e^-})$, where W is the averaged energy needed to produce a quantum. W is different for scintillation photons (W_γ) and ionized electrons ($\mathrm{W}_{\mathrm{e}^-}$). They are (13.8 ± 0.9) eV [175] and (15.6 ± 0.3) eV [176], respectively. The difference from using a common value is incorporated into the fluctuations of n_γ and n_{e^-} [172]. The effective W-value for photon/electron generation, adopted by the scientific community, is (13.7 ± 0.4) eV [172]. However, more recent studies place W around $\sim$ 11 eV [177, 178], generating some tensions with the commonly adopted value. It has been shown that reconstructing $\mathrm{E}_{\mathrm{dep}}$ with both signals enhances the energy resolution because the light and the charge fluctuations are anti-correlated, whose summed uncertainty is smaller than individual ones [179].

Given the difference in yields, comparing the reconstructed energy from NR and ER is not straightforward. Two scales of energy are often used: $\mathrm{keV}_{\mathrm{er}}$ and $\mathrm{keV}_{\mathrm{nr}}$ for ER and NR, respectively. The two scales are related by the energy-dependent Lindhard factor L [180, 169] such as $\mathrm{E}_{\mathrm{dep,\,nr}} = \mathrm{E}_{\mathrm{dep,\,er}}/L$. L accounts for the signal quenching resulting from heat loss, and it can be described as:

$$L = \frac{k\, g(\epsilon)}{1 + k\, g(\epsilon)}, \tag{3.1}$$

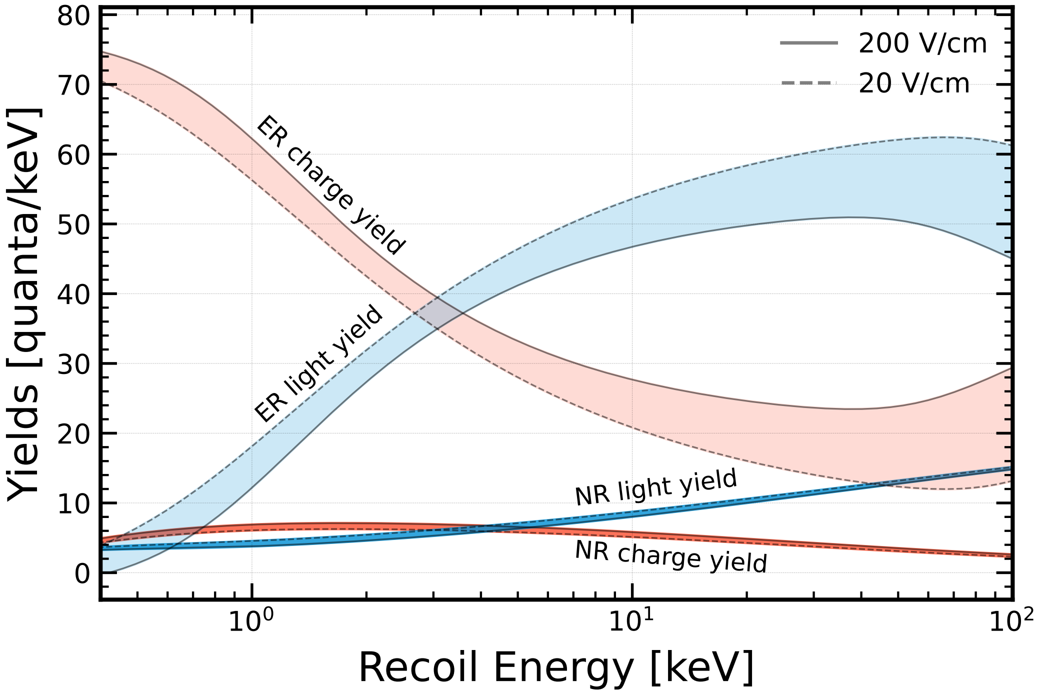

Figure 3.3: Scintillation (red) and ionization (blue) yields for ER (light colors) and NR (dark colors). The edges of the bands represent the yields for two electric fields: 20 V/cm (dashed lines) and 200 V/cm (solid lines). The plot has been made using the NEST software [174].

where $k = 0.133Z^{2/3}A{-}1/2$ is a proportionality constant between the electronic stopping power and the velocity of the recoiling nucleus [168] and $g(\epsilon) = 3\epsilon^{0.15} + 0.7\epsilon 0.6 + \epsilon$ is an energy-dependent quantity, proportional to the ratio of electronic stopping power to nuclear stopping power. The energy dependence is hidden in the dimensionless quantity $\epsilon = 11.5\ (E_{\mathrm{dep}}/keV)\ Z^{-7/3}$ [180]. In the previous expression, A and Z are the nucleon and nuclear charge numbers.

3.2 Dual-phase time projection chamber

Time projection chamber (TPC), invented by David R. Nygren at Lawrence Berkeley National Laboratory [181], is a common type of detector used in particle physics. This type of detector utilizes electric fields, often combined with magnetic fields and a sensitive volume of gas or liquid, to reconstruct the interaction features. The XENON experiment uses liquid and gas xenon dual-phase TPC to perform a 3D event imaging, energy reconstruction, and particle identification through simultaneous measurement of the scintillation and the ionization signals.

The dual-phase TPC operation principle is sketched in Fig.3.4. Typically of cylindrical shape, it records the scintillation signal (S1) with two arrays of VUV-sensitive photosensors, e.g., photomultiplier tubes, placed at the extremities of the detector. An electric field perpendicular to the two photosensor arrays causes the ionization electrons, which survive the recombination from the interaction site, to drift toward the liquid-gas interface. Here, a second intense electric field across the two phases extracts the electrons into a thin gas layer. Under the effect of the intense electric field, the electrons are accelerated, and they gain sufficient energy to produce a second light signal (S2), proportional to the number of electrons, during the inevitable collisions with xenon atoms along their path [182].

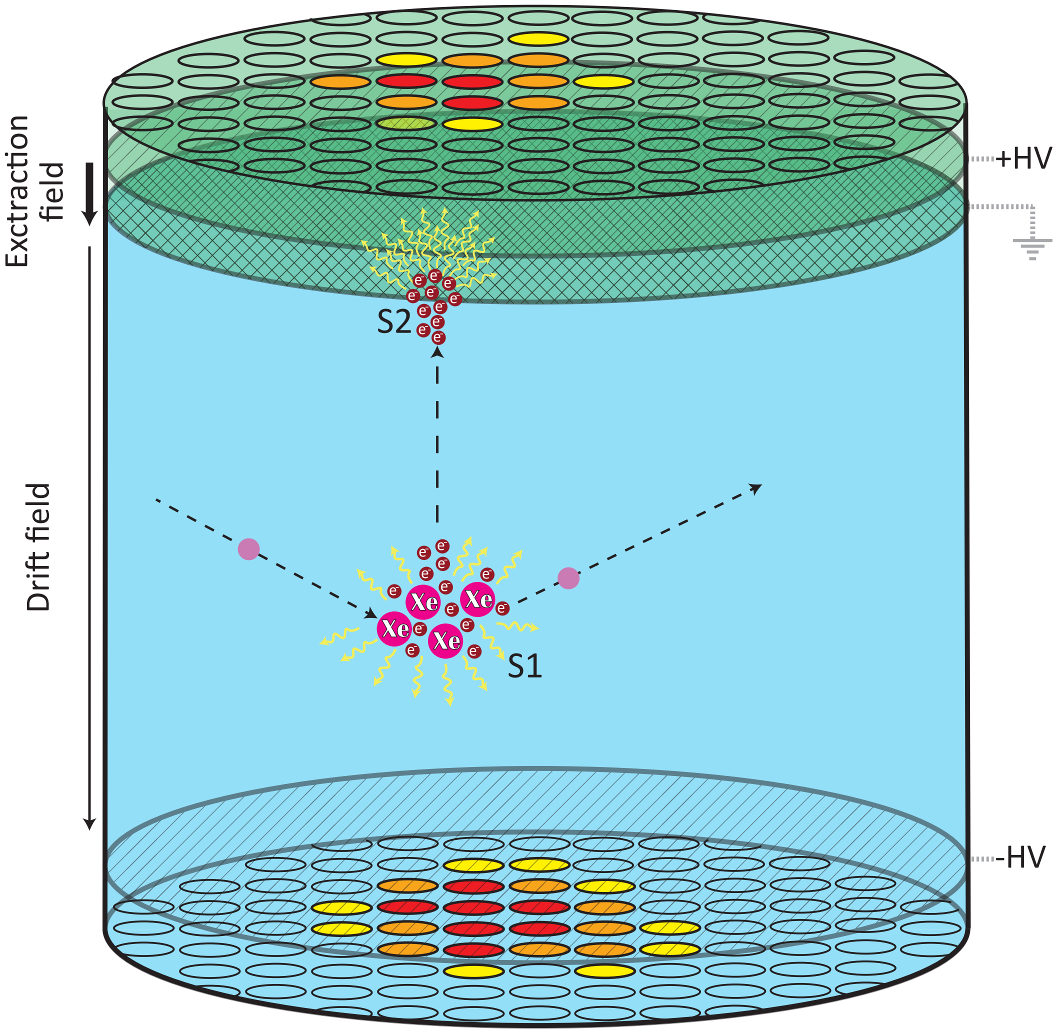

Figure 3.4: Detection principle of a dual-phase time projection chamber. The particle interaction in the liquid volume leaves behind ionization and excitation tracks. The de-excitation and part of the free electrons produced contribute to the prompt scintillation signal S1. An external electric field drifts part of the electrons toward the liquid-gas interface. Here, an intense electric field across the interface extracts the electrons. The electrons gain enough energy to excite the surrounding atoms while drifting toward the anode. As a consequence, a second scintillation signal, S2, is produced. The intensity is proportional to the number of extracted electrons. The signals S1 and S2 are collected by photosensors placed at the detector ends. The combination of S1 and S2 can infer the incoming particles' interaction position, energy, and nature.

The (x,y) position of the interaction is extracted from the light pattern of the S2 signal on the top photosensor array. The drift time, namely the time difference from the instantaneous S1 and the delayed S2, is used to reconstruct the interaction depth (z position). One needs to account for detector efficiency to reconstruct the energy using (S1, S2). Defining g_1 (g_2) as the ratio between the number of photons (electrons) produced and detected, the E_{dep} can be reconstructed as:

$$E_{\mathrm{dep}} = W \times \left(\frac{S1}{g_1} + \frac{S2}{g_2} \right), \tag{3.2}$$

where W, the averaged energy to produce either a scintillation photon or an ionized electron, has already been discussed in section 3.1. Eq.3.2 is valid for ER events, whereas the Lindhard factor in Eq.3.1 needs to be considered to reconstruct the energy from NR events.

The g_1 and g_2 are detector parameters obtained by studying the anti-correlation between S1 and S2 using different mono-energetic calibration sources, as shown in Fig.3.5. The yields can be obtained for each calibration source by taking the average S1 and S2 responses divided by the true energy. By inverting Eq.3.2, it can be shown that the light yield (LY=S1/E) and the charge yield (QY=S2/E) follow a straight line, of which the axis intercepts are g_1/W and g_2/W (see the right panel in Fig.3.5):

$$\mathrm{QY} = -\frac{g_2}{g_1}\mathrm{LY} + \frac{g_2}{W} \tag{3.3}$$

Before calculating the detector parameters, the S1 and S2 signals must be corrected for detector effects, which distort the original signal. These corrections will be discussed in section 5.3.

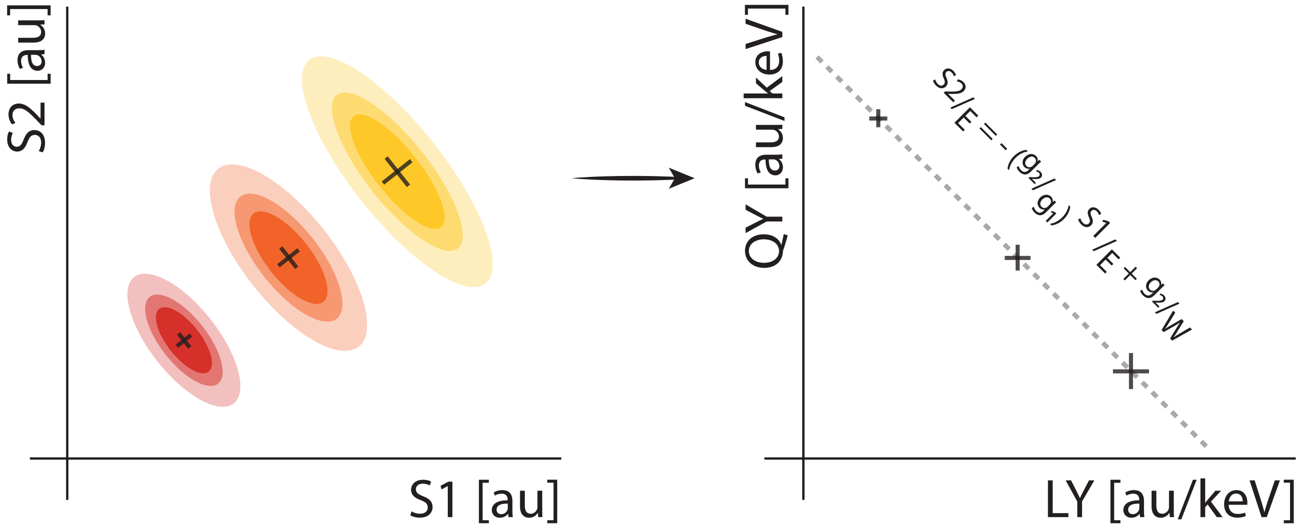

Figure 3.5: Sketch of anti correlation of S1 and S2 for mono-energetic lines (left). The mean light and charge responses are used to extract the detector parameters g_1 and g_2 (right).

The particle discrimination is performed in the (S1, S2) parameter space, as shown in Fig.3.6. The figure shows that ER and NR events lie in two bands, one on top of the other. Due to the different yields, the light-to-charge ratio for NR is different from that for ER. For a given energy deposition in keV_{er} one has $(S2/S1)_{NR} < (S2/S1)_{ER}$. The ability to discriminate between ER and NR is quantified as the portion of the ER band which falls below the median of NR band. This parameter, called ER-leakage, is energy dependent, and is influenced by the condition of the detector. It has been shown that high g_1 values lead to better ER-NR discrimination, while the dependence on the electric field is more muted. Typically, ER-leakage values are $\mathcal{O}(10^{4\div5})$ for electric fields of $\mathcal{O}(100\ \text{V/cm})$. This translates to $\sim 99.9\%$ ER rejection with 50% NR acceptance [183].

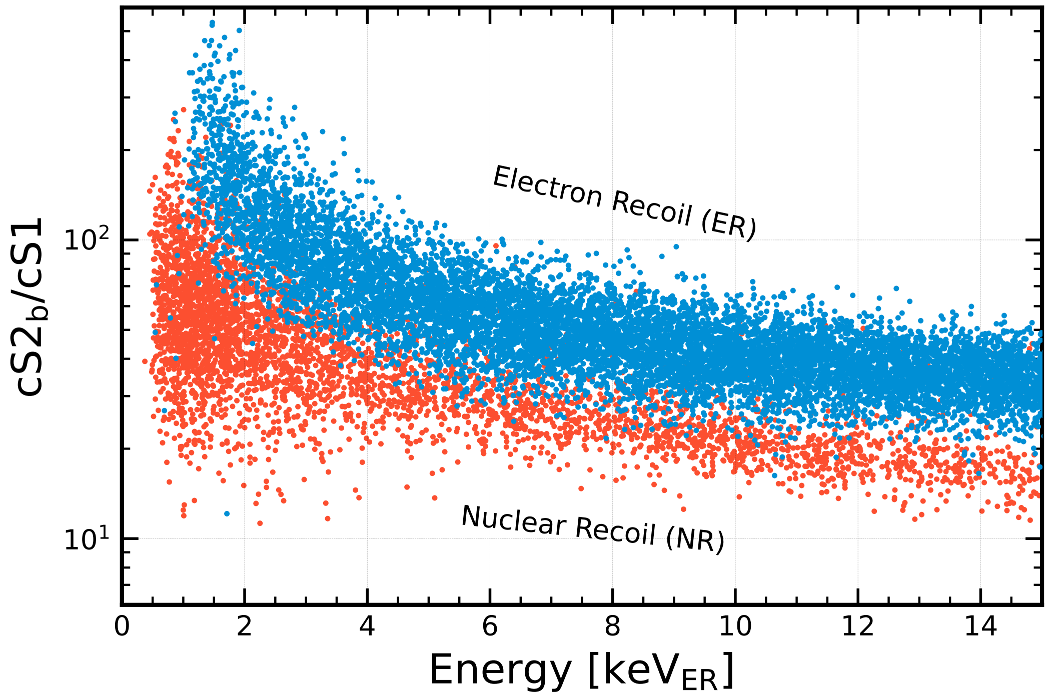

Figure 3.6: Discrimination of nuclear recoil (red) and electron recoil (blue) based on the charge-to-light ratio. Data from XENON1T. The NR data points are from a ^{241}AmBe calibration, while the ER data points are from a ^{220}Rn calibration. The letter *c* on the y label stands for corrected; namely, the signals have been corrected for the detector response. The letter *b* in the subscript of S2 means that only the bottom PMT array was considered. XENON1T, given $g_1 = (0.142 \pm 0.005)$ PE/γ, $g_2 = (11.4 \pm 0.02)$ PE/e^-, and drift field $\mathcal{O}(100$ V/cm), measured (0.3 ± 0.1)% ER-leakage between 3 and 70 PE in cS1. This translates to for every 1000 NRs, there are 3 ERs, below the median of NR band [184, 185].

3.3 The XENONnT experiment

The XENONnT experiment is the 4th phase of the XENON project. Most of the service systems and infrastructure have been inherited from the XENON1T experiment. The increased target mass required a new design of the TPC with a new inner cryostat vessel. The detector was designed such that the XENON1T outer cryostat could host it. The total xenon inventory in XENONnT weighs 8.6 tons. This required new systems to handle and purify the larger xenon volume. To achieve the sensitivity goal of $\mathcal{O}(10^{-48}\ \text{cm}^2)$ SI WIMP-nucleon cross-section, the veto system was upgraded by adding a neutron veto system to the existing muon veto. A schematic view of the experiment is shown in Fig.3.7[2]. The inherited gas purification system and the krypton distillation column were insufficient to achieve the required xenon purity and background level. A new liquid xenon purification system and an online radon distillation column were

---

[2] Here there is the link for a remote tour of the underground laboratories.

installed. Additionally, a new storage system (ReStoX II), with further backup-up bottles, was added to the present system (ReStoX I) to cope with the enlarged xenon inventory. The data acquisition (DAQ) and slow control (SC) systems were scaled up to account for the extra photosensor readout channels and new components [186, 187].

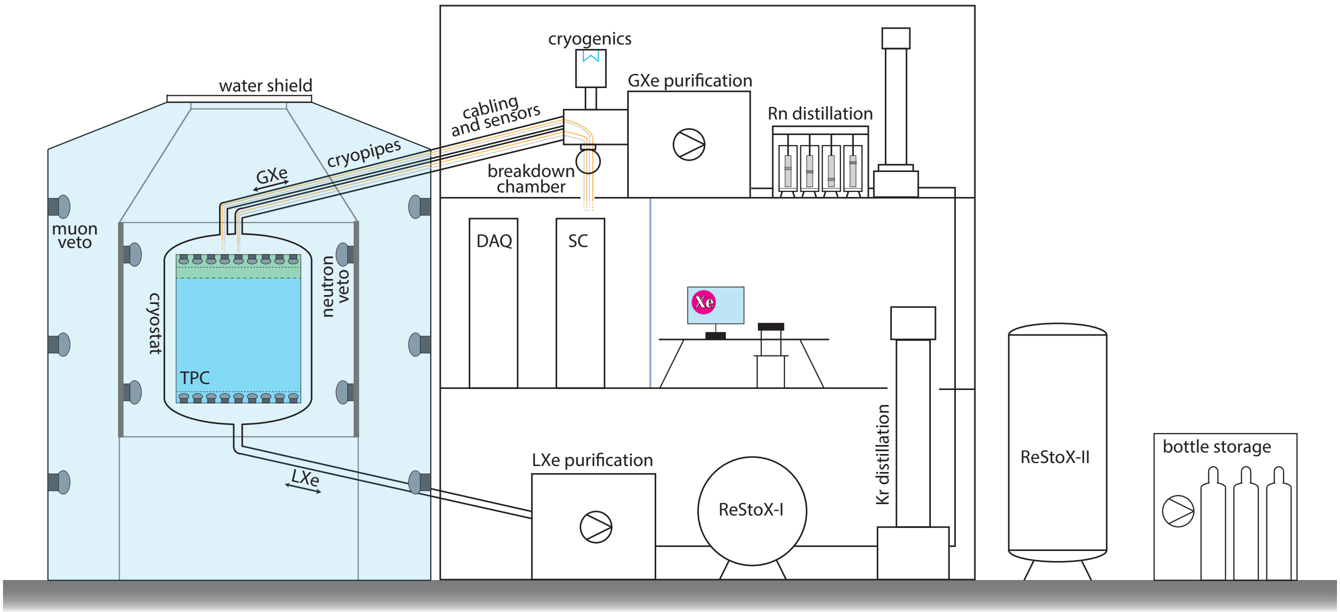

Figure 3.7: Schematic view of the XENONnT experiment. The TPC is at the center of the water tank, which works as a support structure for the muon veto. The neutron veto is mounted around the outer cryostat. Next to the water tank, a 3-floor service building hosts the experiment's infrastructure. The experiment is carried out in Hall B at LNGS (Italy).

The XENONnT dual-phase time projection chamber and the various systems that enable its operation are described in the next section. Following, the main challenges that the XENONnT experiment experienced and still has to face are summarized together with the adopted solutions. A brief discussion on the primary physics goal of the XENONnT experiment is presented at the end of this section.

3.3.1 The XENONnT TPC

The XENONnT TPC consists of a hollow cylinder with a diameter of $\sim$ 1.34 m filled with 5.9 tons, out of 8.6 tons, of liquid xenon, hosted in a double-walled vacuum-isolated cryostat. The TPC volume is surrounded by 24 polytetrafluoroethylenes (PTFE) reflector panels, whereas two arrays of photomultiplier tubes (PMTs) placed at the top and the bottom of the cylinder define the vertical dimension. The support structure for the PMT arrays consists of a perforated oxygen-free copper plate with a 21 mm thickness secured to the TPC structure. A total of 494 3" Hamamatsu R11410-21 PMTs, divided into the two arrays, is placed in copper plate holes with their windows looking inside the TPC cylinder. The PMTs are fixed to the copper by specific clamps from the back and the front by a 10 mm thick PTFE reflector that holds the PMT from their windows. The top PMT array is inserted into a stainless steel diving bell and immersed in gaseous xenon. The diving bell is used to keep the position of the liquid-gas interface constant. The drift field is generated by means of a cathode placed at 60 mm above the bottom PMT array and a gate electrode located slightly below the liquid-gas interface. The distance between the gate electrode and the liquid-gas interface can be adjusted depending on the TPC operation. Currently, the distance is equal to 5.1 mm. These two electrodes, separated by $\sim$ 1.486 m at liquid xenon temperature, demarcate the active region. An anode electrode is placed 8 mm above the gate to establish the extraction field within the liquid-gas interface. Two screening electrodes placed at 5.3 mm and 40.7 mm above and below the bottom and top PMTs protect the photosensors from the electric fields. All the electrodes consist of custom-made parallel stainless steel wires with a $\mathcal{O}(100\ \mu\mathrm{m})$ thickness and a pitch of $\mathcal{O}(5\ \mathrm{mm})^3$. Two and four additional wires, for the gate and the anode, respectively, are installed perpendicular to the other wires to minimize the effect of gravitational and electrostatic sagging. Two concentric sets of oxygen-free copper field shaping rings permit the uniformity of the drift field. Both inner and outer cryostats have domed upper sections with several access ports connecting the TPC to the rest of the infrastructure. Two double-walled vacuum-insulated pipes host the cabling for the PMTs and the cryogenic and the gas purification lines. The liquid purification line is located at the bottom of the cryostats through a single port. A rendering of the XENONnT TPC is shown in Fig.3.8 [151]. Additional technical information can be found in [186, 187].

3.3.2 The vetos and auxiliary systems of XENONnT

Like a *matriòska*, the XENONnT experiment consists of 3 detectors, one inside another. Everything is enclosed by a massive stainless steel tank filled with $\sim$ 700 tons of pure water. By design, the water should be doped with gadolinium salt to enhance tagging efficiency for the veto systems; however, while this thesis was written, the experiment operated only with pure water. The dual-phase TPC sits at the center of the tank, and it is surrounded by a cage made of PTFE reflective panels equipped with a total of 120 Hamamatsu R5912-100-10 8" PMTs, facing the cryostat. Optically separated from the outside, this cage acts as a neutron veto (nVeto) by tagging events in coincidence with the TPC [188]. This veto system is meant mainly to reduce the radiogenic neutron background, produced through spontaneous fission (SF) or (α, n) reactions in the detector materials, which scatter at least once in the TPC and then are detected in the nVeto. In the nVeto region, the neutron will be moderated and eventually captured by the hydrogen - or gadolinium by design. The capture leaves behind a deuterium atom ^{2}H, whose decay produce a 2.2 MeV γ-ray, which undergoes Compton scattering, leaving electrons to produce Cherenkov light. The detection with gadolinium is similar, for more details refer to [189]. The water tank provides effective shielding from the environmental background and supports the Cherenkov muon veto (mVeto) system, which uses 84 Hamamatsu R5912ASSY 8" PMTs to register Cherenkov light produced from cosmic muons passing through the water tank [190]. The three detectors are rendered in Fig.3.9. The figure also shows the calibration tubes for deploying sources close to the TPC.

The other auxiliary systems needed for the experiment are hosted in a three-floor building next to the water tank, as shown in Fig.3.7. Starting from the top of the building, one can find the cryogenic system, the gas purification system, and the radon distillation column. In addition, PMT cables, sensors, and electrode cables are extracted from the xenon region into the air by a special breakdown chamber equipped with

---

[3] The pitch is the center-to-center distance between two adjacent cables.

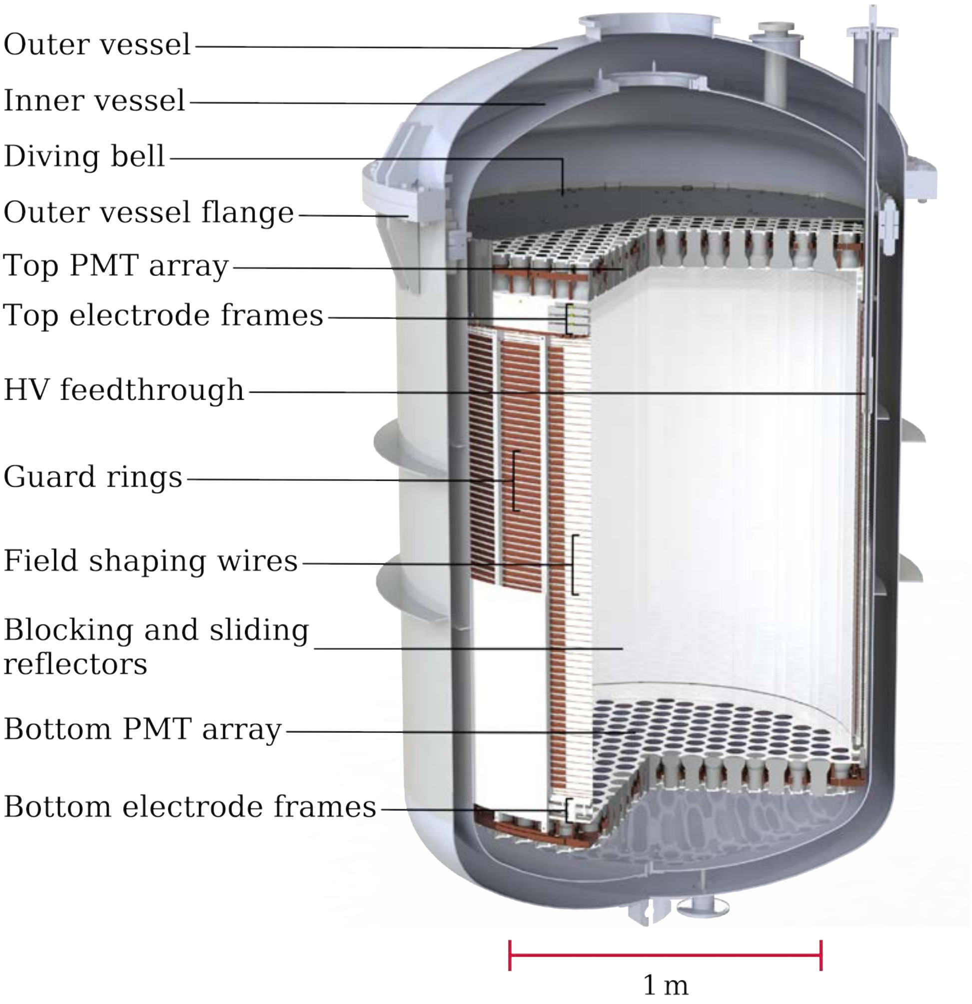

Figure 3.8: A rendering of the XENONnT TPC with the main components labeled. Illustration from [151].

potted feedthroughs located in the cryogenic tubes. These cables are routed into the second floor, where the DAQ and the SC are housed. The liquid purification line and the krypton distillation column are placed on the first floor. The xenon storage systems are located on the first floor (Restox I) and outside the building (Restox II).

3.3.3 XENONnT challenges

Over the last 20 years, the XENON project moved from a few kilogram detectors to ton-scale mass, drastically lowering the background, with the result of improving the sensitivity on the spin-independent WIMP-nucleon cross-section by three orders of magnitude, from $\sim 10^{-44}$ cm^2 [191] to $\sim 10^{-47}$ cm^2 [192]. This has been possible thanks to the many developments and breakthroughs in the xenon community. Reference [79] contains a more detailed discussion of the new technology used in the current experiments and the R&D program towards an *ultimate* liquid xenon-based detector. The following sections collect some of the challenges, particularly relevant to this thesis, that the XENON collaboration faced in the design/operation of the experiment.

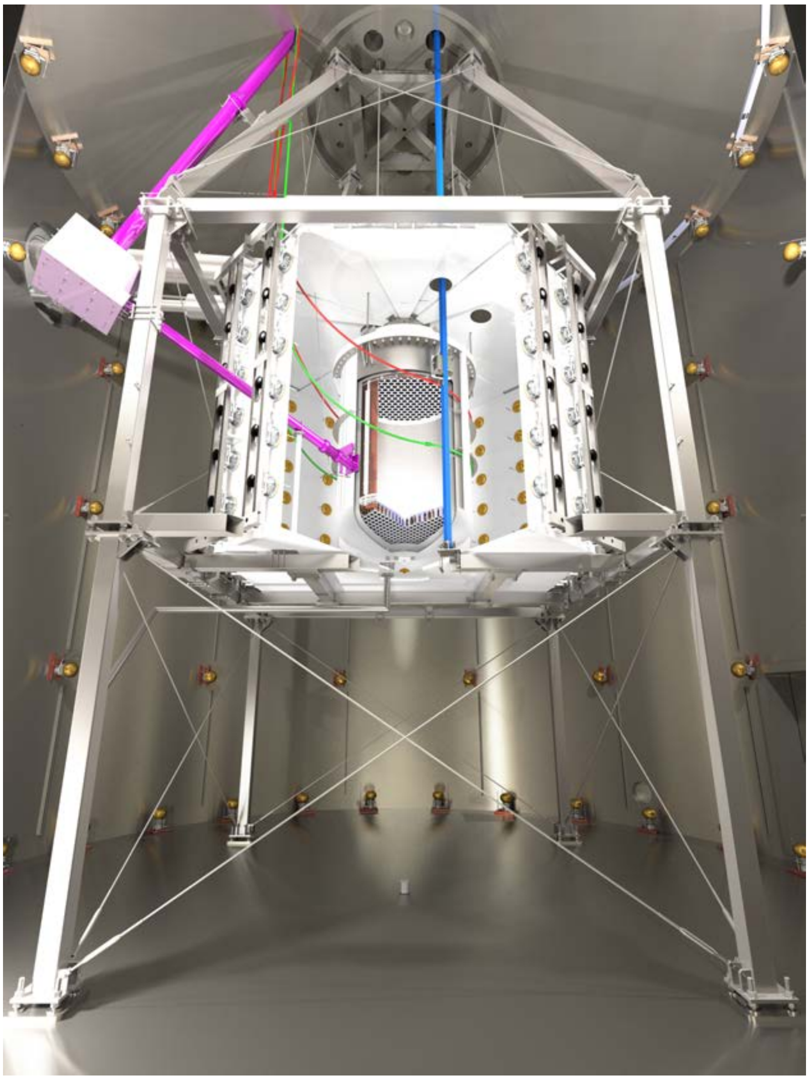

Figure 3.9: A rendering of three detectors that make the XENONnT experiment. The neutron veto at the center of the water tank surrounds the TPC. Optically separated from the neutron veto, there is the muon veto, supported by the water tank structure. The red and green tubes, called U-tubes, deploy external radioactive sources near the TPC for calibration. By design, a neutron generator (in purple), consisting of the source box and the collimator, is present. At the time of this thesis, it was not installed yet. In blue is the so-called I-belt, which can also host external calibration sources. Figure by J. Piennar.

Material selection

For any rare-event search, selecting low-radioactivity construction materials is fundamental. The leading radioactive isotope are ^{232}Th, ^{238}U, ^{235}U, ^{40}K and their progenities, as well as ^{60}Co and ^{137}Cs. Another important isotope is ^{222}Rn, a noble element produced in the decay of ^{226}Ra, continuously released into the xenon target by every surface in contact with it. All the XENONnT components have been selected after an extensive radioassay program that included gamma-ray spectroscopy, mass spectrometry, and ^{222}Rn emanation measurements. Several high-purity germanium detectors operating in underground locations (LNGS at 3800 m.w.e. [193, 194, 195], Vue-des-Alpes at 620 m.w.e. [196, 197], and MPIK Heidelberg at 15 m.w.e. [198])[4] were used to estimate the activity of radionuclides in detector materials. In addition, mass spectrometry techniques [199] were used to estimate the number of primordial nuclides (^{238}U and ^{232}Th), particularly dangerous being radiogenic neutron sources. The activities of the selected materials were then propagated to XENONnT WIMP sensitivity projection via Monte-Carlo simulations that informed the collaboration about their impact and, thus, the high quality of the screening campaign [151]. Similarly, the radon emanation measurements [200] were fundamental to achieve the XENONnT goal of $\mathcal{O}(\mu\text{Bq/kg})$ ^{222}Rn activity.

Compared to XENON1T screening results, roughly 17 % reduction for material backgrounds and a factor three reduction of the ^{222}Rn level in the liquid Xe has been achieved. In addition, a meticulous cleaning procedure, optimized for each of the different materials, was performed before detector assembly to mitigate every contamination, e.g., dust or residual greases, accumulated on material surfaces during production, storage, and handling [201].

Xenon purification

Impurities can dramatically reduce the intensity of light and charge signals in the xenon target. Even though liquid xenon is transparent to its scintillation light, VUV-absorbing impurities, such as water vapor and oxygen, can attenuate the light signal. The light intensity I decreases as $I(x) = I(0)\ e^{-x/\lambda_{\text{att}}}$ where $I(0)$ is the original scintillation signal and x is the path length covered by the light. The intensity decrease is governed by the attenuation length λ_{att}, defined as the sum of the reciprocals of absorption length λ_{abs} that describes real absorption and loss of photons, and the scattering length λ_{scat} that represents elastic scattering of photons without any energy loss [202].

Similarly, the number of electrons available for the charge signal might be reduced during the drift by impurities with a high electron-attachment probability, such as O_2 or N_2O. The exponential attenuation of electron concentration can be expressed as a function of the so-called electron drift lifetime τ_e that describes the average time before an impurity captures electrons. The observed ionization signal $N_e(t)$, for a given drift time t is given by the following relation: $N_e(t) = N_e(0)\ e^{-t/\tau_e}$, where $N_e(0)$ is the initial ionization signal. Hence, τ_e is the time that the ionization signal is reduced by a factor e [162].

Hence, the higher the impurities' concentration, the higher the light and charger attenuation. The XENONnT purification system aims to remove impurities to concentrations below 10^{-9} ($^{\text{mol}}/_{\text{mol}}$). The removal of electronegative impurities from the gas is done by two hot-getters (SAES MonoTorr), where high-speed circulation ($\sim$ 52 slpm during the science data taking) is achieved by the new custom-built magnetic piston pumps [203]. The gas purification is not sufficient to purify 8.6 tons of xenon. The XENONnT purification requirements are achieved further by to a novel liquid purification system with a flow a volumetric flow of 1 – 4 LPM, equivalent to 4 – 16 t/d [204, 187]. This new technology requires the development and selection for several cryogenic components, e.g., cryogenic liquid pump or cryogenic filtering technology. Two cryogenic filters are used in the XENON experiment, one extremely efficient but with high ^{222}Rn em-

---

[4] m.w.e. stands for meter water equivalent and it is a standard measure for showing cosmic ray attenuation in underground laboratories. It is related to the laboratory depth and the overburden material density.

anation for intense purification (copper-impregnated spheres, Q5) and one for the science data-taking period (ST707 pills filter). The electron lifetime achieved has exceeded all expectations, reaching up to 20 ms (far above the maximal electron drift time equal to $\sim$ 2.2 ms in the first science data-taking period, see chapter 6), whereas XENON1T achieved only 650 μs [205].

Xenon distillation

Without deploying the Kr and Rn distillation columns, the background level reduction would not be sufficient, even considering the careful material screening selections. The ^{85}Kr distillation was already designed and constructed for XENON1T, and $\sim 10^{-15}$ ^{nat}Kr/Xe concentration was demonstrated [206]. The distillation technique in XENONnT is based on the difference in vapor pressures between Kr and Xe. Since Kr is lighter than Xe, it is more volatile. Hence, in a static liquid xenon reservoir in equilibrium with a gaseous phase above, the more volatile krypton is likely to migrate into the gaseous phase and be extracted accordingly. In XENONnT, liquid xenon samples are constantly extracted, and the krypton concentration is measured through highly sensitive rare gas mass spectrometry (RGMS) technique [207]. During the first science data taking, the measured ^{nat}Kr level was $\sim$ 56 ppq [208]. The ^{85}Kr needs particular attention since its low energy deposition can negatively affect the detector sensitivity: it is a β-emitter with a half-life of 10.76 yr. For 99.56 % of the time, it decays to the ground state of ^{85}Rb with an energy endpoint of 687 keV. It can also decay to a 173.1 KeV excited state of rubidium, but it is less likely to happen (0.44 % branching ratio) [209].

With the reduction of the krypton level, the ^{222}Rn became the most dangerous background. Radon is continuously emanated from any detector surface into the target material. Its half-life of 3.8 days [210] is long enough for a homogeneous mixing within the active detection volume. However, the radon decay is not the problem for the dark matter search but rather its β-emitting daughter ^{214}Pb. With a half-life of 26.8 minutes, the ^{214}Pb undergoes a pure β decay to ^{214}Po. The polonium can be generated in several excited states, but for the dark matter search, the ground state β decays ($\sim$ 13% branching ratio) is the most concerning [211]. The pure β decays induces ER events in low energies of the region of interest of the dark matter searches, contributing significantly to the leakage discussed in section 3.2. XENONnT demonstrated that an online radon removal system, based on cryogenic distillation, can be used to reduce the ^{222}Rn activity concentration to < 1 μBq/kg, with a circulation flow of $\sim$ 90 kg/h. The distillation technique is again based on the different vapor pressures, but in this case, xenon is more volatile than radon [212].

Photosensors

Dual-phase xenon TPCs rely on the detection of $\sim$ 175 nm VUV-scintillation light. So far, photomultiplier tubes (PMTs) are still the most reliable photosensors available in the field. Thanks to their high signal amplification, low noise, and good VUV-light detection efficiency, they are perfect for xenon-based dark matter experiments, which rely on single photon detection. The PMT type used by the XENON collaboration (Hamamatsu R11410-21) has been developed together with the Hamamatsu to improve the performances at liquid xenon temperature and minimize the radioactive content [213]. XENONnT has 494 PMTs in total, 178 of which were inherited by XENON1T. The remaining PMTs have been newly produced by Hamamatsu. Despite being reliable photosensors, PMTs suffer from specific problems, e.g., random light emission or vacuum degradation. Hence, the 368 new PMTs were tested in liquid and gaseous xenon to verify their long-term operational stability. The test campaign was performed by Stockholm University, Max-Planck-Institute für Kernphysik (MPIK) in Heidelberg, and at the University of Zurich [213]. The outcomes of the testing campaign, combined with radioactivity screening measurement, have been used to select PMTs and arrange them in XENONnT TPC.

Once the PMTs were installed and the TPC started to operate, their performances had to be optimized for the detector condition to maximize the single photon detection efficiency. Meticulous commissioning was done in the early stage of the XENONnT experiment, where the PMT performances were optimized in view of the science data-taking. Later, the main PMT performances, e.g., signal amplification and single photon detection efficiency, have been monitored throughout the whole period of science data-taking. This is necessary to ensure the delivery of high-quality data.

The Ph.D. work summarized in this manuscript focuses partially on PMTs. Chapter 4 will discuss the testing campaign and the PMTs assembly in the XENONnT TPC. Chapter 5 will show the PMT performances during the first science data-taking period.

3.3.4 Main physics goals of the XENONnT experiment

The XENONnT experiment has been designed primarily for WIMP searches. The main physics channel is the WIMP-nucleon elastic scattering. Considering the designed operating conditions and background expectations, XENONnT can probe $\mathcal{O}(10^{-48}\ \mathrm{cm}^2)$ SI cross-sections assuming a 4 t fiducial volume and 5 years of livetime [151], more than an order of magnitude better than its predecessor XENON1T [192].

Given the expected sensitivity of multi-ton scale detectors, the search for coherent elastic scattering of solar ^{8}B neutrinos [103, 104] will be one of the main physics channels as well. XENONnT, with the expected improvement in background reduction and enhancement in xenon purity, is expected to play a leading role in this search [96].

The analysis of low-energy ER data in XENONnT had the same priority level as the WIMP searches. This is motivated by the XENON1T results, which observed an excess over known backgrounds between 2 and 3 keV$_{\mathrm{er}}$ consistent with a solar axion model with 3.4σ significance, but also explainable by considering tritium ^{3}H as an additional background component [214]. For this reason, XENONnT performed, for the first time in the DM direct detection field, a simultaneous ER and NR blind analysis. The ER and the NR bands, below 20 keV, were unavailable until the analysis framework was completed. The WIMP search and the low-energy ER analysis are discussed in chapter 6.

A new physics channel, never explored before in the XENON project, is presented in this manuscript. Using the first XENONnT science run data, the nucleon and the di-nucleon disappearances in ^{129}Xe were investigated. These invisible nucleon decay channels belong to baryon and the lepton violation processes [120]. Previous xenon-based experiments, e.g., DAMA/LXe [143], looked for these exotic channels without finding any evidence above the background. Positive detection of these processes would revolutionize our knowledge, helping us understand the origin of the asymmetry between matter and anti-matter in the Universe [109]. Chapter 7 is devoted to an in-depth discussion of this analysis.

In conclusion, thanks to the extraordinary detector performances and the ultra-low background level achieved, XENONnT can probe several new physics channels. It has a broad science program ranging from DM searches to neutrino physics, including the search of xenon double-weak processes, such as neutrinoless double β decay ($0\nu\beta\beta$) of ^{136}Xe or double electron capture decay (2νECEC) of ^{124}Xe [215], and other baryon or lepton violation processes such as the invisible nucleon search.

4

XENONnT photosensors

from testing to assembly in the TPC

The photosensor R&D has played a fundamental role in improving the sensitivity of the XENON experiment. Detecting VUV-light efficiently while keeping the radioactive budget low and ensuring performance stability at cryogenic temperature is challenging. This process has required a direct work relationship with Hamamatsu and a meticulous testing and feedback routine. The XENON group at the University of Zurich (UZH) has a long tradition with the photosensor R&D. The current PMT model used in XENONnT (3" Hamamatsu R11410-21) was the result of a long development campaign where UZH played a key role [216]. As described in section 3.3.3, XENONnT doubled the number of TPC photosensors, many of which were newly produced. Due to the high failure rate of PMTs (79 of the 248 PMTs) during the XENON1T operation, prior to putting faulty photosensors in XENONnT, a careful testing campaign was required: Every PMT was characterized and monitored in gas and liquid xenon for at least 2 weeks in an environment similar to the XENONnT TPC condition. Once the PMTs were selected, they were installed in the XENONnT TPC following a dedicated cleaning and assembly procedure.

The chapter is organized as follows: first, the PMT operation principle is summarized, and the design of the 3" Hamamatsu R11410-21 is discussed. Following, the main steps in the test campaign and the results obtained are presented. The chapter ends with the description of the PMT installation in XENONnT TPC.

4.1 Design and operating principle of XENONnT PMT

Despite being an old technology, the study of photomultiplier tubes is not yet completed. This is not surprising since it is a technology that embraces several basic pieces of knowledge, from the physics of photoemission to optics, from signal processing to electronics. PMTs are high-gain, typically operated with a wide-bandwidth ($\mathcal{O}(100$ MHz)), devices able to detect single photons. Handling them requires expertise as well as caution. However, the amount of knowledge gained significantly since the first PMT was available in the market. Nowadays, VUV-sensitive photomultiplier tubes are operated for long periods of time with good performances in a liquid xenon environment and little deterioration.

This section summarizes the PMT working principle, focusing especially on the 3" Hamamatsu R11410-21 used in the XENONnT experiment. Apart from the specification on the XENON photosensors, a detailed review of PMTs can be found in [217, 218].

4.1.1 PMT operating principle

The objective of a PMT is to transform the information conveyed by the incident light into a readable electrical signal. Fig.4.1 shows a photomultiplier tube's schematic and operation principle. The components represented are specific for XENONnT PMTs, which will be discussed in section 4.1.2. The PMT consists of an evacuated tube with an input window, in which the photocathode is deposited by evaporation in the inner face. The window material depends on the incident light wavelength. The XENONnT PMTs use a quartz window which is optimized for VUV light transmission. Through the photoelectric effect, an electron is emitted from the photocathode after absorbing incident light, and the electron produced is called photoelectron (PE). A focusing electrode establishes the right electric field, according to the geometry of the tube, to accelerate and collect the PEs towards the dynodes chain. The power supply for operating the PMT is provided through outgoing stems connected directly to the dynode chain. The collision with the dynodes is such that a cluster of secondary electrons is emitted at each step of the chain. If the amplification of the initial electrons is large enough, a readable charge per unit of time at the last dynode step, the anode, will be produced. This signal can be read as voltage drop or as current. The PMT output has embedded all the information of the incident light, such as the intensity [217].

The ability of light detection depends on the PE production efficiency, quantified by the *quantum efficiency* (QE): the ratio of the number of PEs produced to the number of incident photons. The QE for a given tube is wavelength dependant, and it needs to be maximized according to the PMT's application. Once the PE is produced, it must be collected efficiently at the first dynode. This efficiency is quantified by the *collection efficiency* (CE), which is related to the electric field configuration inside the tube. After reaching the dynodes, the PE is multiplied throughout all the stages by the emission of secondary electrons. The amplification is a statistical process governed by the number of secondary electrons emitted per primary electron, δ, and their fluctuation. A semi-empirical relationship describes the amplification at each dynode: $\delta = a \times V^k$, where a and k are PMT constants and V is the interdynodes voltage. Hence, for a dynodes chain with n stages, the electron multiplication, or gain G, is: $G = a \times V^{kn}$ [218]. XENONnT PMTs operating at ~ -1.5 kV have a typical $\mathcal{O}(10^6)$ signal amplification.

It can often happen that some steps of the amplification chain are skipped. For instance, an electron emitted by the photocathode could miss the first dynode, leading to a smaller signal output. Similarly, secondary electrons produced at the first dynode can backscatter toward the photocathode. The electrons will eventually return to the first dynode following the electric field, but the impact is less violent, thus the amplification smaller [218]. This process produces under-amplified signals, which must be considered to

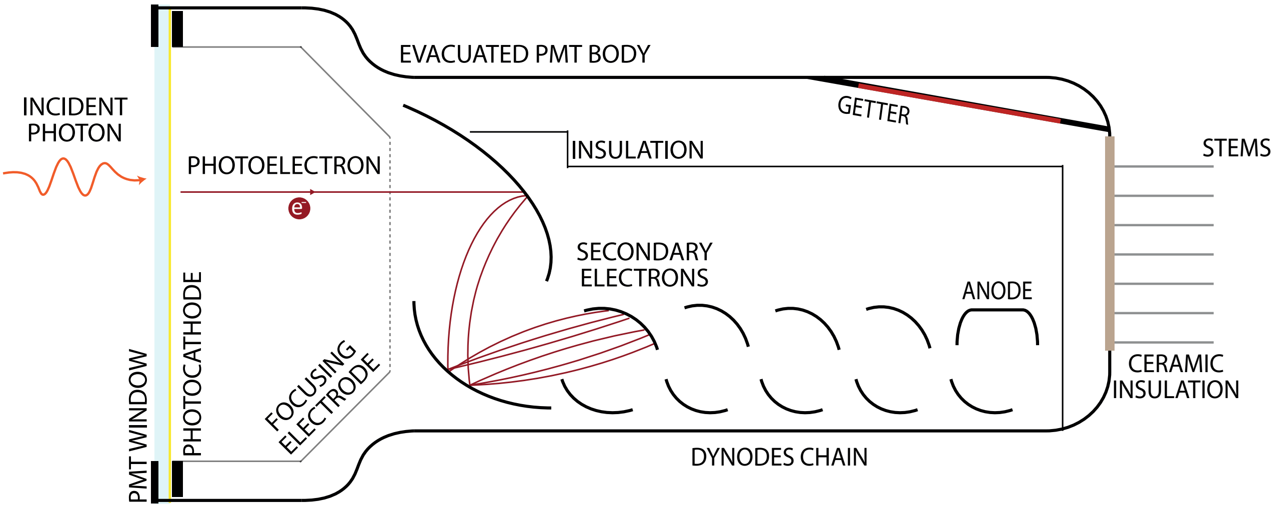

Figure 4.1: A schematic figure of R11410 PMT. The figure is inspired by [219]. The incident light that passes through the PMT window interacts with the photocathode, and a PE is ejected inside the evacuated PMT body. The PE is led by an electric field, established by a focusing electrode, toward a dynodes chain. The PE follows the differential potential among subsequent dynodes, and secondary electrons are produced at each collision with the dynodes. The power is externally supplied to the dynodes through outgoing stems. Eventually, all the produced electrons are collected in the last dynode - the anode - and if the signal amplification is high enough, it can be read [217]. Several components represented in the schematic are specific for 3" Hamamatsu R11410-21, and they will be discussed in section 4.1.2.

interpret the PMT output properly. Another interesting proposed source of under-amplified signals is due to incident photons that interact directly with the first dynode [220, 221]. This effect and other imperfections in the multiplication chain are difficult to describe. Different models are suggested, which can lead to different interpretations of the PMT output, e.g., gain.

The ability of PMT to detect a single photon also depends on the level of dark currents: a small amount of current not originated by incident light. The causes of dark currents are several: scintillation from glass caused by cosmic rays or field emission inside the PMT body rather than intrinsic radioactivity. The most dominant source is thermionic emission from the photocathode and dynode surface. Due to their high electron-escape probability material composition, also known as work function, it is very likely for an electron to jump into excited states and overcome the vacuum level barrier, making itself free [217]. Dark current is extremely voltage-dependent: the higher the power supplied to the PMT, the higher the spurious current. On the other hand, especially for the thermionic component, lowering the operating temperature helps to decrease the dark currents.

Ideally, for each electron produced at the photocathode, the PMT should respond with a single charge pulse at the anode with a *transit time* characteristic of the type of PMT. However, to some extent, all the PMT suffers from spurious small pulses right after the signal pulse. This so-called *afterpulses* (AP) can happen with $\mathcal{O}(10\ \text{ns})$ time delays, mainly caused by elastic scattering electrons on the first dynode, or with $\mathcal{O}(10\ \mu\text{s})$ delays. One origin of the latter AP is the presence of residual gases in the evacuated photomultiplier tube. During their path toward the dynodes chain, the accelerated electron can bump into residual gases, ionizing them. These positive ions will accelerate in the direction of the photocathode, impinging against it and producing many PEs, resulting in a delayed pulse. The AP time difference and amplitude are linked to the ion that generates it. The AP rates should be kept as low as possible to avoid bias in the PMT signal readout. Furthermore, as it will be discussed in section 4.2.2, an increasing AP rate would suggest a PMT body vacuum leak, threatening its stability. The electric field configuration of Hamamatsu R114101-21 is such that the time that the ion takes to reach the cathode is almost independent of where it is produced and depends mainly on its mass-to-charge ratio M/Q:

$$t = \left(1.134\ \mathrm{V}^{1/2}\ \mu\mathrm{s}\ \mathrm{cm}^{-1}\right)\sqrt{\frac{L^2}{V_0}\frac{M}{Q}}, \tag{4.1}$$

where L [cm] and V_0 [V] are the distance and the voltage difference between the photocathode and first dynode, respectively [216]. To use Eq.4.1 M/Q must be expressed as a dimensionless quantity equal to the number-of-nucleons/units-of-charge, i.e., $M/Q_{H^+} = 1$, $M/Q_{Ar^+} = 40$, $M/Q_{Xe^{++}} = 65$, and $M/Q_{Xe^+} = 131$. In the case of XENONnT PMTs, $L = 4.1$ cm and $V_0 = 323.4$ V if the PMT is operating at -1.5 kV. Thus: $t_{H^+} \approx 0.26\ \mu s$, $t_{Ar^+} \approx 1.63\ \mu s$, $t_{Xe^{++}} \approx 2.08\ \mu s$, and $t_{Xe^+} \approx 2.96\ \mu s$ [216].

The last source of concern for PMTs that this manuscript aims to emphasize is *light emission*: a process where a PMT can produce individual photons at a wavelength such that the PMTs themselves are sensitive to it. Previous studies attempt to explain this process, e.g., charge-up of the ceramic component of the PMT. However, it is not fully understood [222, 223]. The concern is that a PMT with a high light emission rate can also trigger the surrounding sensors, and the likelihood of mimicking a real event is high. If the light emission rate is too high can significantly damage the sensitivity to a few photon events. Therefore, as shown in section 4.2.2, every tested PMT with high light emission rate was not considered for the XENONnT experiment.

An ideal PMT should always provide a signal proportional to the number of incident photons. However, this input-output linearity is valid in a finite region, called *dynamic range*. The linearity is lost when the incident light is too intense, and the photocathode can not provide enough PEs. Loss of linearity can also occur at the level of the dynodes chain if too many secondary electrons are produced. On the one side, the dynodes can provide a finite number of secondary electrons. On the other side, the charge repulsion in the electron cloud leads to some electrons not being collected at the anode. These two processes are the origin of linearity loss at the anode. Overlinearity can occur as well, usually if the PMT base current is too low. In this case, the opposite current generated by the secondary electrons on their way to the anode will reduce the potential difference between the last dynode and the anode. Since the power supplied does not change, the potential loss is redistributed to the other dynodes, increasing the signal amplification in the first stage of the chain. The linearity characteristics depend only on the current value for a fixed supply voltage and are usually optimized for analysis purposes [217]. Section 4.1.2 contains the precautions used in XENONnT to achieve a wide dynamic range.

The uniformity of the response of the photocathode and anode with respect to the position and angle of the incident light is another key factor to consider. Whereas a spatial uniformity response is rather easy to achieve, angular uniformity always degrades for high incident angles. As it will be shown in section 6.5.2, this information must be considered for a proper detector simulation. XENONnT uses the angular dependence of the QE described in [224]. It is the result of two competing effects: the Fresnel transmission through the PMT window and the absorption probability in the photocathode. As the incident angle increases, the transmission decreases, but the absorption probability increases because the pho-

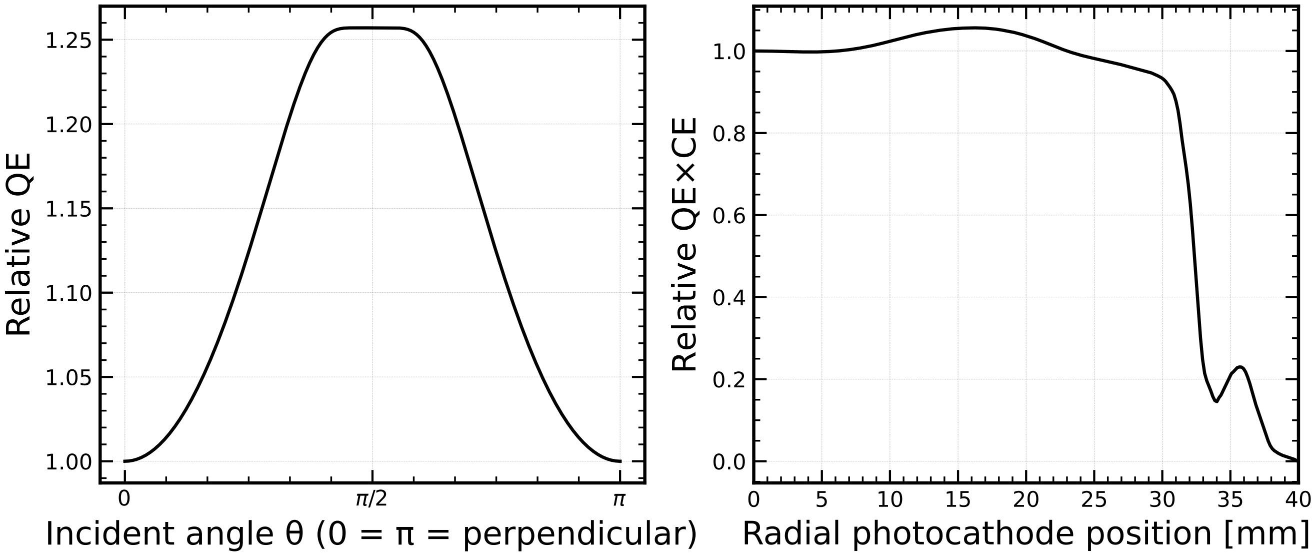

Figure 4.2: PMT spatial and angular uniformity responses. (Left) Relative XENONnT PMT QE as a function incidence angle, where 1 corresponds to the nominal QE provided by the Hamamatsu. (Right) Averaged XENONnT relative PMT efficiency versus radial position of the photoabsorption. The curve is normalized to center of the PMT. Curves taken from [225].

tons pass through a greater effective thickness [225]. The left panel in Fig.4.2 shows the relative QE, with respect to perpendicular incident light, for a given incidence angle. The PMT response as a function of the radial position of the photoabsorption provided by Hamamatsu is considered, which combines both the radial dependence of QE and CE. In addition, the UZH group in the XENON collaboration also provided an independent spatial uniformity measurement for R114101 PMTs, consistent with the Hamamatsu measurements [226]. The average XENONnT PMTs curve, normalized for the response at the center of the PMT (90 % [227]), is shown in the right panel of Fig.4.2.

Finally, it has been observed that the PMT response to one photon does not always correspond to one PE. The probability of emitting two PEs, called DPE emission, is $\sim 20\%$ for XENONnT PMTs at VUV wavelength [228]. In itself, the DPE emission is not a problem. However, it needs to be propagated correctly when the PMT output is analyzed and simulated. After a long correspondence with the PMT manufacturer and verifying the method by which quantum efficiency is measured, the XENON collaboration concluded that the QE provided by Hamamatsu included the DPE probability.

4.1.2 Design of R11410-21 PMT

The R11410 PMT is a 3-inch diameter tube produced by Hamamatsu for xenon-based detectors. The model *21* is used in the XENON experiment, which was the result of a collaboration with Hamamatsu to improve its performance at the temperature of liquid xenon and reduce its radioactivity. In this section, the different PMT components are presented.

The PMT body is made of Kovar, an iron-nickel-cobalt alloy with a high magnetic permeability to shield the inner parts from external magnetic fields, which could otherwise affect the PMT performance. A VUV-transmitted window delimits the PMT body. The window is made of quartz (synthetic silica) because it has low ultraviolet light absorption. The PMT photocathode is based on *bialkali*, a compound of two al-

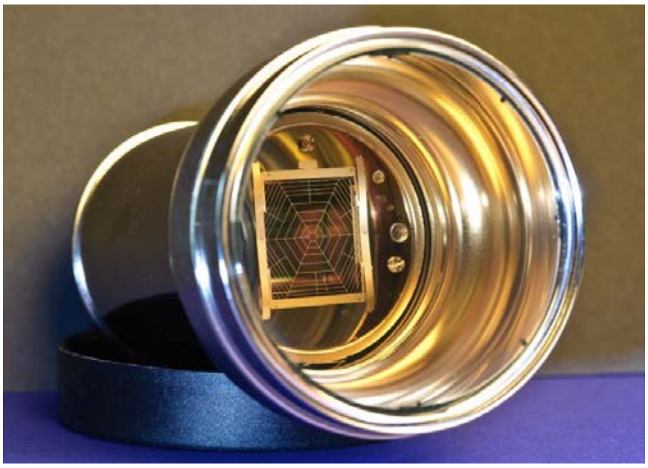

Figure 4.3: A 3-inch Hamamatsu R11410-21 photomultiplier tube used in XENON experiment.

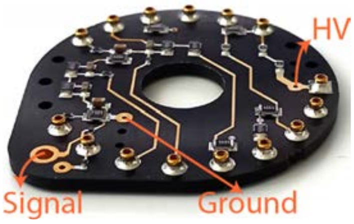

Figure 4.4: Voltage divider circuit, as known as base, to operate the XENON PMT.

kali metals with antimony[1] to enhance the QE at short wavelengths. As discussed in section 4.1.1, a low photocathode resistance is preferable for a better linearity response to avoid saturation effects for large signals [229]. Hamamatsu achieves the right resistance by including a small bismuth in the photocathode composition. This photocathode design guarantees 34 % QE on average [213]. On the back side of the PMT, the stems use ceramic material to insulate the connections to the individual dynodes. The dynodes chain consists of a *linear-focused* structure, supported by an L-shape insulator, made of 12 amplification stages [230]. This dynodes chain provides fast time response with a transit time of $\sim$ 125 ns [216] and a spread of $\sim$ 9 ns [213], a collection efficiency above 90 % [216], and signal amplification of $\mathcal{O}(10^6)$ at −1.5 kV [213]. The PMT contains a strip of undisclosed getter material that activates itself at low temperatures, which helps to reduce the AP rate [213]. When gas molecules strike the getter material, they combine with it chemically or by absorption, reducing the residual gas within the PMT body that can otherwise lead to after-pulses. However, noble gases like He, Ar, and Xe are unaffected by the getter. Fig.4.3 shows a picture of the XENONnT PMT.

Alongside the performance optimization, different material compositions were investigated to minimize the PMT contribution to the total background budget in the experiment. Gamma-ray spectroscopy [193, 195] and glow-discharge mass spectrometry [231] were used to infer the intrinsic radioactivity of the individual PMT construction materials. From one version to the other, the overall radioactivity was significantly reduced to an acceptable level [219]. The expected NR background within $(4, 50)$ keV in XENONnT originated from spontaneous fission or $(\alpha$, n) reactions in the PMT materials had been estimated to be $\mathcal{O}(0.03)$ (events/(t × yr)) in 4 t fiducial volume [151]. Hence, PMTs do not limit the sensitivity of the experiment. Material alternatives are still being investigated to reduce the impact of the photosensor on the background contribution for future xenon-based detectors.

The power to operate the PMT is provided externally by small printed circuit boards (base)[2] connected directly to the dynodes through the stems. The XENON PMT base, shown in Fig.4.4, represents the first

---

[1] The exact composition is unknown, it is a Hamamatsu secret.

[2] DuPont$^{\mathrm{TM}}$ Cirlex©, a thick all-polyimide laminate sheet material, has been used as board substrate. Fralock is the exclusive worldwide licensee and manufacturer of Cirlex© [230]

step in the data acquisition, from which the anode signal is read out. The base design has been unchanged since XENON1T [229], and it is shown in Fig.4.5. A negatively biased photocathode and a grounded anode scheme are used. A grounded anode reduces the noise fluctuation in the PMT readout induced by the electrical components, e.g., high-voltage power supply. The downside is that the PMT body is at the same photocathode potential, which requires meticulous electrical insulation with the surrounding. The resistor chain was designed to minimize heat dissipation and fulfill the linearity requirements. The total resistance is $R_{tot} = 92.5$ MΩ. For a bias voltage of -1.5 kV, the PMT base current is $I = 16.2$ μA, leading to a power dissipation of 0.024 W. Considering 494 PMTs in XENONnT, the total power from the base is $\sim$ 12 W. As shown in Fig.4.5, the first dynodes have a high voltage drop and, consequently, a high electric field. This choice has been taken to improve the CE [229]. The last dynodes chain stages also benefit from a high voltage drop, which establishes a high electric field that overcomes the repulsive force in the electron clouds at the last amplification stages. Moreover, parallel to the last resistors, capacitors are present to further improve the linearity by spreading the output current over time. However, since the capacitors need time to recharge, they do not help with the saturation due to the high signal rate. This base design helps to achieve good linearity up to a signal current of $\sim$ 30 mA at a signal rate of 200 Hz, sufficient to maintain linearity response for $\mathcal{O}(\mathrm{MeV})$ events [229]. As well as the PMT, the base production required a careful choice of each component, e.g., resistors, capacitors, and soldering material. As mentioned in section 3.3.3, the materials have been selected after a radioassay campaign. Then, these were provided to an external company[3] for assembly. More detail on the production can be found in [232].

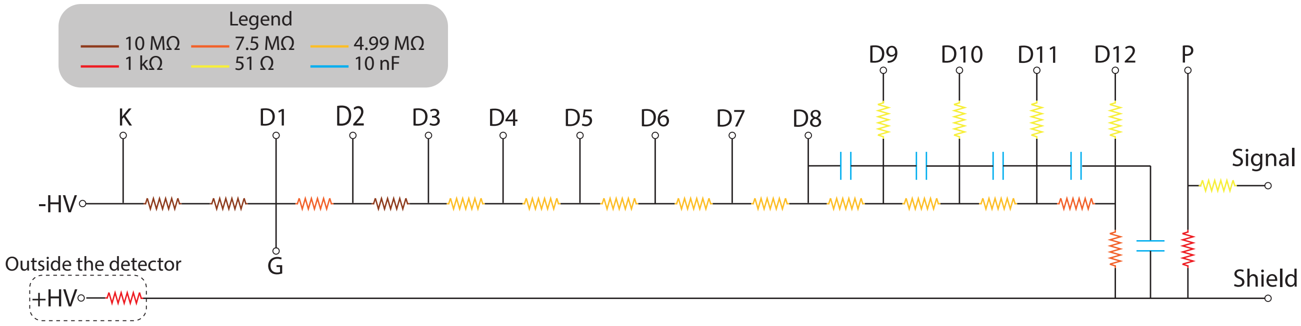

Figure 4.5: Resistor chain adopted in the PMTs of XENONnT's TPC. Illustration adapted from [229].

4.2 The XENONnT PMT testing campaign

Of the 494 XENONnT PMTs, only 153 were inherited from XENON1T. The remaining 341 PMTs were chosen among 368 PMTs according to their time stability and performance in liquid/gas xenon environment. The testing campaign of these 368 PMTs has been carried out by the Max Planck Institute for Nuclear Physics in Heidelberg, Stockholm University, and the University of Zurich. A total of 105 PMTs were tested in the testing facility MarmotX at UZH. The testing campaign, which ended in a publication [213], is presented in the following sections.

---

[3] The same company used to assemble the base of XENON1T. The company is called Elfab.

4.2.1 MarmotX facility

The MarmotX facility comprises a double-walled vacuum-insulated cryostat, which can host up to 10 3” PMTs. A render of the facility is shown in Fig.4.6. An in-depth description of the full setup can be found in [233]. An aluminum/PTFE support holds the PMTs in a two-array structure with the windows facing each other, as shown in Fig.4.7. The support structure is also used as filler to minimize the xenon needed ($\sim$ 19 kg). The PMT characterization is performed using a blue LED ($\lambda \sim 470$ nm) placed at the center of the setup. A total of 8 Pt100 resistant thermometers are placed at several depths of the inner chamber to monitor the xenon temperature.The gas xenon is stored in aluminum bottles next to the setup, and the filling is performed through the dedicated gas system described in [233]. The warm gas is injected into the cryostat from the top, where a pulse tube refrigerator (PTR) liquefies it (model Iwatani PDC08, 24 W of cooling power at 164 K). The PTR cold head is wrapped in heating foil and controlled by a proportional-integral-derivative (PID) controller (Cryo-con 32) to adjust the temperature of the chamber. The thermal radiation losses from the inner cryostat to the rest of the room are minimized by wrapping the inner cryostat into multi-layer insulation (MLI) foil. The outer vessel is evacuated to provide thermal insulation. A vacuum pressure gauge is used to monitor the pressure during the operation. In case of emergency, a liquid nitrogen bottle can provide additional refrigeration power if the inner pressure rises above 2.5 bar. However, a safety mechanism is present if the pressure overtakes the maximum safe pressure for R11410 PMT ($\sim$ 3 bar) [232]. In this case, a spring-loaded pressure-release valve will open, and the xenon will be vented.

The PMTs are powered by an Iseg EDS-F-130n 16-channel high voltage module, and their signal is read by two CAEN V1724 digitizers after $\times 10$ amplification with a Phillips 776 amplifier. An additional copy of the amplified signal is routed into a CAEN N845 discriminator, whose output passes to a CAEN V260 scaler for PMT rate monitoring. The data acquisition and processing are based on custom-made softwares [233].

4.2.2 Testing campaign result

The PMT testing was performed in an environment as close as possible to the XENONnT condition, namely a temperature of $\sim$ 175 K and a pressure of $\sim$ 2.3 bar. Every batch of 10 PMTs went through two cooling cycles. The PMT parameters, such as gain, AP rate, and total event rate, were monitored daily during the test. The testing was performed in liquid and gas xenon environments for at least one week in each of them. Furthermore, the arrangement of the two arrays allows dedicated measurements to evaluate the *light emission* rate.

Gain characterization

XENONnT PMTs are expected to have $\sim 10^6$ amplification at ~ -1.5 kV. This was verified for every PMT. The characteristic gain curve as a function of supply voltage, described in section 4.1.1, was demonstrated at each cooling cycle. For every PMT, the a and k parameters are extracted from the so-called *HV-scan*: consecutive gain measurements at increasing supplied voltage. An example from the testing campaign is shown if Fig.4.8. In the testing campaign and XENONnT experiment, the gain is computed using the *model independent method* [234]. To extract the relevant single PE information, this method relies only

Figure 4.6: Render of the MarmotX testing facility. The PMTs are hosted in a two-array structure inside the inner cryostat and inserted inside the outer cryostat. The region among the two cryostats is evacuated to ensure good thermal insulation. The xenon is liquefied at the top by the PTR. Several ports allow the cable connection from the air to the xenon side to perform the PMT testing. Figure by J. Franchi.

Figure 4.7: Render of the PMT support structure used in the MarmotX testing facility. The two-sided structure of PMT arrays can be appreciated. Figure by J. Franchi.

on statistical argument rather than the more conventional single PE fit. Comparing a PMT response to a low-intensity light with the response of no light makes it possible to derive the PMT signal amplification. The full description of the method is in section 5.1.3. All the tested PMTs showed the expected gain performance through the gas and liquid periods.

Afterpulses characterization

The afterpulses characterization was performed via high LED intensity illumination. The larger the AP triggering pulse, the better the AP resolution since each PE in the main pulse can produce an AP. At the same time, AP characterization is more effective with fast-triggering pulses to avoid pulse overlapping. The fea-

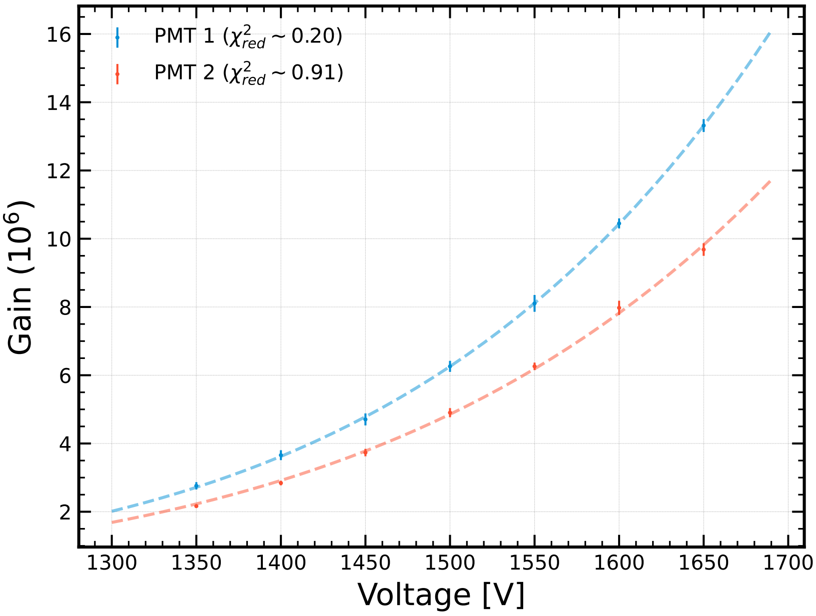

Figure 4.8: Example of HV-scan results for two PMTs during the PMT testing campaign. The exponential trend of the gain as a function of the supplied voltage has been investigated. The χ^2 goodness-of-fit test suggests a good match with the gain model described in section 4.1.1. None of the tested PMTs showed a discrepancy with the expectation.

tures of delayed pulsed within 5 μs to the triggering pulse were analyzed. The top panel of Fig.4.9 shows the two-dimensional histogram of the AP integrated charge as a function of the time delay between the main LED signal and the AP. Three regions in the histogram can be identified. At a small time delay, there is a highly populated region **A**1 with AP signal $\mathcal{O}(1\,\text{PE})$, most likely generated by backscattering electrons at the first dynode. A second region with the same AP intensity, **A**2, can be identified. Its time distribution extends up to several μs, and there is no clear theory of their origin. Finally, the testing campaign aims to study the last region **A**3. APs due to residual gas would show up in this region at some precise time delay proportional to their charge-to-mass ratio. As discussed in section 4.1.2, the events at $\sim$ 2.7 μs are connected to the presence of xenon inside the tube, whereas the presence of argon is linked to the population at $\sim$ 1.6 μs. It is improbable that residual traces of xenon are introduced during manufacturing since the xenon concentration in the air is very low (0.086 ppm [235]). Hence, any xenon-related APs, even at a low rate, indicate poor sealing of the PMT. This technique of leak-checking was already used by XENON1T [216] and PandaX-I [236], and it proved to be very efficient in detecting very small vacuum degradation. On the contrary, argon is very abundant in the atmosphere (concentration of $\sim 1\,\%$ [237]), and it can leak into the PMT body during manufacturing.

The presence of AP is more evident if the two-dimensional histogram is projected onto the time delay axis, as shown in the bottom panel of Fig.4.9. A good PMT is shown in blue, and a leaky PMT is shown

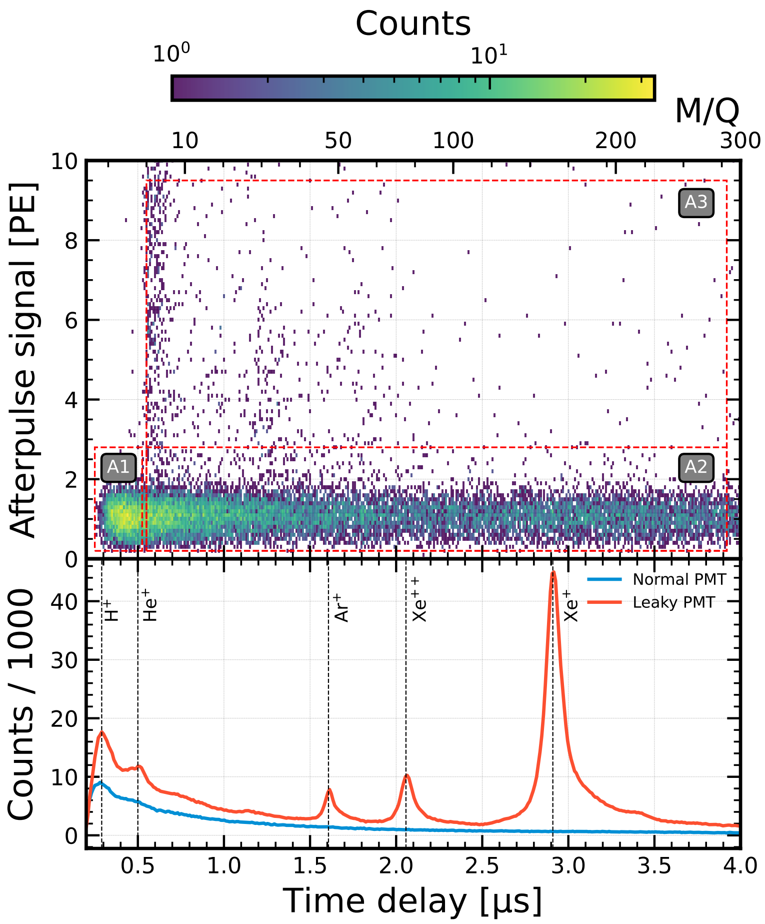

Figure 4.9: The top panel shows the two-dimensional histogram of AP size and its time delay. The three regions described in the text are highlighted. The bottom panel depicts the projection on the x-axis of the two-dimensional histogram. A good PMT is shown with the blue line, while a bad PMT is with the red line. The presence of Ar^+, Xe^+, and Xe^{++} APs is evident.

in red. From the fit of the peak correspondent to the specific ion, the AP rate is extracted, defined as the fraction of photoelectrons in the main signal that induces an afterpulse. This parameter was used for rating the tested PMTs. PMTs showing xenon AP rates were excluded from XENONnT, as well as those with high argon AP rates ($> 0.3\ \%$) and those with increasing AP rate over time.

Light emission study

As described in section 4.2.1, the amplified PMT signal is also fed to a CAEN N845 discriminator and then to a CAEN V260 scaler. The discriminator threshold is set to 11 mV, equivalent to $\sim$ 0.5 PE signal for $5{\times}10^6$ signal amplification. The combination of discriminator and scaler is used to monitor the total PMT rate. No conclusion on the DC rate can be drawn with this measurement because the total rate also includes the scintillation in the xenon produced by cosmic rays. However, its monitoring is useful for evaluating the stability of the PMT at cryogenic temperatures. An example of total rate evolution for two facing PMTs is shown in Fig.4.10. No strong fluctuation has been observed, which indicates the high reliability of R11410-21 PMT at cryogenic temperature. The rate spikes correspond to LED pulses from the gain and AP measurements.

The inlet plots of Fig.4.10 show the results of the dedicated measurement for detecting light emission. Since the light emission is voltage-dependent, the measurement evaluates the trigger rate of one PMT while decreasing the power supply of the facing one. If the trigger rate of the one PMT decreases while turning down the voltage of the facing one, it is possible to conclude that the facing PMT is emitting light. The two PMTs in Fig.4.10 do not exhibit any trace of light emission. PMTs in which it was identifying unusually high emission rates were excluded from the final PMT list for XENONnT. More information about *light emission* test can be found in [232].

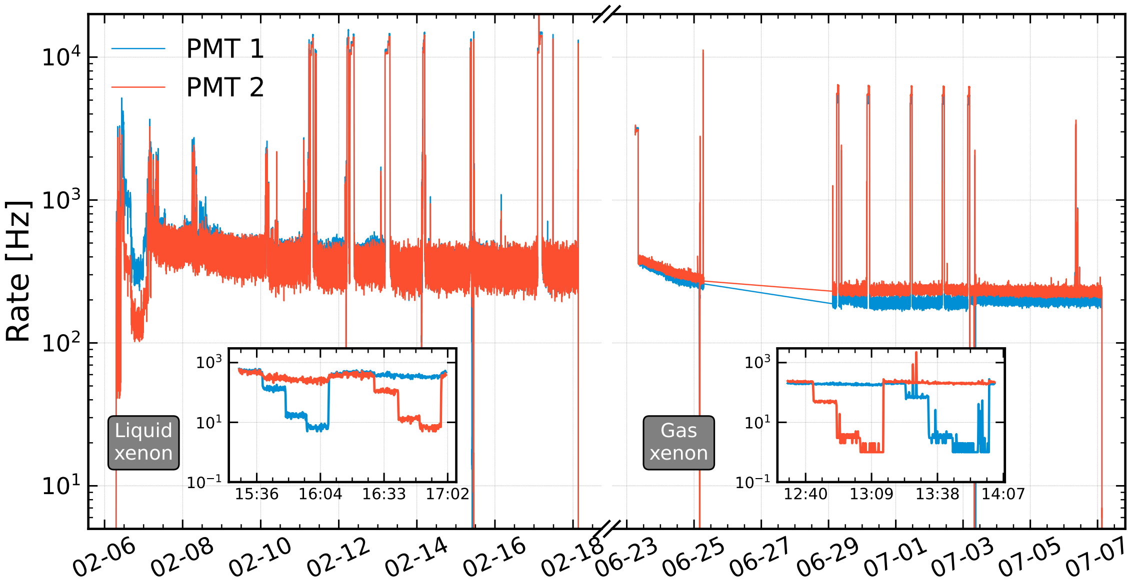

Figure 4.10: Evolution of the event rate of two facing PMTs during the testing campaign. The left side shows the liquid xenon period, while the right shows the gas xenon period. The rate spikes correspond to LED pulses from the gain and AP measurements. The inlet plots show the light emission measurement performed during the test. For these PMTs, there is no evidence of light emission.

Another category of light emission was investigated: intermittent light emission, where occasionally a PMT shows very strong light emissions which could last a few seconds, often called *flashes*, up to hours or even days. XENON1T observed that this intermittent light emission was often triggered by a high rate of signals [216]. Therefore, during the test campaign, a so-called high-illumination stress test was performed in liquid and gas xenon. Over two periods of several hours, the PMTs were illuminated with an LED intensity of $\mathcal{O}(10^5\ \mathrm{PE})$, comparable to the most active calibration periods of XENON1T, and the total rate was monitored. In a few cases, this triggered strong light emissions of $\mathcal{O}(10\ \mathrm{kHz})$. As a result, these photosensors were excluded for XENONnT. For a more detailed discussion on strong light emission, refer to [232].

4.2.3 Conclusion

The results of the testing campaign are shown in Tab.4.1. Of the 368 new PMTs, 105 were tested at the University of Zurich. Contrary to XENON1T PMT testing campaign, all the newly purchased XENONnT PMTs were tested over a period of at least two weeks, one in liquid xenon and one in gaseous xenon environments to mimic the bottom and top PMT arrays condition in a dual-phase XENON TPC.

It was proven a sensitivity to xenon-related afterpulse rates on the order of 10^{-5} %, sufficient to detect the smallest identified leaks in XENON1T PMTs. This level of sensitivity permitted to improve considerably the photosensor's quality. Six PMTs were disqualified due to an increasing afterpulse rate from xenon or argon atoms due to vacuum degradation. Other seven PMTs were rejected due to a high rate of nitrogen afterpulses, likely due to air leak or the release of a large amount of nitrogen trapped within the PMT [213].

Particular attention was paid to the identification of light emissions. Only five out of 368 tested PMTs were disqualified due to $\mathcal{O}(\text{kHz})$ light emission. Other six PMTs were identified to have intermittent high-rate light emission and therefore excluded [213].

Two PMTs were excluded from the final PMT list because they could not be turned on, most likely due to damage during transportation. The remaining PMTs and the 197 PMTs selected from XENON1T were graded according to their performances [238]. At each problem, such as micro and low-rate intermittent light emission as well as argon afterpulse rates, was assigned a certain number of penalty points. In addition, points were given to PMTs manufactured in batches containing several other PMTs that had developed severe problems. The rating was used for photosensor selection and for the arranging in XENONnT TPC. The results of this PMT testing campaign resulted in a publication [213].

	Tested	Accepted	Sealing problem	Light emission	Other problems
In total	368	342	13	11	2
At UZH	105	100	2	2	1

Table 4.1: Summary of the XENONnT PMT testing campaign. Adapted from [232].

4.3 Installation of XENONnT PMTs

After completing the PMT testing campaign in the winter of 2019, the photosensors were shipped to LNGS. In the following months, the PMT arrays were assembled in a clean room in the above-ground facility a LNGS, following specific cleaning procedures for PMTs, the cables, and the bases. The next sections first discuss the PMT cables, their properties, their installation scheme, and the cleaning procedure adopted. The PMT bases production and cable connectors used in XENONnT are shown together with the cabling design. The PMT array assembly will follow, and the chapter ends with the underground installation of the XENONnT TPC.

4.3.1 The XENONnT PMT cables

As shown in Fig.3.7, all the PMT cables[4] are guided from the TPC to the third floor of the service building next to the water tank through two cryogenic pipes. One pipe is inherited from XENON1T, designed to host cable for up to 432 PMTs. The final design of XENONnT TPC included 494 PTMs. Thus, a new pipe was installed to host the extra cabling. The pipes also host the infrastructure for the cryogenic operation, as well as the cabling for temperature sensors and liquid level sensors. Two different types of cables are used to read out the PMT signals and supply them with high voltage. The signal readout uses PTFE-insulated coaxial cables, RG196A/U. The voltage and the ground return are provided with Kapton© insulation, single silver plated copper wires, AWG 30, rated up to 2 kV. The PMT cabling is such that every PMT is independent. Namely, the power supply can be chosen individually. This is essential for performance optimization and excluding certain PMT in case any problem arises. The extra cabling required for XENONnT was selected through radon emanation measurement and radioactive screening campaign as described in section 3.3.3. The results are described in [232, 201].

The end of each pipe is connected to a vacuum-tight vessel, called breakout chamber, equipped with several vacuum-potted feedthroughs. There, the cabling and other connections are carried out from the xenon atmosphere into the air. Fig.4.11 shows a picture during the installation of the XENONnT potted feedthroughs. The cables are sealed into the flanges with black epoxy. A total of eight coaxial cable feedthroughs are needed, each containing 72 cables potted in a DN 63 CF flange. All of them were purchased new for XENONnT. The Kapton© wires are potted in DN 40 CF flanges, with either 104 or 80 wires each. Out of the seven needed for XENONnT, four were inherited by XENON1T, and three were purchased new. The signal cables are routed from the breakout chambers to the DAQ, one floor below, using a metal rank and cable ties. In the DAQ room, they are connected to the dual channel Phillips 776 amplifiers. The ×10 amplified signal is guided to CAEN V1724 digitizers. Furthermore, the top PMTs ×0.5 amplified signal is also digitized for high energy analysis. On the airside, Kapton© wires are collected into 52-pin Radiall connectors [239] and plugged first into a custom-made filter box, designed to reduce the noise produced by the voltage supply, and then into the voltage boards CAEN A7030LN or CAEN A1536LN. The shielding of the coaxial signal cables is fixed to the common ground through a 50 cm long Kapton© wire, called ground return, directly in the PMT base. The voltage power supply provides the common ground, which is kept floating to avoid ground loops [240].

To facilitate installation, the cabling scheme is divided into three sections. First, the cables directly soldered into the PMT base go to a connector at the top of the cryostat. The second section runs into the cryo-pipes to the breakdown chambers, where the cables are connected to the third section, which consists of the potted feedthroughs, and then into the DAQ room. The actual electrical connection is made via MMCX pins for the signal cables on the xenon side and SMB for the amplifier connection. D-subminiature pins and sockets instead make the high-voltage connection. Since the grounding scheme is common to all the PMTs, the high voltage returns from the bases are collected into a common connector, called *ground return collector*. The cabling scheme is sketched in Fig.4.12. The top and bottom PMT array cables on the xenon side have a different length of 1.5 m, as shown in the sketch[5]. To avoid any time delay

---

[4] Both HV and signal cables running in the cryogenic pipes are 9.6 m long.

[5] The cables of the top and bottom PMTs are 2.20 m and 3.70 m long, respectively.

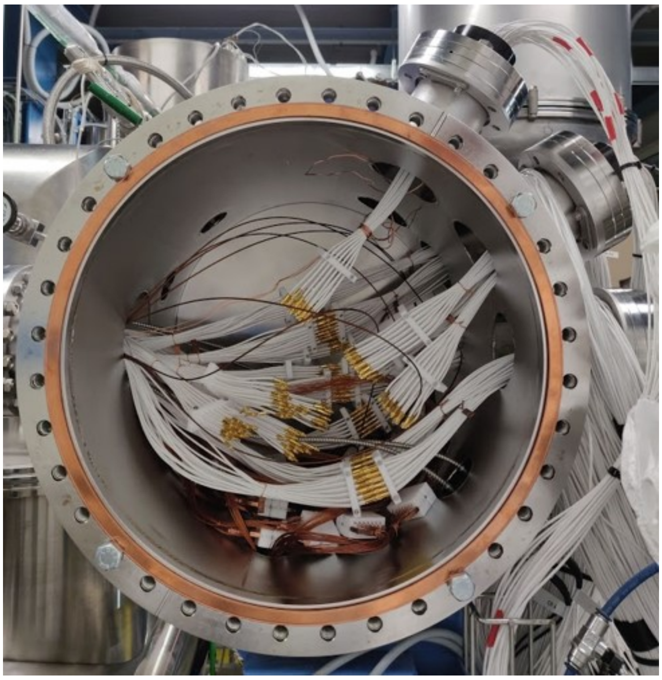

Figure 4.11: XENONnT vacuum breakdown chamber during the cables' installation. The cables from the TPC arrive from the left. The potted feedthroughs, visible at the top right of the picture, do the passage from the xenon to the air.

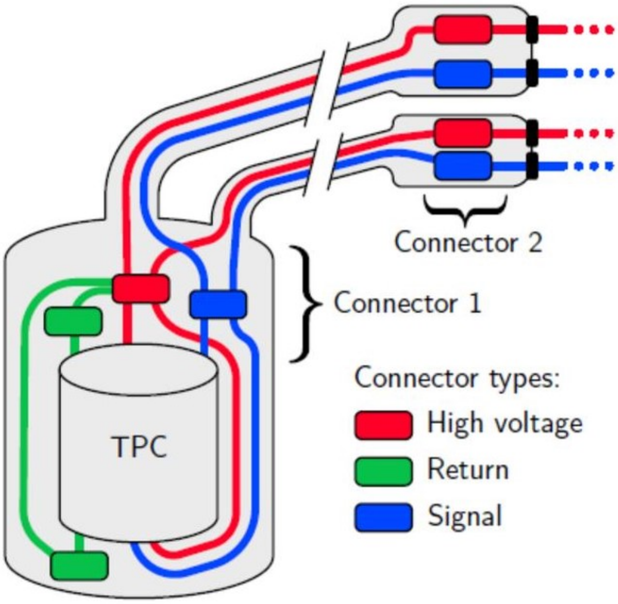

Figure 4.12: XENONnT cabling scheme. The rectangular blocks represent the position of the connectors. Figure by A. Brown.

between the signal from the two arrays, the coaxial cable length is adjusted on the air side. Specifically, the top PMTs have 6.75 m cables from the vacuum breakdown chambers to the amplifiers, while the bottom PMTs have 5.25 m cables, both with 25 cm in the potted feedthroughs. Further information on the cabling can be found in [241, 232].

4.3.2 The XENONnT PMT connectors

Fig.4.12 shows where the three cable sections are joined: first at the top of the cryostat, near the pipes' entrances, and then in the two breakout chambers. To provide structure, the PMTs are divided into groups of 24, called *PMT array sectors*. Each type of cable from a sector is collected in custom-made connectors made by PTFE, free-oxygen copper, and stainless steel [241]. They are meant as a support structure and to help during the installation. The coaxial cable connector, the high voltage wires connector, and the ground return collector are shown in Fig.4.13. As described in section 4.3.1, the ground return collector contains the grounding return from a PMT sector. Then, two redundant Kapton© wires are routed from the ground return collector into a dedicated hole in the high-voltage connector. Hence, the high voltage connector can host up to 26 Kapton© wires, where two of them are reserved for the ground returns and 24 for the PMT power supply. Whereas, the signal connector can host up to 24 coaxial cables.

Each PMTs array is divided into 11 sectors, as shown in Fig.4.14. The grouping was chosen to minimize the length of the cables. Besides sector 5, which contains 13 PMTs, and sector 12 with only one PMT, all

(a)

(b)

(c)

Figure 4.13: Connectors used for PMT cables in XENONnT. From left to right: signal connector, high voltage connector, and ground return collector.

the other sectors have 24 PMTs. Sector 12 does not have any connectors because its cables are collected into sector 5 connectors. Thus, the bottom PMT array has 10 sector effectively. The cables from the bottom array are routed toward the top of the TPC by 6 PTFE cables-guides on the outer side of the TPC wall.

The same cabling scheme adopted on the xenon side is used for the air side. Hence, there is a one-to-one correspondence between the Radiall connector, the HV boards, and the amplifier with the PMT sector. These helped to reduce the electronic noise and human mistakes during installation.

The cables are prevented from being too loose thanks to PEEK cable ties applied all along the cables bunch, particularly close to the connectors. Moreover, the cable ties were laser engraved with an identification code to help the connections. The PEEK cable ties were not used for the old pipe, since there was already an identification copper plate for each bundle of cables.

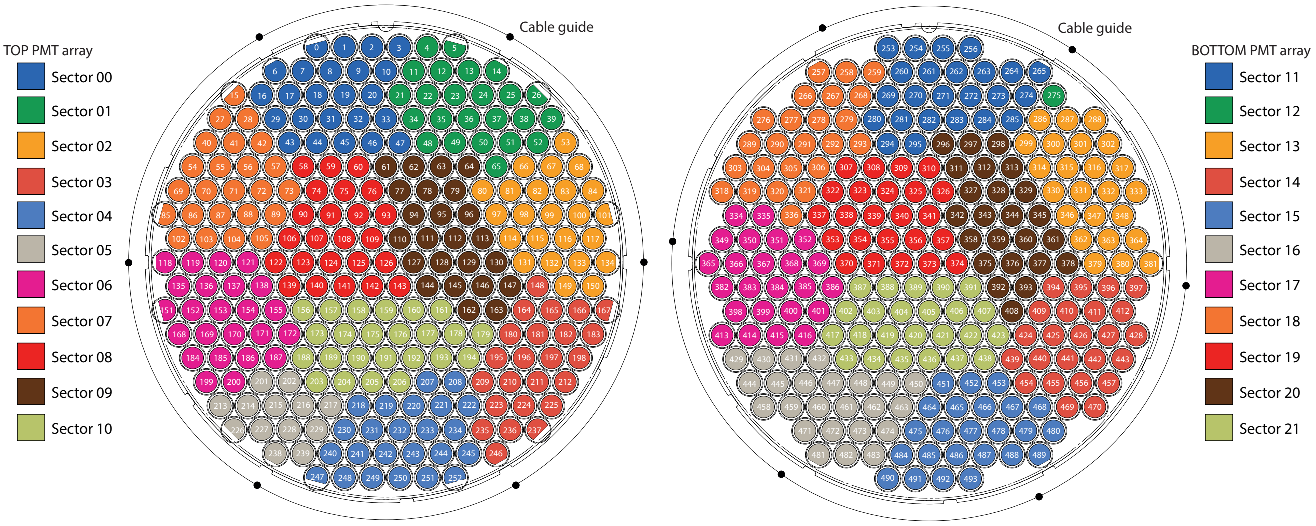

Figure 4.14: The scheme of PMT sectors adopted in XENONnT. The positions of the cable guide, used for the bottom PMT cables to route them towards the top, are also shown.

4.3.3 Cables and bases production, assembly and cleaning

A total of 567 PMT bases were produced for XENONnT. The printed circuit board (PCB) comes from Fralock in the USA, which has the exclusive patent for Cirlex production. The circuit components were the same ones used in XENON1T, except for the resistance 1 kΩ and 51 Ω [232] (see Fig.4.5). Every component was produced or purchased in abundance to have sufficient material for radioassay via γ-ray spectrometry or the ICP-MS technique, as described in section 3.3.3. The sum of individual screening results is compatible with the full base assemble results [200]. The behavior of every fully assembled base was tested by applying -1.5 kV and verifying the voltage drop across each resistance and total voltage output. For this test, a dedicated tool was provided by the UZH electronics workshop. The test was performed twice, before and after soaking the bases in liquid nitrogen. The thermal stress allowed for the identification of the problematic bases. Out of the 567 bases tested, 66 did not pass the test. The problem was identified with a broken connection in one of the three *vias*, which connect the two layers on either side of the PCB. Even though there were sufficient bases for XENONnT, the UZH electronic workshop successfully repaired them.

The coaxial cables were initially purchased from Habia, the company that provided XENON1T cables. However, the results of radon emanation measurement were ×30 larger compared to the rate of the XENON1T samples ((0.34 ± 0.12) µBq/m) [232]. Thus, the manufacturer was changed to Huber+Suhner. They produced the total length of cable required in five batches, eventually grouped in 3, with an acceptable level of radon emanation of (on average $\sim$ 1.5 µBq/m) [200]. The Kapton© cables for the high voltage and ground return were procured from Accu-Glass. Their radon emanation was measured to be (0.41 ± 0.15) µBq/m), a factor four smaller than the coaxial cables per unit of length [200].

The coaxial cables and Kapton© wires have been soldered to the bases by Elfab, using a screened solder wire. Before the soldering, the bases were arranged on acrylic support structures replicating the PMT sectors. After the soldering from Elfab, every electric connection was tested again. Eventually, the acrylic supports, with the bases and the cables, were shipped to LNGS for cleaning and assembly.

Every component of the XENONnT experiment was cleaned in a ISO-5[6] clean room in the above-ground facility at LNGS. In this manuscript, we will not review the procedure for each material since it has been extensively discussed in a recent publication [201]. However, it is important to mention that every component had a different cleaning recipe depending on the material composition. The general approach was ethanol wiping, immersion in a decreasing agent, and/or warm ultrasonic bath (US) with an acid solution. The components were then rinsed with deionized water and dried with ethanol o nitrogen gas. The US bath is important for removing surface contaminations. However, it was not used for the bases to avoid any damage from vibrations in the electrical circuit. The bases were instead only rinsed with deionized water and flushed with nitrogen. In Fig.4.15, a picture shows the PMT XENONnT cable cleaning operation. Once the components were cleaned, they were wrapped in plastic foil and stored in a second cleanroom at the above-ground facility at LNGS to keep them clean. Further information can be found in [232, 200].

---

[6] International Organization for Standardization (ISO) classifies the clean room based on the maximum concentration of particles such as dust and airborne particulates. An ISO-5 clean room is 10^5 per m^3. For an ISO-6, it is 10^6 per m^3.

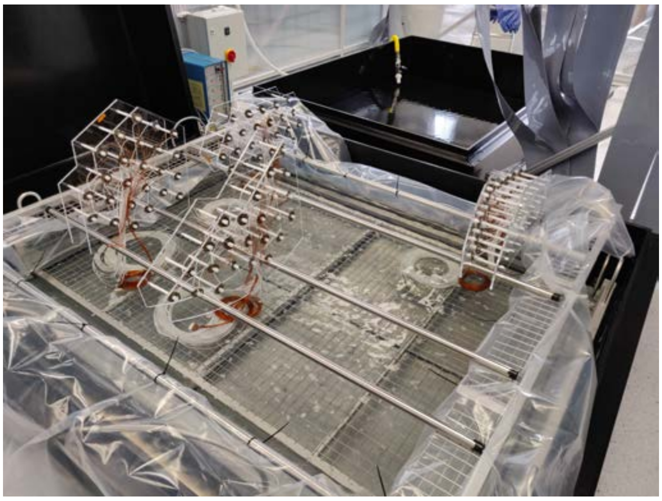

Figure 4.15: Ultrasounds bath for cleaning of PMT cables. The acrylic support structures were held by bars, and only the cables were inside the bath.

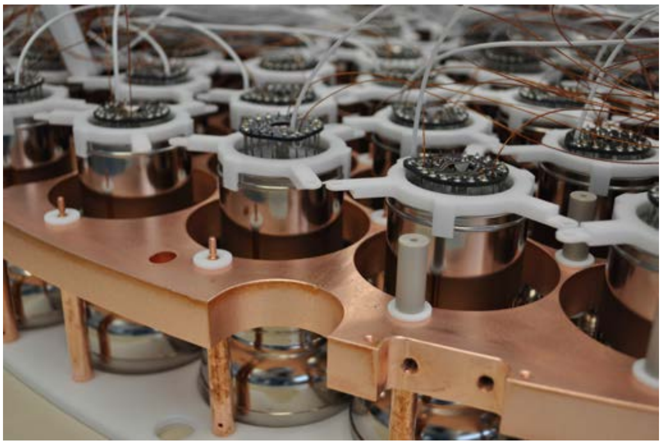

Figure 4.16: Picture during the PMT array assembly. PMTs inserted in the dedicated hole in the copper structure and held from the window by the PTFE panel, visible at the bottom. PTFE clamps from the back of the PMT body ensured their position.

4.3.4 The PMT array assembly

Two PMT arrays in the XENONnT TPC hold 253 photomultipliers at the top and 241 at the bottom. Both PMT arrays consist of a single perforated oxygen-free high conductivity copper (OFHC) plate, providing stability and flatness. Two PTFE discs are fixed on the OFHC plate on the side that looks at the active volume. They work as light reflectors and support for the PMT body. The PMTs are inserted in the hole of the copper plate, and their body is kept in position thanks to clamps mounted on their back and attached to the OFHC plate, which slides in the radial direction to account for the thermal contraction. The PMT are arranged in a compact hexagonal structure to maximize light collection efficiency. In Fig.4.16, a picture of the PMT array is shown.

The PMT arrays assembly, which took place in the fall of 2019, was performed in the ISO-5 cleanroom at above-ground laboratories at LNGS. Previous to that, the array structures were already cleaned and assembled. Then, the PMTs were introduced in the cleanroom following a rigorous procedure. First, they were cleaned with ethanol-soaked wipes for degreasing and blown with nitrogen to remove the dust. These operations were done near the cleanroom entrance, on a clean surface, and the PMTs were handled with latex gloves. Afterward, the PMTs were brought into the ante-cleanroom, called *gray room*. Here they were wiped thoroughly with ethanol by an operator dressed in cleanroom clothes. Once introduced into the cleanroom, they were immersed and gently shaken into an analysis-grade ($> 99.9\,\%$) absolute ethanol bath. The ethanol was changed every $\sim$ 50 PMTs. They were then wiped with cleanroom wipes and flushed with compressed nitrogen. Maximal attention was given during these operations to avoid moving around any dust. The PMTs were inspected, and if the examination was positive, they were inserted in the specific position following the PMT scheme shown in Fig.4.14. A picture during the PMT assembly operation is shown in Fig.4.17. Note that the PMT array structure was already assembled and placed on a clean desk on the PTFE side at the time of this operation. Finally, the corresponding PMT base was extracted from the acrylic structure and inserted in the PMT stems. In some cases, the cables detached from the bases, and the soldering was performed inside the cleanroom. This was far from ideal. However, no other solution was available: all possible precautions during the soldering were used, e.g., extracting the fumes while soldering and making a physical separation with cleanroom wipes from the rest of the material.

After a sector was completed, the signal connector and the HV connector were mounted while Elfab assembled ground return collectors. Once the connector was completed, the electrical contacts were tested for all the PMTs. Once the whole array was assembled, it was inspected again. Traces of copper and PEEK dust were founded and removed. Furthermore, several bases had traces of solid black/brown residuals. These were gently removed using ethanol-soaked wipes. In Fig.4.18, it is shown a picture of the XENONnT bottom PMT array fully assembled. Once the cleaning requirements were satisfied, the full PMT array was tested in a light-tight box inside the cleanroom. Every PMTs high-voltage was ramped up to -1.3 kV, and their response was verified through an oscilloscope. The power supply and the oscilloscope were placed outside the cleanroom, and their cables were run through a special inlet in the cleanroom walls. From the full 494 PMTs, only one showed no signal. The base was damaged during the operation and successfully changed. Eventually, the PMT arrays were placed in storage boxes with a flushing nitrogen atmosphere to prevent contamination until the TPC assembly.

Figure 4.17: Picture during the PMT array assembly in above ground cleanroom at LNGS. The PMTs were placed in the array following the cabling plan, after installing the corresponding base.

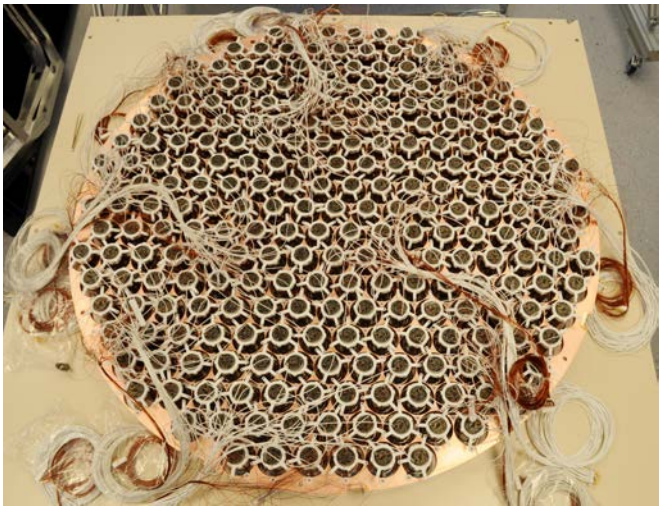

Figure 4.18: Picture of the XENONnT bottom PMT array fully assembled.

4.3.5 The XENONnT TPC installation

Once all the XENONnT detector components were ready, cleaned, and pre-assembled, the TPC assembly began. In 10 days, from February 24th to March 5th, all the individual pieces were assembled in the above-ground cleanroom by a team of $\sim$ 20 people. The timing was essential. The TPC was not supposed to be in contact with air for too long to minimize radon progeny plate-out [242]. On March 5th, the assembled

TPC, sealed in a protective Mylar bag, was transported underground and installed inside the water tank. Here an ISO-6 cleanroom, mounted around the outer cryostat dome, hosted the TPC for the final operation before closing the cryostats. The main phases of the TPC assembly, above-ground and underground, are summarized below, together with the tests performed before tightening the cryostats.

Building the TPC above-ground

From the XENONnT TPC description in section 3.3, it is possible to grasp the complexity of the detector and the countless components that make it up. Before starting the TPC assembly, each of these was cleaned and pre-assembled, if possible, as for the PMT arrays described previously. The TPC was assembled from top to bottom and from the inside to the outside.

First, the stainless steel bell was lifted into the support structure, and the top PMT array was fixed below it. The PMT cables were gently routed out from the bell thanks to recesses in the OFHC plate, corresponding to the position of the cable guides in Fig.4.14. PEEK cable ties were used along the cables' bundle to reduce the force applied to the soldering point.

Afterward, the field cage was assembled, starting with PTFE pillars supporting the 71 field shaping wires, and the 48 PTFE panel reflectors were slid between the pillars. The copper field shaping wires were then mounted on the outer side of the PTFE reflector. Every two consecutive wires were connected via a resistor. Once the inner structure of the field cage was completed, the 64 copper field shaping rings were installed, from bottom to top to provide stability. The rings were made of two pieces held together with stainless steel screws. The second resistor chain that connects consecutive rings was mounted at the fastening point. Approaching the top of the field cage, the optical fiber for PMT calibration was inserted in the 250 μm holes in the PTFE panels before installing the last rings. A total of 24 PMMA fibers were placed equidistantly in two rings of 12, at 25 cm and 20 cm from the gate electrodes [243]. Following, the PTFE cable guides were installed in correspondence to the PTFE pillars. Eventually, the remaining rings were installed.

Next, the top electrode stack, composed of the gate electrode, the anode, and the top screening electrode, was positioned at the top of the field cage, and everything was fixed to the top PMT array under the bell. Lastly, the bottom PMT array, with on top of it the bottom screening electrode and the cathode, was fixed at the field cage. Note that the bottom PMT array had to be flipped. This was a delicate procedure performed at the beginning of the TPC assembly. In Fig.4.19 the bottom electrode stack, on top of the bottom PMT array, is shown. Finally, the bottom PMT cables were fixed to the TPC structure, as shown in Fig.4.20. Then, the full TPC was sealed into a Mylar bag for transportation to the underground laboratories.

The installation of the TPC underground

Before the TPC was brought underground, the cabling was installed and tested. The installation of the new pipe was performed several weeks in advance, some information can be found in [232]. The potted feedthroughs were installed during the TPC assembly above ground to minimize the operation time in the breakout chambers, which needed to be open for the cable connections. Once the feedthroughs were installed and the cables connected, the electric connection of all cables in the pipe and potted feedthroughs were tested with a multimeter in test mode. Also, the old XENON1T cables were tested. The multimeter

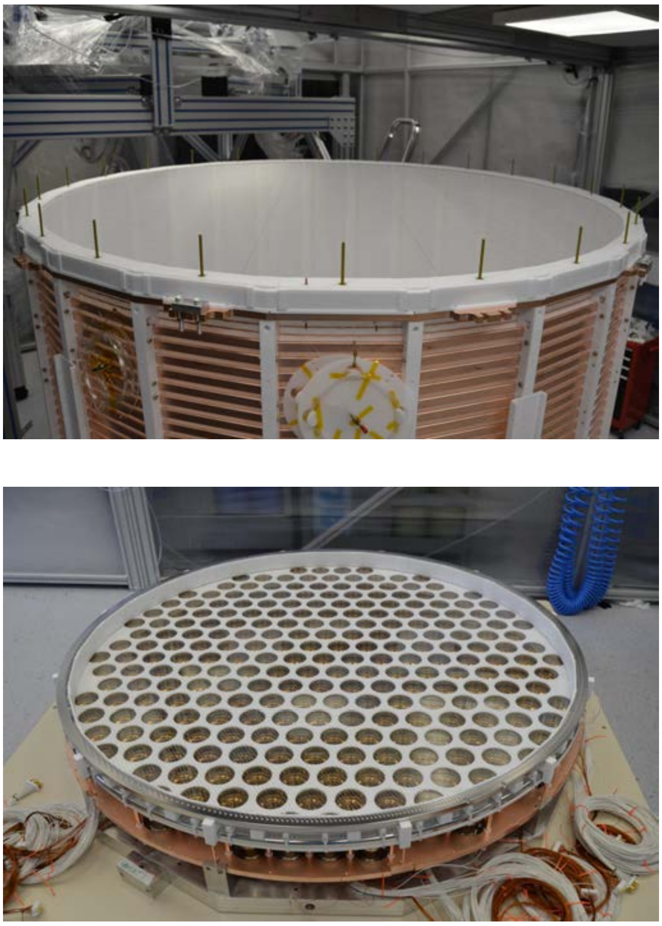

Figure 4.19: Pictures of the top field cage with the gate electrode on top of it (top) and bottom electrode stack on top of the bottom PMT array (bottom) during the TPC assembly in the above-ground cleanroom at LNGS.

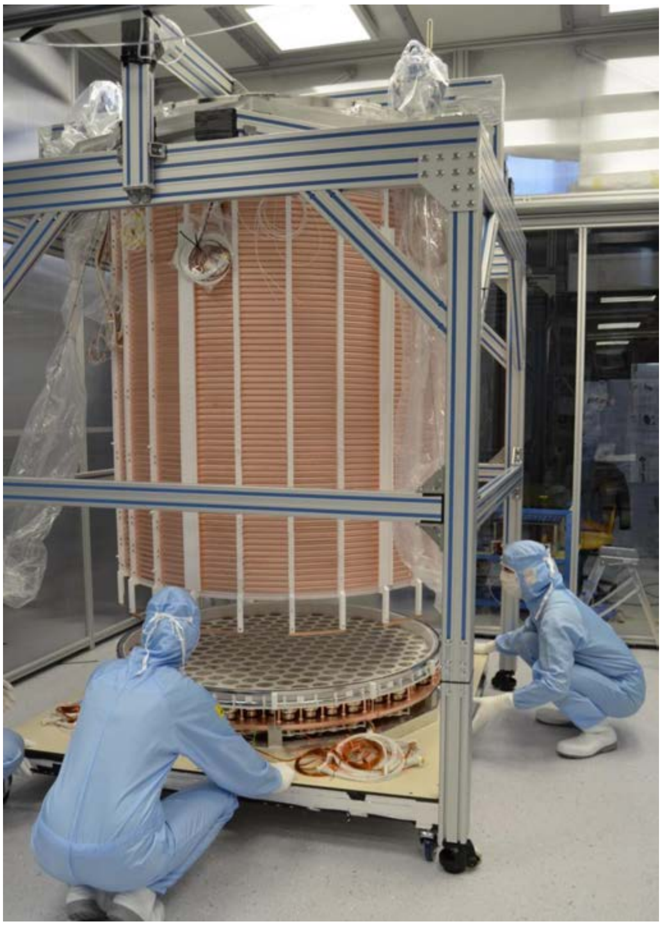

Figure 4.20: Final operation during the above ground TPC assembly. Installation of the stack of bottom electrodes and bottom PMT array below the TPC field cage.

emits an audible indication if a complete path is detected. Hence, one person was in the service building touching each MMCX or D-sub pin in turn, and one in the water tank touched the other end of that cable. This helped to identify some swapped cables which were in the wrong connector hole and other broken ones, which were promptly fixed. Among all the infrastructure held by the pipes, there are four silica fibers for PMT calibration. A dedicated potted feedthrough in the breakout chamber connects the silica fibers on the xenon side to PMMA fibers on the air side. As well as for the cables, the fibers were tested by shining light from the feedthrough connector. One fiber did not transmit light and repairing it was impossible. Hence it was not used. Furthermore, one fiber broke during the cabling operation inside the water tank. However, two fibers were sufficient for PMTs calibration, as shown in section 5.2.2.

Once the TPC was underground, it was lifted inside an ISO-6 cleanroom below the cryostat domes at the center of the water tank. With the TPC hanging in the support structure, all the PMT cables have been routed on the top of the stainless steel bell and connected to the corresponding connectors. To avoid floating cables and fiber, both were fixed to the bell using PEEK clamps. Since only two silica fibers were available, only 12 PMMA fibers were connected. During the procedure, one Kapton© cable was cut and immediately repaired using a spare HV connector for the electrodes. Unfortunately, during the operation, 2 of the 12 available fibers were pulled out from their position in the PTFE panles [243].

Next, the level meters sensors were installed around the field cage. In total, eight, two long and two medium to monitor the liquid xenon level during the filling and four short for fine level monitoring. Moreover, seven temperature sensors (Pt100) were placed around the TPC and at the entrance of the pipes. In addition, the connections of the electrodes were tested, and the xenon piping was installed. Finally, the TPC was lifted to its final position. During the lifting, a coaxial cable of a short-level meter was pinched, but it was repaired. Lastly, the PTFE panels were placed all around the bottom part of the shaping rings as further protection when closing the cryostat and to improve the insulation between the cathode and the cryostat. In Fig.4.21, a few salient moments during the underground TPC installation are collected.

The inner cryostat was then ready to be closed, and then, the elicoflex® gasket was placed at the top of the inner cryostat, which was then lifted and closed. Immediately after, the outer cryostat was lifted and closed. The detector was evacuated at this point, and the commissioning started.

(b)

(a)

(c)

Figure 4.21: Some highlights of TPC's underground installation. (a) TPC lifting inside the cleanroom at the center of the water tank. (b) Operation during the PMT cable connections and fiber installation. (c) From left to right: Francesco Lombardi, Adam Brown, Sebastian Lindemann, and myself.

5

Characterization and performance optimization of XENONnT PMTs

from commissioning to science data taking

The XENONnT TPC was installed and sealed on the 25th of March 2020, after which the detector was evacuated until July 7th 2020 to reduce outgassing. This has been done especially for tritium mitigation (see section 6.1). This period was interrupted two times when the TPC was filled with nitrogen gas for radon emanation measurements. The filling started in the summer of 2020 with room-temperature gas xenon. At this point, the circulation and purification lines were commissioned. Furthermore, the krypton was distilled from all the xenon inventory throughout this period. The TPC was then cooled down, and the liquid xenon filling started. It took from August 2020 to October 2020 to fill the 8.6 tonnes of liquid xenon in the inner cryostat. At the same time, the neutron veto was mounted, and thereafter the water tank was filled. While the xenon was cleaned through the gas and the liquid purification lines, the electrodes were tested, and in December 2020, the first XENONnT (S1, S2) event was observed. Suddenly, after a tripping event of the cathode, the bottom electrodes stack appeared as they were shorted together. Namely, the resistance between the cathode electrode and the bottom screening mesh was 0. From that point, it was impossible to raise the cathode voltage above $\sim$ 3 kV without experiencing a cathode tripping. This event defined the choice of the electric field configuration adopted in the first science run data taking (SR0). During the winter and the first part of the spring of 2021, the remaining infrastructures were commissioned, e.g., the radon distillation column, and the analysis framework was developed. During this period, the TPC configuration was optimized in view of the science data taking.

This chapter focuses on the PMT commissioning. First, the PMT calibration system and analysis are presented. The PMT configurations adopted for the SR0 are then discussed as the PMT performance during the science data taking.

5.1 The PMT calibration

At least once per week, the PMT responses to blue light were calibrated. As during the testing phase, the time evolution of PMT gains and APs rate must be monitored. Furthermore, an additional parameter was considered - the single PE acceptance, or in short SPE acceptance - which will be defined in section 5.1.4. This section presents how the PMT data are acquired and processed. The methods used to compute the gain and SPE acceptance in XENONnT are reviewed in detail.

5.1.1 The PMT calibration system

During the commissioning and later in science data taking, the PMTs were calibrated weekly by shining blue light through the optical fibers described in section 4.3.5. The fibers are part of a light calibration system, as shown schematically in Fig.5.1.

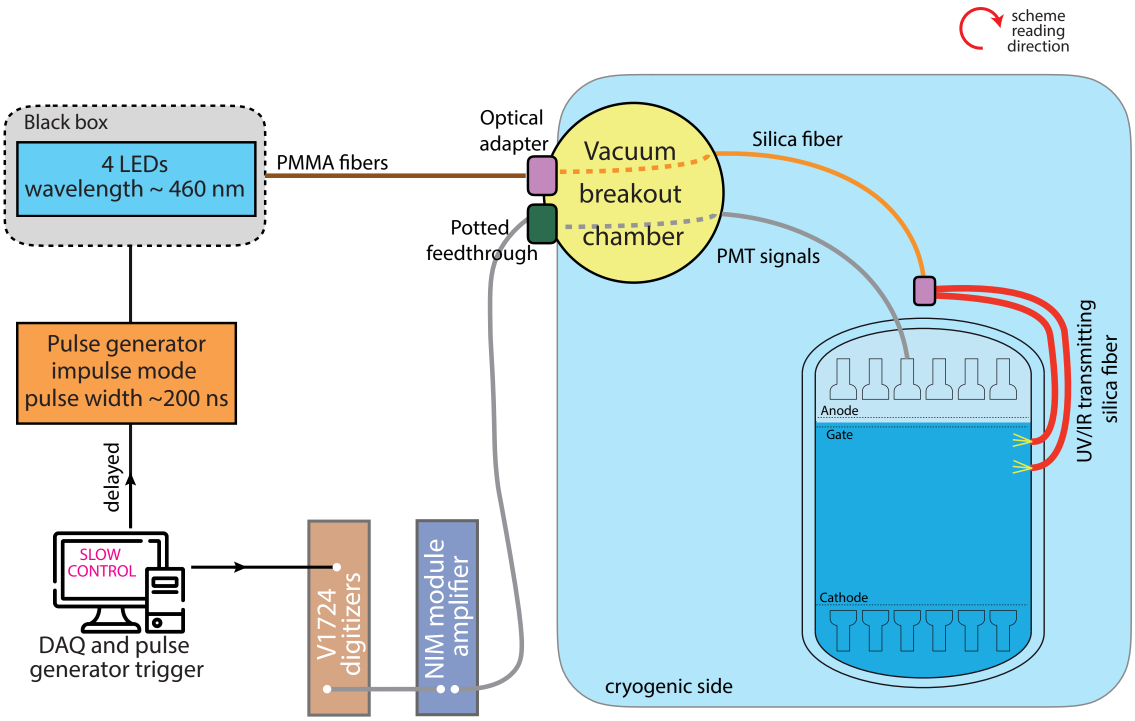

Figure 5.1: Sketch of calibration system used in the XENONnT experiment to calibrate the PMTs in the TPC. Figure by C. Capelli.

The PMT calibration system consists of a remotely-controlled pulse generator (Berkeley Nucleonics Corp. model 505) coupled to four blue light emitting diodes (LEDs ~ 460 nm, Farnell element14 KINGBRIGHT L-813PBC-Z). The pulse generator triggers the photon emission from the LEDs, and the light runs through the optical fibers into the TPC. The fibers have already been discussed in section 4.3.5; more information can be found in [243]. The same external trigger for shining light initializes the data acquisition (DAQ) shown in section 4.3.1. The normal data-taking mode and the PMT calibration share the DAQ system, but PMT signals are acquired in a triggerless mode [240]. The frequency of the DAQ trigger ($\sim$ 2.4 kHz) allows for very fast PMT calibration. Moreover, since different PMT calibrations require different data, the acquisition window is adjustable. Lastly, the pulse generator trigger is delayed with respect to the DAQ trigger. The time difference between the two triggers can be set according to the type of calibration.

5.1.2 The PMT calibration processing

The data processing of XENONnT is new compared to its predecessor XENON1T. It is fully written in *python* and based on the *strax* (STReam Analysis for Xenon TPCs) software [244]. Strax is open-source code meant for xenon detectors and takes care of low-level data handling, namely the front-end signal processing, storage, and data reduction. For the high level, e.g., peak finding or event building, a custom private software still based on strax, called *straxen* [245], is used. The digitized PMT signals, called *raw records*, are processed by different *plugins*[1] with a hierarchical organization: The datatype from one plugin is fed into the subsequent one until the (S1, S2) events are built. The processing of the PMT calibration signals is simpler compared to normal data. Each PMT signal is processed by *LED calibration* plugin, which extracts the integrated charge (area) and the signal amplitude in a pre-defined time window.

The gain and the SPE acceptance data-taking mode share the same DAQ configuration. The data taking last for $\sim$ 3 minutes, for total statistics of 4×10^5 events. The acquisition window is fixed and consists of 160 digitizer samples, corresponding to 1.6 µs given the 10 ns digitizer sampling rate. This array of raw records is called a waveform. The pulse generator is $\sim$ 800 ns delayed to the DAQ trigger to place the LED signal around the 80th time sample. An example of LED arrival time distribution per PMT is shown in Fig.5.2. The first 40 samples, where no LED induce events are expected, are used to compute the waveform baseline. Hence, the baseline is subtracted from the PMT output, and the negative signal is considered to have positive pulses for convenience.

The signal area and amplitude are extracted from the [78, 116] sample window. This window considers the arrival LED time spread and the typical size of PMT signal, which is around 150 ns. This interval ensures that all the PMT signal is considered. A further precaution is taken for the area calculation. To account for the systematic error on the integration window due to the position of the LED signal, which can slightly change, the final result is the average of 6 values, where the right integration limit is two samples wider for each window. Fig.5.3 shows waveforms from PMT calibration data taking and the different windows used in the *LED calibration* plugin.

The PMT calibration was performed each Friday at 3 p.m. (CEST) by the LNGS shifters. The calibration is done via an automatic script provided by the slow control infrastructures. The script sets the run data-taking mode, as well as the pulse generator for the different analyses, and initializes the calibration. The data processing, the data uploading into the database, and into the computing facility used for the analysis

---

[1] A plugin is an algorithm that adds functionality to the software. It processes some information given back new one. Without altering the features prior to processing.

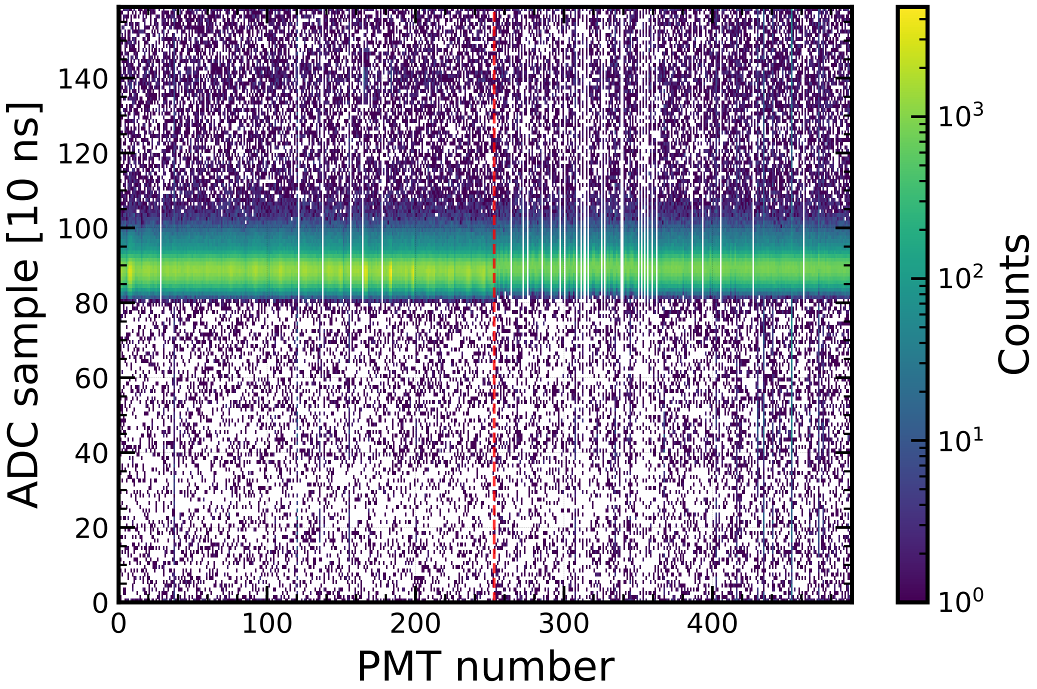

Figure 5.2: Two-dimensional histogram of LED arrival time per PMT. The y-axis shows the ADC sample at which the LED light arrives, and the x-axis shows the PMT number. The vertical white lines are in correspondence with the turned-off PMTs. The dashed red line represents the division between the PMTs of the top and bottom arrays.

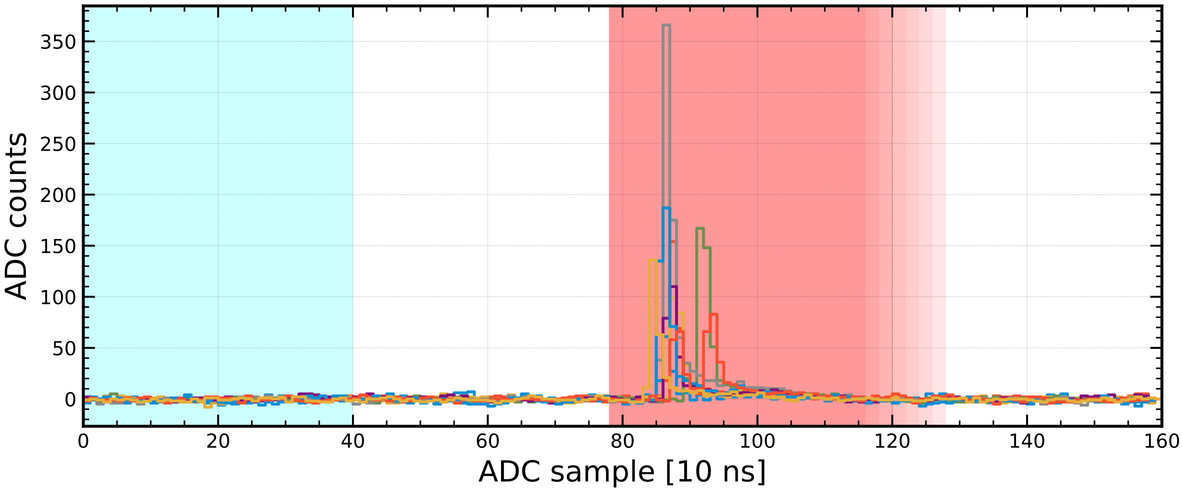

Figure 5.3: Example of PMT waveforms during the calibration. The light blue region is used to evaluate the baseline, while the red region is used for the signal characterization: charge integration and pulse amplitude. The shaded red regions represent the six right integration limits for signal area computation.

in XENONnT (e.g., the University of Chicago servers *Midway* [246]) are automatized. A *cron job*, running on *Midway*, analyzes the PMT calibration data and saves the results into a database used for bookkeeping. On top of that, the summary of calibration results is sent to the XENONnT slack workspace to facilitate the monitoring.

5.1.3 The gain calculation

Knowing how much charge corresponds to one PE, namely the gain, is the first step of the detector energy calibration. From the gain, the *charge-to-photoelectron* conversion factor is computed for each PMTs such that their output signals can be combined. Therefore, a PMT response requires a periodical calibration, typically relative to the mean of the charge distribution corresponding to an SPE. In lieu of the more common single PE fitting with a Gaussian or more complicated function, in the XENON experiment the gain is extracted using the model-independent method [234]. This method is based on a simple statistical interpretation, avoiding any analytical approximations of the PMT response.

For a given light intensity shining into the PMT, the number of PEs produced is described by Poisson statistics. In the context of the model-independent method, the mean number of PEs produced per number of incident photons at each DAQ trigger is called *occupancy* (λ), expressed in units of PE/trigger. The total area spectrum can be written as the sum of the nth PE spectrum times its probability $P(n|\lambda)$. Given the linear response of a PMT, the nth PE component is an n-times repeated convolution of the SPE spectrum with itself. Therefore, the mean of PMT response is simply the λ times the mean of the SPE spectrum. A similar conclusion can be drawn for the variance. Nevertheless, the PMT noise, e.g., dark count, is always present, even if the PMT is illuminated. Hence, the noise contribution must be subtracted to extract the true SPE mean and variance. Noise B and signal T are independent, and their mean E and the variance V are additive. Eq.5.1 shows how the single PE (represented by the letter ψ) calibration parameters are computed. The complete derivation can be found in the original pubblication [234]:

$$\begin{aligned} E[\psi] &= \frac{E[T] - E[B]}{\lambda} \\ V[\psi] &= \frac{V[T] - V[B]}{\lambda} - E^2[\psi] \end{aligned} \tag{5.1}$$

This method is robust up to $\mathcal{O}(10\text{ PE})$, unlike the fitting method. In addition to this, the lack of understanding of the under-amplified component discussed in section 4.1.2 introduces a bias in the fitting method. The fitting result depends on which model is used to describe the PMT response and how the model accounts for the under-amplified events.

The occupancy λ is the only not trivial parameter to derive. It can be computed from the number of events with 0 photon-induced PEs N$_0$ ($P(0|\lambda) = e^{-\lambda}$, then $\lambda = -\ln(P(0|\lambda))$) and the total number of events N: $\lambda = -ln(N_0/N)$. There are several ways to estimate N$_0$. In XENON, it is derived by comparing the counts of the LED-on area spectrum (A$_S$) and LED-off area spectrum (A$_B$) below a certain threshold, where no LED-induce signals are expected. Fixing the total number of events N in both LED-on and LED-off spectrum, and given that in the LED-off data no LED-induce signals are present, the proportion in Eq.5.2a is valid, and N_0 can be derived. Thus, the λ and its error can be estimated following Eq.5.2b and Eq.5.2c, where f is A_B/N.

$$A_B : N = A_S : N_0 \tag{5.2a}$$

$$\lambda = -ln\left(\frac{A_S}{A_B}\right) \tag{5.2b}$$

$$\delta\lambda = \frac{e^{\lambda} + 1 - 2f}{f N} \tag{5.2c}$$

The original paper [234] shows that the systematic error $\delta\lambda$ is minimal for $\lambda \sim 2$ PE/trigger. To have this condition for all the PMT, and given the size of XENONnT TPC, three different LED settings are required. Those are called *light levels*. An example of XENONnT LED-off and LED-on area spectra, with different λ, is shown in Fig.5.4.

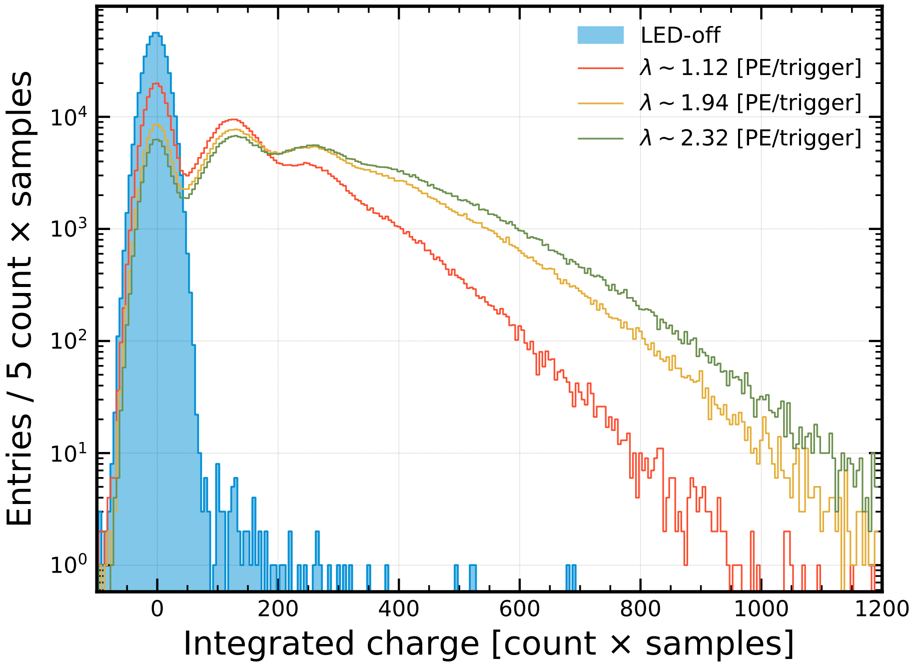

Figure 5.4: Example of PMT integrated charge spectra with different light settings, thus different occupancies. The LED-off spectrum is shown in blue.

The occupancy is then computed for several thresholds, but always in a region without expected photon-induced events. This region corresponds to the negative side of the 0 PE peak, also called the pedestal. The estimated λ is the first value with a relative error smaller than 2 %. The error is computed following the original paper [234]. Fig.5.5 shows an example of λ as a function of the threshold. The trend approaches a plateau where the relative error requirement is fulfilled.

Once the occupancy λ is estimated, the mean of the SPE spectrum is calculated using Eq.5.1. The statistical uncertainty is estimated using the derivation in [234]. The systematic uncertainty due to the occupancy is also considered, and the total error is the sum in quadrature of the two uncertainties as:

$$\begin{aligned} \delta E[\psi]_{\text{stat}} &= \frac{\lambda(E^2[\psi] + V[\psi]) + 2V[B]}{N\,\lambda^2} + \frac{E^2[\psi]\,(e^{\lambda} + 1 - 2f\,)}{f\,N\,\lambda^2} \\ \delta E[\psi]_{\text{sys}} &= \left(E[T] - E[B]\right) \times \frac{\delta\lambda}{\lambda^2} \end{aligned} \tag{5.3}$$

The single PE mean gives the amplification, or gain (G), of one PE through the dynodes chain. Knowing G, the PMT output can be translated into PE number. This conversion factor is computed as follows:

$$G = \frac{E[\psi]\;\Xi}{Z\,A\,e^{-}} \tag{5.4}$$

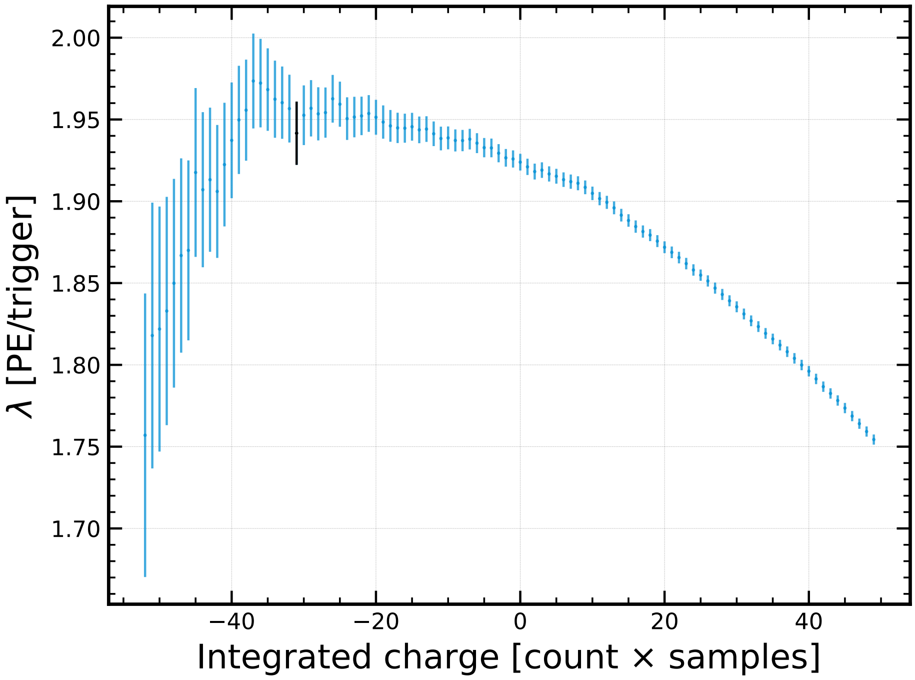

Figure 5.5: Occupancy as a function of integrated charge threshold. The estimated occupancy that fulfills the relative error requirement is shown in black.

where Ξ is the digitizer dynamic range in the ADC (2.25 V for 14-bit CAEN v1724), Z is the impedance input to the digitizer (50 Ω for the model used in the experiment), A is the amplification before the digitizers (which in XENON is $\times 10$), and e^- is the electron charge in Coulomb. Typical $E[\psi]$ in XENONnT PMT operating at −1.5 kV is of $\mathcal{O}(100 \text{ count} \times \text{samples})$, equivalent to $\mathcal{O}(10^6)$ signal amplification.

5.1.4 The SPE acceptance calculation

The SPE acceptance defines the fraction of 1 PE acquired for a given digitizer threshold. It is a fundamental parameter for setting the *self-trigger threshold* in the data acquisition pipeline. The self-trigger threshold is the first hardware cut placed on the data. It acts on the amplitude of the PMT signal, and it defines whether a signal is recorded or not.

The method used for computing the SPE acceptance is inherited from XENON1T [247]. It is based on a noise-subtracted amplitude spectrum obtained by the difference between LED-on the LED-off amplitude spectra. The SPE acceptance, as a function of the ADC threshold, is defined by the Eq.5.5, where n_i is the counts in the i$^{\text{th}}$ bin, in ADC, of the noise-subtracted amplitude spectrum. Knowing the single PE acceptance at the self-trigger threshold, typical 15 ADC, is fundamental for evaluating the detection efficiency properly:

$$\mathrm{SPE_{acc}}(\mathrm{ADC}) = 1 - \frac{\sum_0^{ADC_{thr}} n_i}{\sum_\infty n_i} \,. \tag{5.5}$$

The calibration data used for this analysis share the same DAQ configuration with the gain calibration. Thus, the signal amplitudes are extracted from the same time window discussed in section 5.1.2. However, the illumination is very different. For the SPE acceptance, a low λ is required. Otherwise, the presence of events larger than 1 PE (called many-PE events here) would distort the result. In XENONnT, a $\lambda \sim 0.2 \div 0.3$ PE/trigger is used for the SPE acceptance calibration. Having in mind the Poisson probability mass function, such occupancies lead to $P(n \geq 2|\lambda) = 1 - P(n < 2|\lambda) = 1 + e^{-\lambda}(1 + \lambda) \sim 1 \div 3\ \%$ events with integrated charge > 1 PE.

Although small, the fraction of many-PEs is considered in the calculation of SPE acceptance. The data-driven SPE acceptance can be written as the true SPE acceptance $\varepsilon_{1\text{ PE}}$ plus the many-PEs acceptance $\varepsilon_{\geq 2\text{ PE}}$, both multiplied by their Poisson probability coefficient. Hence, the $\varepsilon_{1\text{ PE}}$ can be computed by inverting the Eq.5.6a and assuming 100 % acceptance for the many-PEs term:

$$\text{SPE}_{\text{acc}} = \varepsilon_{1\text{ PE}} \times P(1\text{ PE}|\lambda) + \varepsilon_{\geq 2\text{ PE}} \times P(\geq 2\text{ PE}|\lambda) \tag{5.6a}$$

$$\varepsilon_{1\text{ PE}} = \frac{\text{SPE}_{\text{acc}} - \overbrace{\varepsilon_{\geq 2\text{ PE}}}^{1} \times P(\geq 2\text{ PE}|\lambda)}{P(1\text{ PE}|\lambda)}\ . \tag{5.6b}$$

The noise subtraction is meant to remove the 0 PE events. However, the LED-off spectrum requires a correction before the subtraction since the two datasets do not have the same normalization. In other words, the occupancy is different. Assuming that no real SPE signals have amplitude less than a given ADC counts t, the correction factor c is such that the integral of the LED-on and LED-off spectrum is the same below t. The SPE acceptance is computed for 3 different correction factors (t) as follows:

$$c(t) = \frac{\sum_{i=0}^{t} n_i^{LED-on}}{\sum_{i=0}^{t} n_i^{LED-off}}\ , \tag{5.7}$$

where t varies from 4 ADC to 6 ADC. This helps to evaluate possible systematic due to the spectra subtraction. Given the linearity between amplitude and integrated charge in the PMT response, the correction factor is nothing more than the occupancy seen from another perspective. Fig.5.6 shows the steps to calculate the SPE acceptance. The noise-subtracted spectrum is roughly Gaussian but deviates at low amplitudes due to under-amplified PEs.

The SPE acceptance is fundamental to evaluate the detection efficiency. Given n_{phd} detected photons, the probability of producing n_{h} hits above the self-trigger is the SPE acceptance. Then, the SPE acceptance is an input for the binomial process $\text{P}(n_{\text{h}}|n_{\text{phd}}, p)$ that describes the photon detection:

$$P(n_h|n_{phd}, p) = \binom{n_{phd}}{n_h} p^{n_h}(1-p)^{n_h - n_{phd}} \tag{5.8}$$

5.1.5 Important remarks

Being the first step of energy reconstruction, the PMT performances must be well understood. The reliable XENONnT light calibration system allowed for quick and high-statistics PMT performance characterization, from which the main PMT parameters are derived. As shown in the next sections, the PMT performance time evolution is essential for interpreting the physics data correctly. The flexibility and automation of the PMT's weekly calibration and data processing made it possible to alleviate the analyst's workload and focus energy on data analysis. Lastly, unlike the more classic fitting approach, the model-independent method utilized to derive the PMT gain and SPE acceptance proved to be stable, yielding

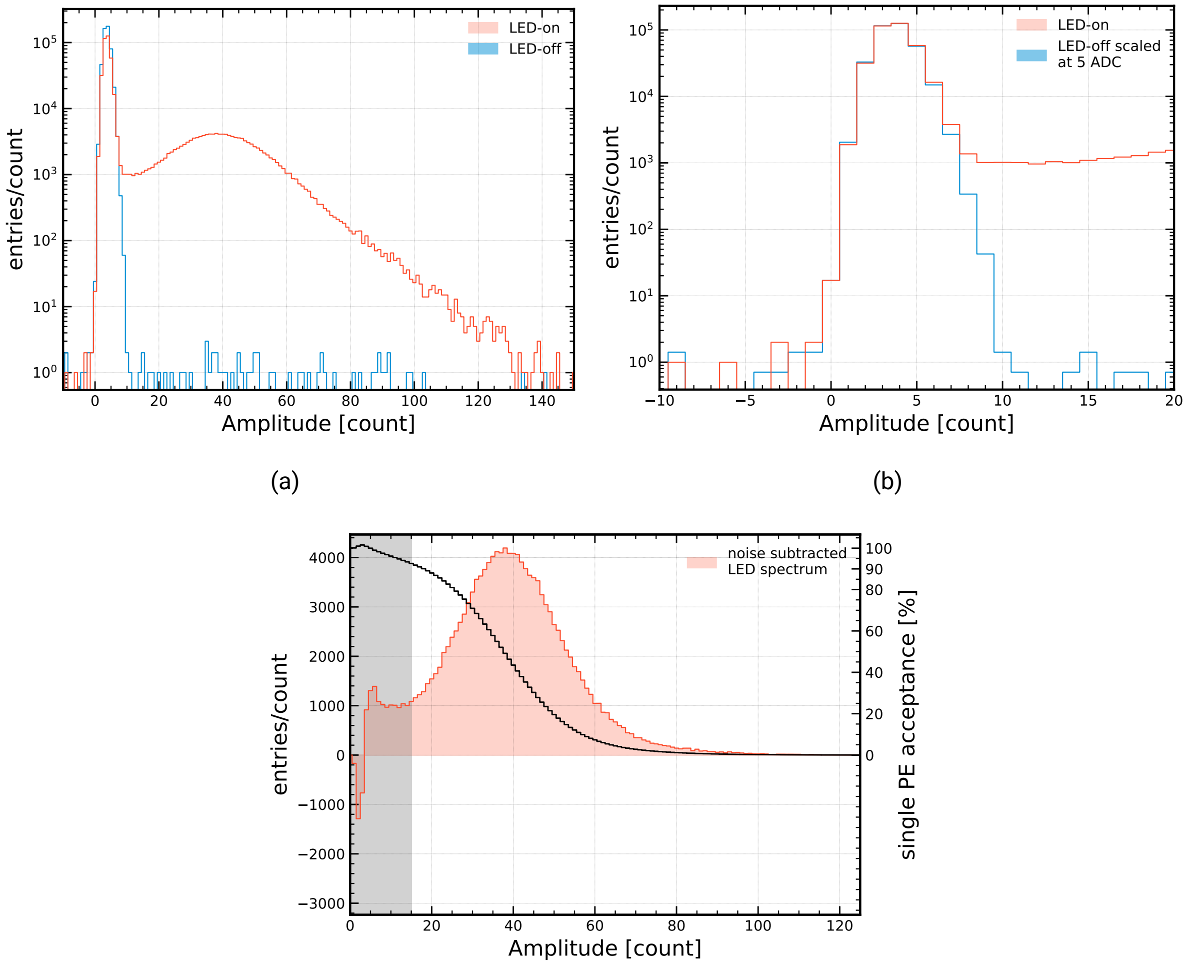

(a)

(b)

(c)

Figure 5.6: Representation of the method used in XENONnT for calculating the SPE acceptance. (a) The SPE acceptance calibration data are shown: LED-off (blue) and LED-on (red) amplitude spectrum. (b) The LED-off spectrum is scaled to match the LED-on pedestal. Then, the SPE spectrum is obtained by the subtraction of these two. (c) The derived noise-subtracted LED spectrum, interpreted as the SPE spectrum, is shown. The black solid line shows the SPE acceptance as a function of the signal amplitude.

consistent results, although the conditions of the TPC changed over time: from vacuum to liquid xenon. This will be emphasized in the following sections. Given the high number of photosensors (494) this was essential. In particular, for the gain estimation, a stable, solid, and fast analysis was mandatory to provide XENON analysts with reliable physics data.

In the following sections, the characterizations of the PMT during the various commissioning stages are discussed in detail. The performance of gain and SPE acceptance during the first XENONnT science data acquisition is then presented.

5.2 PMT commissioning phase

As previously said in the introduction to this chapter, more than one year passed from the cryostat's closing until the beginning of the science data taking. During this time, three main commissioning periods can be identified: the outgassing and nitrogen phase, the TPC cooling and liquid xenon filling phase, and the detector optimization phase.

The first phase was used to troubleshoot the cabling and verify the status of the photosensors as well as the PMT calibration system. The second period was utilized to characterize and study the PMT performances. The PMT characterization results were then employed in the last period to optimize the working condition in view of the science data-taking mode. This section outlines the main operations and analysis performed on the PMTs during the XENONnT commissioning phases.

5.2.1 Outgassing and nitrogen phase

While the last operations for closing the cryostat were ongoing, the PMT cabling was completed. The cabling scheme was introduced and explained in section 4.3.1. Its schematic is represented in Fig.4.12. Signal cabling was reasonably simple, while high-voltage cabling presented some complications. First, the pins in Radiall connector[239] were not held tightly, and often their position had to be fixed by opening the connector and pulling out the pins. Second, some filter box connectors were slightly damaged and needed repair.

Before tightening the outer cryostat, as soon as the TPC was light tight, the PMT high-voltages were ramped up one by one to −1.3 kV, and the PMT signals were inspected with an oscilloscope. This helped to debug the slow control and to find any problematic PMTs. During these tests, the 9 PMT did not work. For six of them, the problem was with the pin of the Radiall connectors, either in the cable connector or in the filter box. A picture during the operation on the Radiall connectors is shown in Fig.5.7. These PMTs were successfully recovered. PMT 354 and 386 did not show any electrical contact between the ground and the signal. This was caused by damage to the PMT base connection, which was impossible to solve. The last PMT, 427, could not be ramped above −1.1 kV, probably because of damage to the vacuum sealing. In addition, the pin on the Radial connector corresponding to PMT 185 was damaged to the point that the entire Radiall connector had to be changed. In conclusion, all the problems related to the Radiall connector were solved.

While checking the PMT signals with the oscilloscope, it was realized that the PMTs in sectors 6 and 10 were inverted and mirrored, respectively (see Fig.4.14 for reference). This was further proved during the detector commissioning and fixed from the software side by re-mapping the digitizers.

After the TPC was sealed, the optical fibers and the automatic script for PMT calibration were tested. Several PMTs were connected to the oscilloscope while turning on and off the LEDs. All four LEDs available were working. A picture of the oscilloscope during this operation is shown in Fig.5.7. There, it is possible to see the PMT signals corresponding to the LED light. The debugging of the PMT calibration script pointed to a missing NIM/TTL converter module between the DAQ trigger and the pulse generator, which was installed immediately afterwards.

Around the beginning of April, the PMTs were ramped to different voltages throughout the TPC evacuation period and monitored over time. No significant PMT-related issues were observed during this time besides for PMT 362, which could not operate stably above –1.4 kV. This outgassing period helped study the noise condition and perform the so-called *noise hunting*. Thanks to a mobile setup equipped with an antenna and connected to the oscilloscope, it was possible to investigate each active component in the DAQ room, which could produce noise in the PMT readout. In addition, dedicated noise runs consisting of individual externally triggered 500 μs waveforms were acquired. The noise amplitude, its root mean square (RMS), and the noise power spectrum for each PMT were analyzed [248]. The overall noise condition was already quite good. However, a few PMTs had slightly bigger baseline fluctuation: PMT 453 was particularly noisy with a baseline RMS of $\sim$ 4 ADC counts, whereas the average was a factor $\sim$ 2 smaller [248]. The source of this noise was investigated by plugging these PMTs and the antenna output into an oscilloscope. The antenna was brought close to active components in the DAQ room, e.g., the power supply, to verify if it was the source of the noise. In a positive case, the same frequency pattern observed in the PMTs baseline would have also appeared in the oscilloscope channel of the antenna. No correlation was observed between the noisy PMTs and the DAQ room instrumentation. Therefore, no actions were taken. However, the noise condition did not adversely affect the data quality and performance of these PMTs, as shown in the section 5.3.1 by the high SPE acceptance obtained in SR0.

After the noise hunting campaign, the weekly PMT calibration for gain, SPE acceptance, and APs rates started. The vacuum pumps worked almost uninterruptedly until July 2020, except for two periods where the TPC was filled with nitrogen gas for radon emanation measurements.

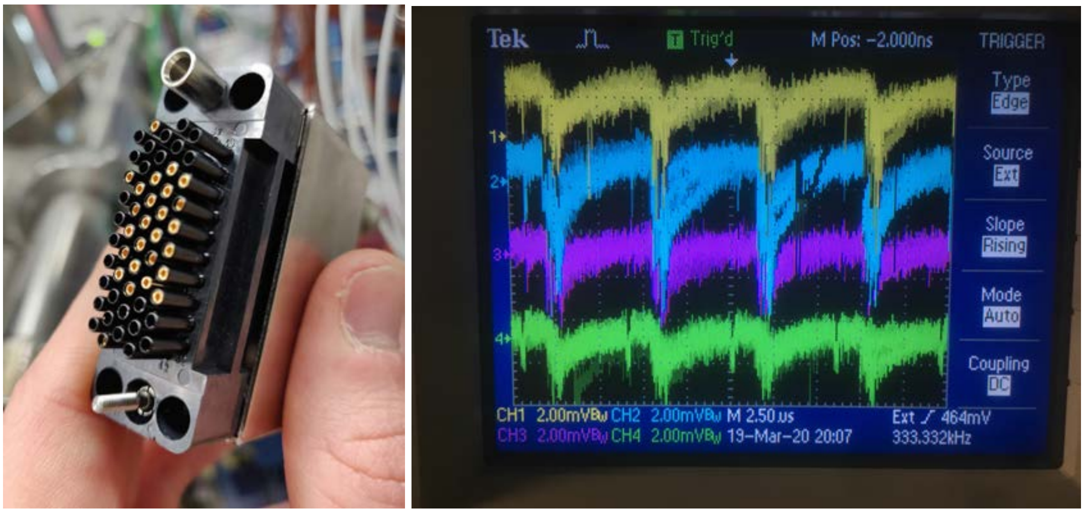

(a) (b)

Figure 5.7: (a) Multi-pin connectors manufactured by Radiall are used for high-voltage cables. Here it can be seen that some d-sub pins are slightly pushed inward. Nearly 70% of the problems found in defective PMTs during the first commissioning phase was due to Radiall connectors. (b) PMT signals were observed at the oscilloscope during the LED test before sealing the inner cryostat.

5.2.2 Cooling and xenon filling phase

In June 2020, the TPC vacuum was broken by the first warm xenon gas in the detector. The test of electrodes began and continued during the cooling period. The TPC was ready for the liquid xenon phase only at the end of August 2020. In the meantime, the neutron veto was assembled, and the external calibration infrastructures were arranged around the outer cryostat. During the cool down, the PMT gains were monitored. Rather than for PMT response characterization, the monitoring was useful for following the stability of the detector during several ongoing operations. During the XENON1T testing campaign, a correlation was observed between the PMT gain and the temperature of the xenon. First, $\mathcal{O}(10~\%)$ gain increases during the cooling, followed by $\mathcal{O}(1~\%)$ decreasing after the liquid xenon filling. Then, the gain stabilized with the stabilization of the thermodynamic condition [216]. A similar gain increase was observed at the beginning of the XENONnT cooling phase, as shown in Fig.5.8 for a few random PMTs. However, the subsequent decrease shown in Fig.5.8 was not due to the temperature but to the change in the PMT applied voltages, as shown by the top panel. Furthermore, the lack of calibrations in September 2020 does not help to study the correlation. Due to the neutron veto operation around the cryostat, it was decided to turn off the PMTs during September.

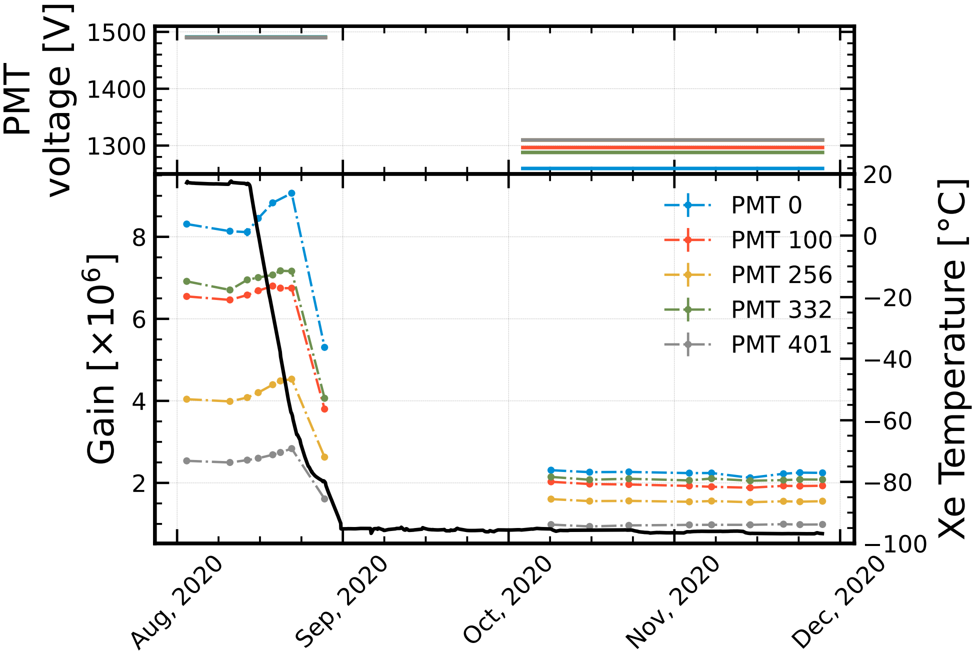

Figure 5.8: Evolution of the gain for 5 random XENONnT PMTs in the first part of the commissioning phase. The black solid line shows the xenon temperature in the cryostat over time. The onset of the cooling phase at the end of August correlates with the increase in earnings. Nothing can be said afterward due to the lack of calibrations during September. Moreover, the top panel showed that the PMT high voltage settings were changed when the liquid xenon filling started.

The filling lasted almost four months, and in November, the 8.6 tonnes of liquid xenon were accommodated in the TPC. Even though the water tank was still open, the detector characterization began. The PMTs were turned on, and different electric field configurations were tested. Since there was no water to shield the detector, the interaction rate of events was expected to be significantly high. As a precaution, the PMTs were not continuously turned on to avoid damage from the high illumination.

During an electrode test, while ramping up the cathode from –11.5 kV to –12 kV, a burst on the event rate was observed, and immediately after, the DAQ crashed. From this point on, the resistance between the cathode and the bottom screening electrode was almost zero, suggesting a short between these. The physical connection of the two electrodes is probably due to a broken wire from the cathode touching the electrode below. This event determined the low electric field ($\sim$ 23 V/cm) used during the SR0 since the cathode was no longer stable above $\sim$ 3 kV. The PMTs were not damaged by this event, and their performances, according to the subsequent PMT calibrations, did not change. Eventually, the water tank was closed in December and filled with deionized water. Later, at the beginning of the 2021, the optimization of the performances started.

During this period, two major PMT characterizations were performed. As soon as the thermodynamic conditions and the liquid level were stable, the light levels for SPE acceptance, gain, and AP data-taking were optimized. Given that not all 24 fibers were usable, several *light levels* were necessary to fulfill the occupancy requirement for the calibrations. Only the settings adopted for the gain and SPE acceptance calibration are shown here. Both required three settings for the pulse generator, with gradually larger values of LED input voltages. The objective was to reach a uniform light distribution within the PMT arrays. The voltages are 5.8 V, 6.95 V, 7.3 V for gain calibration, and 4.1 V, 4.3 V, 4.4 V for SPE acceptance calibration. Considering the LED-off runs, the required runs are four for both calibrations. The estimated occupancies for these light levels are shown in Fig.5.9. The data refers to July 7th, 2021.

At this point in the commissioning phase, the characteristic gain curve was derived for every PMT as a function of the supply voltage. The gains were calculated for seven calibration runs with the high voltage varying from −1200 V to −1500 V in 50 V steps. This measurement, called *HV-scan*, was already conducted during the vacuum phase. This analysis aimed to derive the a and k parameters of the gain model presented in section 4.1.1 for all the PMTs. At the point of the HV-scan, not all the PMTs were on. The list of omitted PMTs is: 156, 164, 260 (bias only up to −1250 V), 352, 354, 362, 386, 393, and 427. More information will be provided in section 5.2.3. The parameters were extracted with the *least-squared fit method*, and the χ^2 goodness-of-fit test was used to evaluate the quality of the outcomes. The fit results of $\sim$ 3% of the 485 working PMTs were not optimal. Given the low percentage, the reasons were not thoroughly investigated. Fig.5.10 shows the average gain characteristic curve for the XENONnT PMTs, whereas the distribution of k for the two HV-scan is shown in Fig.5.11; the results agree with each other. The parameter k defines the steepness of the gain curve, which does not dependent on the PMT surrounding condition. In contrast, the parameter a defines the absolute signal amplification and, as shown in Fig.5.8, is correlated with the temperature condition where PMT operates. Since the two HV scans were taken in different TPC temperature conditions, the parameters a were not compared.

Not only were the gains studied during the HV-scan, but also the single PE features, such as the acceptance and the resolution. The SPE acceptance at 15 ADC counts was computed for each high voltage step using the method described in section 5.1.4. The SPE acceptance as a function of the gain is shown in Fig.5.12: at $\sim 2 \times 10^6$ signal amplification, the SPE acceptance at 15 ADC is above 90 % on average.

For the SPE resolution, instead of the model-independent approach, the 1 PE means and the variances were extracted by fitting the SPE area spectrum with the model described in [249]. The fitting approach is used to easily compare the results to the testing campaign results [213]. In Fig.5.13 the SPE resolution, defined as $\sigma_{\mathrm{SPE}}/\mu_{\mathrm{SPE}}$, as a function of the gain is shown. The SPE resolution obtained during the testing campaign is shown with black crosses. The values estimated in this work are slightly higher than the test-

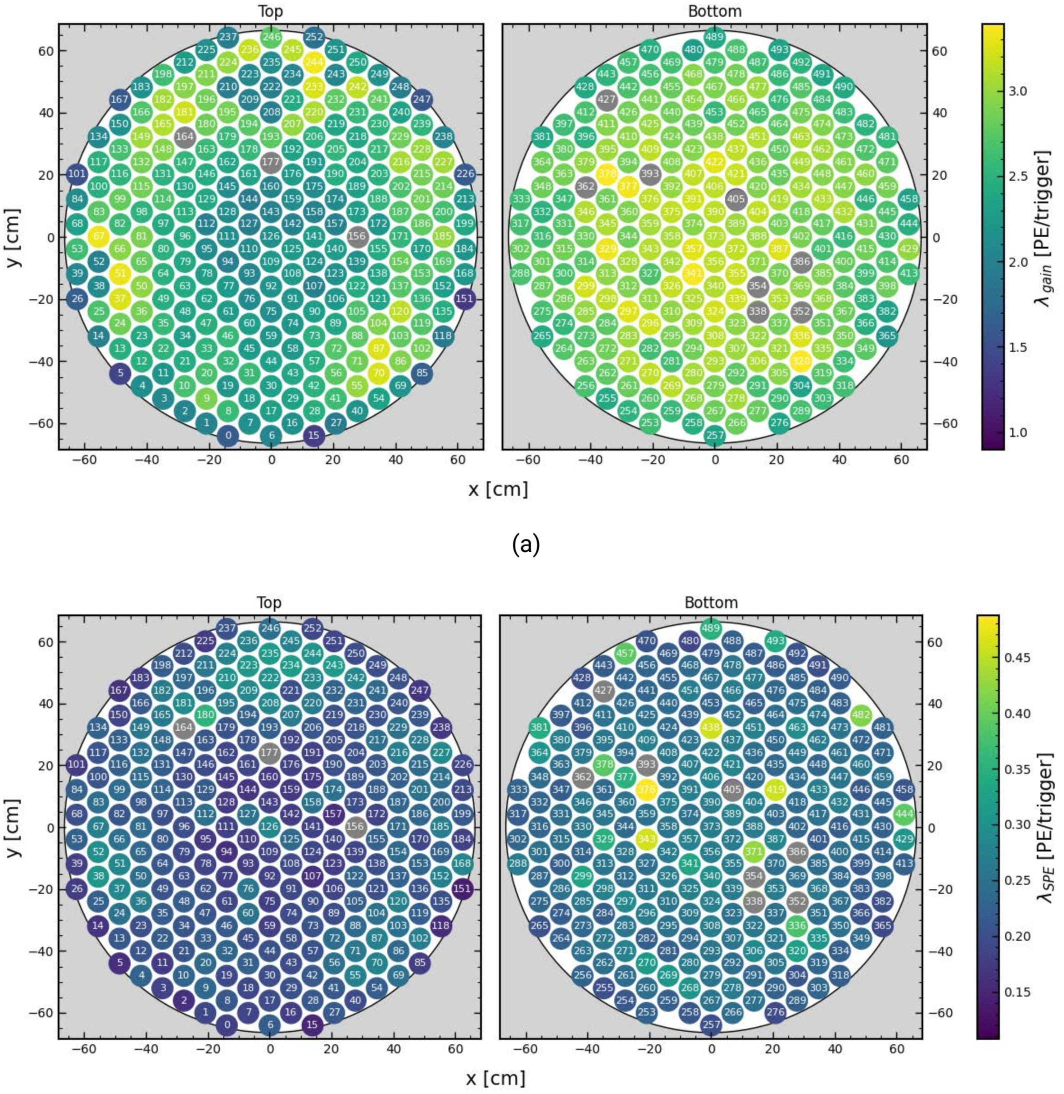

(a)

(b)

Figure 5.9: Estimated occupancy λ for the gain calibration runs (a) and SPE acceptance runs (b) during SR0. Three LED voltages are necessary for gain and SPE acceptance for having an average occupancy ∼ 2 PE/trigger and ∼ 0.4 PE/trigger, respectively. The PMTs in gray were off when these data were acquired.

ing campaign results. However, it should be mentioned that all XENONnT PMTs were considered in this work, while the SPE resolution of the test campaign was estimated using a subset of new PMTs. Hence, a difference was expected. The results agree with each other even after ∼ 2 years. This demonstrates the stability and reliability over time at cryogenic temperatures of these photosensors.

The HV-scan results are not an end in themselves. In the following sections, it will be shown that the PMT features, as a function of the voltage supplied, were used to identify the optimal condition for each PMT to maximize the detector performance during science data taking.

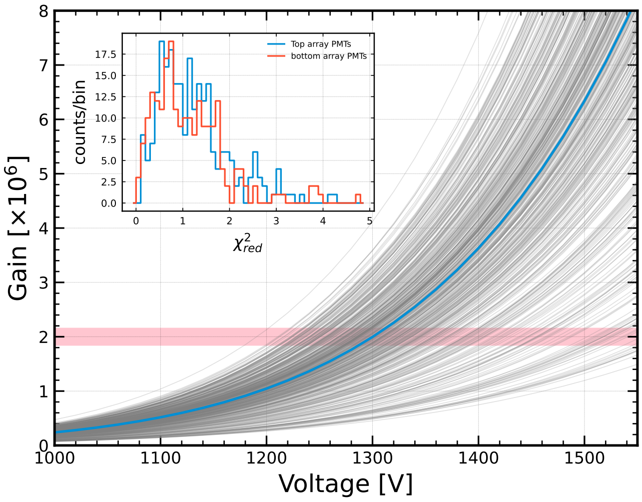

Figure 5.10: The gain characteristic curves of PMTs are shown with solid gray lines as a function of supplied voltage, while the solid blue line represents the average curve. The light pink horizontal band emphasizes the voltage region at which the PMT would have a ~ 2 million gain. The inset shows the distribution for the reduce χ^2 from the gain curve fits: blue for the top array and red for the bottom. Overall the gains are well-described by the model presented in section 4.1.1.

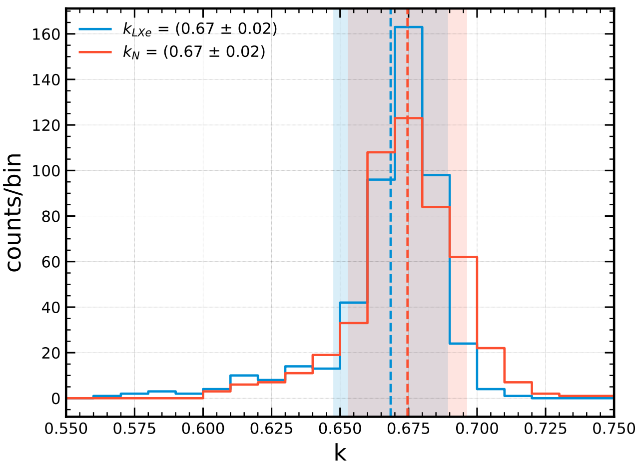

Figure 5.11: Distribution of PMTs' characteristic gain parameter *k*. These are extracted from *HV-scan* calibration during the vacuum phase (red) and liquid xenon phase (blue). The average values agree with each other.

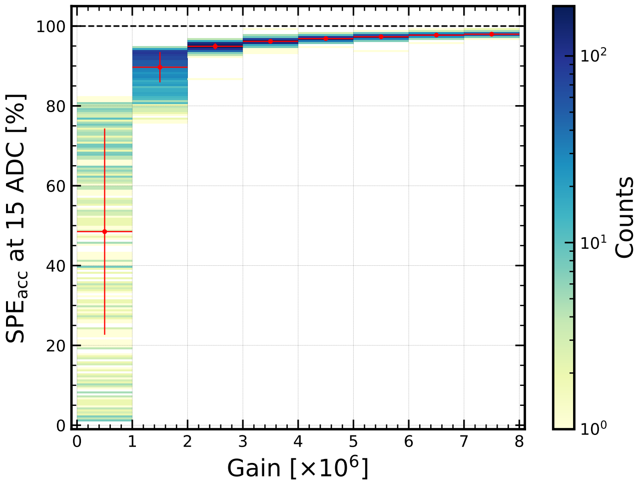

Figure 5.12: With the color map, the two-dimensional histogram of SPE acceptance as a function of the PMT gain is shown. The red crosses represent the mean and the standard deviation for each gain bin.

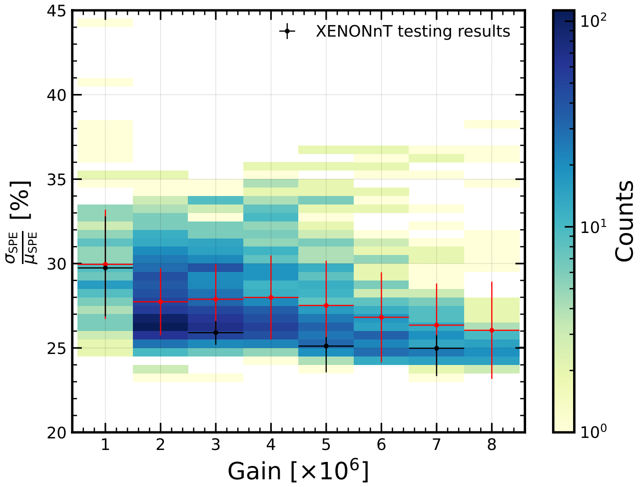

Figure 5.13: With the color map, the two-dimensional histogram of SPE resolution as a function of the gain is shown. The red crosses represent the mean and the standard deviation for each gain bin, while the black crosses are the SPE resolution derived during the testing phase [213]. The results are consistent with each other.

5.2.3 Performances optimization for science run 0

The detector commissioning ended in May 2021. During the first part of the year, the detector condition was optimized in view of the first science run data taking of XENONnT. During this time, the liquid xenon was purified using Q5 filters (see section 3.3.3), which allowed it to reach an unprecedented electron lifetime of $\sim$ 20 ms (max drift time in SR0 $\sim$ 2.2 μs). The downside is that the Q5 filters have a high radon emanation rate. Therefore, a long radon distillation campaign began after the purification, and the filter was exchanged. At the same time, the detector response was characterized. The electron extraction efficiency was optimized by finding the optimal liquid level [187]. In addition, the power supplied to the topmost ring of the field cage, which by design is independent of the rest, was optimized to find an optimal potential drop between consecutive field-shaping elements that would minimize field inhomogeneity [250].

Of the several optimization studies, the PMTs' working voltages were also investigated. The optimization was performed by taking the following steps:

- A dedicated PMT noise analysis was performed. It consists of studying the PMT baselines using DAQ trigger data with a long acquisition window to be sensitive to low-frequency noise. The median and the standard deviation of PMT baselines were investigated in depth. Actions were foreseen for PMTs particularly noisy, but none of the analyzed ones raised concern. An exception was PMT 405, which had intense noise fluctuations. Therefore, it was removed from the final SR0 PMTs list. The bottom PMT array was noisier, with several outliers, as shown by the pedestal RMS distribution in Fig.5.14. The different noise condition of the two arrays is probably due to the different HV boards used to supply the voltages. Furthermore, the length of the top and bottom HV cables is different, which could play a role. The outcome of this study was used as input to decide on the digitizer self-trigger thresholds.

- The results of the HV-scan presented in section 5.2.2 were used to align the PMT gains to $\sim 2\times10^6$. A limit was set to the maximum HV for a given PMT to avoid any aging problems due to the high voltage. We aimed to limit the maximum HV to not more than −1.4 kV. With this condition, the SPE acceptances at 15 ADC counts were analyzed. The objective was to have an overall acceptance above 90 %. This required raising the high voltage of $\sim$ 100 PMTs above the limit. The resulting HV map is shown in Fig.5.15, and the SPE acceptances at 15 ADC counts are shown in Fig.5.16. Ultimately, only 27 PMTs required a high voltage of −1.5 kV. After this operation, the noise analysis was repeated without showing any relevant difference.

- The afterpulses rate with the HV configuration shown in Fig.5.15 was analyzed to identify any absolute increase: The new HV configuration did not result in any increase in the AP rate. The time evolutions of the AP rates were also considered for the final PMTs list. Some PMTs showed the presence of xenon, as well as argon, afterpulses. For the majority, the rate was stable and below 0.1%. PMT 177 showed a large and growing xenon leakage. The main problems, however, came from nitrogen APs. In total, 10 PMTs were excluded from the SR0 PMT list due to increasing nitrogen APs, probably due to the failure of the PMT getter.

Eventually, the results from the noise analysis and the absolute trigger rate during regular data taking were used for setting the digitizer threshold for each PMTs. As explained previously, the noise conditions were acceptable, and only a few PMTs required a threshold greater than 15 ADC counts. Tab.5.1 summarizes the SR0 self-trigger threshold. Furthermore, three additional PMTs were excluded: PMT 28 showed

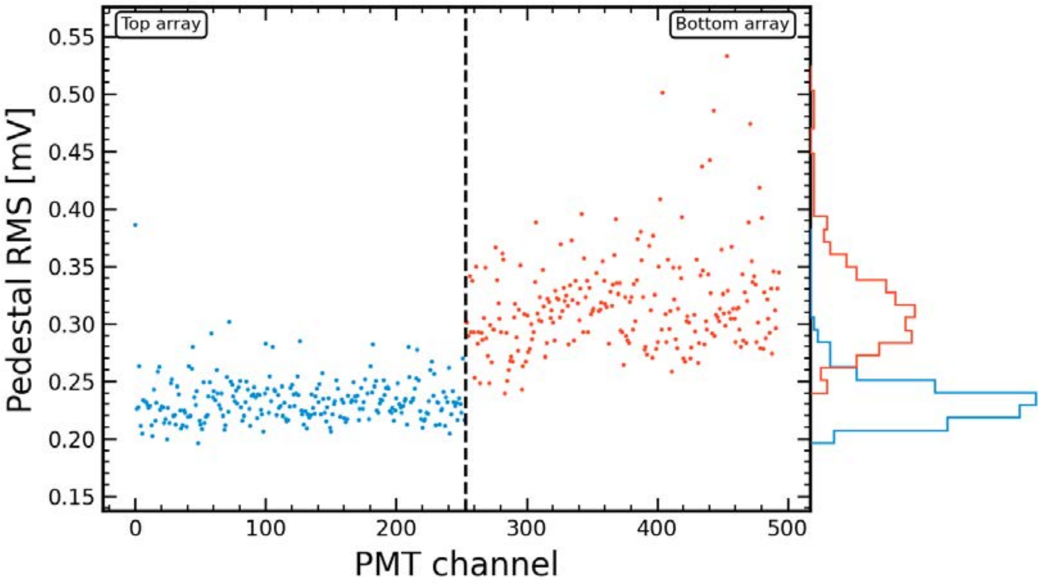

Figure 5.14: Root-mean-square of noise pedestal fro each PMT. In blue are shown the top array PMTs, whereas in red are displayed the bottom array PMTs. The data are extracted using dedicated noise runs as described in the text. The data can be taken as a reference of noise condition for SR0.

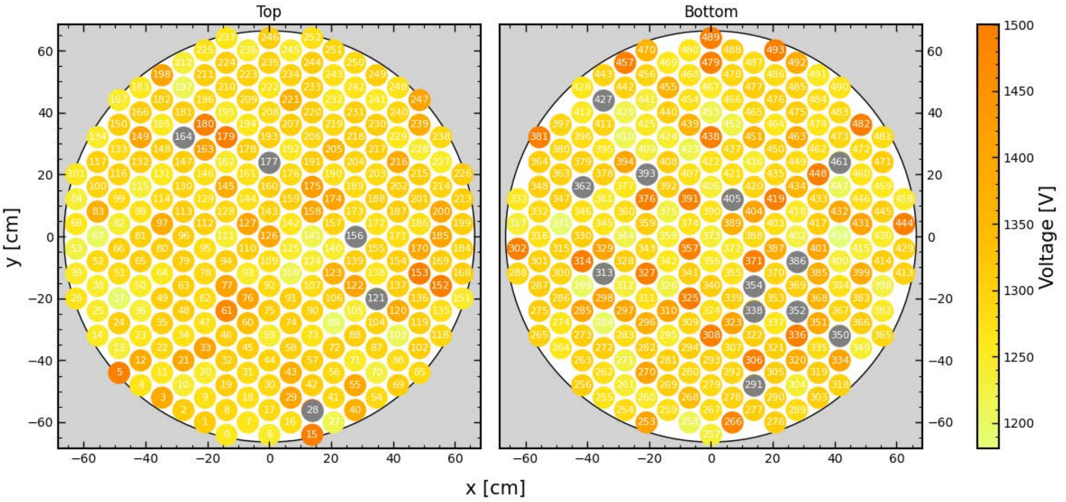

Figure 5.15: XENONnT PMT voltage setting used in SR0. The PMTs in gray are the sensors excluded from the science run.

an unstable gain, whereas PMTs 338 and 362 suffered from light emission. In total, 17 PMTs were omitted from the SR0 PMT list. The PMT numbers and their problems are summarized in Tab.5.2. Finally, Fig.5.17 shows the gain distribution at the beginning of the first science run. The PMTs in gray are the sensors excluded from the final list.

PMTs	387	402	404	434	448	453	471	The rest
ADC threshold	20	19	19	20	20	30	20	15

Table 5.1: Self-trigger threshold configuration for XENONnT SR0.

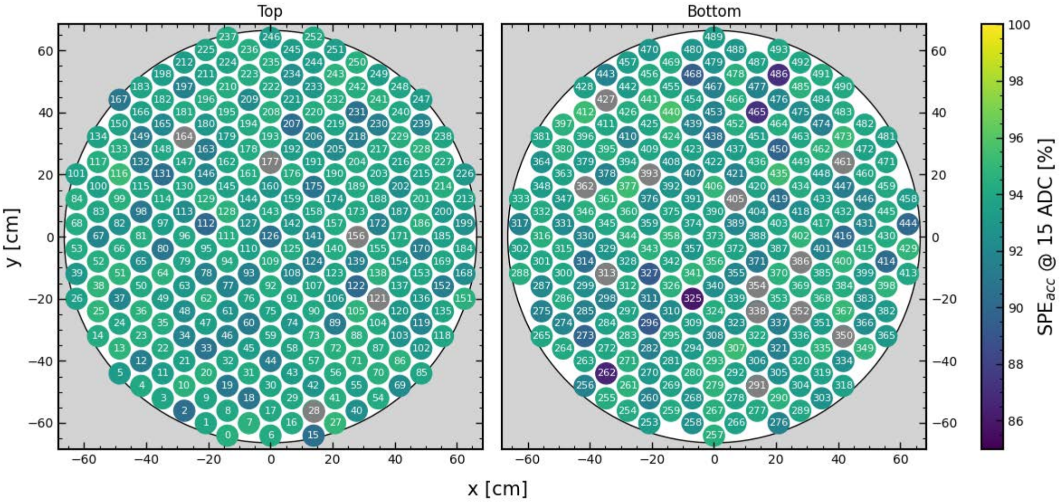

Figure 5.16: Distribution of SPE acceptance at 15 ADC. The data can be taken as a reference for SR0. The PMTs in gray are the sensors excluded from the science run.

Problems	Xe AP	N_2 AP	Light emission	Unstable gain	High noise	Cables problem
PMT numbers	177	121, 156, 164, 291, 313, 350, 352, 393, 427, 461	338, 362	28	405	354, 386

Table 5.2: PMTs excluded from XENONnT SR0 PMT list. Organized according to the problem.

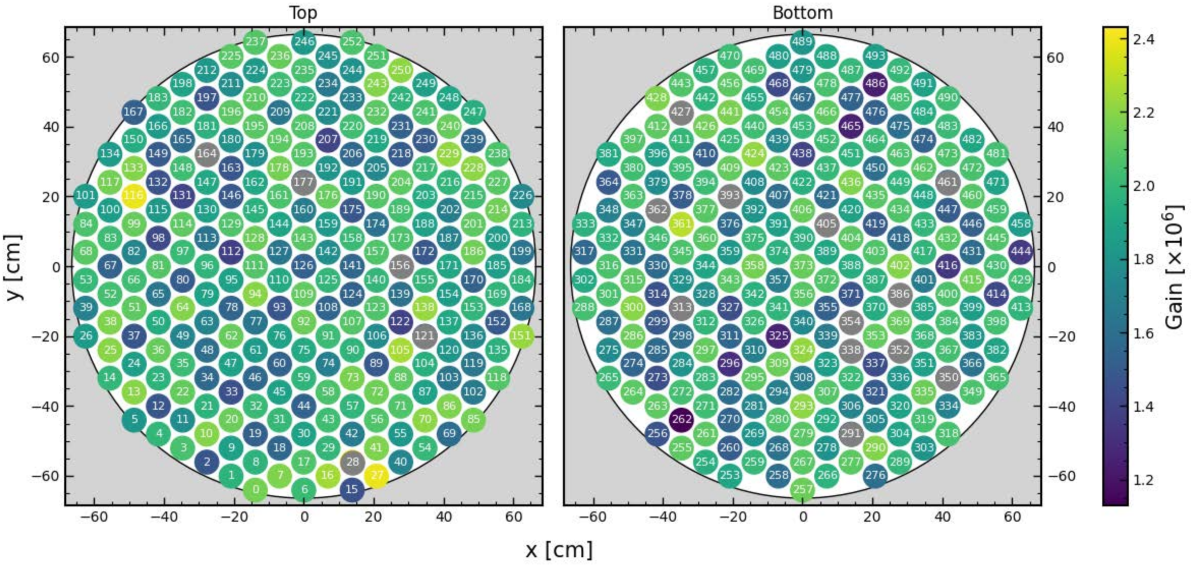

Figure 5.17: XENONnT PMT gain distribution. The data can be taken as a reference for SR0. The PMTs in gray are the sensors excluded from the science run.

5.3 Performance of the PMTs during the first science run

Once the science data taking started in May 2021, the PMTs configurations were frozen until it ended in December 2021. During all data taking period the PMTs were calibrated every Friday: the noise condition was evaluated, the gain estimated, the SPE acceptance monitored, and the AP rate measured. The main objective of the weekly calibration was to understand the time behavior of the PMT response and propagate it through the analysis pipeline. Often, more than one calibration per week, even per day, was performed, especially during the deployment of calibration sources, such as ^{220}Rn and ^{241}AmBe. One period was excluded from the time behavior study. On June 16th and 17th, the DAQ room temperature in the service building increased due to an air conditioning failure. The digitizers were unreliable during this period, thus it was chosen to remove the results of the corresponding calibrations.

In this section, the gain and SPE acceptance performances throughout SR0 are discussed. Furthermore, the derived PMT response model necessary for the detector response simulation is presented.

5.3.1 Time monitoring of PMT performances

The PMTs omitted from the analysis have been shown in Tab.5.2. Besides the PMTs that were physically off[2], the other PMTs were omitted on the software side. The PMTs list was updated at the end of SR0, according to the time evolution of the PMT performances. Only the worst PMTs were omitted, but many others showed a non-constant gain trend over time. This time-dependence behavior required careful modeling to ensure that no bias was propagated on the data processing side.

Gain changes, at constant power supply, can be caused by different phenomena. For example, aging or decreasing gain of PMTs after high illumination. In XENONnT, there is no aim for a theoretical description of the time evolution, but rather an effective characterization based on a custom dynamic Savitzky-Golay filter to smooth the gain trend over time is used. Eventually, the gain model of a PMT is the average over the monitoring period unless any fluctuations larger than an empirical threshold ($2.5\ \%$) are present. The time model of the gain can also account for the change of voltages, which was never the case in SR0. Out of 485 PMTs used in SR0, only the gain model of 24 PMTs was not averaged out[3]. In Fig.5.18 is shown the weekly gain calibration results for 3 random PMTs and, in grey, their SR0 time model of the gain. One of the three PMTs, 255, is an example of a not averaged gain model.

The SPE acceptance was also monitored throughout the SR0. On average, both top and bottom PMT arrays had an SPE acceptance above $90\ \%$ at 15 ADC counts and, most importantly, stable throughout the science run data taking, as shown in Fig.5.19. Rather than the acceptance at 15 ADC counts, knowing the acceptance at the self-trigger threshold is more important. As explained in section 5.1.4, the SPE acceptance also includes the contribution of events larger than 1 PE. Therefore, it must be corrected to derive the true SPE acceptance. Given the stability of the PMT performances, the final true SPE acceptance at the self-trigger threshold was computed considering one calibration (June 3rd, 2021). Finally, knowing the occupancy λ for the SPE calibration run, the true SPE acceptance ε_{1PE} can be computed from Eq.5.6. The Fig.5.20 shows $\varepsilon_{1\ \mathrm{PE}}$ for all SR0 PMTs.

---

[2] The PMT physically off during SR0 were: 156, 164, 177, 352, 354, 362, 386, 393, and 427

[3] The PMTs with a not averaged gain model over time in SR0 are: 3, 5, 12, 33, 55, 61, 127, 152, 163, 175, 198, 255, 266, 288, 296, 299, 302, 326, 341, 351, 378, 390, 453, and 466

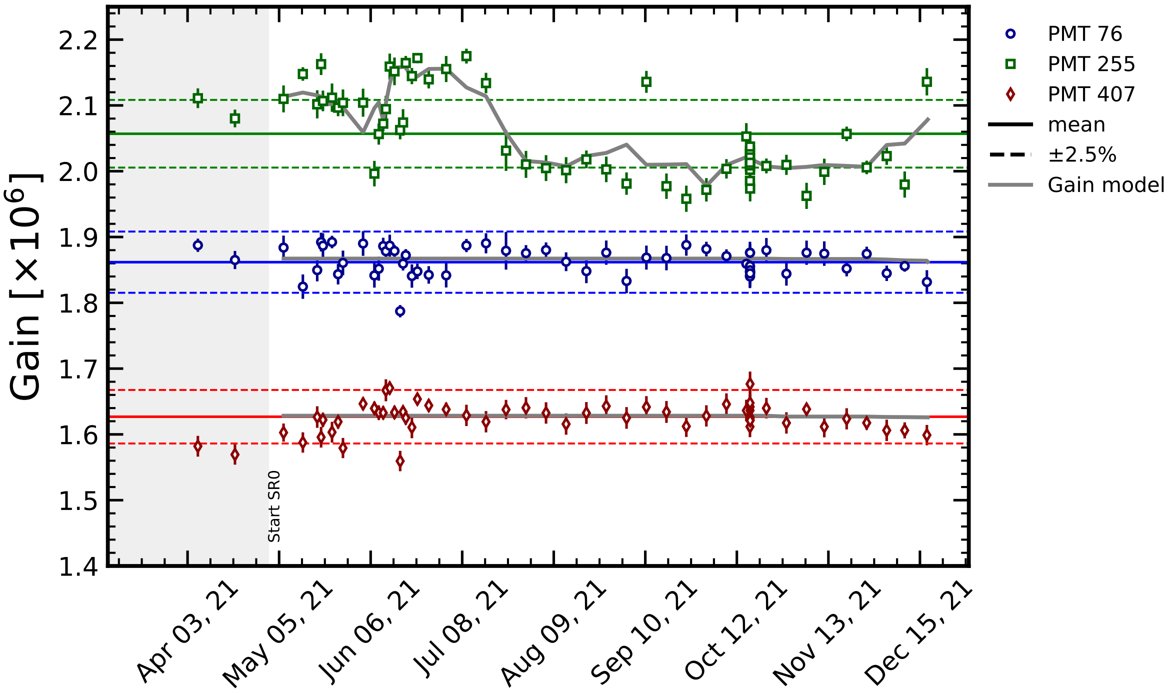

Figure 5.18: Example of time evolution of PMT gain during SR0 for 3 random PMTs. The commissioning period shown by the grey area is not considered for the modeling. the horizontal solid lines represent the average gain over the full SR0, and the dashed horizontal lines show the ±2.5 % variation of the average gain. The gain models used for data processing are shown with the gray solid lines. PMT 255 is an example of a not averaged gain model due to the fluctuations above 2.5 %.

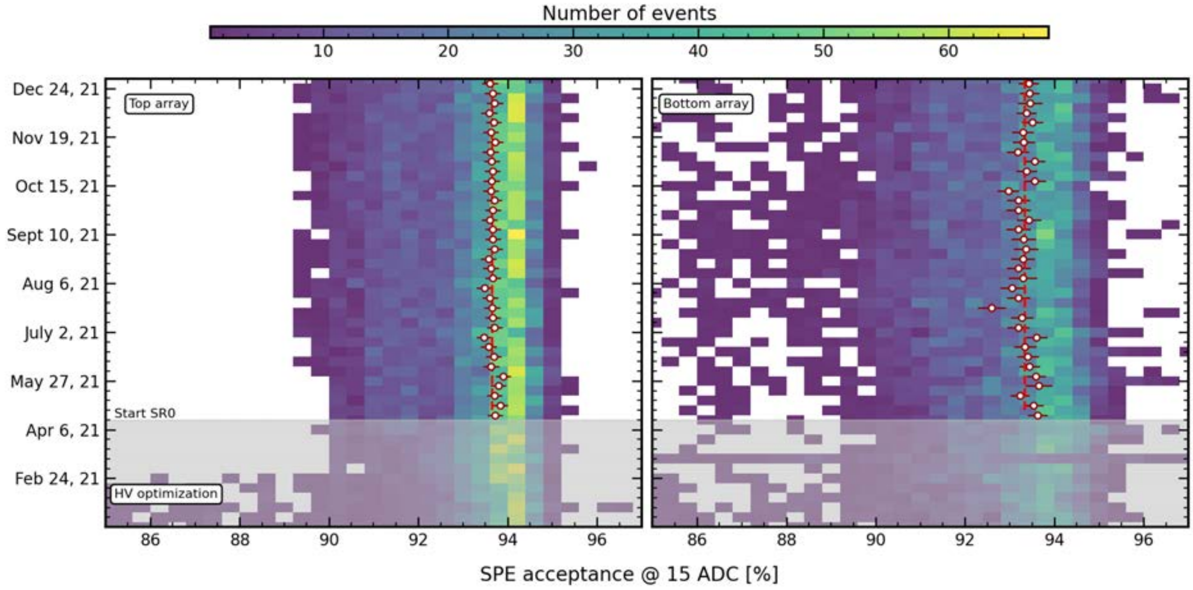

Figure 5.19: The color map shows the distribution of PMTs SPE acceptances at 15 ADC during SR0. The red dots show the SPE acceptance means for each time bin. The commissioning period shown in grey is not considered.

On average, the top PMT array $\varepsilon_{1\ \mathrm{PE}}$ was (91.49 ± 0.09) %, while for the bottom PMT array was (90.98 ± 0.17) %. The difference between the two arrays is due to the higher average self-trigger threshold for the bottom PMT array, which reflects its slightly worse noise condition.

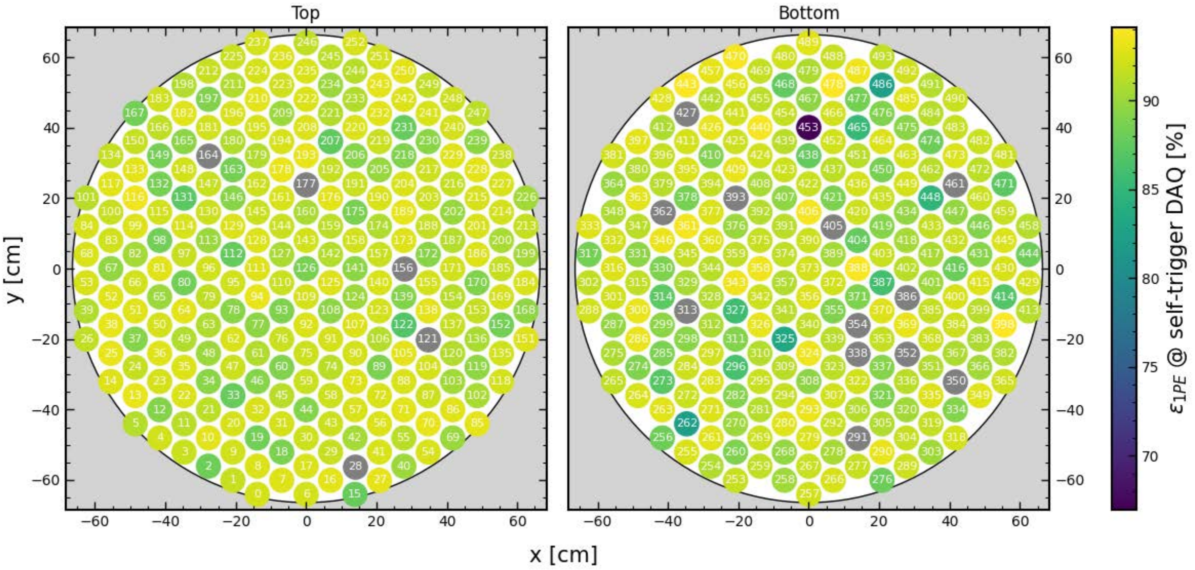

Figure 5.20: Distribution of true SPE acceptance $\varepsilon_{1\ \mathrm{PE}}$ at the DAQ self-trigger threshold. The data can be taken as a reference for SR0. The PMTs in gray are the sensors excluded from the science run: either they were physically off, or they were excluded by software (see the text).

5.3.2 SPE shape

One last piece of information is extracted from the SPE acceptance calibration runs, namely the SPE charge spectrum. The shape of SPE charge spectrum is required for a full detector response simulation, which starts from the energy deposition up to the S1 and S2 signals generation. The *probability distribution function* (pdf) of the single PE area spectrum is derived from a dedicated SPE acceptance calibration with even lower illumination and higher statistics compared to normal SPE acceptance data taking mode. The SPE pdf was derived for all the XENONnT PMTs and used into the so-called *WFsim* [251], the XENONnT software for realistic (S1, S2) simulation. Additional information on the XENONnT simulation framework will be presented in section 6.5. The following paragraphs discuss the derivation of the SPE pdf.

A 10 min SPE acceptance calibration with particularly low illumination was performed. The unusual length of the data taking ensured 10^6 events, two orders of magnitude higher than the regular SPE calibration. The low illumination was such that the mean occupancy was $\sim$ 0.04 PE/trigger, restricting the contribution of $>$ 1 PE events below 0.3 %. Like for the SPE resolution discussed in section 5.2.2, the *pdf* was extracted by fitting the PMT output with the model described in [249].

In the paper [249], an analytical expression for the shape of the charge spectrum is derived for every PE contribution as a weighted (w) sum of the normal distribution (N) *pdf*, for the multiplication process, and the exponentially modified Gaussian (EMG) *pdf* for the background events, e.g., dark counts. Moreover, each term is scaled with the Poisson term (P) given the estimated occupancy λ. The full expression is:

$$\begin{aligned} f(x) = {} & \mathrm{P}(0;\lambda)\Big((1-w)\mathrm{N}(x;\mu_0,\sigma_0) + w\mathrm{EMG}(x;\mu_0,\sigma_0,c_0)\Big) \\ & + \mathrm{P}(1;\lambda)\Big((1-w)\mathrm{N}(x;\mu_1+\mu_0,\sqrt{\sigma^2+\sigma_0^2}) + w\mathrm{EMG}(x;\mu_1+\mu_0,\sqrt{\sigma_1^2+\sigma_0^2},c_0)\Big) \\ & + \mathrm{P}(k\geq 2;\lambda)\Big((1-w)\mathrm{N}(x;k\mu_1+\mu_0,\sqrt{k\sigma_1^2+\sigma_0^2}) + w\mathrm{EMG}(x;k\mu_1+\mu_0,\sqrt{k\sigma_1^2+\sigma_0^2},c_0)\Big) \end{aligned} \tag{5.9}$$

The pedestal contribution (k=0), the 1 PE peak (k=1), and the multi-PE contribution are separate for convenience. Here, the same syntax as the original paper is used. Hence, *x* is the PMT charge output, μ_0 and σ_0 are the pedestal mean charge and its width, while μ_1 and σ_1 are for the PE induce events, and c_0 governs the exponential tail in noise processes.

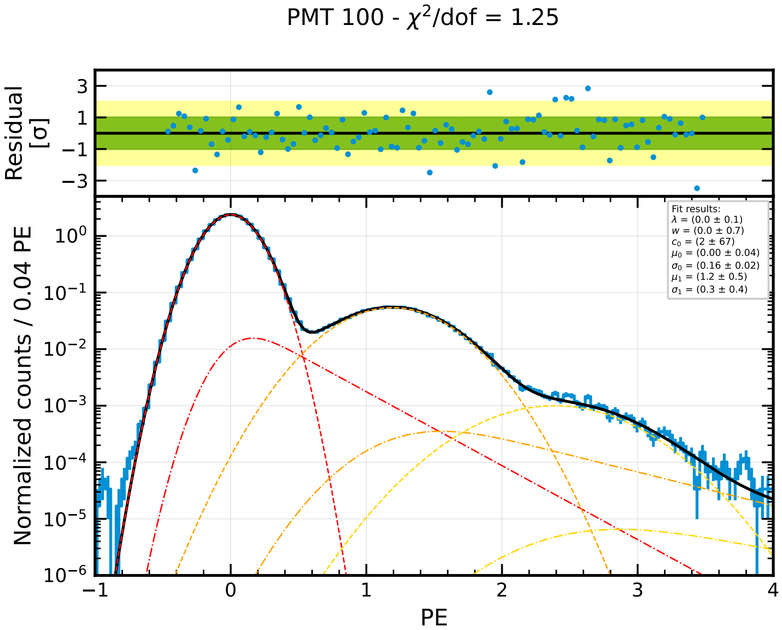

Figure 5.21: Example of PMT charge spectrum fit using the model described in Eq.5.9. The fit results are collected in the legend. Each PE component is represented. The 0 PE, 1 PE, and 2 PE components are shown in red, orange, and yellow, respectively. The Solid lines represent the normal distribution (N), whereas the exponentially modified Gaussian (EMG) is displayed with dashed lines. The top panel shows the residuals in units of σ. The green and yellow bands show the 1σ and 2σ regions, respectively.

The procedure for extracting the SPE charge *pdf* consists of several steps, which are summarized below.

1. The parameters in Eq.5.9 are extracted by the maximum binned likelihood fit of the PMT area spectrum. Reasonable input and fit constraints can be derived from the LED-off and LED-on spectra features. Fiq.5.21 shows an example of the fit result. The fitted values are used as input for step 3.
2. The objective is to extract the SPE charge *pdf*. Hence, the LED-on is manipulated to obtain the SPE charge spectrum. The manipulation consists of subtracting the spectrum of the LED-off from that of the LED-on after scaling them so that the pedestals coincide. Next, the low-charge region is smooth using a Savitzky-Golay filter. This procedure is summarized in Fiq.5.22.
3. Even though the original paper [249] does not discuss any under-amplified processes, it was decided to include this component in the exponential modified Gaussian. This choice provides a good analytical description of the noise-subtracted SPE charge spectrum. Therefore, three scaling parameters are used to match the noise-subtracted SPE charge with the sum of pedestal EMG and the entires 1 PE and multi-PE contributions. An example of the scaling is shown in Fiq.5.23.

4. The pedestal EMG plus the entire 1 PE contribution after the scaling is used as SPE *pdf*. Since the PMT noise is simulated separately in the *WFsim* software, the μ_0 and σ_0 were factored out from the *pdf*. Theoretically, if the SPE description is correct, the mean of the *pdf* should equal 1 PE. However, a difference of $O(\pm 1\,\%)$ was observed for many PMTs, although consistent with 1 PE considering the uncertainty of fit. To avoid propagating this bias into S1 and S2 simulated signals, the SPE charge *pdf* is scaled such that the mean is equal to 1 PE. The averaged XENONnT SPE charge *pdfs* is shown in Fiq.5.24.

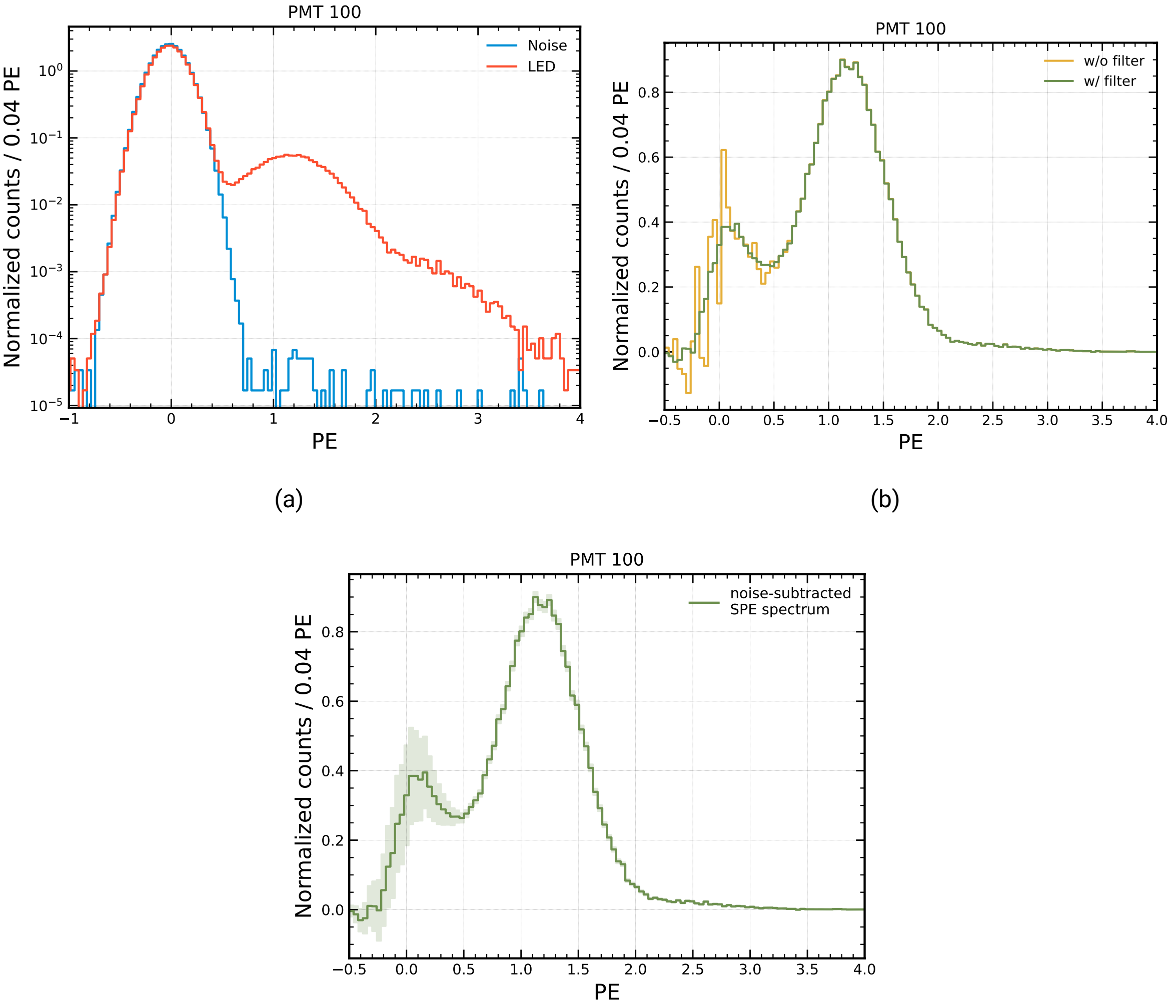

(a)

(b)

(c)

Figure 5.22: Procedure to derive the SPE charge spectrum from the calibration data. (a) The LED-off (blue) and LED-on (red) SPE charge spectra are shown already with the scaling applied to LED-off spectrum matching the two pedestals. (b) The scaled LED-off spectrum is subtracted from the LED-on, and the noise-subtracted spectrum is derived. The latter one is shown in yellow. Then, the low charge region is smooth for reducing the fluctuation. The smoothed noise-subtracted spectrum is displayed in green. (c) The derived SPE charge spectrum is shown, together with its uncertainty computed from the Poisson fluctuations of LED-on and LED-off.

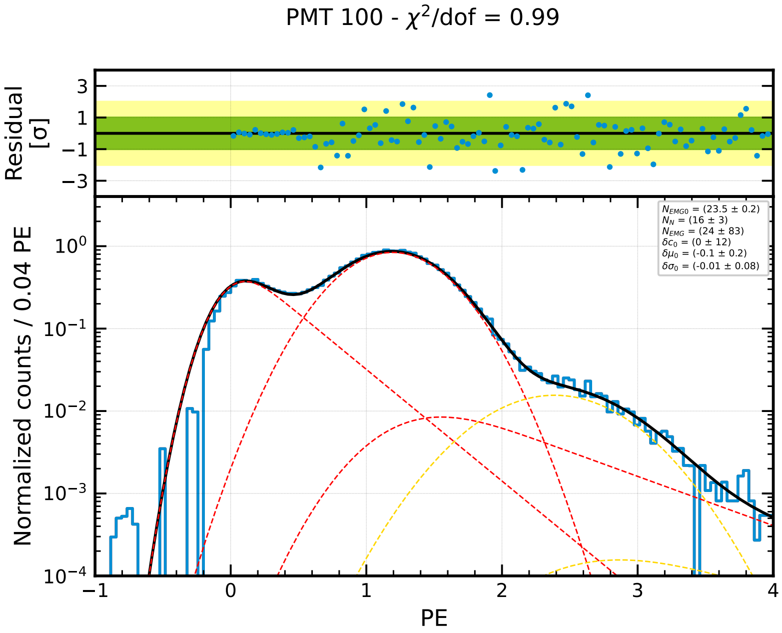

Figure 5.23: Example of fit of SPE charge spectrum. The results of the scaling parameters are collected in the legend. The red lines represent the SPE charge *pdf*, while the yellow one represents the 2 PE component. The top panel shows the residuals in units of σ. The green and yellow bands show the 1σ and 2σ regions, respectively.

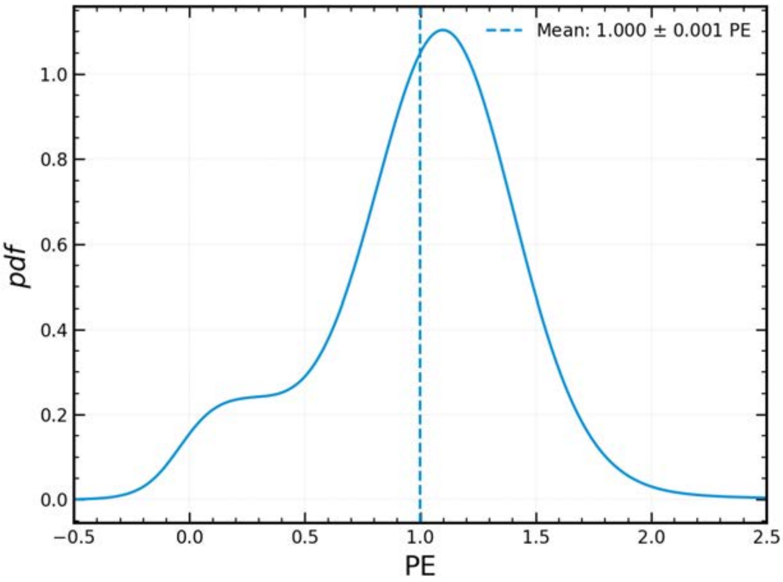

Figure 5.24: The average SPE charge spectrum *pdf* for the PMTs of XENONnT's TPC is shown. The vertical line indicates the mean of the pdf.

All the difficulties in extracting the SPE charge *pdf* lie in the fact that a detailed PMT response model does not exist, especially evident in describing the low-charge region. Other possible directions were considered, such as implementing the backscattering process for the under-amplified photoelectron events [252], but the improvement was not significant. The results obtained here have to be considered as an effective shape. The model describes the data well, with an average reduced χ^2 goodness of fit test of ~ 1.8. The SPE pdfs thus obtained were used to produce realistic background and signal templates.

6

First science run of XENONnT

The first XENONnT science run data taking (SR0) started in May 2021 after the detector commissioning described in section 5.2, and it lasted until mid-December. During this period, the xenon temperature, pressure, and liquid level above the gate electrode were stable at (176.8 ± 0.4) K, (1.890 ± 0.004) bar, and (5.02 ± 0.20) mm, respectively. In section 5.2.3, the PMT operating conditions adopted during SR0 were shown. The electrical short between the bottom screening electrode and the cathode limited the electric field configuration. The XENONnT TPC operated with a drift field in the active region of 23 V/cm. With this configuration, the maximal drift time corresponds to 2.2 ms. Sporadic and localized high rates of single electron events limited the extraction field intensity through the liquid-gas interface to 2.9 kV/cm. When these events occurred, the extraction field was turned off, and data acquisition stopped until they disappeared. The purification and distillation campaign performed during the detector commissioning allows achieving a ^{222}Rn level of ~ 1.7 μBq/kg and an electron lifetime of ≥ 10 ms.

Even though the electric fields were far from the design values, the response of the TPC was sufficient to acquire high-quality science data. The XENONnT collaboration performed low-energy ER and WIMP analyses with SR0 physics data in a blind manner, withholding analysis of events within the electronic and nuclear recoil bands below 20 keV until the analysis framework was deemed reliable.

A summary of the SR0 data-taking strategy is presented as a starting point. Following, this chapter presents the XENONnT analysis pipeline. The data processing and the event correction due to detector effects are discussed, followed by data selection criteria utilized in low-energy ER analysis and WIMP search. Then, the TPC energy calibration with scintillation and ionization signals is presented. Next, the XENONnT simulation framework is outlined, focusing on the points relevant to this manuscript. The signal and background modeling is then introduced, together with the characterization of the ER and NR bands. The results of the SR0 low-energy ER and WIMP analysis are summarized at the end of the chapter.

6.1 A brief summary of the first XENONnT science run

The physics search dataset was collected from July 6th to November 10th, 2021 with a total livetime of 97.1 days. The rest of SR0 consisted of external or internal calibrations for detector response characterization.

Every two weeks, a ^{83m}Kr source was injected in the xenon volume to monitor the stability and calibrate the energy reconstruction and position dependencies in the detector response. The calibration source is introduced in xenon volume by letting the gas xenon flow through a ^{83}Rb source, which decays to ^{83m}Kr with a half-life of 86.2 days [253]. The ^{83m}Kr subsequently decays via emission of 32.1 keV and 9.4 keV conversion electrons with a half-life of 1.83 hours [254, 255]. The previous experiment demonstrated that no ^{83}Rb traces are introduced with this design [256, 150].

A ^{241}AmBe source, deployed in different positions around the outer cryostat, was used at the beginning of the SR0 to characterize the NR response. The ^{241}AmBe source generates neutrons with energies up to 10 MeV via the following nuclear reaction [257]:

$$\begin{aligned} &^{241}\text{Am} \rightarrow\ ^{237}\text{Np} + \alpha \\ &^{9}\text{Be} + \alpha \rightarrow \text{n} +^{12}\text{C}^{*} + Q(5.704\ \text{MeV}), \end{aligned} \tag{6.1}$$

where the α particles, emitted from ^{241}Am, have an average energy of $\sim$ 5.5 MeV [258, 259]. In addition to the neutrons, a 4.44 MeV gamma is simultaneously emitted from carbon de-excitation [260]. The coincidence between the gamma in the neutron veto and the neutron in the TPC allows for the selection of a (almost) pure nuclear recoil dataset, improving the characterization of the NR response. The calibration system also permits the placement of the ^{241}AmBe source far from the TPC but still inside the neutron veto, such that the neutrons produced are detected only by neutron veto. This calibration configuration was adopted in SR0 to evaluate the neutron veto tagging efficiency, equal to $\sim$ 68% [188].

Two sources were used for ER response characterization, injected in the xenon volume. The calibration with ^{220}Rn source, which provides a continuous ER spectrum at low energies thanks to its β emitter daughter ^{212}Pb [261], was performed after the ^{241}AmBe calibration. In addition to the ER band modeling, this calibration was essential to validate the energy threshold. Moreover, the data from ^{220}Rn source were extensively used to develop most of the data selection criteria utilized in the analysis [208]. The second ER calibration source, ^{37}Ar, provides low-energy events of 2.82 keV via (K-shell) electron capture [262]. It was primarily used to understand further the detector response near the energy threshold [208]. To avoid unwanted ^{37}Ar contamination in the physics search dataset, the source was injected at the end of the SR0.

The summary of the SR0 livetime acquisition is shown in Fig.6.1. In addition, other operations were performed, e.g., PMT calibration with LED light. Before the ^{37}Ar injection, a dedicated xenon recirculation scheme was used where the main water-removal getter was bypassed to increase the water and enhance the tritiated water concentration inside the xenon target. Tritium might provide an explanation for the XENON1T low-energy ER excess discussed in section 3.3.4. Therefore, this data-acquisition mode, tritium-enhanced (TED), was performed to constrain a possible tritium contamination [208].

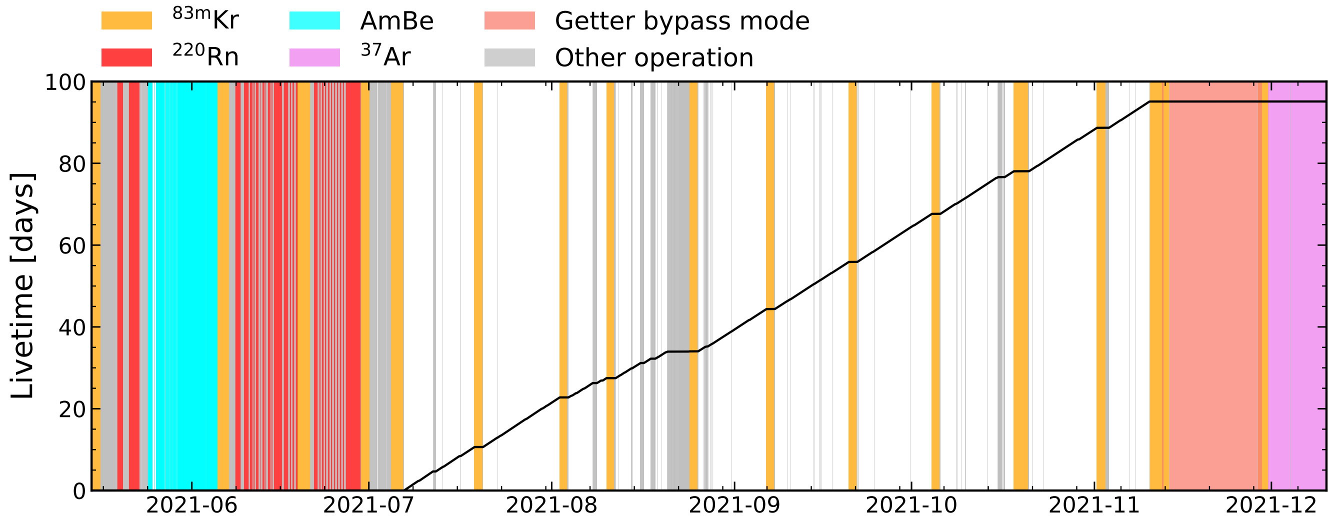

Figure 6.1: XENONnT SR0 WIMP search livetime accumulation. The colored regions represent the different calibrations performed during SR0, except for the gray one corresponding to when the detector was not taking data or when the PMT calibration was performed.

6.2 Data processing pipeline

This section presents the XENONnT processing pipeline, based on strax [244] and straxen [245]. The software, which take care of data acquisition and first processing, and event building, respectively, have already been introduced when the PMTs calibration was discussed (see section 5.1.2). The following section discusses how straxen builts (S1, S2) events from the PMT-hits. Event distortions, resulting from spatially dependent detector response, are then presented along with the correction used to mitigate them.

6.2.1 Event building

There are several steps in the data processing to go from PMT-hits to a fully reconstructed (S1, S2) event. First, the PMT waveforms in ≥ 700 ns time window are grouped to form peak sub-cluster, *peaklets* [240]. Peaklets that show saturation[1] are corrected at this stage with the same method used in XENON1T [263].

The peaklets are then classified using the number of contributing PMTs, the signal rise time (time to reach 10 % of the peak's area), and the fraction of the area observed by the top PMT array (area fraction top, AFT). S1-like peaks are assumed to consist of only one peaklet, with at least 3 contributing PMTs within 100 ns (3-fold coincidence) and sharp rise time, as well as low AFT. Peaks that do not fulfill S1 requirements and have at least 4 contributing PMTs are classified as S2 peaks. It is also possible that some peaklets do not fulfill either the S1 or the S2 requirement, e.g., PMT dark counts. In this case, the peaklets are classified as unknown and are not processed further. Later, S2-like peaks are re-clustered according to the time intervals between the peaklets. The small drift velocity - equal to (0.676 ± 0.006) mm/µs - challenges S2 merging due to the large drift time and long S2s [240]. The merging and peak classification algorithms were optimized based on waveform simulations, e.g., the boundary of rise time as a function of AFT for S1-peak classification.

---

[1] In general, a PMT output saturates either when the signal is larger than the dynamic range of the digitizers or when the signal is larger than the maximal current that the voltage divider board can handle. See section 4.1.1 for more information.

An (S1, S2) event is then defined by the largest S2 peak[2], called triggering peak. This S2 peak should be $>$ 100 PE and with less than 8 peaks with an area at most 50% of the its total area in a ±100 ms window around its center [240]. The left extension of the event window is 2.45 ms, a little larger than the maximal drift time, and the right extension is 0.25 ms, with respect to the center of the S2 triggering signal. If the window contains other S2s bigger than 100 PE, the time windows are combined. Then, the largest S1 in the window is paired with the largest S2 [240]. The straxen event building working principle is summarized in the diagram in Fig.6.2.

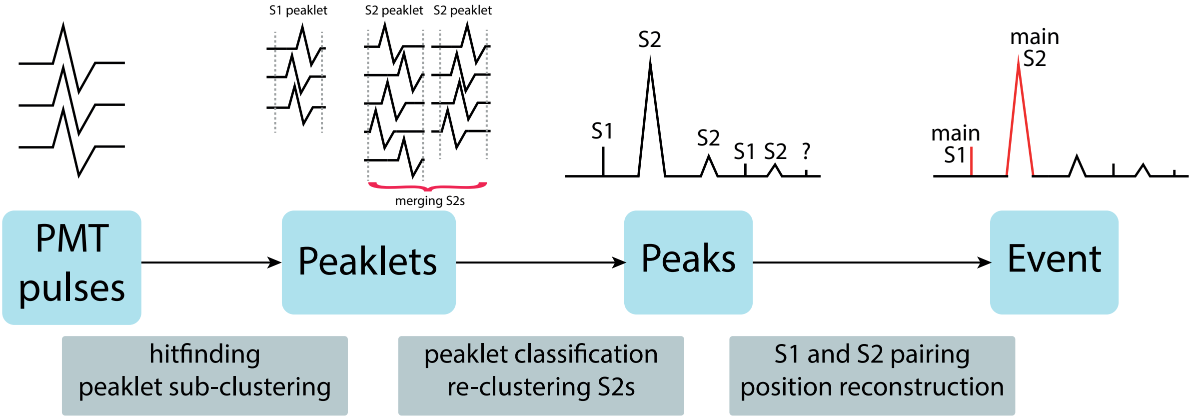

Figure 6.2: The working principle applied in straxen to build (S1, S2) events starting from PMT pulses and passing through intermediate objects (blue tiles). The main processing steps are reported (grey tiles). Diagram adapted from [264].

The S2 top array light pattern is fed into three different neural networks (multilayer perceptron, convolutional neural network, and graph constrained network [265]), which compute the (x, y) event position independently. The algorithms are calibrated using simulated data from an optical Monte Carlo simulation [240]. The position from the multilayer perceptron is used in the analysis, while the cross-validation among the three algorithms is used to improve position reconstruction. Eventually, the central time difference of S1 and S2 is used to reconstruct the z event position, giving the electron drift velocity. The waveform of an (S1, S2) event is shown in Fig.6.3, where the insets show the PMT hit patterns of the two signals.

6.2.2 Event corrections

As seen in section 3.1, the S1 and S2 signals are proportional to the number of photons n_γ and the number of electrons n_e, respectively, which originate from particle interaction in the xenon target. However, various position-dependant detector effects distort the observed S1 and S2. Therefore, the observed signals must be corrected for these detector effects before extracting any features, such as position or deposited energy.

The corrections are mainly derived using ^{83m}Kr calibration data. This source can be easily dispersed uniformly in all detector regions, and its two-step decays provide a clear signature for data selection. The corrections were continuously validated throughout SR0 thanks to the bi-weekly ^{83m}Kr calibration

---

[2] Within the event time window, there might be more than one S2 peak, but only the largest one is considered as triggering signal.

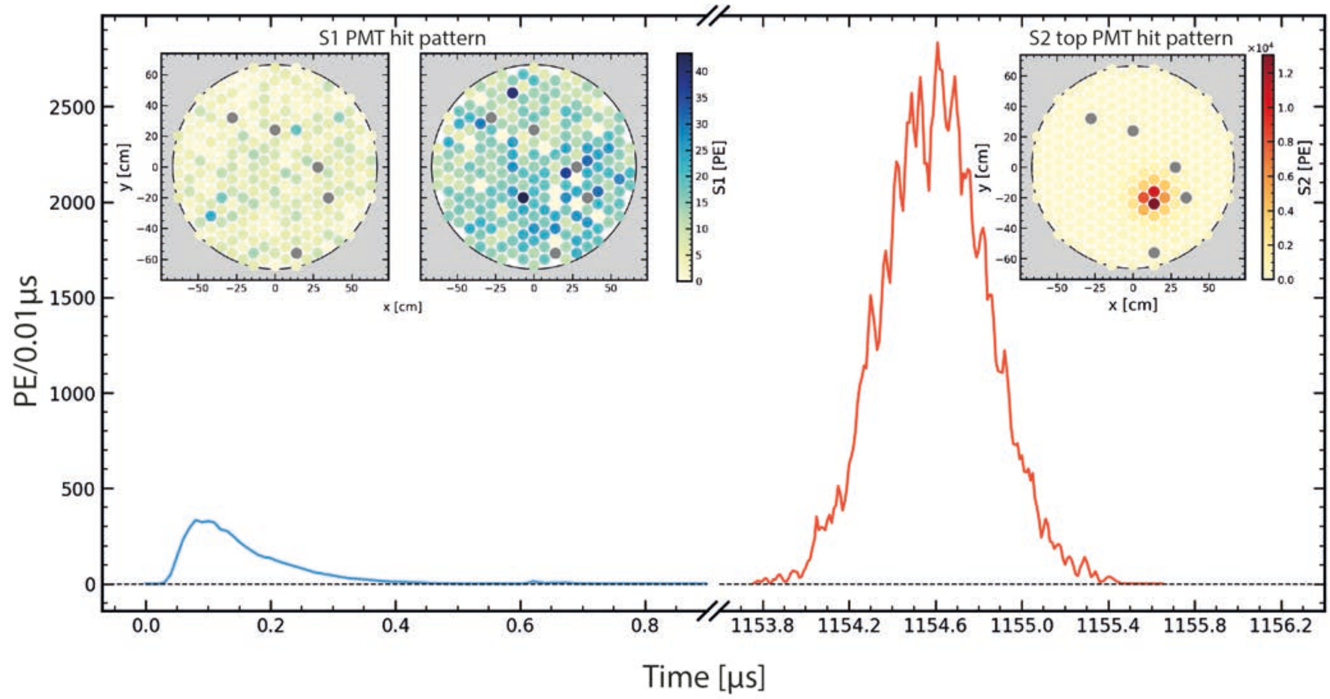

Figure 6.3: Example of XENONnT (S1, S2) waveform. The S1 is in blue, while the S2 is in red. It is possible to appreciate the difference in timing and area. The S1 signals are very fast, with a typical size of $\mathcal{O}(0.1\ \mu\mathrm{s})$, whereas the S2s have a time width of $\mathcal{O}(1\ \mu\mathrm{s})$. From left to right, the inset plots represent the S1 hit pattern (top and bottom array), and the S2 top array hit pattern, respectively. While S1 is distributed over both arrays, S2 is localized more in a few PMTs of the top. Indeed the S2 light distribution in the top array is used to reconstruct the (x, y) event position. The z position is computed considering drift time, namely the central time difference of the two signals. In this case, the drift time is $\sim$ 1154 µs, equivalent to a detector depth of $\sim$ 78 cm.

campaigns, and their temporal evolution was considered in the data processing. After correcting the observed signals for the detector effects, stable light and charged yields were achieved in SR0 with fluctuations below 1 % and 3.1 %, respectively. This section briefly summarizes the signal corrections applied to XENONnT data.

Position correction

Describing the XENONnT TPC design, in section 3.3.1, it has been shown that the uniformity of the drift field in the active target is ensured by two concentric sets of field shaping rings. Even with these precautions, the electric field is never completely homogeneous due to edge effects[3] and charge accumulation in the PTFE that distort the field lines [266, 267]. The drift field is bent towards the center of the TPC, producing a radial inward bias in the reconstructed event position, progressively worse approaching the cathode. This effect must be correct for, for reliable three-dimensional position reconstruction, which is essential for position-dependent signal corrections and background suppression.

These distortions are corrected using a data-driven map, called field distortion correction (FDC), based on $^{83\mathrm{m}}$Kr calibration. The FDC stretches the observed radial distribution of $^{83\mathrm{m}}$Kr calibration data so that its limit matches the TPC dimension. Using voxelized $^{83\mathrm{m}}$Kr data in (r_{obs}, ϕ_{obs}, z_{obs}) a correction map f

---

[3] A TPC is nothing more than a giant capacitor. As with every capacitor, the electric field lines distort at the edges.

is derived. Subsequently, the correct event depth is obtained using Pythagoras theorem and assuming a straight trajectory for the drift electrons. Thus, the r and z correction can be expressed as:

$$\begin{aligned} r_{\text{corr}} &= \mathrm{f}(r_{\text{obs}}; \phi_{\text{obs}}; z_{\text{obs}}) \\ z_{\text{corr}} &= -\sqrt{z_{\text{obs}}^2 - (r_{\text{corr}} - r_{\text{obs}})^2}, \end{aligned} \tag{6.2}$$

where the observed and corrected positions are indicated with subscripts ”obs” and ”corr”.

The approach described here is valid if no charge-insensitive volume (CIV) is present. The CIV is a region in the TPC where the drift field lines do not end up at the gate electrode but instead into the PTFE panel. Then, no charge signals can be observed from this region. The COMSOL Multiphysics® [268] electric field simulation in XENONnT suggests that a CIV is present near the cathode [266]. This is confirmed from data analysis, e.g., spatial distribution analysis of α-decay from ^{220}Rn. The data-driven FDC map does not include the CIV effect, but the electric field simulation results are fed into simulator software for consistent signal and background simulation. Hence, if a bias is present in the position reconstruction for the signals, it would be present also in the simulation. The presence of CIV was used to inform the choice of the fiducial volume in the final analyses, and its uncertainty is propagated into the estimated fiducial mass.

In Fig.6.4, the effects of the FDC map on $^{83\text{m}}$Kr calibration data is shown. The estimated CIV is shown as well defined as the region below the 90% electron survival probability line.

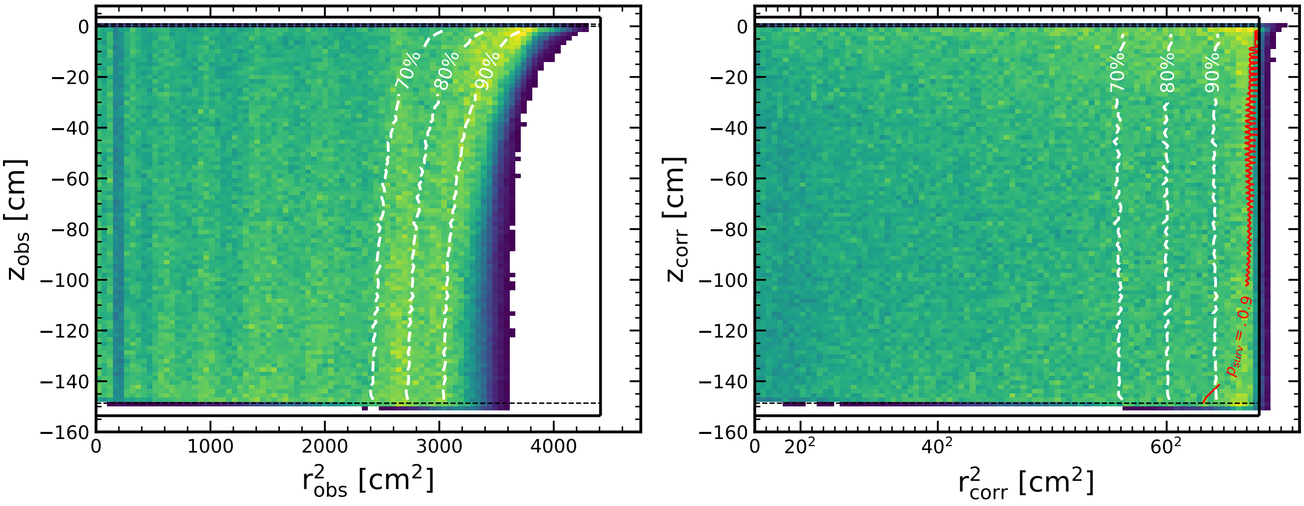

Figure 6.4: Reconstructed $^{83\text{m}}$Kr events positions without (left) and with field distortion correction (right). The data distribution iso-percentiles are shown with dashed white lines before and after applying the FDC. In the corrected position, the 90 % electron survival probability limit is shown in red, derived by electric field simulation [266]. The charge insensitive region is defined as the area below this line, where the probability of observed charge signal is below 90 %.

S1 corrections

In section 3.1, it was shown that the amount of photon n_γ produced for a given energy deposition E, and electric field V_{field} is described by the photon yield $PY = PY(E; V_{\text{field}})$. This is generally different from the amount of light detected because not all the photons reach the sensors, and the probability of producing a detectable signal in the PMTs is not 100 %. The probability of detecting a photon depends on the position in which it was emitted: Different photon trajectories lead to different detection probabilities. Therefore, the amount of light observed per unit of deposited energy - known as light yield (*LY*) - carries spatial dependencies which need to be accounted for in the data processing.

The relative 3-dimensional *LY* map $f(x, y, z)$, normalized to the average *LY*, from the 41.5 keV ^{83m}Kr events, was used to correct the light signal in XENONnT. The corrected S1, called cS1, is obtained as follows:

$$\begin{aligned} f(x,y,z) &= \frac{LY(x,y,z,V_{\text{field}},E)}{\widehat{LY}} \\ cS1 &= S1 \times f(x,y,z) \end{aligned} \tag{6.3}$$

Before extracting the *LY*, the observed 41.5 keV S1s are manipulated to remove the drift field inhomogeneities effects. Since the *PY* depended on the electric field, the drift field inhomogeneities can also lead to position-dependent n_γ for the same energy deposited. However, the drift field inhomogeneities have different impacts for different energy deposition (see Fig.3.3). Therefore, this effect needs to be factored out from the correction map. This was done using the *LY* field-dependent model from [269], and the XENONnT COMSOL Multiphysics® [268] electric field simulation. The relative variation of *LY* with respect to the average because of the electric field inhomogeneities is evaluated over the full volume and factored out from the light signal such that: S1 → S1$_{\text{fec}}$, where the subscript "fec" stands for field effect corrected. Thus, using 41.5 keV S1$_{\text{fec}}$, the 3-dimensional *LY* is extracted as $LY(x,y,z,V_{\text{field}},E) = S1(x,y,z,V_{\text{field}},E)_{\text{fec}}/E$, and thus the correction map is computed. The XENONnT map $f(x, y, z)$ is shown in Fig.6.5. Approaching the top of the TPC the correction factor gets smaller than 1, reflecting the higher collection efficiency at a small depth.

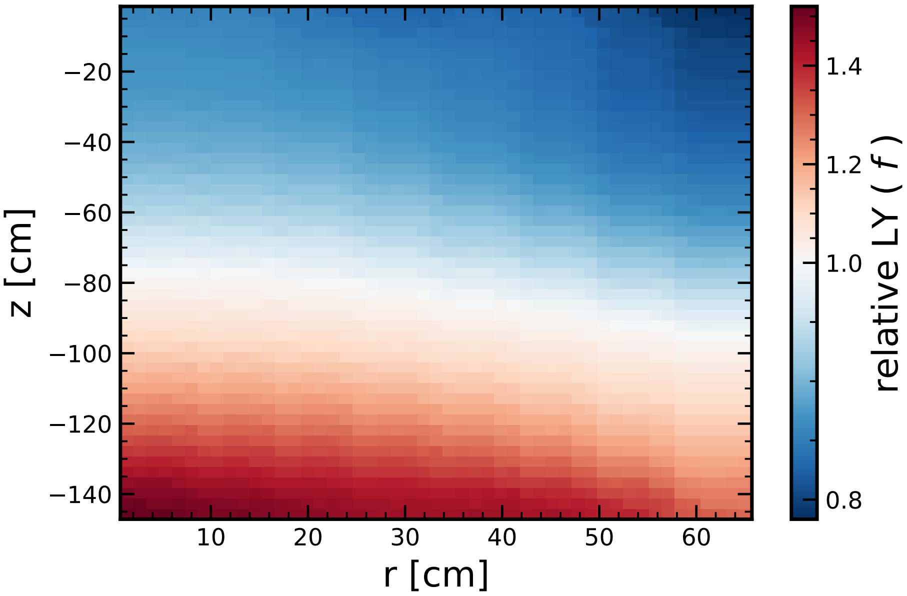

Figure 6.5: Relative light yield map extracted from ^{83m}Kr calibration data, used for S1 correction in XENONnT.

S2 corrections

In section 3.3.3, the loss of charge signals due to electronegative impurity in the xenon and how it can be described with the electron lifetime τ_e has been discussed. The S2 area will decrease with the increasing concentration of electronegative impurities, such as O_2, which can capture the electrons while they drift. The loss of charge exponentially increases with the drift time *t*, causing a significant dependence of the S2 area with the z position. Thus, the observed S2 is corrected, and $cS2^0$ is defined considering the exponential loss governed by τ_e:

$$cS2^0 = S2 \times e^{-t/\tau_e} \tag{6.4}$$

To calculate τ_e, several sources were used, all distributed uniformly within the detector volume: α events from ^{222}Rn, ^{83m}Kr calibration data, and ^{37}Ar calibration data. As it was done for S1 correction, the S2 signals are corrected for the electric field inhomogeneities before extracting the electron lifetime. Additionally, a purity monitor system [205] on the liquid purification line was used to monitor τ_e. The electron lifetime was monitored throughout SR0, and the different estimations were cross-checked. All the different estimations were consistent within a few percent, and eventually, the time model of τ_e extracted from ^{83m}Kr data was used in the XENONnT data processing. An example of S2 area, with FDC applied and the effect of field inhomogeneities disentangled, as a function of drift time for one ^{83m}Kr calibration campaign is shown in Fig.6.6. The extracted τ_e for this data is (15.8 ± 0.7) ms, consistent with the average SR0 valued of $\sim$ 15 ms.

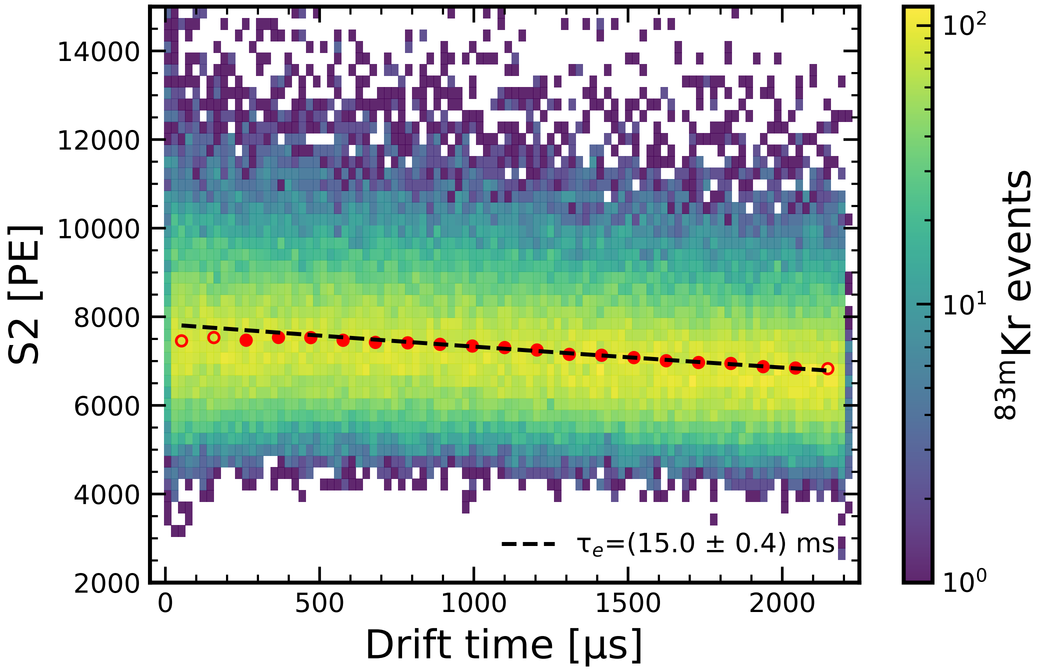

Figure 6.6: The color map shows the S2 area, as a function of the drift time, data from one ^{83m}Kr calibration campaign. The median value is extracted from the projected distribution into the drift time, here shown in red, and the exponential trend is fitted. The red points with white face color are omitted in the minimization routine. From the fit, represented here with a dashed black line, the τ_e is extracted. For these data, τ_e is equal to (15.8 ± 0.7) ms.

In addition, the S2 is corrected for spatial effects such as light collection efficiency, single electron gain[4] and electron extraction efficiency, as well as PMTs detection efficiency. As for the S1 corrections, assuming that the same deposited energy should give the same S2 yield, ^{83m}Kr calibration data were used to build a relative S2 yield map $C(x_{\mathrm{obs}}; y_{\mathrm{obs}})$. This correction targets the detector distortions where the S2 signals are produced. Thus, these are based on the observed positions. The $C(x_{\mathrm{obs}}; y_{\mathrm{obs}})$ is used to correct cS2^0 as follows:

$$cS2 = \frac{cS2^0}{C(x_{\mathrm{obs}}; y_{\mathrm{obs}})} \tag{6.5}$$

A correlation between the electron lifetime and spatial effects corrections is plausible, given the redundancy of the data utilized. The two corrections were iterated to mitigate the correlation until no difference from the previous iteration was observed. The $C(x_{\mathrm{obs}}; y_{\mathrm{obs}})$ map from the total S2 used in the data processing is shown in Fig.6.7. In XENONnT SR0 there are three S2 correction maps: one for the S2 signal observed from the top array, one for the bottom array, and one for the total S2 signal. If only the contribution of one PMT array is considered, then the corresponding map is used to derive the cS2 signals. At the center of the TPC and along the perpendicular wires located on the gate and anode grids, installed to mitigate their sagging, the measured single electron gain is a few percent larger than the average ($\sim$ 32PE/e$^-$) leading to a correction coefficient larger than 1. However, the extraction efficiency is the main reason for $C > 1$. The electrode distance is slightly smaller in the center of the TPC than in the outer regions, leading to a higher extraction field and, therefore, higher extraction efficiency. This is more noticeable along the perpendicular wires, where the extraction efficiency is $\sim$ 70 %, whereas in the rest of the TPC it is, on average, $\sim$ 53 %.

Other corrections

The median of the lone hits area[5], namely peaklets where only one PMT exceeds the self-trigger threshold, was monitored during SR0. These events are mainly due to PMT dark counts, but some scintillation light is also present. The lone hits area should be constant, with a mean approximately equal to 1 PE. However, a decreasing trend over time was observed during ^{220}Rn and ^{241}AmBe calibration, which stabilized during the physics data taking. The correlation of this trend was cross-checked with many parameters, from the xenon temperature to the PMT after-pulses rate. No clear culprit was identified. To avoid any bias in the detector characterization, an ad hoc lone hits correction was developed. The correction consists of an empirical time-dependent model of the relative median to the average value during physics data taking. This correction was applied only to S1 signals area since S2 correction already included it. Fig.6.8 shows the median lone hits evolution during SR0, together with the empirical model used for the correction.

During SR0, the data taking was affected by sporadic and localized high-rate single electron events (hot-spots). The extraction field was turned off when this transient effect appeared in the detector. After a few hours, the anode electrode was ramped up again. Hence, an additional time-dependent correction on S2 was used to account for the variations in the single electron gain (SEG) and extraction efficiency (EE) during the ramping and the moment immediately after. The time evolution of SEG and EE during XENONnT SR0 from which the correction model was derived are shown in Fig.6.9

---

[4] The single electron gain is defined for S2 signals, and it is the number of PE generated by one electron. It differs from the detector parameter g_2 if the electron extraction efficiency is less than 100 %.

[5] The area of a lone hits signal is computed as the integrated charge within -30 ns and +200 ns with respect to the signal maximum.

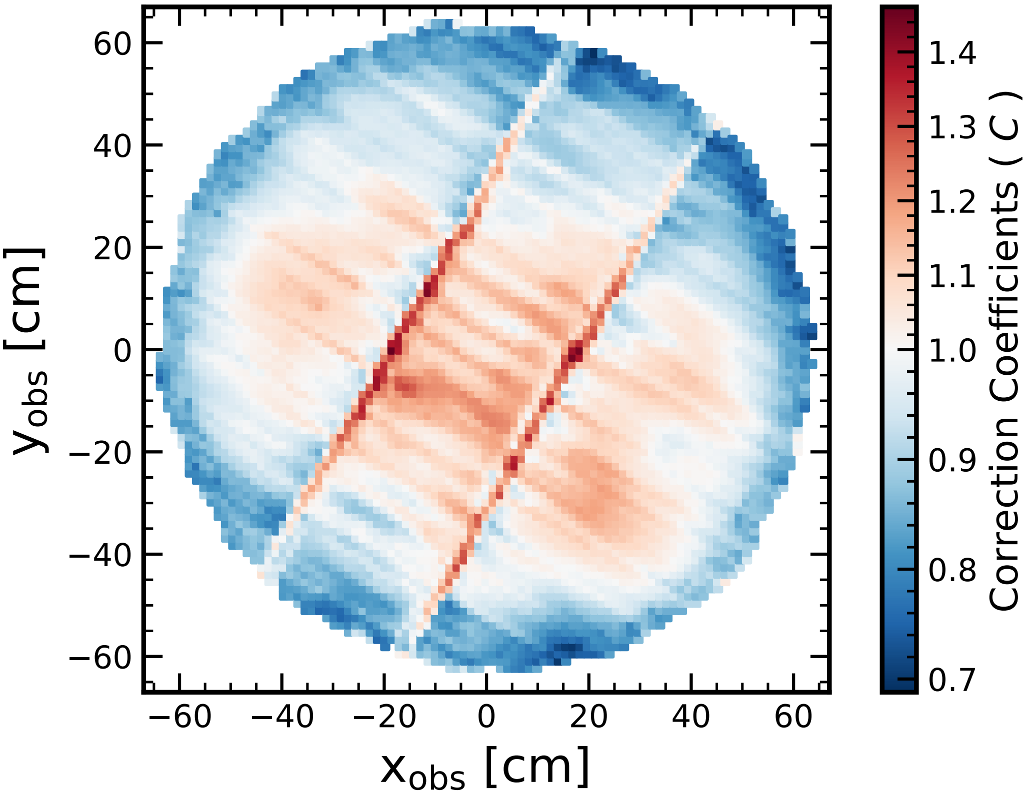

Figure 6.7: Relative S2 yield map extracted from ^{83m}Kr events, used for S2 correction in XENONnT. The two parallel features crossing the TPC are the perpendicular wires on the gate and anode grids installed to mitigate their sagging. Along the wires and in the center part of the TPC, the single electron gain and extraction efficiency are higher, leading to a correction factor ≥1.

6.3 Data quality criteria

At this stage of the analysis, the corrected (S1, S2) events suffer from the presence of unphysical events, e.g., partially reconstructed events or accidental S1-S2 pairings, as well as unwanted event topologies. In XENONnT, various data selection criteria were used to improve data quality and reject unphysical events. These selections, called in jargon *cuts*, were developed using calibration data, mainly from ^{220}Rn source, and when it was possible, using the waveform simulation software (WFsim) [251]. Their acceptances, namely the fraction of good events that survived the cut, were studied on the calibration data using the *N*-1 *method*, which consists of evaluating the Nth cut acceptance after applying the remaining N-1 cuts. Following [270], the uncertainties were taken as the shortest 68.3 % confidence interval of the efficiency probability distribution. The latter can be derived knowing that the N-1 efficiency estimator follows a binomial distribution and applying the Bayes' theorem. Alternatively, the uncertainties in the acceptances were inferred using the Clopper-Pearson method [271], in which the Binomial distribution is approximated with the Beta distribution **B**, and the latter is used to compute a 68 % confidence interval. The two un-

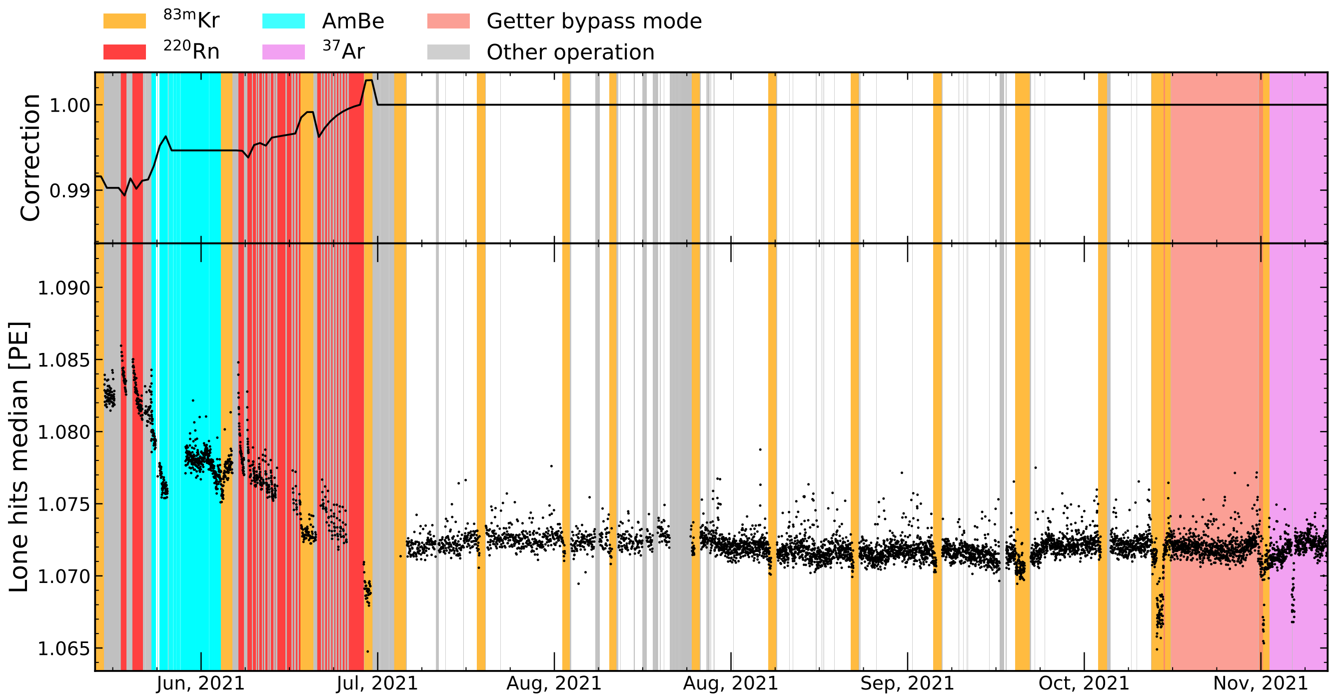

Figure 6.8: The median lone hits evolution during SR0 (bottom), with the time-dependent empirical model used for the S1 signal area correction (top).

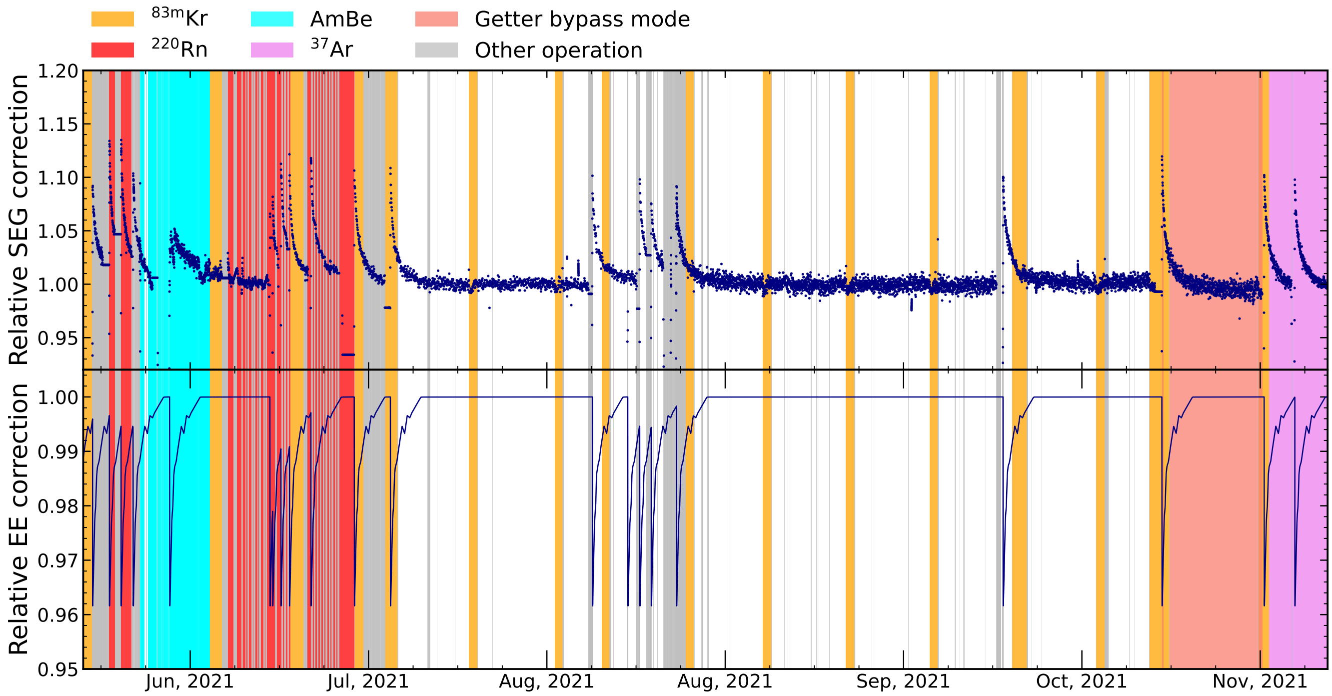

Figure 6.9: The relative SEG (top) and EE (bottom) evolutions during XENONnT SR0, due to the anode cycling induced by the appearance of hot spots, are shown by the scatter points. The colored bands indicate the SR0 calibration period as well as the other operation.

certainties method are complementary, and in SR0 analyses, the Clopper-Pearson method was preferred over Bayes estimations. The N-1 cuts applied before the acceptance computation provide a clean data sample but still with a fraction of unwanted events. Hence, the acceptances derived from this method must be interpreted as the lower limit of the true acceptance.

The following sections present a summary of XENONnT cuts, focusing on the ones developed in the context of this Ph.D. thesis: the S1 area fraction top cut and S1 pattern likelihood cuts. The performances of these selections and their efficiency are discussed.

6.3.1 Cuts overview

The XENONnT cuts presented here are not *universal*. Every physics search has its cut list, depending on the nature of the searched signal. The primary searches in XENONnT, namely the WIMP analysis and the low-energy ER analysis, aim to reject multiple scatter events, i.e., those events due to multiple energy deposition from a single interacting particle inside the active xenon target, creating multiple S2s.

The XENONnT cuts used for the SR0 data analysis can be grouped into four classes:

Time-based cuts reject events that happen close in time with a muon or a neutron veto detector trigger. Furthermore, events partially acquired because the DAQ was in *busy state* due to ongoing processing are rejected by these cuts. Of the same idea, these cuts exclude the data acquired in hot-spot proximity (see section 6.2.2). These selection criteria act as live time reduction.

Topology-based cuts are developed to reject specific signal types. For instance, *S2 single scatter cut* rejects events with an alternative S2 ascribable to a secondary interaction. In addition, the S1 and S2 light patterns information are also used to reduce the multiple scatter population. Similarly, the fraction of total S2 observed from the top array is used to reject events in the gas phase. Wrong S1 and S2 pairings, known as accidental coincidence (AC), are rejected by dedicated cuts based on machine learning algorithms that look for several signal features, e.g., percentile area or signal rise time. Cuts based on S1 features, such as time width or relative area fraction among PMTs contributing to the same events, are used to reduce events triggered by PMT after-pulses.

Uphysical events cuts discard reconstructed (S1, S2) pair where the signal features are inconsistent with the detector response prediction. For instance, *S2 width* cut rejects events with S2 time width different from the expectation based on the electron drift velocity and longitudinal diffusion constant, the parameters that govern the size of the electron cloud during the drift. Furthermore, a selection criterion based on the fraction of S1 signal collected by the top array, which is purely a geometrical factor, is used to reject unphysical events.

Mis-reconstructed event cut reject events for which not all S1 or S2 is collected, e.g., from the charge insensitive volume or close to the PTFE wall. Furthermore, these cuts remove events with the three reconstructed positions very different from each other.

6.3.2 The S1 area fraction top cut

For a given observed signal, the area fraction top (AFT) is the fraction of the total light observed by the top array. Any observed photon will be seen by the top or bottom array, and the probability depends purely on the location of the event and the detector geometry. Given a reconstructed event occurring in a (x,y,z) position in the detector, it is possible to evaluate its level of credibility, in the sense of being a physically motivated event, based on the comparison of the observed S1 AFT with the expected one, drawn either from optical simulation or extracted from a data-driven map. AC events or events where some signal information is lost will have unphysical S1 AFT, and they can be identified through this technique and rejected. The AFT can be described as a binomial process. From its statistical description, it is possible to compute the probability that something at least as extreme as a given event could happen (p-value) and use it to define a well-motivated selection criterion: S1 AFT cut [272].

Mathematical description

For a sequence of n independent experiments, the number of scintillation photons detected (the $S1$ area), the probability of k number of successes, namely the fraction of the total signal collected by the top array (the $S1_{\text{top}}$ area), is derived from the binomial distribution with success probability p (the AFT probability) and failure $q = 1 - p$.

The binomial distribution is discrete, but the S1 area is not an integer. Thus, the complete Euler Γ function is used to implement the continuous counterpart of the binomial distribution $B(S1_{\text{top}}; S1, AFT)$ as follows:

$$\begin{aligned} B(S1_{\text{top}}; S1, AFT) &= Pr(X = S1_{\text{top}}) = \\ &= \frac{\Gamma(S1+1)}{\Gamma(S1 - S1_{\text{top}} + 1)\Gamma(S1_{\text{top}} + 1)} AFT^{S1_{\text{top}}} (1 - AFT)^{S1 - S1_{\text{top}}} \end{aligned} \tag{6.6}$$

$B(S1_{\text{top}}; S1, AFT)$ is such that in the limit of integer values, it approaches the discrete binomial distribution case. In Fig.6.10, the continuous counterpart of the binomial distribution from some combination of $(S1, AFT)$ is shown in blue, while the discrete binomial distribution is shown in orange. It is possible to see in the first panel that in the case of an integer $S1$, the two curves intersect each other for integer $S1_{\text{top}}$ as desired.

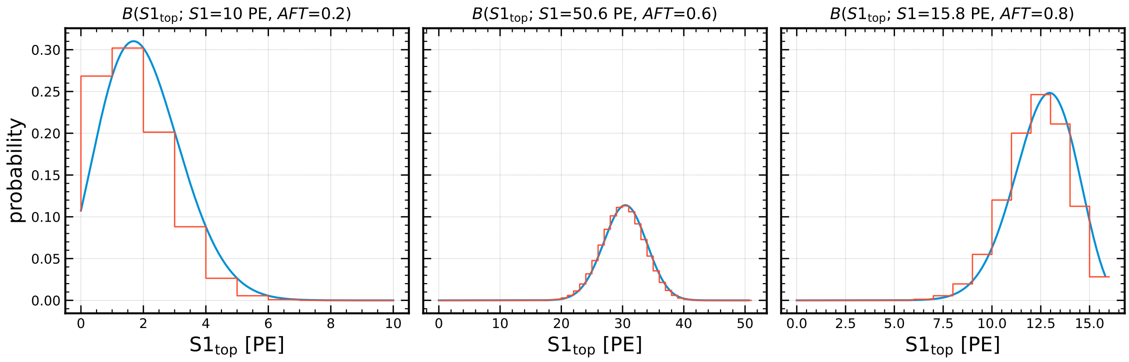

Figure 6.10: Three examples of continuous counterpart of binomial distribution with blue solid lines and the discrete one in orange. The value used for the distributions is written in the panel's title.

The p-value, on which the cut is based, is computed from the cumulative distribution function $CDF(S1_{\text{top}}; S1, AFT$ implemented in straxen as follows:

$$\begin{aligned} CDF(S1_{\text{top}}; S1, AFT) &= Pr(X >= S1_{\text{top}}) = \\ &= \frac{\Gamma(S1+1)}{\Gamma(S1 - S1_{\text{top}})\Gamma(S1_{\text{top}} + 1)} \int_0^{1-AFT} t^{S1 - S1_{\text{top}} - 1} (1 - t)^k dt \end{aligned} \tag{6.7}$$

The p-value, also called binomial test, is computed for every reconstructed event considering the field distortion corrected position. The binomial test is two-sided whenever possible, namely, whenever a j value exists on the other side of the distribution mode such that $B(j;n,p) = B(k;n,p)$, where k is the observed value. The secant method root-finding algorithm [273] is used to estimate j. In Fig.6.11, some examples of the binomial distribution and p-values as functions of $S1_{top}$ are shown.

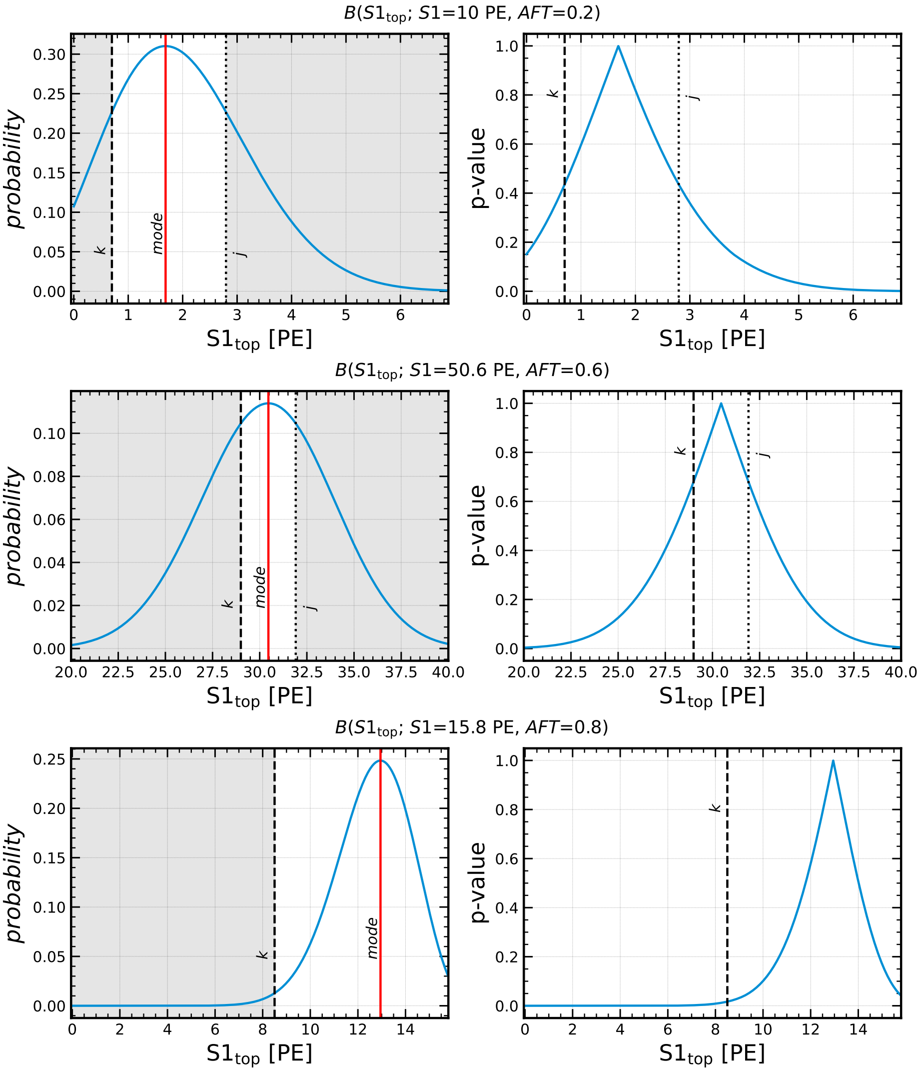

Figure 6.11: Three examples of continuous counterpart of the binomial distribution and the corresponding p-value as a function of $S1_{top}$. The vertical lines represent a random k (dashed black), its correspondent j, and the mode (red). The values of k are chosen randomly, and they are meant to help the reader visualize the secant method and how the p-value is computed. The p-values for the random values k are represented by the gray region.

Data-driven ^{83m}Kr AFT probability map

Ideally, the probability of *AFT* should be derived from TPC optical simulations of xenon scintillation light. However, for the first XENONnT science result, it was decided to use a ^{83m}Kr data-driven *AFT* map. The procedure for generating the map is similar to the relative *LY* map discussed in section 6.2.2. All the SR0 ^{83m}Kr data with the FDC applied were considered. First, the event volume distribution was voxelized, namely, the TPC volume was sliced down with respect to z (48 bins, each ~ 3 cm thick), to r (8 bins, each

$\sim$ 4 cm wide), and the azimuthal angle θ such that the volume of each (z, r, θ) bin was equal. Furthermore, consecutive *z* slices have 90 rotation on the azimuthal angle. The bin statistic was $\geq$ 2000 events which ensures statistical fluctuation below 2 $\%$. Then, the *AFT* probability was extracted for each bin. To do this, the *AFT* frequency histogram was fitted with a Normal distribution. The mean of the Normal distribution was taken as the *AFT* probability of (x, y, z) center of the bin. The discrete map was then interpolated using the cKDTree nearest-neighbor interpolator [274]. Given the (x, y, z, AFT) input points, this interpolator builds a space-partitioning data structure called k-d tree to find the closest *AFT* neighbors points given a (x, y, z) position. The interpolation, shown in Fig.6.12, is used to retrieve the AFT probability for a given position and use it for the p-value calculation.

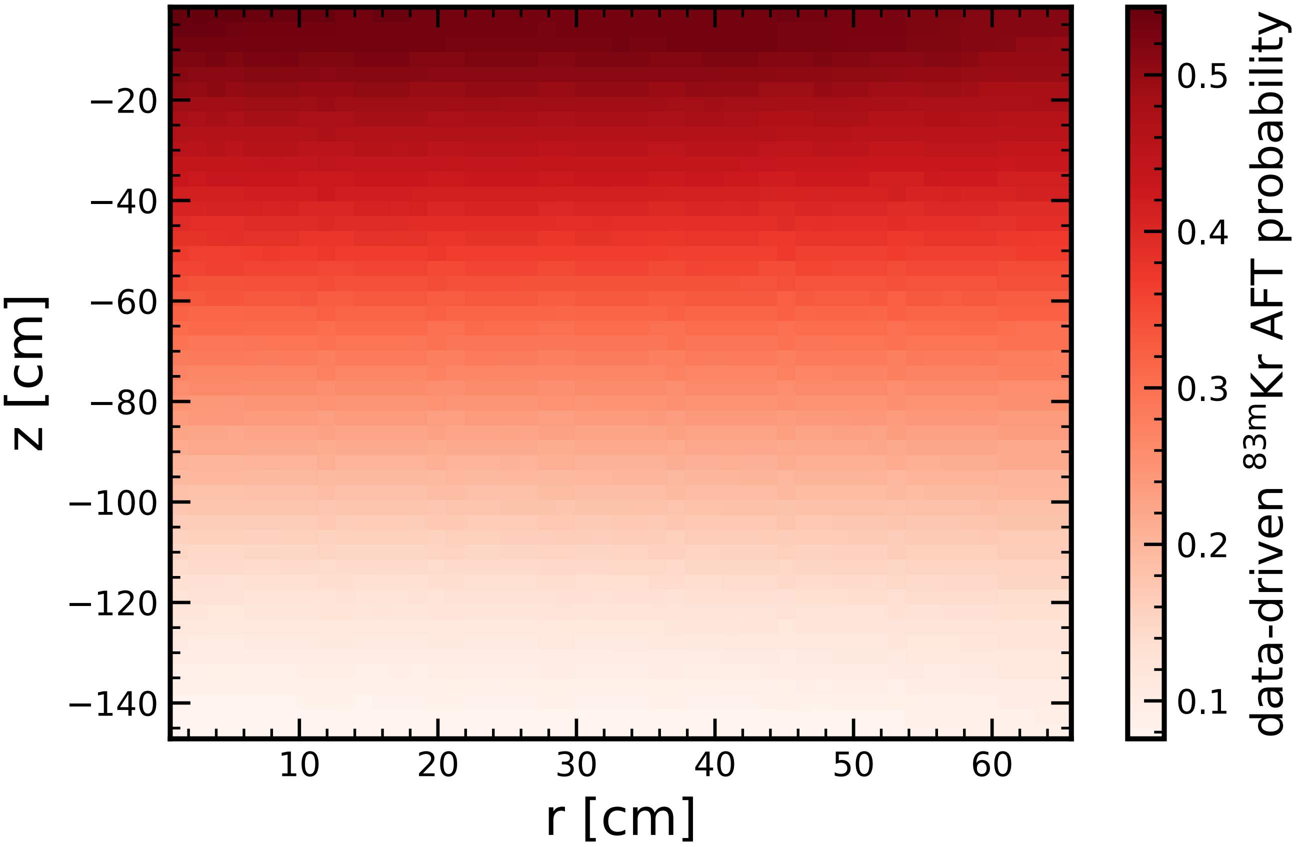

Figure 6.12: Interpolated data-driven AFT probability map from ^{83m}Kr calibration data as function of r and z. The fraction of scintillation light observed by the top PMT array in XENONnT goes from a maximum of ~54 % for shallow events to ~0.9 % for events occurring near the cathode.

The S1 AFT cut definition and performances

The XENONnT data quality is improved by rejecting those (S1, S2) events with a low p-value. The choice of the p-value threshold was informed by the data-driven acceptance study with ^{220}Rn calibration data. Fig.6.13 shows the N-1 acceptance for three p-value thresholds investigated as a function of S1, where the uncertainties were derived using the Clopper-Pearson method [271]. The objective of an acceptance at

$\sim$ 99 % imposed a p-value threshold equal to 0.001. This low limit ensured a flat acceptance on a wide S1 range, with an average value equal to (98 ± 1) %. Once the threshold was decided, the cut acceptance was investigated using the other calibration sources, e.g., ^{37}Ar, for which the acceptance values were consistent with the ^{220}Rn data-driven acceptance.

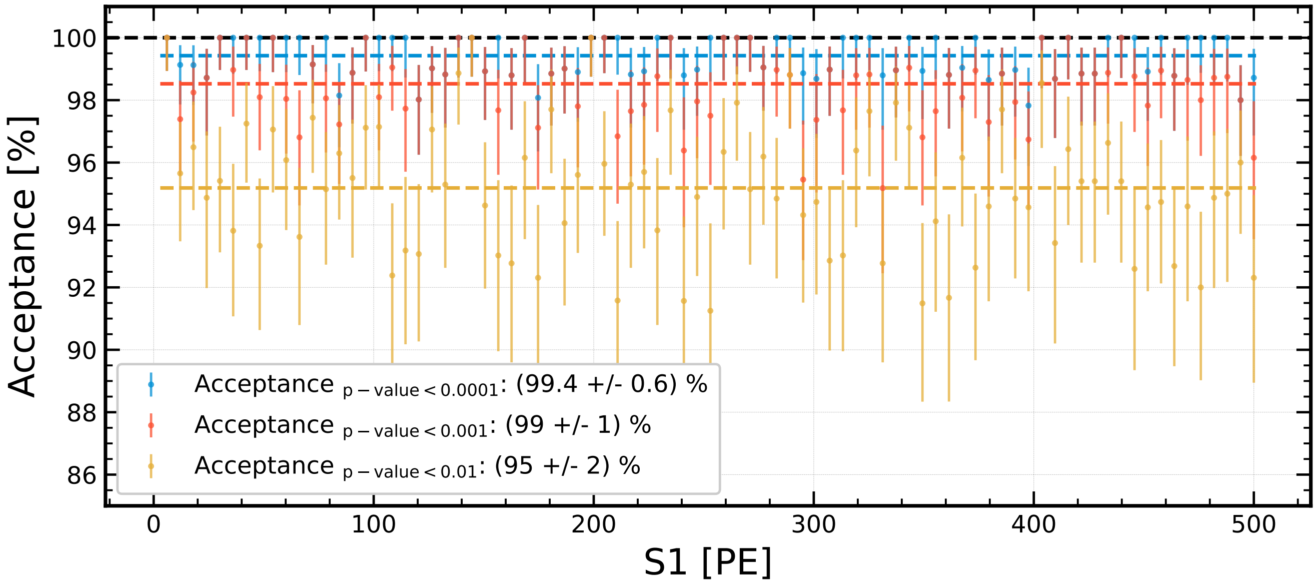

Figure 6.13: Data-driven acceptance of the S1 AFT cut from ^{220}Rn calibration data as a function of S1. Three p-value thresholds were investigated: 0.01 (yellow), 0.001 (orange), and 0.0001 (blue). The average acceptances for S1 < 500 PE are reported in the legend and shown in the plot with the colored dashed lines.

The effect of S1 AFT cut on ^{220}Rn calibration data is shown in Fig.6.14. The survived events are shown in a red-yellow colormap, while the rejected events are presented in a blue-purple colormap. The rejected events lying on the extremes of the main distribution are unreliable, given their low p-value, and they fall into the definition of unphysical. The region delimited in red is associated with AC events. A vertical distribution at $S1_{AFT} \sim 10$ % it is likely due to AC events made by cathode photoionization S1 and random S2. The region delimited in blue instead is associated with unwanted events occurring in the gas phase.

6.3.3 The S1 pattern likelihood cuts

The S1 light pattern discrimination criterion has a long history in the XENON experiment, starting from XENON100 [275]. The data quality criteria that will be presented are built to reject those events that are reconstructed as single S1 and single S2, but which are genuinely multiple scatter events. If the energy depositions of an interacting particle are too close in space and time, the detector won't be able to separate the multiple light and charge signals, and they will be reconstructed as one (S1, S2) pair. However, the associated S1 and S2 hit patterns will likely be inconsistent with single scatter events. The lights will spread more, and the PMTs signal distribution will often have more than one evident pattern. Statistical interpretation of S1 and S2 hit patterns are used in XENONnT to discriminate these events. Particular dangers are those events with one or more scattering sites in charge insensitive volume, for which the reconstructed S2 is smaller. Such events would suddenly appear in the lowest part of the ER band with

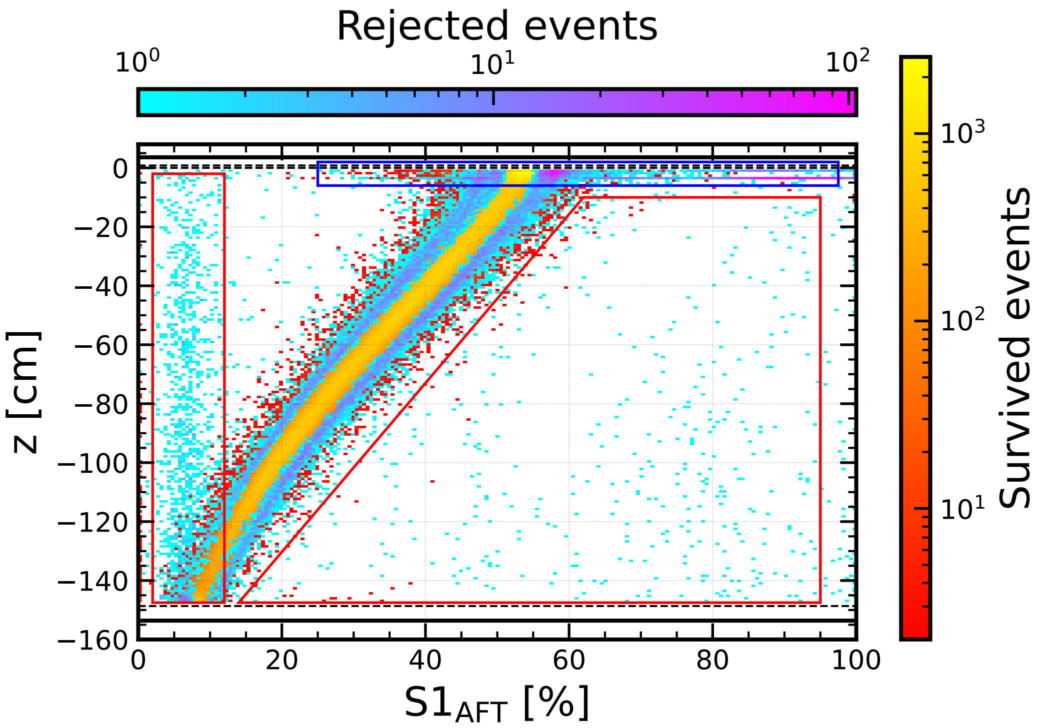

Figure 6.14: Example of the S1 AFT cut on ^{220}Rn calibration data. The surviving events are shown in a red-yellow colormap, while the rejected events are presented in a blue-purple colormap. The rejected population lying on the extreme of the main distribution are unreliable events, given their low p-value, and they fall into the definition of unphysical. The region delimited in red is associated with AC events. A vertical distribution at $S1_{AFT} \sim 10$ % it is likely due to AC events made by cathode photoionization S1 and random S2. The region delimited in blue instead is associated with unwanted events occurring in the gas phase.

the risk of being interpreted as a nuclear recoil. These ER leakage (see section 3.2) are called gamma-X events. While the S2 is not fully collected, the S1 is, and the anomalous pattern can be used to reject them. Similarly, neutrons from detector materials with interaction in the charge insensitive volume – called neutron-X – can be identified and rejected through the signals pattern information.

Several cuts based on the likelihood ratio of the observed S1 pattern and the expected one, derived from optical simulation, were developed in SR0 to reject gamma-X and neutron-X and, therefore, to improve the quality of ER and NR bands and their modeling. Furthermore, the discrepancy between the observation and the expectation proved to be effective in rejecting mis-reconstructed (S1, S2) pairings.

Mathematical description

Given an S1 event occurring at the (x,y,z) position in the TPC, the amount of light observed by each PMT can be described as a Poisson process with mean λ derived by optical simulated light collection efficiency map (see section 6.5.2). The likelihood of a specific pattern, consisting of the observed light per PMT Q, can be computed and compared with a competing distribution where the mean of the Poisson process is equal to the observed light Q. Thus, anomalous S1 light patterns can be rejected based on the likelihood ratio.

The likelihood ratio test is the simplest since the model is completely specified. The Poisson process for the PMT light detection is expanded to the continuous regime using Euler Γ functions. As discussed in section 4.1.1, $\sim 21\,\%$ of the time one detected photon results in two PE. This is accounted for in the PMT detection process by a scaling parameter ξ. Hence, the PMT probability distribution function used is:

$$f(Q,\lambda) = \frac{\lambda^{Q/\xi}}{\Gamma(Q/\xi+1)} e^{-\lambda} \tag{6.8}$$

Considering all the PMTs, the likelihood function is:

$$L(Q|\lambda) = \prod_{\mathrm{i}}^{\mathrm{PMT}} f(Q_\mathrm{i};\lambda_\mathrm{i}) \tag{6.9}$$

As mentioned before, a measurement of the goodness of one statistical model with respect to a competing one can be evaluated using the ratio of their likelihoods. The statistic test is done by comparing the likelihood of a pattern Q given a model λ, to the likelihood of the ideal case where $Q = \lambda$.

$$R = \frac{L(Q|\lambda)}{L(Q|\lambda \equiv Q)} \tag{6.10}$$

Instead of using directly Eq.6.10, it is possible to consider $\lambda_{LR} = -2\log R$. The advantage is that, when every PMT is well illuminated, λ_{LR} approaches a χ^2 distribution with N degrees of freedom equal to the number of contributing PMTs-1. Thus, the λ_{LR} is implemented in straxen as follows:

$$\lambda_{LR} = -2log(R) = 2\sum_{\mathrm{i}}^{\mathrm{PMT}} \left(Q_\mathrm{i} log\frac{Q_\mathrm{i}}{\lambda_\mathrm{i}} + \lambda_\mathrm{i} - Q_\mathrm{i} \right) \tag{6.11}$$

S1 PL cuts definitions and performances

In XENONnT three λ_{LR} are computed: using the total S1 pattern ($\lambda_{LR,total}$), the top array S1 pattern ($\lambda_{LR,top}$) and the bottom array S1 pattern ($\lambda_{LR,bottom}$), and therefore three *S1 pattern likelihood* cut are defined. The reason for having separate statistical tests for the top and bottom arrays is that depending on the event position, one array will have more information and, thus, a better chance of discriminating good events. In an ideal world, the asymptotic relation $\lambda_{LR} \sim \chi^2$ could be used to derive a p-value for each event, and they could be accepted or rejected according to that. However, these cuts are meant for low-energy searches, e.g., WIMP analysis, where only a small fraction of PMTs is illuminated, hence the asymptotic relation does not hold.

In XENONnT SR0, the rejection boundaries were defined on a 99 % quantiles of λ_{LR} distribution as a function of the respective S1. Motivated by the fact that the amount of information carried by λ_{LR} is linked to the number of PMTs contributing to an event, $\lambda_{LR,total}$ cut was also based on the number of contributing PMTs. The ^{220}Rn calibration data were used for cut optimization. The data were previously cleaned, applying basic cuts, and a small fiducialization was considered ($r < 64$ cm and $z \in [-140.5; -4]$ cm) to avoid the edges of the TPC where the optical map was less reliable. After dividing the data into slices, in the parameter space under consideration, the 99th percentiles point was computed and used to fit the empirical function. The resulting functions were used as discrimination criteria, i.e., an event was rejected if above the 99th percentiles limit. In Fig.6.15 is shown the S1 total pattern likelihood cut, defined as the logic sum among the two parameter spaces considered. In Fig.6.16 are shown the S1 top and bottom pattern likelihood cuts.

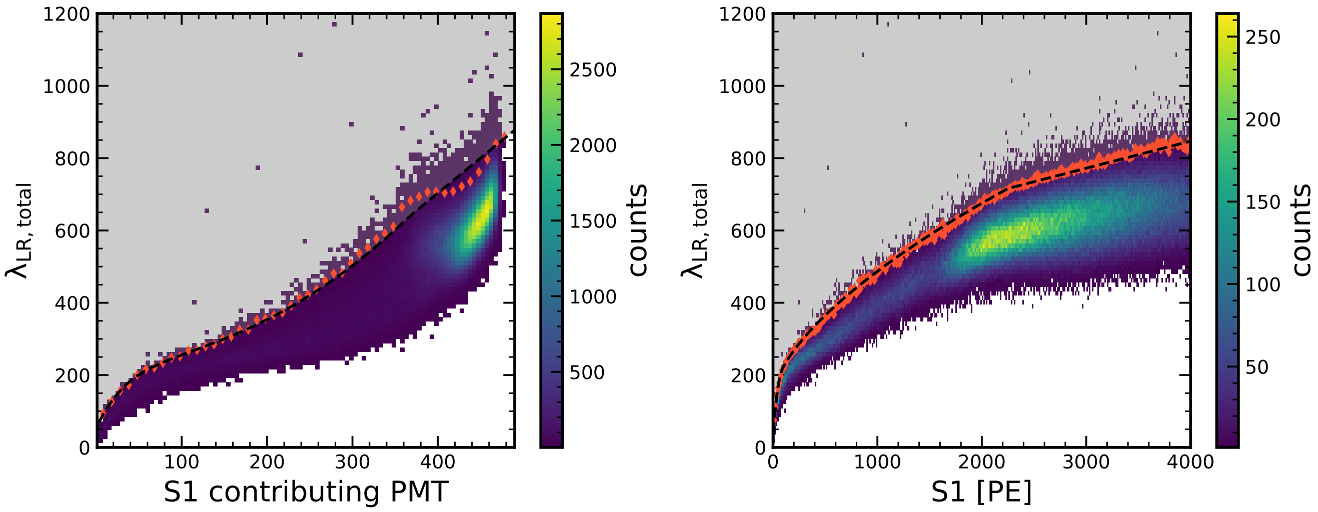

Figure 6.15: The total S1 pattern likelihood cut is the logic sum of the cuts defined as a function of contributing PMTs (left) and S1 area (right). The individual cuts are defined based on the 99th percentiles (red points) of ^{220}Rn calibration data (blue-yellow color map). The percentiles were fitted within the empirical functions (dashed black liens) and used as rejection criteria. The gray regions represent the excluded region by the S1 pattern likelihood cut.

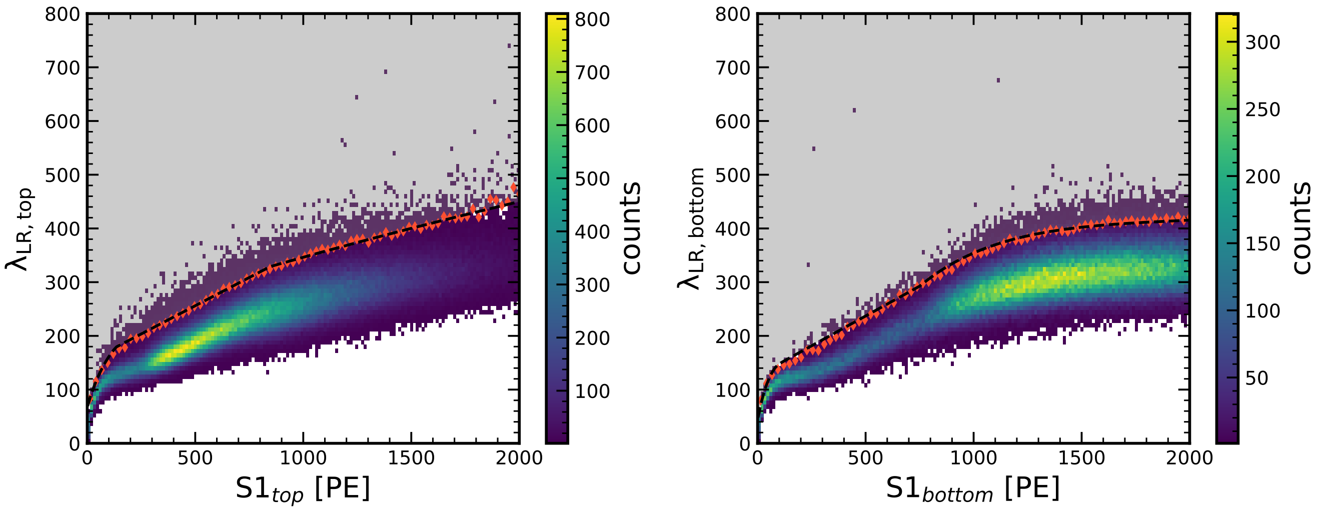

Figure 6.16: The top (left) and bottom (right) S1 pattern likelihood cuts are defined by black solid lines, extracted from the 99th percentiles (red points) derived from ^{220}Rn calibration data (blue-yellow color map). The gray regions represent the excluded region from S1 top pattern likelihood and S1 bottom pattern likelihood cuts, respectively.

The N-1 method was used on ^{220}Rn calibration data to derive the acceptance as a function of S1 size. Similar to the S1 AFT, the Clopper-Pearson method was used to infer the acceptance uncertainties. In Fig.6.17, the acceptances of the three pattern likelihood cuts are shown for S1 $<$ 500 PE. The average acceptances, shown by the colored dashed lines, were $\sim 99\ \%$ as expected by design. Eventually, the $\lambda_{LR,top}$ and $\lambda_{LR,bot}$ were used in the WIMP search and in the low-energy ER analysis since a study on simulated neutron-X and AC events proved that the combination of these two cuts was more effective on rejecting these unwanted population.

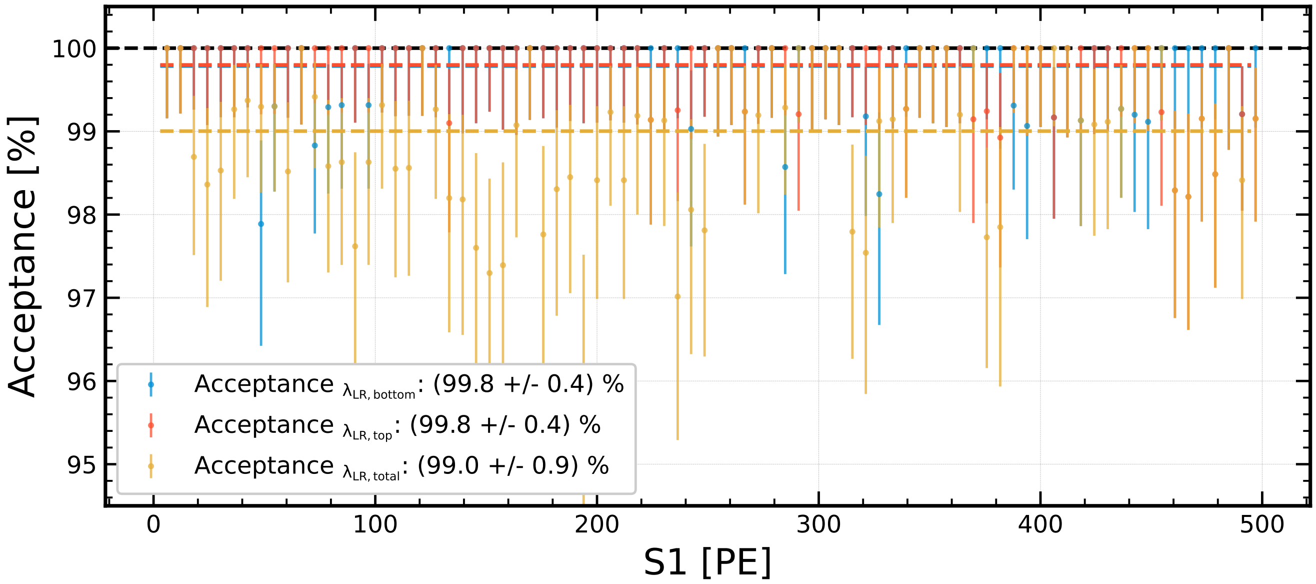

Figure 6.17: Data-driven acceptances of $\lambda_{LR,total}$ (blue), $\lambda_{LR,top}$ (red), and $\lambda_{LR,bottom}$ (yellow) cuts as a function of the S1, derived from ^{220}Rn calibration data. The average cut acceptances for S1 $<$ 500 PE are collected in the legend and shown in the plot with the colored dashed lines.

6.3.4 Total selection efficiency

The total efficiency needs to be considered to interpret the data correctly. This is given by two terms: detection efficiency and selection efficiency. The first depends on the energy threshold and the analysis region of interest (ROI). The WIMP analysis was performed with cS1 $\in$ (0, 100) PE and cS2 $\in$ (126, 12589) PE, equivalent to an energy threshold of $\sim$ 1 keV$_{\text{er}}$ ($\sim$ 3.1 keV$_{\text{nr}}$). The ROI of the low-energy ER analysis instead was (1, 140) keV$_{\text{er}}$ with an S2 threshold of 500 PE. For both analyses, the detection efficiency was governed by the S1 detection efficiency. The ROIs ensure a lower limit on the efficiency of $\sim 10\ \%$, which steeply increases, reaching 100 % above $\sim$ 4 keV$_{\text{er}}$. The impact of the S2 reconstruction efficiency is negligible compared to the S1 detection efficiency: It is expected to be $\sim 100\ \%$ in the energy ranges considered [208, 276].

The selection efficiency is given by the cumulative cut acceptances. A total of 12 cuts were used in the WIMP and the low-energy ER analyses. The final cut acceptances were computed using ^{220}Rn and ^{37}Ar in a 4 tonnes fiducial volume, equivalent to $r < 60.73$ cm and $z \in [-13.6; -134.2]$ cm. Using the N-1 method, the acceptance of individual cuts was evaluated as a function of energy and S1 or S2, depending on which space the cut was defined, and their uncertainty estimate using Clopper-Pearson method [271]. Not all the cuts are included in the total selection efficiency. For cuts that deal with properties unrelated to the event itself, they are deemed as livetime reduction cuts, e.g., time-based cuts. Due to a few different cuts and ROIs, the final acceptances for the low-energy ER analysis and WIMP search are slightly different. The two total efficiencies with the 1σ uncertainty bands are shown in Fig.6.18. The data selections applied in the two analyses are responsible for a efficiency loss of ∼ 20 %. The discontinuity at 10 keV in the total efficiency used in the low-energy ER analysis is because it was derived with the WIMP ROI still-blinded [208]. The decrease at high NR energies in the total efficiency of the WIMP analysis is due to the upper edges of the region of interest [276].

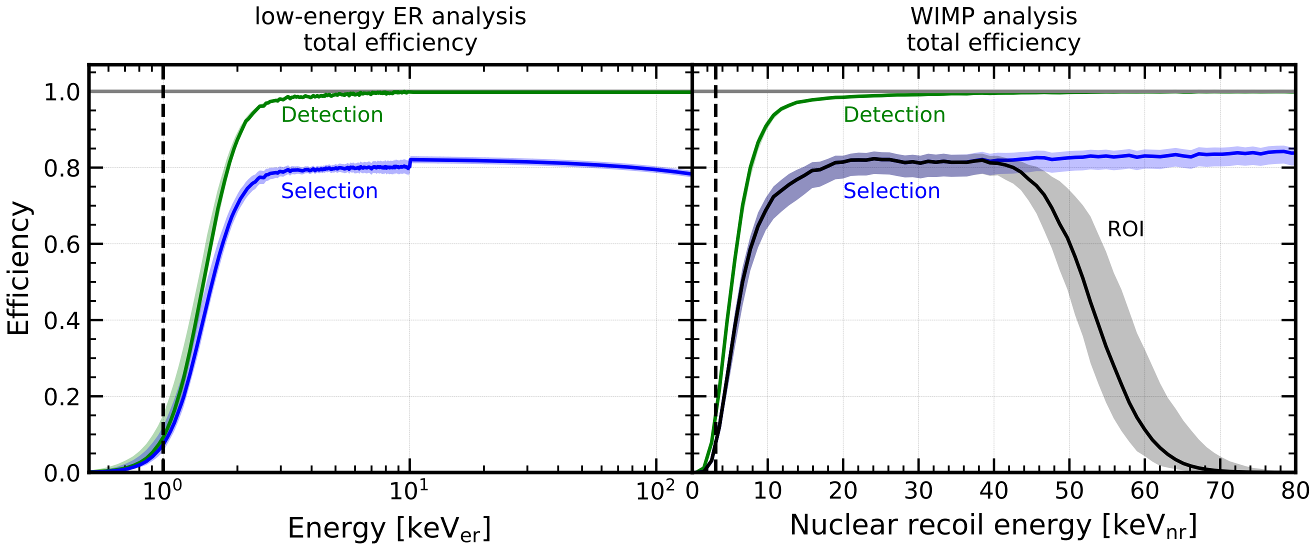

Figure 6.18: Total efficiencies of low-energy ER (left) and WIMP (right) analyses as a function of reconstructed energy expressed in keV$_{er}$ and keV$_{nr}$. The green curves represent the detection efficiency. The blue curves include the efficiency loss due to the data selection in addition to the detection efficiency loss. The black curve in the WIMP efficiency shows the effect of the upper edges of the region of interest. The efficiencies are shown with their 1σ uncertainty band. The black vertical dashed line shows energy thresholds: 1 keV$_{er}$ for the low energy ER analysis and 3.1 keV$_{nr}$ for the WIMP search. Plots reproduced from [208, 276].

6.4 Energy calibration

With the improved data quality thanks to the selection criteria, the anti-correlation of cS1 and cS2 was studied using ^{37}Ar and ^{83m}Kr calibration data, plus the mono-energetic lines from the decay of ^{131m}Xe and ^{129m}Xe, which were produced through inelastic neutron scattering during ^{241}AmBe calibration. The derived charge and light yields are shown in Fig.6.19. The linear fit, shown with a black dashed line, is used to extract g_1 and g_2, defined as the intercepts with the x and y axis, respectively. The detector parameters are found to be $g_1 = (0.151 \pm 0.001)$ PE/photon and $g_2 = (16.5 \pm 0.6)$ PE/electron [208]. As discussed in section 3.1, given the g_1 and g_2 the energy depositions in the TPC by a particle interacting with the xenon can be reconstructed using as $E_{\text{dep}} = W \times (n_\gamma + n_{e^-})$, where $W = 13.7$ eV is used the average energy to produce a charge or light quanta, $n_\gamma = \text{cS1}/g_1$, and $n_{e^-} = \text{cS2}/g_2$. The charge and light yields were also derived from high energy γ lines from radioactive residual in the detector components (1173.2 keV and 1331.5 keV from ^{60}Co [277], and 1460.8 keV from ^{40}K [278]), from the 2.2455 MeV γ events from ^{2}H decay followed by neutron capture on H and the 4.4389 MeV γ events from the carbon de-excitation [260] (see Eq.6.1), both during ^{241}AmBe calibration. However, it has been decided not to consider them in the derivation of g_1 and g_2, to avoid energy bias in the region of interest of low-energy ER analysis.

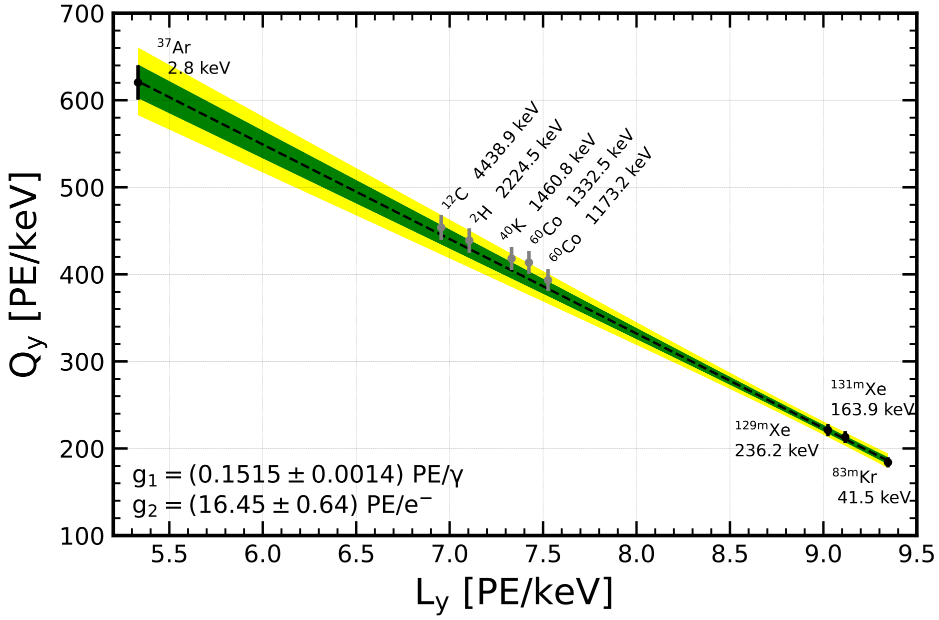

Figure 6.19: The XENONnT SR0 charge and light yields from mono-energetic lines are shown in the panel. The fitted charge and light yield anti-correlation is shown with the dashed black lines, whereas the green (yellow) band represents the 1σ (2σ) model uncertainty. The low-energy data, shown by the black points, have been used to derive g_1 and g_2 detector parameters for energy reconstruction, whereas the high-energy points in grey were omitted.

Next, the energy resolution was derived. Traditionally, the relative energy resolution is computed as σ/μ: the standard deviation and the mean of a Gaussian distribution for each mono-energetic line considered. Then, the energy resolution trend as a function of the reconstructed energy is usually modeled as $\sim 1/\sqrt{E}$, according to a Poisson distribution of the quanta. However, this approach did not replicate the XENONnT observation. This is due to an asymmetry in the peak shape for low-energy lines due to the loss of detection efficiency. Several effects contribute to the loss of detection efficiency: electronic noise, finite detector resolution, under-amplified response of PMTs to photons, and the presence of after-pulses signals. However, the main cause is the DAQ self-trigger threshold, which prevents the recording of low-amplitude PMT signals. The skew Gaussian model [279] showed a better agreement for the mono-energetic line at low energy, whereas no significant skewness was observed at high energy [208]. Therefore, the energy resolution in XENONnT was derived by modeling the shape α - dimensionless - and scale w - units of energy - parameters of the skew Gaussian distribution as a function of the reconstructed energy:

$$\begin{aligned} \frac{w}{E} &= \frac{a}{E} + b \\ a &= c \times E^{(d+1)} \end{aligned} \tag{6.12}$$

where the fitted parameters are $a = (37.2 \pm 0.4) \times 10^{-2}$ keV, $b = (4.36 \pm 0.06) \times 10^{-3}$, $c = (1.999 \pm 0.006)$ keV$^{-(d+1)}$, and $d = (-1.256 \pm 0.002)$.

Having omitted the high-energy lines in derivation of g_1 and g_2 introduced a bias in the energy reconstruction: from $\sim 1\,\%$ at 41.5 keV (^{83m}Kr) up to $2\,\%$ at 236.1 keV (^{129m}Xe). The origin of this bias is given by the DAQ digitization threshold, which deforms the detector response to energy deposition for low-energy events; therefore, an effective approach was utilized in SR0. The energy bias was modeled with an empirical function in reconstructed energy space and propagated into the analyses by reshaping the expected energy spectra [208].

6.5 Optical Monte Carlo-data matching in XENONnT

Most background and signal models, e.g., radiogenic neutron background, derived in the SR0 analysis relied on Monte Carlo (MC) simulations. Every component of XENONnT MC machinery was studied and cross-validated with calibration data to ensure a reliable detector response simulation. Among the different components, the light collection efficiency maps define the fraction of S1 and S2 photons observed per PMT as a function of the event position in the XENONnT simulation chain. These maps, fundamental for PMT pattern simulation and event reconstruction, are based on optical simulations where xenon scintillation photons are homogeneously generated in the TPC volume and propagated until they hit the PMTs or are lost. The fraction of observed or lost photons is influenced by the optical properties of the xenon and surrounding materials. The main optical parameters, e.g., PTFE reflection or light attenuation length in xenon, have been extensively studied in the xenon community. However, they are dependent on the detector conditions, e.g., the polishing and cleaning procedure used in XENONnT for the PTFE panels have an impact on their reflectivity to VUV light, hence the literature values can not be applied easily.

In the context of this thesis work, the XENONnT light collection efficiency map for S1 PMT pattern simulation was derived through a data-MC matching analysis to extract the optimal configuration for the optical parameters. The section is organized as follows: first, a brief description of XENONnT MC software is given, then the methodology for computing the map is presented, and the important optical parameters influencing the photon propagation are discussed. The data-MC matching analysis is outlined at the end of the section.

6.5.1 XENONnT MC framework

The XENONnT MC framework consists essentially of a chain of three packages, where the output of one step is fed to the next. In a nutshell, particle propagation in the detector, interactions, and deposited energies are simulated using the Geant4 toolkit [280, 281], where a precise detector geometry and materials definition are considered. The quanta production followed by an energy deposition is simulated by a custom-made software called EPIX (Electrons and photons instructions for XENON) [282]. EPIX produces the scintillation photons and electrons according to the interaction type, the recoil energy, and the local drift field after applying a micro-clustering algorithm to each of the Geant4 events to group individual energy deposition in the xenon within a radius of $\sim 5\,\mu$m, consisting of the electron-ion thermalization length scale in xenon. This clustering approach reproduces the experimental yields [180, 225]. By default, EPIX uses the light and charge yields from NEST [172]. However, for the WIMP search in SR0, the yield curves derived from the fit of ^{220}Rn and ^{241}AmBe calibration data were used. The last step is the waveform simulator (WFSim) [251], which propagates each quantum (photon or electron) in the TPC for a given field configuration and liquid xenon purity. This includes the conversion of ionization electrons into the S2 light signal, the production of S1 and S2 PMT patterns, and simulating realistic PMT signals for the detected photons combining the SPE probability distribution described in section 5.3.2 with a data-driven SPE waveform. Moreover, the effect of the DAQ, e.g., self-trigger threshold and electrical noise, are simulated. The full chain simulation returns data with a format identical to the real raw records (see section 5.1.2), so they can be identically processed by straxen as done with real data. The flowchart of the full-chain simulation in Fig.6.20 summarises the main steps of the simulation of the XENONnT TPC response. The diagram was taken from [225], where an in-depth and detailed discussion of the XENONnT MC workflow can be found.

6.5.2 Optical simulation

The light collection efficiency (LCE), defined as the fraction of generated photons collected by the PMTs as a function of the photon generation site, is obtained from Geant4 optical simulations. These optical simulations track 175 nm scintillation photons through the detector, considering the geometry and the optical properties of liquid and gas xenon and the surrounding materials, including the photosensors. Given the relative fraction of photons hitting on the PMTs and the detection efficiency, namely the probability that a photon produces a detectable photoelectron signal in the PMT, the photon detection probability g_1' [PE/γ] as a function of (x, y, z) can be derived. The resulting g_1' averaged over the entire TPC volume corresponds to the scintillation gain g_1 used for energy reconstruction. The detection efficiency is partially included in the optical simulation. However, the Geant4 output needs to be corrected for additional PMT effects in order to derive g_1'.

A discussion on the XENONnT geometry and its Geant4 implementation can be found [225, 283]. Several updates were brought during SR0, one of them concerned the PMT photocathode. In the up-to-date XENONnT Geant4 model, the PMT photocathode is implemented considering the quartz window on top of it. When the photon passes from the xenon to quartz volume, Geant4 calculates the reflection and transmission based on Fresnel's law. Once the transmitted photon reaches the photocathode, Geant4 decides whether the photon is reflected, transmitted, or absorbed based on the reflection of thin-layer materials, as described by XMASS PMT model [284]. In the end, the absorbed fraction is corrected according to the quantum efficiency (QE) (see section 4.1.1). Every PMT is treaded individually, using the QE provided by Hamamatsu [213].

The optical simulation output contains detailed information about each event in Geant4, such as which PMT was hit and the trajectory of the photon impinging on it. This information is used to account for the photosensor effect not included in the Geant4 simulations. The corrections applied to the optical simulation output are listed below.

Temperature correction to the QE. A relation between QE and PMT operating temperature has been reported in [285, 286]. The Hamamatsu measurements are performed at room temperature, while the XENONnT PMTs operate at $\sim$ 177 K. At this temperature a ratio of $\overline{\mathrm{QE}_{\mathrm{T_{LXe}}}}/\overline{\mathrm{QE}_{\mathrm{T_{room}}}} \sim 1.1$, has been measured, i.e., 10 % increase of the QE at liquid xenon temperature.

Position correction to the quantum efficiency and collection efficiency (CE) (see section 4.1.1). The correction is inherited from XENON1T. The relative PMT photoabsorption efficiency as a function of PMT radius $f_{\mathrm{corr}}(r)$, provided by Hamamatsu, is used to scale the detection probability [225] (see

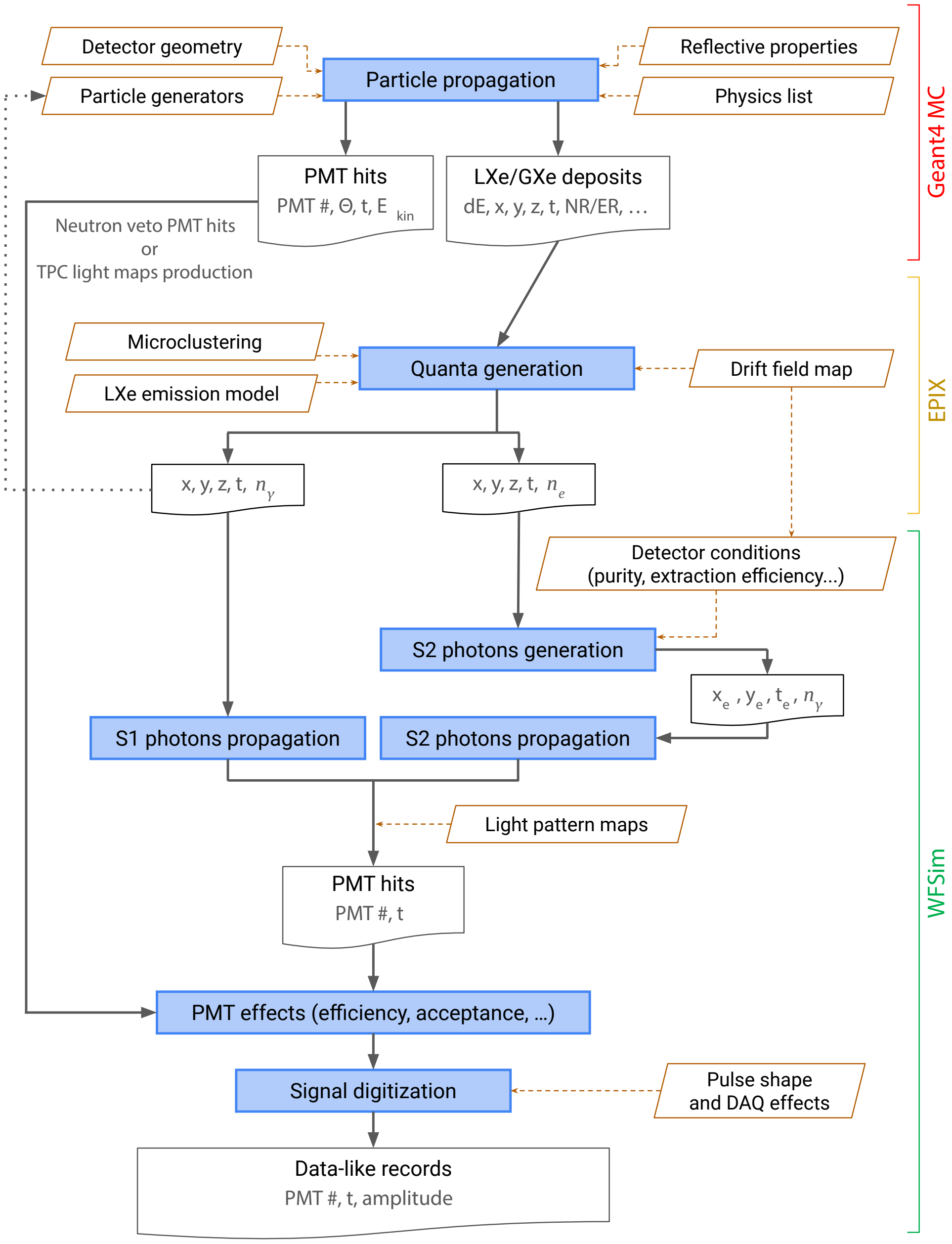

Figure 6.20: XENONnT full chain simulation flowchart with the main packages indicated in the right margin. The particle propagation and interaction in the detector are simulated via the Geant4 toolkit. The precise information about the interactions is used to transform the deposited energy into photons and electrons by EPIX. Eventually, the quanta are processed by the waveform simulator (WFSim), which exports data in a straxen edible format, identical to true data. The diagram has been taken from [225].

Fig.4.2). This correction incorporates both the QE and CE radius dependence, and it is such that it is normalized to the value at $r = 0$. Hence, the actual correction required the multiplication of $\overline{\mathrm{CE}(r = 0)} \sim 0.90$ [227]. The QE and CE have an angular dependence as well. However, no correction is required since it is taken into account directly in the PMT model implemented in Geant4.

Setup correction to the QE due to the method used by Hamamatsu for the measurements. The QE is ratio of the number of photoelectron emitted by the PMT to the number of photons absorbed. It is provided by Hamamatsu, which measures the charge produced directly at the photocathode given a perpendicular incident photon flux, also measured by a standard phototube or semiconductor detector [217]. These measurements, performed at room temperature and vacuum, do not consider the photon reflection at the quartz window. Then the quantum efficiency is underestimated by a factor equal to the perpendicular air-quartz reflection coefficient:

$$\Gamma = \left| \frac{(n_{\text{air}} - n_{\text{quartz}})}{(n_{\text{air}} + n_{\text{quartz}})} \right|^2 \tag{6.13}$$

where n_{air} is 1 and n_{quartz} is 1.59 [287].

In conclusion, the photon detection probability g_1' is derived from the optical simulated LCE map by including the PMT corrections as follows:

$$g_1'(x, y, z) = \frac{N_{\text{detected}}(x, y, z)}{N_{\text{generated}}(x, y, z)} \times \underbrace{\frac{\overline{\text{QE}_{\text{T}_{\text{LXe}}}}}{\overline{\text{QE}_{\text{T}_{\text{room}}}}}}_{1.1} \times \underbrace{\frac{1}{1 - \Gamma}}_{1.05} \times \underbrace{\overline{\text{CE}(r = 0)}}_{0.90} \times f_{\text{corr}}(R) \tag{6.14}$$

The simulated g_1' as a function of (x,y,z) depends on the xenon and the TPC materials, e.g., PTFE, optical properties. The comparison of data-driven g_1' maps with ones derived from the optical simulation was used in SR0 to derive optimal settings for the optical properties, essential for a reliable detector response simulation and efficient position reconstruction. The next section presents the TPC's primary optical parameters for light propagation.

6.5.3 Optical parameters

The propagation of optical photons in the detector is governed by the optical property of the xenon and the surrounding materials. The current optical parameter values adopted in the simulation are the results of knowledge gained during the detector design and the cross-validation of simulation with ^{83m}Kr data-driven LCE map [184, 283].

The amount of scintillation photons observed by the top array depends on the liquid and gas xenon refractive indexes, which define the transmitted and reflected fraction of photons at the liquid-gas interface. The literature measurements assert that the gas xenon refractive index equals one, while the liquid xenon index is larger than unity. Thus, a large fraction of photons from the liquid is reflected back at the interface. There is no commonly accepted value for the liquid refractive index. The published measurements span from $(1.565 \pm 0.002 \pm 0.008)$ [288] to (1.69 ± 0.02) [289]. In XENONnT SR0, the average value of 1.63 was adopted as it was done in XENON1T [151].

The absolute g_1' scale depends on the light attenuation, which consists of scattering and absorption, as explained in section 3.3.3. The scattering length depends on the wavelength of photons, the density of the liquid xenon, and its refractive index [290]. Theoretical calculation and experimental measurements constraint the scattering length between $\sim$ 30 cm to $\sim$ 50 cm [289, 290, 291, 292, 293]. Additionally, xenon scintillation light is very sensitive to impurities. In particular, the light absorption spectra of water overlap with the xenon scintillation spectrum [202]. XENONnT is equipped with water sensors that regularly measure the water concentration of the vaporized liquid xenon circulating from the cryostat. During SR0, the sensors were reading below their sensitivity. Therefore, the water concentration was taken as the minimum readable value: 0.5 ppb (mol/mol). Given the absorption cross-section of water vapor [294], the absorption length λ_{abs} is constrained to be $\geq$ 860 m. The attenuation length is negligible in the gas phase since its small dimension (layer of $\sim$ 8 cm thickness) compared to the expected value given the high purity of the xenon. Thus, as a conservative choice, the same setting for the two phases was taken.

The optical parameters of the reflective PTFE panels are crucial to estimate the number of reflections a photon can undergo before getting lost, its trajectory, and the probability of hitting a PMT. During the detector design phase, studies on the VUV light transmission of PTFE informed on the PTFE thickness (3 mm) to avoid light transmission but not on reflectivity properties [295]. Several PTFE reflectivity measurements are reported in the literature, both in gas and liquid xenon, which suggest up to 99 $\%$ of total reflectivity [296]. However, these values do not directly apply to XENONnT because the surface treatment and the detector condition significantly affect the reflectivity properties. The PTFE reflectivity settings for XENONnT optical simulation were derived by data-MC matching.

Lastly, in the XENONnT Geant4 model, the electrodes are implemented as wires rather than as opaque surfaces as in XENON1T [297]. Hence, their optical property needs to be accounted for in the simulation. The reflectivity values of stainless steel (SS 304) float between $\sim$ 20 $\%$ to $\sim$ 60 $\%$, depending on the exact type and surface [298]. Like in the case of PTFE, the adopted values for the reflectivity of the wires were extracted from the data-MC matching.

6.5.4 Data-MC matching procedure

The XENONnT SR0 LCE map was generated from 2×10^9 photons, homogeneously sampled in (x, y, z) throughout the liquid xenon volume between the top and bottom PMT array. The photon detection probability g_1' was computed from the LCE map by applying the PMT corrections described in section 6.5.2.

The simulation-driven optical properties of the XENONnT TPC were matched to ^{83m}Kr calibration data using a χ^2 fit in 4 parameter spaces simultaneously. These parameter spaces were: g_1', $g_{1,\mathrm{top}}'$, $g_{1,\mathrm{bottom}}'$ and *AFT*, as a function of *z*. The photons detection probabilities $g_{1,\mathrm{top}}'$ and $g_{1,\mathrm{bottom}}'$ were computed considering the photon detected only from the top array and the bottom array PMTs, respectively. The *AFT* was then derived as $g_{1,\mathrm{top}}'/g_1'$.

^{83m}Kr data selection

The matching was performed against the data-driven maps from 32.1 keV events of ^{83m}Kr calibration data, a perfect calibration source for testing spatial detector response, as seen in the previous sections. Using the NEST software [172] and the XENONnT COMSOL Multiphysics® [268] electric field simulation, the number of photons n_γ generated from 32.1 keV β particles was derived. Then, g_1's were computed as $\mathrm{S1}/n_\gamma$ and the *AFT* as $\mathrm{S1}_{\mathrm{top}}/\mathrm{S1}_{\mathrm{total}}$. The values thus obtained were binned in *z*. The median of the distribution of each bin was used in the minimization algorithm and the half-distance of $\pm 1\sigma$ as conservative uncertainty.

Optical simulations generator

A re-weighting approach [299] was used to produce different matching configurations. Starting from an idealized optical configuration, the photon detection efficiency associated with the parameter of interest was rescaled according to the new optical parameter value to produce a new configuration. From every new configuration, the two dimensional distributions of g_1', $g_{1,\mathrm{top}}'$, $g_{1,\mathrm{bottom}}'$, and *AFT* as a function of z were derived. The mean of each z bin was used in the matching process.

The XENONnT Geant4 output file contains which PMT detected a simulated photon, the optical path of the photon in the xenon, and the number of scatters in the PTFE and the wires that the photon undergoes before hitting the PMT. Scaling the *PMT hit weight* associated with these parameters can produce a new matching configuration. For instance, associating PMT hit weight equal to 1 to all events with a certain λ_{abs}, either in gas or liquid xenon, the updated λ_{abs}' configuration can be produced by scaling the weight of $e^{-L(1/\lambda_{\mathrm{abs}}'-1/\lambda_{\mathrm{abs}})}$, where L is the path length of the optical photon.

This re-weighting approach can be used only for processes that do not change the optical path, i.e., it can not generate a new refractive index or scattering length configuration. For this reason, in XENONnT SR0, they were fixed. In addition, the scaling can happen only downwards. Namely, increasing the probability of the process associated with the re-weighting parameter is impossible.

In conclusion, this approach can be used to generate new configurations to fit optical parameters. In XENONnT, using a scaling as:

$$w = \prod_{\mathrm{vol}} e^{-L_{\mathrm{vol}}\left(1/\lambda_{\mathrm{vol,\,new}} - 1/\lambda_{\mathrm{vol,\,gen}}\right)} \prod_{\mathrm{surf}} \left(\frac{R_{\mathrm{surf,\,new}}}{R_{\mathrm{surf,\,gen}}}\right)^{n_{\mathrm{surf}}}, \tag{6.15}$$

where *vol* can be liquid or gas xenon, *surf* can be PTFE or wire (SS), and with *new* and *gen* that represent the update and initial optical configuration, the absorption length λ and the reflectivity R can be estimated.

Data-MC matching results

The liquid xenon refractive index was fixed at 1.63, and the scattering length was 50 cm. Other combinations were investigated, but no significant difference was observed. Given the high purity of the xenon, the fit procedure was insensitive to the liquid or gas absorption length. As described previously, these were fixed to the values suggested by the water concentration (860 m).

The remaining optical parameters were extracted from the data-MC matching, considering the total TPC volume. Compared to Eq.6.14, an additional multiplicative parameter was considered to account for any unknown correction, the impact of which was negligible. Indeed, its best value, equal to (0.99 ± 0.03), is consistent with one. The data-MC matching results are shown in Fig.6.21. The means of the z bins of the two-dimensional distribution of $^{83\mathrm{m}}$Kr data (shown with the color map) are displayed in blue. The simulated XENONnT SR0 light collection information are shown with solid red lines, whereas the results with the previous optical settings are shown in yellow. A significant improvement was obtained in the four parameter spaces compared with the previous optical simulation.

The optical parameters used in the XENONnT SR0 MC framework are summarized in Tab.6.1. The PTFE reflectivity results are reasonable values, considering the measurement performed in similar conditions and similar PTFE treatment. XENONnT PTFE samples are available, which will be used to measure

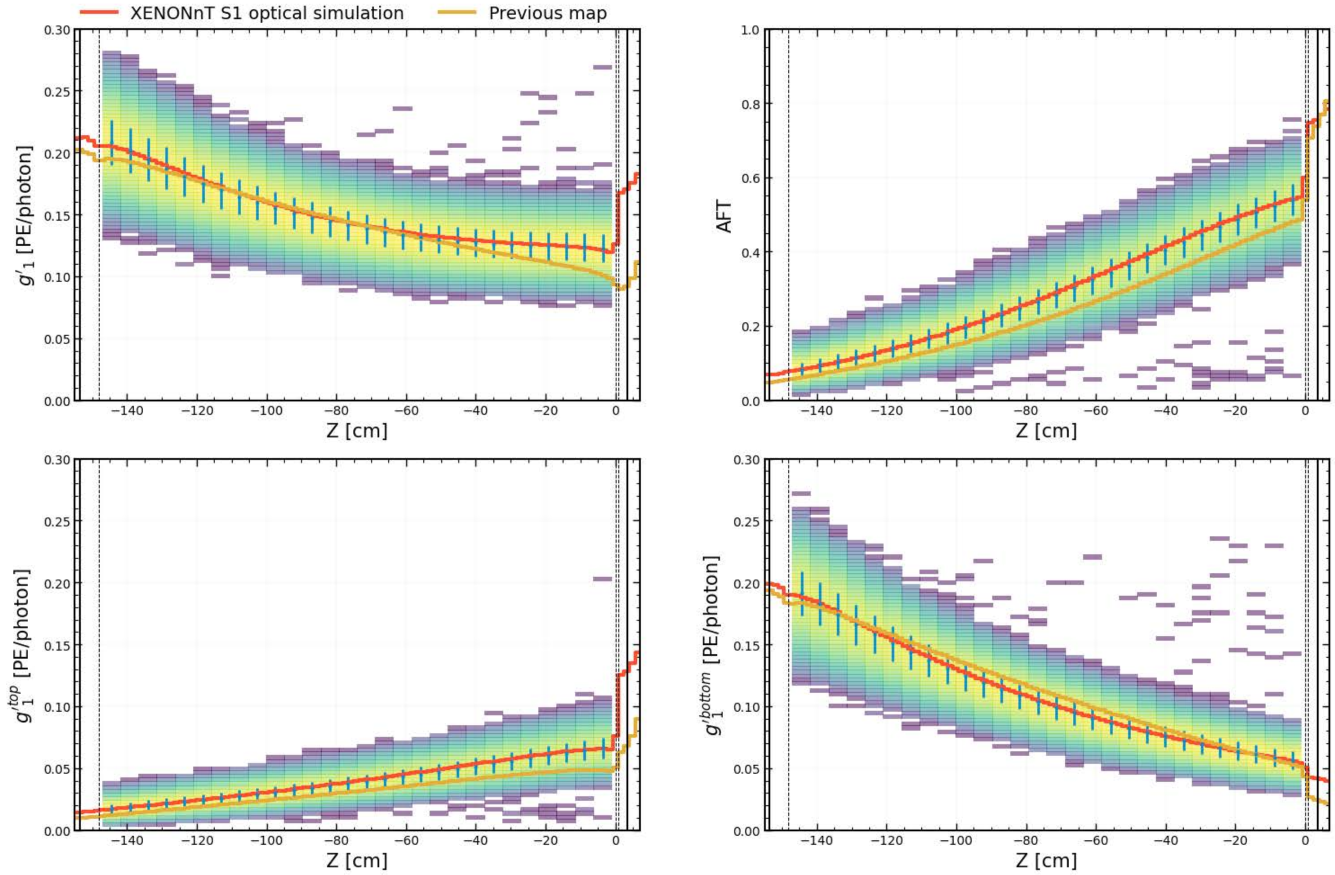

Figure 6.21: Result from data-MC optical matching. The color map represents the two-dimensional histogram of ^{83m}Kr calibration data in g_1', *AFT*, $g_{1,\text{top}}'$, and $g_{1,\text{bottom}}'$ as a function of *z*. The median and the half-distance of $\pm 1\sigma$ of the distribution of each z bin are shown in blue. The XENONnT SR0 results are shown in yellow, while the previous optical simulation is displayed in red. The vertical dashed lines represent, from left to right, the position of the cathode, gate, and anode electrodes, whereas the solid vertical lines are the screening electrodes installed near the PMT arrays.

the reflectivity in liquid and gas xenon, thanks to a dedicated facility at the University of Munster, Germany, (similar to the one used in [295]). Thus, the results obtained in this analysis can be compared with other independent measurements, and the re-weight approach's robustness can be verified. The results for the wire reflectivities are dominated by the fit uncertainties. Given the wire dimensions, their impact on the photon propagation is minimal, making the data-MC matching not sensitive to them.

6.6 Signal and background modeling

So far, it has been shown how the raw waveforms are reconstructed and the event built (section 6.2.1). Then, the detector effect corrections applied on the observed event have been discussed in section 6.2.2, and the XENONnT data quality selections and their efficiency in section 6.3. Lastly, the XENONnT g_1 and g_2 parameters utilized to reconstruct the energy deposition were presented. Moreover, the XENONnT simulation framework used to derive signals and background models has been presented in section 6.5.1. Now, the information for interpreting the physics search data is provided.

Optical parameter	XENONnT optical parameters	Derivation	previous setting
LXe (GXe) refractive index	1.63 (1.00)	From literature	1.63
LXe scattering length	50 cm	From literature	30 cm
LXe/GXe absorption length	$\geq$ 860 m	From water concentration	5000 cm (30 cm)
PTFE-LXE reflectivity	(87 ± 2) %	Fitted	99 %
PTFE-GXE reflectivity	(84 ± 21) %	Fitted	99 %
SS-LXE reflectivity	(19 ± 38) %	Fitted	-
SS-GXE reflectivity	(40 ± 49) %	Fitted	-

Table 6.1: The fitted optical parameters used in the XENONnT Geant4 TPC model and the optical setting used in the previous analysis [151]. No reflectivity of SS is reported for the previous setting since the wires were implemented as opaque disks with 99 % transparency.

First, the low-energy ER and WIMP analysis techniques and the investigated signals are briefly summarized. Then, the primary background sources for these two analyses are discussed. A dedicated section is reserved for detector materials-induced backgrounds.

6.6.1 Low-energy ER and WIMP analysis techniques and the sought-after signals

The low-energy ER and WIMP analyses were performed using the corrected S1 and S2 signals. The choice of fiducial volume was mainly informed by the spatial distribution of the expected background plus the charge insensitive volume estimation. The WIMP search required a tighter fiducialization to minimize the surface backgrounds (see section 6.6.2). The low-energy ER and WIMP fiducial masses were (4.37 ± 0.14) t [208] and (4.18 ± 0.13) t [276], respectively.

Events with S2 > 500 PE and reconstructed energy $E_{er} \in (1, 140)$ keV were used in the low-energy ER analysis. The study models the reconstructed energy spectrum with and without the sought-after signals through an unbinned maximum likelihood fit. As explained in section 3.3.4, the low-energy ER analysis looked for the presence of solar axions, an enhanced neutrino magnetic moment, and bosonic dark matter. The XENON1T signal model for enhanced neutrino magnetic moment and bosonic dark matter was used in XENONnT SR0 [214], whereas the solar axions signal was updated to include the Inverse Primakoff effect [300]. The theoretical energy spectra were converted into reconstructed energy space by accounting for detector efficiency (see section 6.3.4), and they were smeared using a skew Gaussian energy resolution described in section 6.4. The energy bias discussed in section 6.4 was propagated into the expected signals.

The WIMP search was performed with cS1 $\in (0, 100)$ PE and cS2 $\in (126, 12589)$ PE. These ranges correspond to $E_{er} = (0.7, 14.3)$ keV, equivalent to $E_{nr} = (3.1, 60)$ keV. The SR0 WIMP physics search data were interpreted using three-dimensional extended unbinned likelihoods. The parameter spaces considered were cS1, cS2, and the corrected radii of events. As discussed in section 1.3.1, the expected WIMP signal was derived. The differential rate for a given WIMP mass and cross-section was computed using the Standard Halo Model parameters suggest in [27]. The theoretical differential rate was fed into the detector response model, similar to the one described in [184] but optimized for XENONnT conditions in order to derive the (cS1, cS2) expected distribution.

6.6.2 Backgrounds sources

The discussion on background sources, especially the ER components, is kept short since a more detailed discussion is presented later in section 7.2.4.

The radioactive decays of ^{85}Kr and ^{222}Rn constitute the primary ER background sources in XENONnT. The ^{nat}Kr is present in the atmosphere and contains a small isotopic fraction of ^{85}Kr. During the procurement of xenon, extracted from the atmosphere, a residual concentration of krypton mixes with it. Through RGMS measurement of xenon samples, the ^{nat}Kr content was measured to be (56 ± 36) ppq during SR0, making it a sub-dominant background. Assuming ^{85}Kr/^{nat}Kr concentration as 2×10^{-11} (mol/mol) [301], the RGMS measurement can be propagated for constraining the ^{85}Kr activity [208]. Every detector component emanates ^{222}Rn into the xenon target. It is a concerning background due to its β emitter daughter ^{214}Pb. From the study of ^{218}Po and ^{214}Po α-decays, the ^{214}Pb activity is constrained between $(0.777 \pm 0.006_{\text{stat}} \pm 0.032_{\text{sys}})$ µBq/kg and $(1.691 \pm 0.006_{\text{stat}} \pm 0.072_{\text{sys}})$ µBq/kg [208].

The ^{222}Rn is the main background below 40 keV$_{\text{er}}$, while above, the two-neutrino double-beta ($2\nu\beta\beta$) decay of ^{136}Xe becomes the dominant contribution [208]. The measured isotopic abundance in the xenon inventory is equal to (8.97 ± 0.16) % (mol/mol), and it is used to constraint its contribution, assuming the half-life measured by the EXO-200 collaboration [302]. Similarly, the double-electron capture (2νECEC) decay rate of ^{124}Xe can be constrained using the isotopic abundance, equal to (0.101 ± 0.006) % (mol/mol) and assuming the half-life measured by the XENON1T experiment [215]. However, in the low-energy ER analysis, this component was left free to vary without constraint [208]. Other unconstrained backgrounds important for low-energy ER analysis are ^{133}Xe and ^{131m}Xe, from neutron capture of ^{132}Xe and neutron inelastic scattering onto ^{131}Xe during ^{241}AmBe calibration, and ^{83m}Kr from calibration leftovers [208].

A background source important for both ER and NR regions are the neutrinos. The elastic scattering of solar neutrinos on atomic electrons [104] constitutes a background component in the ER region, although not dominant [208]. Solar, atmospheric, and diffuse supernova (DSN) neutrinos contribute to the NR background through CEνNS [103, 104]. These contributions were computed using the standard solar neutrino fluxes and SM cross-sections [303, 304], considering the effect of electron-nucleus binding energy [305], convolved with the detector response. A 10 % uncertainty is assigned to the solar neutrino flux based on the Borexino measurement [306].

The accidental coincidence background from random S1 and S2 pairing concerns both ER and NR regions [208, 276]. It mainly affects the NR analysis since the distribution in (cS1, cS2) parameter space partially overlaps with the NR band. However, due to the low drift field condition, the AC distribution extends also in the ER region. The AC model is data-driven, constructed using unpaired S1s and S2s samples from the physics data and randomly paired to build a high-statistics artificial data. The AC model was validated against calibration data, e.g., ^{222}Rn and ^{37}Ar. A conservative 5 % uncertainty on the expected rate was derived from the validation.

The surface background are events happening near the TPC wall, originating from the ^{222}Rn progeny plated out on the inner surface of the PTFE panels. These background events tend to lose a fraction of their charge in the PTFE panels, resulting in a low charge-to-light ratio that might be misidentified as a nuclear recoil. Furthermore, this loss of charge close to the wall leads to inwards bias in the position reconstruction, causing the leaking of these events into the fiducial volume [93]. This type of background is important for NR searches. In XENONnT a data driven approach using ^{210}Pb and ^{210}Bi events, from the ^{222}Rn decay chain, was used to derive the (cS1, cS2, r, z) distribution. The wall model was validated using the not-blinded physics search data below the NR band and with cS1 < 100 PE [276].

The neutrons constitute the most dangerous background for the WIMP searches since their interaction features resemble the ones expected from WIMPs. They are produced by spontaneous fission or (α, n) reactions in detector materials or cosmic muons interacting in the rock and concrete surrounding the detector. The cosmogenic neutrons are suppressed using the veto system, while the radiogenic neutrons require careful modeling. The estimation of neutron yields and energies originating from various detector materials is based on the *full chain simulation* described in 6.5.1. The full chain simulation was tuned using the neutron events from ^{241}AmBe calibration data. Then, similar to [151], the material radioassay results [201] were used as input in full chain simulation to calculate the energy and spatial features of the radiogenic neutron background. The prediction was tested on a multiple scatter population in the physics search data. The data-driven and simulation-driven predictions did not agree: the simulation predicted a factor $\sim$ 6 smaller contribution, most likely due to underestimation of radionuclide concentration in the detector materials. The origin of this discrepancy is an object of study in the collaboration. Following the analysis plan, the data-driven rate estimate is used in the WIMP search [276].

6.6.3 Review of radiogenic ER material background prediction

Gamma radiations from the decay of long-lived radionuclides contained in the materials of the detector contribute to the ER background budget via Compton interactions in the active target. While the X-rays are efficiently suppressed thanks to the active shielding property of xenon, the higher energetic γ-rays have high penetration length and can leak into the inner region of the TPC. The evaluation of their contribution is fundamental for background prediction.

Following the same approach as in [307, 225], the decay of the radioactive isotopes and their daughters were simulated using the Geant4 software. For each combination of material and radionuclide, $\mathcal{O}(10^{8\div9})$ parent nuclei were simulated uniformly within the respective detector component. As described in section 3.3.3, the concerning radioactive isotopes are ^{238}U, ^{235}U, ^{226}Ra, ^{232}Th, ^{228}Th, ^{40}K and their progenies, as well as ^{60}Co and ^{137}Cs. Almost all the simulations were already performed for the XENONnT projection study [151], except for the ^{238}U nuclide. Due to incorrect treatment of the decay chain in the Geant4, the simulations needed to be recreated. Due to time constraints, simulations were redone for detector components with the highest contamination, namely the cryostats and the PMTs.

Geant4 outputs were processed using custom software called nSort, inherited by XENON1T. nSort processes the simulated Geant4 events, merging subsequent energy depositions based on a data-driven single-to-multi-site spatial resolution map. Therefore, the single site population can be selected based on the number of energy clusters. Since the low-energy ER analysis and the WIMP search are performed with single-site energy deposition events, the spatial resolution map is fundamental for deriving a reliable material background. At the stage of these analyses, this map was not yet derived. The knowledge from XENON1T was used. However, using the not-validated map had a low impact on the ROIs of the analyses since only single-site events are expected at energies $\leq \mathcal{O}(100\ \text{keV})$, as it will be shown in section 7.1.3.

The single-site events occurring in the low-energy ER fiducial volume were then selected, and their energy spectrum was smeared using the XENONnT energy resolution described in section 6.4. The smeared energy spectrum was normalized according to the equivalent simulated time T_{eff}, namely the time needed for the number of simulated events N_{sim} to occur in a real detector, computed as follows:

$$T_{\text{eff}} = \frac{N_{\text{sim}}}{M_c \times A_c}, \tag{6.16}$$

where M_c and A_c are, respectively, the component mass considered and its specific activity (Bq/kg) of the parent nuclei. Therefore, the expected rate is given by:

$$r = \frac{N_{\text{ss}}}{T_{\text{eff}} \times M_{\text{fv}} \times \Delta \text{E}}, \tag{6.17}$$

where N_{ss} are the simulated events reconstructed as a single-site occurring in the selected fiducial volume, M_{fv} is the liquid xenon mass inside the fiducial volume, and ΔE is the analysis ROI.

For the specific activity A_c, the radioassay results from XENON1T and XENONnT screening campaign were used [307, 225, 201]. The activities were updated considering the radionuclides decayed from the screening day until the beginning of the SR0 (May 1st, 2021). The activities were then scaled according to the exponential decay law, besides for ^{226}Ra and ^{228}Th. These two radionuclides belongs to ^{238}U and ^{232}Th decay chains, respectively. Therefore, as the ^{226}Ra and ^{228}Th nuclei decay, they are produced again by the decay of the parent nuclei. This was considered in the analysis using the Bateman [308] equation for the activity evolution. The A_c used for normalizing the material background are summarised in table Tab.6.2. If no activity above the background was found in the radioassay, an upper limit at 90 % confidence level was given. As a conservative choice, this was used to normalize the relative spectrum. The error on the specific activity can be propagated, through the T_{eff}, into the expected energy spectrum and used to constrain the material backgrounds. A detailed review of XENONnT material backgrounds can be found in [307, 225].

The radionuclide most affected by the time elapsed is ^{60}Co since it has a half-life (5.3 years [277]) comparable to the livetime of the experiment. Although the ^{60}Co concentration has decreased compared to screening measurement, it remains one of the most abundant radionuclides in the materials, especially in the stainless steel cryostats, making it the dominant contributor, followed by ^{40}K. Similar to [208], the total material energy spectrum in the low-energy ER fiducial volume can be considered flat below 140 keV with an average rate estimated as (2.4 ± 0.4) events/(t × yr × keV).

		specific activity A_c [μBq/kg]							
Component	Mass [kg]	^{60}Co	^{137}Cs	^{40}K	^{226}Ra	^{228}Th	^{232}Th	^{235}U	^{238}U
Cryostat vessels	1169	3.1(0.4)	0.36(0.02)	2.11(0.7)	0.6(0.2)	0.3(0.3)	0.3(0.2)	0.4(0.3)	3(3)
Cryostat flanges	640	12.2(0.4)	< 1	< 5	< 4	0.21(0.08)	0.4(0.1)	0.06(0.03)	1.4(0.6)
Bell and electrodes$^{(1)}$	112	1.0(0.2)	0.17(0.02)	1.6(0.6)	0.5(0.2)	0.3(0.3)	0.3(0.2)	0.6(0.3)	3(2)
PTFE$^{(2)}$	56	//	< 0.03	2(1)	0.06(0.03)	0.1(0.1)	0.08(0.04)	< 0.06	0.12(0.1)
Copper$^{(3)}$	455	0.02(0.03)	< 0.02	0.3(0.3)	< 0.02	0.03(0.05)	0.03(0.05)	< 0.3	0.80(0.01)
PMTs and bases$^{(4)}$	98	0.57(0.06)	0.15(0.09)	1(3)	0.5(0.6)	0.4(0.2)	0.30(0.09)	0.4(0.1)	9(3)
nVeto PMT windows	113	< 1.67	< 6.91	750(70)	525(20)	555(40)	531(40)	30(8)	525(150)

Table 6.2: Radioactivity levels in μBq/kg adopted in the XENONnT SR0 for the detector components, with uncertainties in parenthesis. Upper limits are given at 90 % confidence level. The activities are averaged by mass over all the individually simulated sub-components. $^{(1)}$SS diving bell and SS frames of the electrodes. $^{(2)}$TPC pillars, blocking and sliding reflector panels, and PMT holders. $^{(3)}$Support structure of the PMT arrays, support rings of the TPC, and inner and outer field shaping rings. $^{(4)}$The total mass corresponds to 494 PMTs and PMT bases.

6.7 Results

Both analyses used the full SR0 physics search data, which consists of 97.1 days. Given the slight difference in data selection used for the WIMP search compared to the low-energy ER analysis, the livetime of the first one decreased to 95.1 days. As described in section 6.6.1, the estimated fiducial masses are (4.37 ± 0.14) tons [208] and (4.18 ± 0.13) tons [276] for the low-energy ER analysis and WIMP search, respectively.

The ER and NR blinded regions were unveiled in two different periods. The ER band was revealed in July 2022 after validating the detection performances, e.g., efficiency, resolution, and acceptance as a function of the reconstructed energy. Before that, the ~ 14.3 days of tritium-enhanced data were unblinded, showing no evidence of a tritium-like excess. Therefore, the tritium was not included in the low-energy ER background model [208].

The unblinding of the NR region occurred subsequently as soon as both recoil models showed good agreement with the calibration data. The ER band fit was done using ^{220}Rn and ^{37}Ar calibration data, whereas the NR band model was derived by fitting the ^{241}AmBe calibration data. Both fits were performed within the WIMP ROI [276]. The band models are necessary to derive the micro-physics model that governs the scintillation process in the detector, from which the WIMP expected signal is derived. In Fig.6.22, the XENONnT SR0 ER and NR bands in the (cS1; cS2) parameter space, extracted from calibration data, are shown. The solid lines represent the median, while the dashed lines delimit the $\pm 2\sigma$ region [276]. As discussed in section 3.2, the ER band fraction below NR-mean is often used to characterize the sensitivity for liquid xenon TPC: a larger leakage fraction means larger ER backgrounds in the region where WIMP signals are expected. From the data-driven ER and NR band, the ER leakage was found to be $\sim 10^{-2}$ for cS1 smaller than 100PE, corresponding to a discrimination power of ~ 99 % [309].

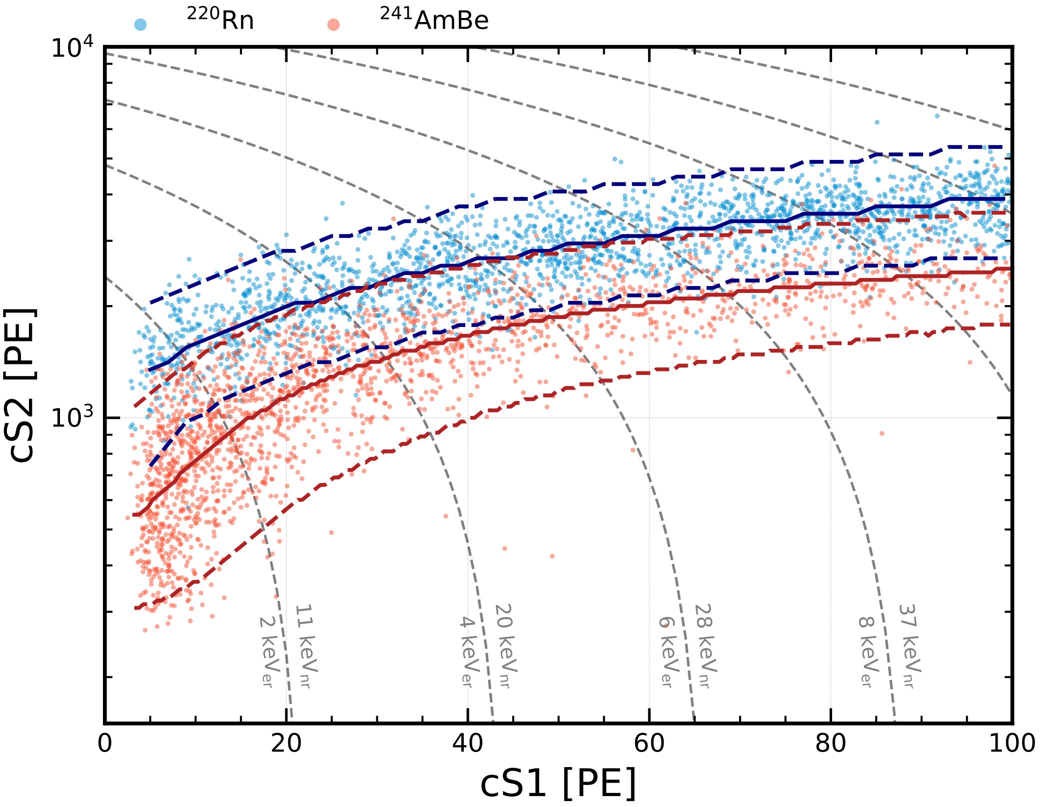

Figure 6.22: In blue the ^{220}Rn calibration data used for ER detector response characterization are shown, where in red the ^{241}AmBe calibration employed for NR detector response characterization are displayed. The solid lines represent the median response, while the dashed line delimits the $\pm 2\sigma$ region. After accounting for the signal quenching, the gray dashed lines show the ER energy scale and the equivalent NR.

6.7.1 Low-energy ER analysis results

The unbinned maximum likelihood fit in reconstructed energy space was performed by keeping the NR region below ER median -2σ blinded. The result of the background-only fit is shown in Fig.6.23, and the fit values are collected in Tab.6.3, as well as the constraints applied in the likelihood minimization. No evidence of an excess above the background was found. Hence, the 90 % confidence level upper limits on solar axions, an enhanced neutrino magnetic moment, and bosonic dark matter signals were estimated from the background-only result [208]. The tritium hypothesis was also tested with the SR0 physics search data, and, like for the TED data, no evidence for ^{3}H was revealed.

6.7.2 WIMP search results

As seen in section 6.6.1, the SR0 WIMP physics search data were interpreted using an extended unbinned likelihoods in (cS1, cS2, *r*), where *r* is the radius of the reconstructed event. Each background and signal distribution were defined and normalized in this three-dimensional space. The likelihood includes two science data terms, one for the events reconstructed within 4.45 cm from the perpendicular wires (on-wire region) and one for the rest (off-wire region) [276]. Similar to [184], the likelihood includes a calibration

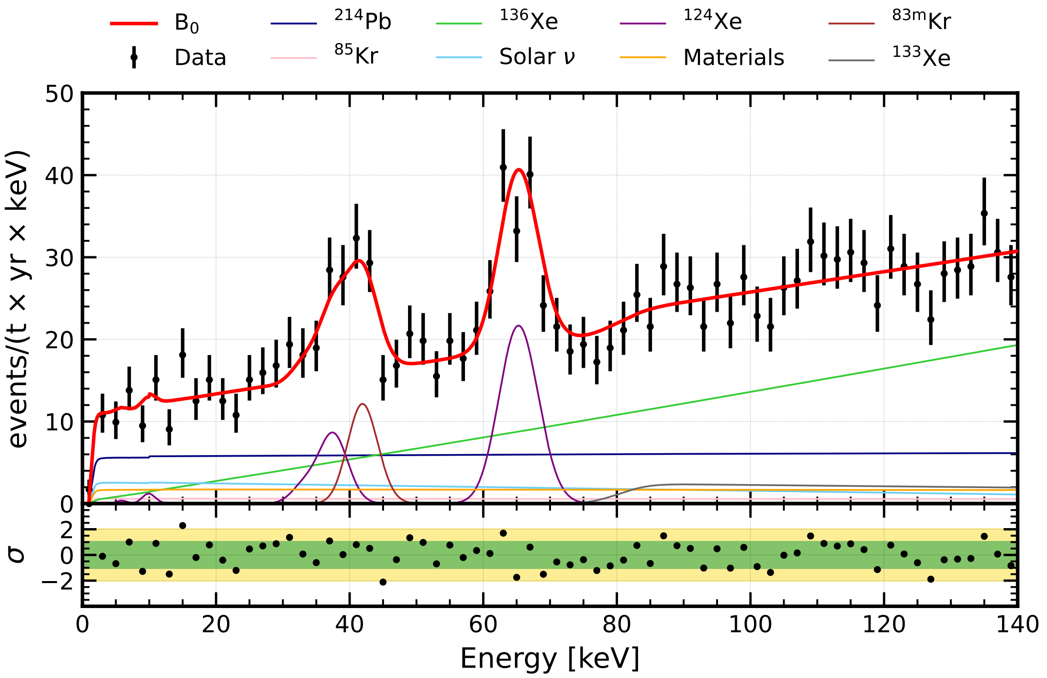

Figure 6.23: In black the reconstructed energy spectrum of SR0 physics search data used in low-energy ER analysis are shown. The background-only fit B$_0$, the results of the sum of the components listed in the legend, is shown in red. The subdominant AC background is not shown. Plot reproduced from [208].

Component	Constraint	Fit
^{214}Pb	(570, 1200)	960 ± 120
^{85}Kr	90 ± 60	90 ± 60
Materials	270 ± 50	270 ± 50
^{136}Xe	1560 ± 60	1550 ± 50
Solar ν	300 ± 30	300 ± 30
^{124}Xe	-	250 ± 30
AC	0.70 ± 0.04	0.71 ± 0.03
^{133}Xe	-	150 ± 60
^{83m}Kr	-	80 ± 16

Table 6.3: Low-energy ER analysis fit constraint and the result of the background-only fit for each component in (1, 140) keV. Table reproduced from [208].

term that runs over the ^{220}Rn calibration data. This is meant to constrain the ER band shape. Lastly, several terms are constrained by independent measurements, e.g. AC expectation value, and these are implemented as auxiliary Gaussian terms in the likelihood. Further details on the analysis approach can be found in [276].

The profile log-likelihood ratio, identical to the one used in the XENON1T WIMP search analysis [184], was used as the test statistic for both testing signal hypothesis and for determining the confidence interval. The inference procedure was decided before the unblinding. As suggested by the dark matter community [310], only the upper edge of the confidence interval would be reported unless signal evidence above 3σ is present in the data. Due to the low event rate, the test statistic distribution is obtained using simulated datasets, where both the science and calibration were drawn from their model distributions. The confidence intervals are constructed using the Feldman-Cousins approach [311].

Several signals from a wide range of WIMP masses were tested against the background-only hypothesis. The DM search data in (cS1, cS2) parameter space used in SR0 are shown in Fig.6.24. The spatial distribution can be found in [276]. The shaded regions represent the background components. The contour region of a 200 GeV/c^2 WIMP signal is also shown for reference.

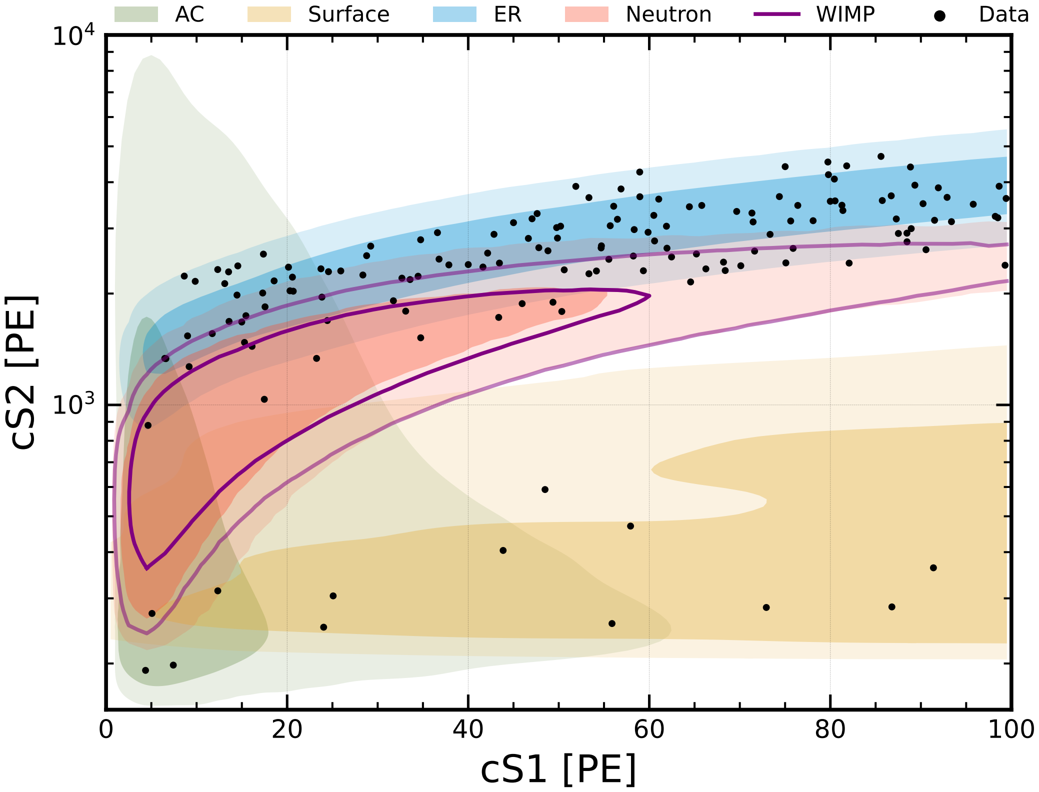

Figure 6.24: XENONnT SR0 data used WIMP search are shown as black points. The 1σ (dark) and 2σ (light) expected background regions are shown as reported in the legend. The color scheme follows the legend. The solid purple lines represent the 1σ and 2σ contour level for the expected signal from a 200 GeV/c^2 WIMP. Plot reproduced from [276].

The signal strength was derived from the likelihood fit for each WIMP mass considered. In Tab.6.4 the number of events predicted for each background according to the best fit of the 200 GeV/c^2 WIMP hypothesis are collected. None of the tested WIMP signals were statistically significant [276].

Therefore, an upper limit is placed on the spin-independent WIMP-nucleon scattering cross-section at 90% confidence level [276]. To avoid limits better than the expected sensitivity due to large background downward fluctuations, the limits are constrained following [312]. A conservative rejection power threshold of 0.5, corresponding to the median unconstrained limit, was used in the SR0 WIMP search. The

Component	Constraint	Fit
ER	134	135^{+12}_{-11}
Neutron	$1.1^{+0.6}_{-0.5}$	1.1 ± 0.2
CEνNS	0.23 ± 0.06	0.23 ± 0.06
AC	4.3 ± 0.2	4.32 ± 0.15
Surface	14 ± 3	12.0^{+0}_{-4}
Total Background	154	152 ± 12
200 GeV/c^2 WIMP	-	2.4
Observed		152

Table 6.4: Expected number of events according to the likelihood fit for events with cS1 $\in (0, 100)$ PE and cS2 $\in (126, 12589)$ PE. These numbers are valid for the SR0 lifetime. The constraints applied in the fit are shown with the expected counts for the background component. The best-fit result for a 200 GeV/c^2 WIMP is shown as well. The local discovery significance, p=0.07, is not significant [276].

XENONnT constrained (unconstrained) limits derived in SR0 are shown in Fig.6.25 with solid (dashed) black line, together with the 1 and 2σ sensitivity band. As a comparison, the limits from LZ [90] collaboration and PandaX-4T [92] collaboration, as well as the XENON1T limit [93], are shown. The lowest 90 % CL upper limit achieved with SR0 is 2.58×10^{-47} cm^2 at 28 GeV/c^2, for masses above $\sim$ 100 GeV/c^2, the limit is 6.08×10^{-47} cm$^2 \times (m_{\mathrm{WIMP}}/(100\mathrm{GeV/c}^2)$.

As presented in section 1.3.1, WIMPs may couple to the nuclear spin. Following the procedure of [313], the spin-dependent interaction was investigated, assuming couplings to either protons or neutrons in the nucleus. No significant excess above the background was observed, and similar to the spin-independent search, a 90 % CL upper limit on the coupling strengths as a function of WIMP masses was set. The limits are collected in [276].

6.8 Conclusions

The reported results of the first ER and NR blinded analysis of XENONnT science run 0 proves that sensitive beyond standard model searches can be performed with the XENONnT detector, even though the TPC was not operating at the design configuration. A good understanding of the detector response was achieved. The improved simulation software was essential for this goal, thanks to which a fast and complete detector characterization was possible.

The blind search of new physics in the low-energy ER region shows no excess above the background, excluding the beyond SM interpretations of the XENON1T excess. Upper limits at 90 % confidence level on solar axions, bosonic DM models, and solar neutrinos with an enhanced magnetic moment were set. Additionally, the presence of tritium on top of the background-only hypothesis was rejected. The

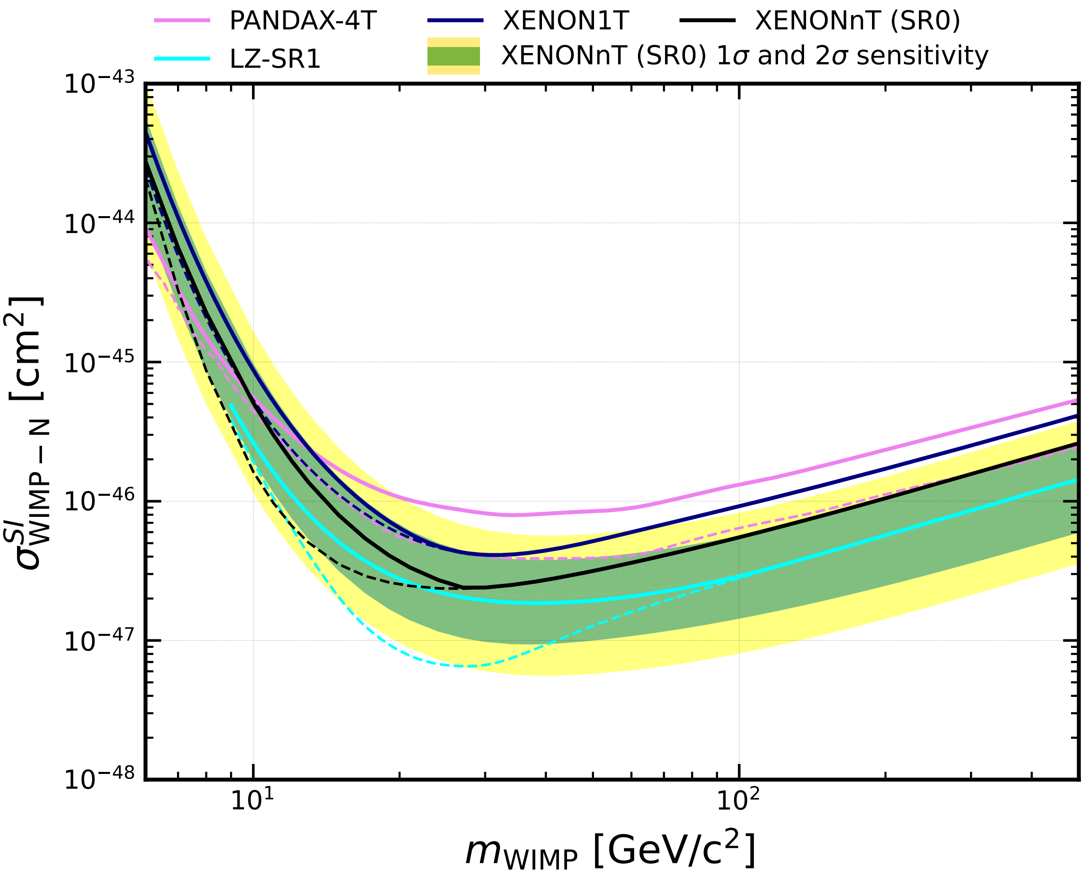

Figure 6.25: The XENONnT constrained SR0 90 % (CL) upper limit on the cross-section of WIMP-nucleon spin-independent elastic scattering is shown with the solid black line, whereas the dashed line represents the unconstrained limit [276]. The green-yellow band shows the 1σ and 2σ distribution of 90 % median sensitivity according to the background-only fit result. As a comparison, the limits from LZ [90] collaboration (cyan) and PandaX-4T [92] collaboration (violet), as well as the XENON1T limit [93] (blue), are shown.

5.8×10^{-26} (mol/mol) tritium concentration was excluded at 90 % CL [208]. The average measured ER background rate within (1; 30) keV$_{\mathrm{er}}$ is (15.8 ± 1.3) events/(t × yr × keV$_{\mathrm{er}}$ [208], a factor ∼ 5 lower than the predecessor XENON1T [214]. Among dark matter direct detection experiments, XENONnT achieved the lowest background rate in this energy range. This result was made possible thanks to the meticulous selection of each detector component and the suppression of the ^{85}Kr and ^{222}Rn levels by the upgraded xenon purification system. For the first time, the ER spectral shape is mostly determined by $2\nu\beta\beta$ decay of ^{136}Xe and 2νECEC decay of ^{124}Xe, two second-order weak processes. In addition, focusing on energies below ∼ 10 keV$_{\mathrm{er}}$), the elastic scattering of solar neutrinos on atomic electrons constitutes the second largest background component after the ^{214}Pb.

For the WIMP search, also performed in a blinded fashion, the best fit to the SR0 data is compatible with the background-only hypothesis. The WIMP discovery p-value indicates no significant excess, leading to 90 % CL upper limits on the WIMP-nucleon coupling strength. The achieved XENONnT sensitivity resulted in a factor 1.7 improvement at WIMP mass of 100 GeV/c^2 compared to XENON1T.

The long drift field poses some challenges to accidental coincidence background suppression. The measured contribution in the WIMP search is approximately twice compared to XENON1T [93]. A discussion within the collaboration has started to decide if it is worth stopping the data taking and opening the detector to replace the electrodes. No decision has been made so far. Furthermore, the presence of the perpendicular wires in the top electrode stack made the characterization of the detector more difficult. The design of future detectors needs to consider the XENONnT experience to avoid further complications.

The XENONnT veto system, particularly the new neutron veto, has surpassed the most optimistic expectations, helping to reduce the neutron background by a factor $\sim$ 3, with respect to XENON1T, in the WIMP range of interest [188]. Even though the neutron background has been reduced, it remains larger than the prediction. This difference is currently under investigation and a possible cause is a wrong estimate of radionuclide concentrations in the cryostats materials. Looking ahead, the neutron tagging efficiency of the neutron veto will further improve with the gadolinium doping of the veto water.

I would like to conclude with a note on PMTs. The rigorous testing campaign, performed before the TPC assembly, fundamentally impacted the XENONnT results. Their performances over time improved with respect to XENON1T. Only the 3 $\%$ of PMTs were removed from the XENONnT SR0 PMT list, whereas in XENON1T, the 14% of the total PMTs were excluded [93].

7

Search for nucleon disappearance in ^{129}Xe with the first XENONnT science data

The XENONnT experiment was designed for dark matter searches, particularly in the form of WIMPs. As was shown in previous chapters, the detector performance was optimized for a low energy range up to $\mathcal{O}(100\ \mathrm{keV_{er}})$. However, the unprecedented background level achieved during the SR0 allows for the investigation of additional physics channels at energies previously unattainable in XENON experiments.

This chapter presents the search for nucleon disappearance in ^{129}Xe, using the SR0 XENONnT data. This analysis aims to find hints for baryon number violation. These processes are fundamental for understanding the baryon asymmetry of the Universe. The analysis details are discussed in the following sections: It consists of modeling the reconstructed energy spectrum up to 600 keV, with and without the sought-after signals. The range of interest is far above the energy region for which XENONnT's analysis was optimized. This posed several challenges, including understanding the spatial resolution of multiple energy deposits originating from the same interaction and the effect of data quality criteria over a wider energy range than previous analyses.

The chapter is organized as follows: First, the preliminary analysis performed to verify the understanding of the detector in a wider energy range than previous physics searches is presented, along with the tools used for modeling backgrounds and signals; next, the details of the analysis with the XENONnT SR0 data are described, concluding with the results.

7.1 Preliminary studies before the analysis

Discussing the previous steps to validate the tools used is necessary to understand the analysis and its complexity. This analysis resembles the low-energy ER analysis discussed in section 6.7.1, but the energy range is extended to 600 keV. Extending the region of interest involves several complications. Above a few hundred keV, the probability of reconstructing multiple energy depositions from the same interacting particle increases. Therefore, simulation software must correctly replicate single- and multiple-site reconstruction properties to derive simulation-based energy spectra as well as efficiency loss due to applied data quality criteria. In addition, due to limited computer resources, the full chain simulation, introduced in section 6.5.1, was not usable for high-statistics simulations, such as radiogenic background from detector materials. Therefore, an effective simulator was developed for this analysis. Its validation with respect to the full chain simulation is fundamental for deriving reliable expectations for background and signal energy spectra.

The analysis performed to validate the full chain simulation in the energy range of interest is discussed in the next section. The effective simulator of XENONnT, called FastSimulator, is then presented, on which several expected background and signal spectra are based.

7.1.1 Validation of full chain simulation

As shown in Fig.3.1, the γ-ray starts to be more penetrating above a few hundred keV. The most probable interaction for photons at these energies is Compton scattering, for which not all the energy is deposited in one interaction. Likewise, electrons become more penetrating, and the track they leave in the detector becomes appreciable ($\mathcal{O}(1\text{ mm})$). Therefore, with increasing energy, the probability of multi-site energy deposition increases. As this affects signal and background events, the single-site (SS) and multi-site (MS) information, quantifiable by their ratio as a function of the energy, must be properly simulated in the detector response. The validation of the detector response, performed with ^{220}Rn calibration data, is presented in the next paragraphs.

Data selection

The calibration data from ^{220}Rn, through the decay of its daughter ^{212}Pb, provide adequate data for studying the characteristics of SS-MS. ^{212}Pb undergoes a β-decay to ^{212}Bi, with a Q-value of (569 ± 18) keV [314]. ^{212}Bi can be produced in two excited nuclear states with energy (probability) of 415.3 keV (5.01(7) $\%$) and 238.6 keV (81.5(10) $\%$). The γ-rays from nuclear de-excitation are often reconstructed individually and not with the prompt β particle[1], producing true MS events in the detector. The remaining 13.7(10) $\%$ of the time, the decay proceeds with only β emission, producing a low energy true single-site events. Thus, ^{212}Pb provides both event topologies, which can be used to study the reconstruction performances. The reported decay features are taken from [314].

Therefore, the data-driven single- and multi-site information was extracted from ^{212}Pb and compared against dedicated full chain simulations. As explained in section 6.5.1, the full chain simulation returns data with a format processable by straxen. Therefore, the same data selection criteria applied to ordinary data can be applied to full chain simulation output. Indeed, the ^{220}Rn calibration and full chain simulation datasets used for the validation study shared the same selections.

---

[1] The nuclear de-excitation occurs within a few picoseconds, not large enough to distinguish it from the β particle from a timing point of view. However, the mean free path of the γ-rays is a few centimeters; therefore, it is large enough that the two energy deposition sites are resolvable individually.

The data quality criteria used were restricted to only those that showed a satisfactory match between the two datasets in the parameter space in which they are defined. An exception was made for the S1 AFT criterion, which was applied only to calibration data. This selection, which aims to reject mis-reconstructed events which have an unphysical fraction of S1 light collected by the top PMTs, was $\sim 10\ \%$ more aggressive on full chain simulation data than on ^{220}Rn calibration. As described in section 6.3.2, this is an important data quality criterion for rejecting several unphysical events. This selection was included in the analysis justifying it from its data-driven flat acceptance at $\sim 98\ \%$ over a wide energy range. The acceptance derived from ^{220}Rn calibration data, shown in Fig.7.1, was then accounted for in the full chain simulation results.

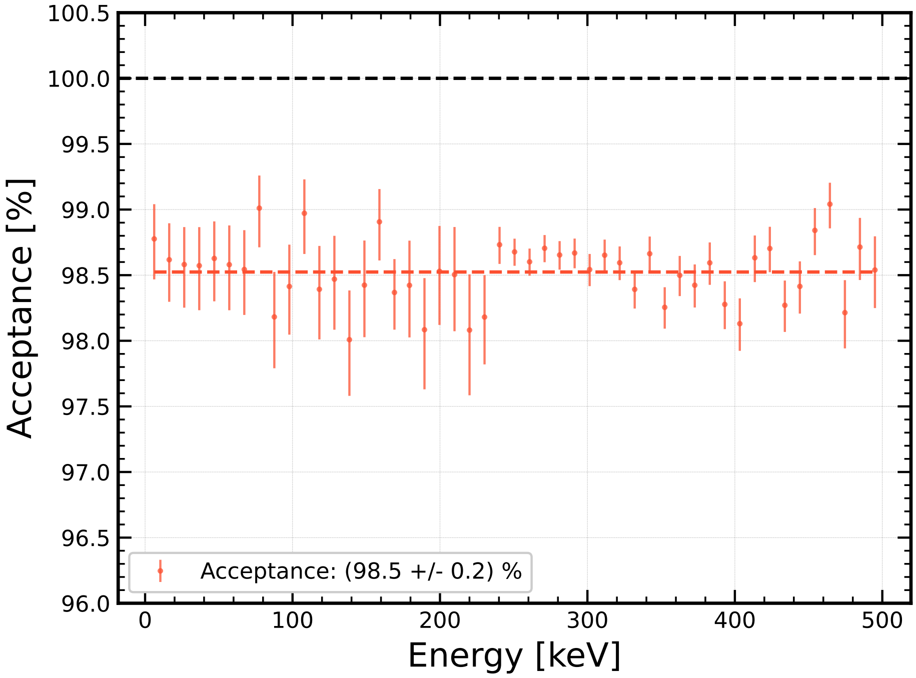

Figure 7.1: Data-driven S1 AFT acceptance, derived from ^{220}Rn calibration data, as a function of the reconstructed energy. The dashed horizontal lines represent the mean cut acceptance (red) and the 100 % acceptance (black).

The full cut list was: CUT_S1_MAX_PMT, CUT_S1_SINGLE_SCATTER, CUT_S1_NAIVE_BAYES, CUT_S1_AFT, CUT_S2_RECON_POS_DIF, CUT_S2_NAIVE_BAYES, CUT_S2_WIDTH. Additionally, as it will be described in the next paragraphs, the CUT_S2_SINGLE_SCATTER was used to distinguish SS from MS. An exhaustive discussion of each selection is presented in section 7.2.2. Additional selections were performed for each validation study, and they are introduced in the following discussions.

Single-site and multi-site resolution

The MS events can be defined based on the size of the secondary reconstructed S2 in an event waveform. If the size of the secondary S2, also called alternative, is not larger than a few percent of the size of the primary S2, the event is labeled as a SS. Otherwise, it is considered a MS event. In Fig.7.2, the selection criterion used in XENONnT to tag SS and MS events is shown. The S2 time width and the light pattern in the PMTs can also be used to identify MS events, but they are less efficient in this energy range. The analysis performed in this manuscript could be extended by including these parameters for SS and MS discrimination.

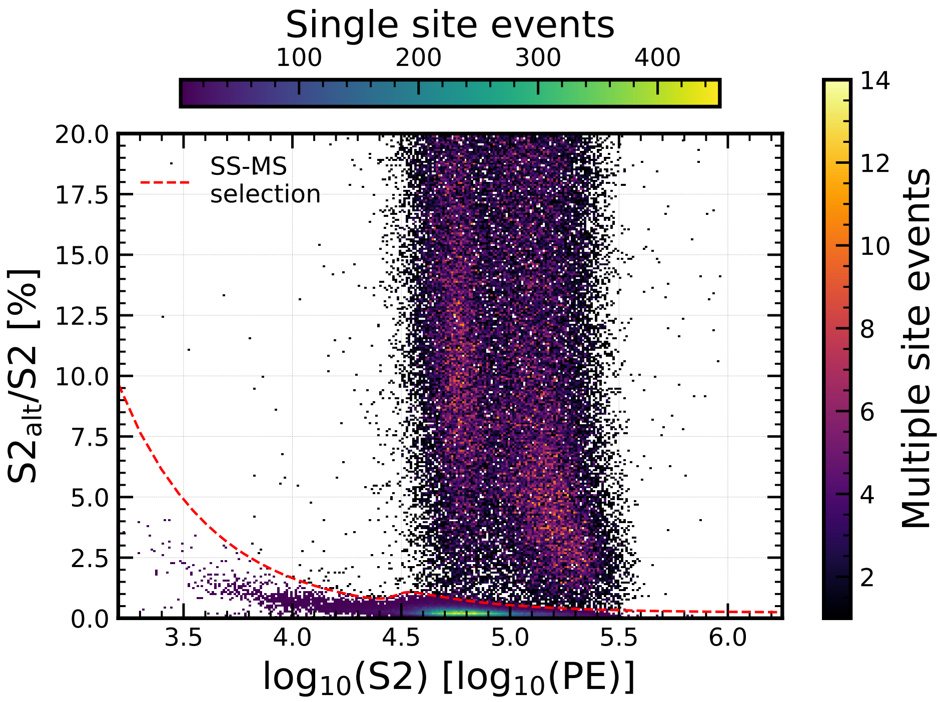

Figure 7.2: Two-dimensional histogram of ^{220}Rn calibration data in the SS-MS discrimination parameter space. The color gradients represent the per-bin density, as indicated by the color bars. The dashed red line represents the selection criterion used in XENONnT SR0 to separate SS (below) from MS (above).

The ability to resolve MS events depends on the detector conditions and the data processing. If an event is a pure SS interaction, no alternative S2 will be present[2] and the classification is straightforward. In the case of true MS events, if the interaction sites are too close in time and space, the S2s produced will overlap, making the classification more difficult. The S2 overlapping probability depends on the drift velocity, S2 size, and event depth. First, the faster the electrons reach the cathode, the lower the diffusion of the electron cloud. Small diffusion translates to small S2 time width. Therefore, high drift velocity means a more pronounced S2-peak shape, making it easier to distinguish multiple energy depositions. This is also true comparing small sizes S2 with bigger ones. Furthermore, the S2 time width increases with increasing depth for a given drift velocity. S2s, which are highly spread in time, may overlap in a larger region, making their reconstruction more complicated. For proper detector response modeling, validating the simulated SS-MS resolution as a function of the event depth is essential.

The SS-MS resolution is the minimum spatial separation between two energy depositions required to reconstruct them individually. As explained previously, the SS-MS resolution depends on the event depth since the diffusion broadens the S2s. Therefore, the minimum z separation (Δz) to reconstruct the true MS events was investigated as a function of event depth.

---

[2] In the event waveform, the chance to have an accidental peak reconstructed as S2 is not null. However, the size of these events is relatively small compared to the true S2 above a few tens of keV.

The validation was accomplished by comparing the z-dependent SS-MS resolution between ^{220}Rn calibration data and a dedicated full chain simulation data. Each simulated event consisted of two ERs with varying energy up to 1 MeV, with a random separation in z to reproduce true MS events. The MS events were selected by inverting the S2 SS selection, and the Δz was studied as a function of the event depth. Fig.7.3 shows SS-MS resolutions based on simulation and data as a function of z. It is possible to conclude that if two consecutive energy depositions are separated in z by less than $\sim$ 1 cm, the event is reconstructed as SS. The funnel shape marks the minimal Δz: True MS events with Δz within the funnel are reconstructed as SS.

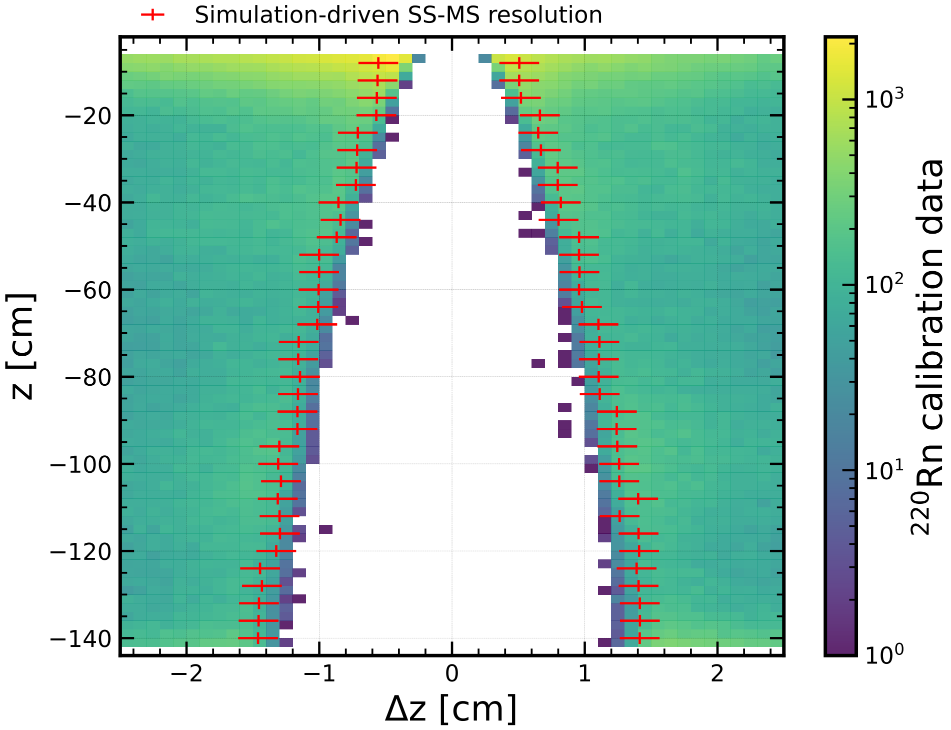

Figure 7.3: With the blue-to-yellow color map are shown the MS ^{220}Rn calibration data used to compute the minimum Δz spatial separation between two energy depositions required to reconstruct them individually (the SS-MS z resolution). The red points show the resolution obtained with a dedicated full chain simulation dataset. The y-axis shows the event depth, while the x-axis shows the multiple energy depositions' correspondent Δz. If two events have a z separation within the white region, they will be reconstructed together. The limit of the data distributions corresponds to the SS-MS spatial resolution.

The data- and simulation-driven resolutions are consistent with each other, although the simulation-driven result foresees a worse resolution, particularly at the bottom of the TPC. The data-driven (simulation-driven) minimal Δz separation to distinguish consecutive energy deposition goes from (0.46 ± 0.05) cm ((0.44 ± 0.08) cm) at the top of the TPC down to (1.40 ± 0.07) cm ((1.29 ± 0.06) cm) at the bottom of the TPC. As a preliminary result, the full chain simulation replicates the correct SS-MS spatial resolution. Ongoing studies aim to extend this analysis to higher energy, e.g., using ^{232}Th calibration source, which would improve SS-MS spatial resolution calibration and the simulated detector response.

Ratio of multiple-site to single-site events

To verify the reliability of the full chain simulation, the MS to SS ratio as a function of the energy was analyzed and compared against the data-driven ratio. Since the MS-SS ratio affects the signal and background energy spectrum shapes, its validation is essential for a robust analysis.

This study used a sample of 6.2×10^7 Geant4 simulated ^{212}Pb decays as an input for the full chain simulation. At later stages of the analysis, it was realized that Geant4 uses different branching ratios for the three states of ^{212}Bi compared to the literature values: 11.89 $\%$ for the ground state, 83.034 $\%$ for the 238.6 keV excited state, and 5.0759 $\%$ for the 415.3 keV excited state. As it will be discussed, this had an impact on the validation.

The S2 SS selection criterion presented previously was used to separate the two populations. A very tight fiducialization, equal to $r \leq 35$ cm and $z \in [-35; -130]$ cm, was used on calibration data to remove the radiogenic background from detector materials as much as possible. Additionally, calibration data reconstructed near the perpendicular wires were removed. The electric field simulation informs that the drift field lines diverge below the perpendicular wires, pushing the electron clouds to one side or the other of the wire. Therefore, the ionized charges from a single event can be split up to the point where multiple S2s are reconstructed.

In the top panel of Fig.7.4, the MS and SS ratios as a function of energy are shown for calibration (blue) and simulation (red) data of ^{212}Pb, together with the statistical uncertainties propagated by the Poisson fluctuations of MS and SS for each energy interval. Both datasets show the same trend. The ratio is nearly flat below 200 keV, steeply increasing approaching the energy of the first nuclear de-excitation decay of ^{212}Pb. The energy at which the two ratios have the increasing step does not match exactly, as shown by the drop around 240 keV in the bottom panel of Fig.7.4. Although it was not verified at the stage of this analysis, the origin of this difference could be a different energy resolution in the full chain simulation. A second change in slope is observed around the second nuclear de-excitation decay. The large errors at high energy are due to a lack of statistics. Due to their high relative uncertainty, the data points above 500 keV were not considered for the comparison. Overall, the data- and simulation-driven MS-SS ratios agree, but a constant offset of ~ 3 $\%$ is present between the two curves as shown in the bottom panel of Fig.7.4. This constant offset can be interpreted as if full chain simulation reconstructs (2.8 ± 0.4) $\%$ fewer MS for the same number of events than the calibration data.

Several hypotheses were put forward. For instance, the difference could be attributed to additional components in the calibration data with a flat MS-SS ratio, e.g., ^{85}Kr or ^{136}Xe, which were not considered in the full chain simulation. At the stage of this analysis, these hypotheses were not proven or disproven. Further studies and additional validation for the full chain simulation must be conducted to understand the origin. The offset ~ 3 $\%$ was used as a systematic uncertainty in the MS-SS ratio for the simulated spectra to avoid signal and background modeling bias.

Single-site energy spectrum shape validation

The SS energy spectra from calibration data and full chain simulation were compared using the ^{212}Pb data sets previously introduced. In the top panel of Fig.7.5, the ^{212}Pb energy spectrum from ^{220}Rn calibration data (blue) and full chain simulation (red) are shown. The spectra were normalized to have an area equal

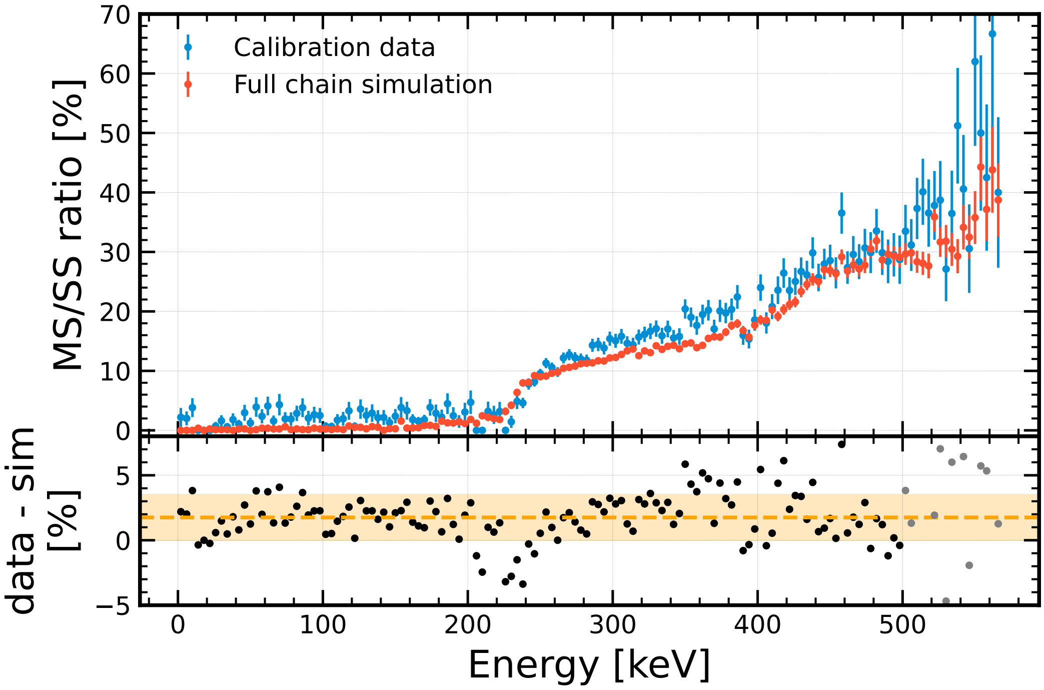

Figure 7.4: The MS-SS ratio as a function of the energy from ^{212}Pb data (blue) and full chain simulation (red) is shown in the top panel. The percentage difference between the two curves as a function of the energy is shown in the bottom panel. The dashed orange lines represent the average (2.8 ± 0.4) % difference, whereas the orange region shows the $\pm 1\sigma_{\mathrm{std}}$ region. The grey points above 500 keV have a high relative error due to the lack of statistics, and they were omitted from the comparison.

to 1. The error bars are derived from the Poisson fluctuation of each energy bin. In addition, the full chain simulation errors also include the 3 % systematic uncertainty discussed previously. Two regions, highlighted in gray, were excluded from the comparison. In the first region, around ~ 160 keV, the calibration data has an excess due to $^{131\mathrm{m}}$Xe decay[3], which was not included in the full chain simulation. The second region, around the first nuclear de-excitation decay of ^{212}Pb, was excluded due to the evident mismatch. As seen in the MS-SS ratio, the origin of this difference could be attributed to the different energy resolutions of the simulation and measured data. Additional studies are ongoing to validate the full chain simulation further.

In the bottom panel of Fig.7.5, the relative difference between the two spectra expressed as a percentage is shown. From the spectra, one notices a negative offset in the naked β region and a positive offset in the β plus γ-ray region. The mean of the relative difference below and above 200 keV is shown with an orange dashed line, whereas the orange regions represent the standard deviation. The observed displacements are (-12 ± 2) % and (6 ± 1) %, respectively. The differences are likely due to the branching ratio used in Geant4 to simulate the decay. An ongoing analysis, not included in this work, will test this hypothesis. This study laid the foundation for precise BR measurements for ^{212}Pb and ^{214}Pb decays with XENONnT using calibration data, the results of which can be used to constrain Pb decays in physics searches where they represent a background.

---

[3] The isomeric state of ^{131}Xe is produced via neutron inelastic scattering during the neutron calibration performed before the radon calibration.

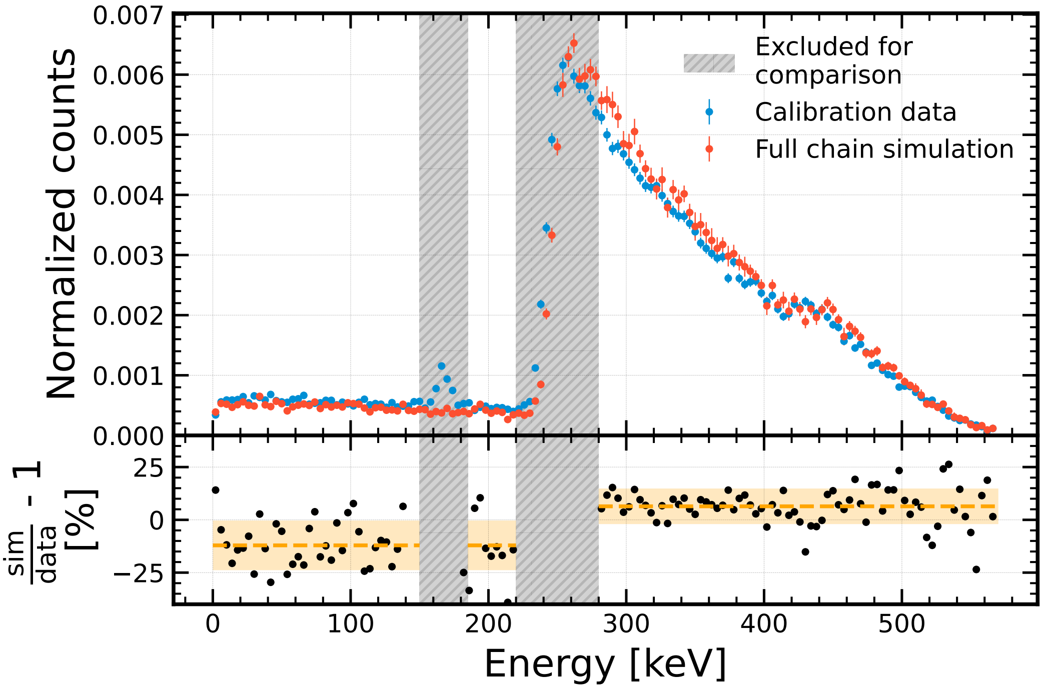

Figure 7.5: ^{212}Pb spectra from ^{220}Rn calibration data (blue) and full chain simulation (red), normalized such to have an area equal to 1, are shown in the top panel. The bottom panel shows the relative difference between the two spectra, expressed as a percentage and a function of the energy. The grey regions were omitted in the spectrum comparison. The two orange dashed lines below and above 200 keV show the average relative difference between the two shapes., whereas the orange region represent the $\pm 1\sigma_{\text{std}}$ region.

Concluding remarks

The recommended ^{212}Pb branching ratios will be implemented in the XENONnT Geant4 model, and new simulations will be produced. These will be used to validate the full chain simulation further. Nevertheless, the current status is promising, and the comparison is already sufficiently good: The SS-MS reconstruction performances are captured well from the full chain simulation, as shown by the SS-MS spatial resolution, and, in addition, a similar MS-to-SS ratio was obtained between the calibration data and the full chain data, despite a constant offset of 3 $\%$. All this motivates the use of this tool in the nucleon disappearance analysis.

7.1.2 The effective simulator: FastSimulator

The full chain simulation could produce all the energy spectra needed in the analysis. However, the computer resources available during this study were not sufficient to obtain significant statistics of each background and signal component ($\mathcal{O}(10^8)$ Geant4 events). Therefore, a more efficient approach was used as it was done in XENON1T [297]. Compared to the full chain simulation described in section 6.5.1, this approach, called *FastSimulator*, consists of skipping the WFsim and, instead, propagating the quanta produced by EPIX through the S1 and S2 light collection efficiency maps and applying an event clustering based on SS-MS *z*-resolution.

In summary, the simulation steps are:

1. Geant4 propagates the particles in the detector geometry and simulates their interactions. The energy deposited in each interaction step, interaction locations, timings, and types of interaction are propagated to the next step;
2. The EPIX software [282, 225] processes Geant4 outputs with a micro-clustering algorithm based on the DBSCAN (Density-Based Spatial Clustering of Applications with Noise) algorithm [315], which groups the energy depositions in the xenon within $\sim 5\ \mu$m, which is the xenon micro-physics recombination scale that has been shown to reproduce the xenon response to deposited energy [180]. After the pre-clustering, primary photons and electrons are generated using the NEST package [172]. As seen in the previous chapters, the production of photons and electrons for each energy deposition requires the electric field intensity at the interaction position and the type of interaction. The latter one is propagated from Geant4 simulation, while the first one is provided using COMSOL Multiphysics® [268] electric field simulation map [266];
3. Ultimately, the FastSimulator software simulates the detector-dependent macro-clustering of nearby S2s through a decision tree classifier [316]. The classifier uses the number of electrons of two consecutive event steps, their interaction depth, and their z separation as input [317]. If the events are merged, the number of electrons and the deposited energy propagated from Geant4 are summed. At the end of the macro-clustering, only the two clusters with the highest number of electrons per simulated event are saved[4]. In contrast, since light propagation is faster than the PMT readout, the number of photons produced at each interaction step is always summed. Finally, the light collection efficiency maps, the average single PE spectrum, and, only for the charge signals, the single electron gain are applied to the resulting numbers of photons and electrons to retrieve S1s and S2s. Eventually, the signals are corrected for the spatial dependence of the detector response (see section 6.2.2), and cS1s and cS2s are extracted.

The S2 single site selection criterion seen previously can be applied to the FastSimulator S2 and alternative S2, and the SS events can be selected. Then, their Geant4 energy can be used to obtain the expected energy spectrum. The energy can also be retrieved from the simulated cS1 and cS2. However, the Geant4 energies showed better agreement with the data, probably due to a suboptimal quanta generation model. A new emission model is currently being tested instead of the default NEST model, which can help improve the simulation of S1 and S2. The effective XENONnT detector response used in this analysis is summarized in the flowchart shown in Fig.7.6 where the main steps are represented, including the FastSimulator.

The FastSimulator was validated against the full chain simulation using the ^{212}Pb energy spectrum. The ^{212}Pb Geant4 simulations used in the previous studies were processed with FastSimulator. The shape of the SS energy spectrum was compared with the full chain simulation spectrum presented in the previous section. Before the comparison, the FastSimulator energy spectrum was smeared using the energy resolution described in section 6.1. The smeared energy spectrum was then convolved with an empirical description of the observed energy bias (see section 7.2.2). In addition, selection efficiency must be taken into account. In contrast to energy resolution and energy bias, a different derivation of selection

---

[4] Straxen does not save more than two S2s. For consistency, only two energy clusters are saved in FastSimulator. This is a topic of discussion in the collaboration whether to change it or not.

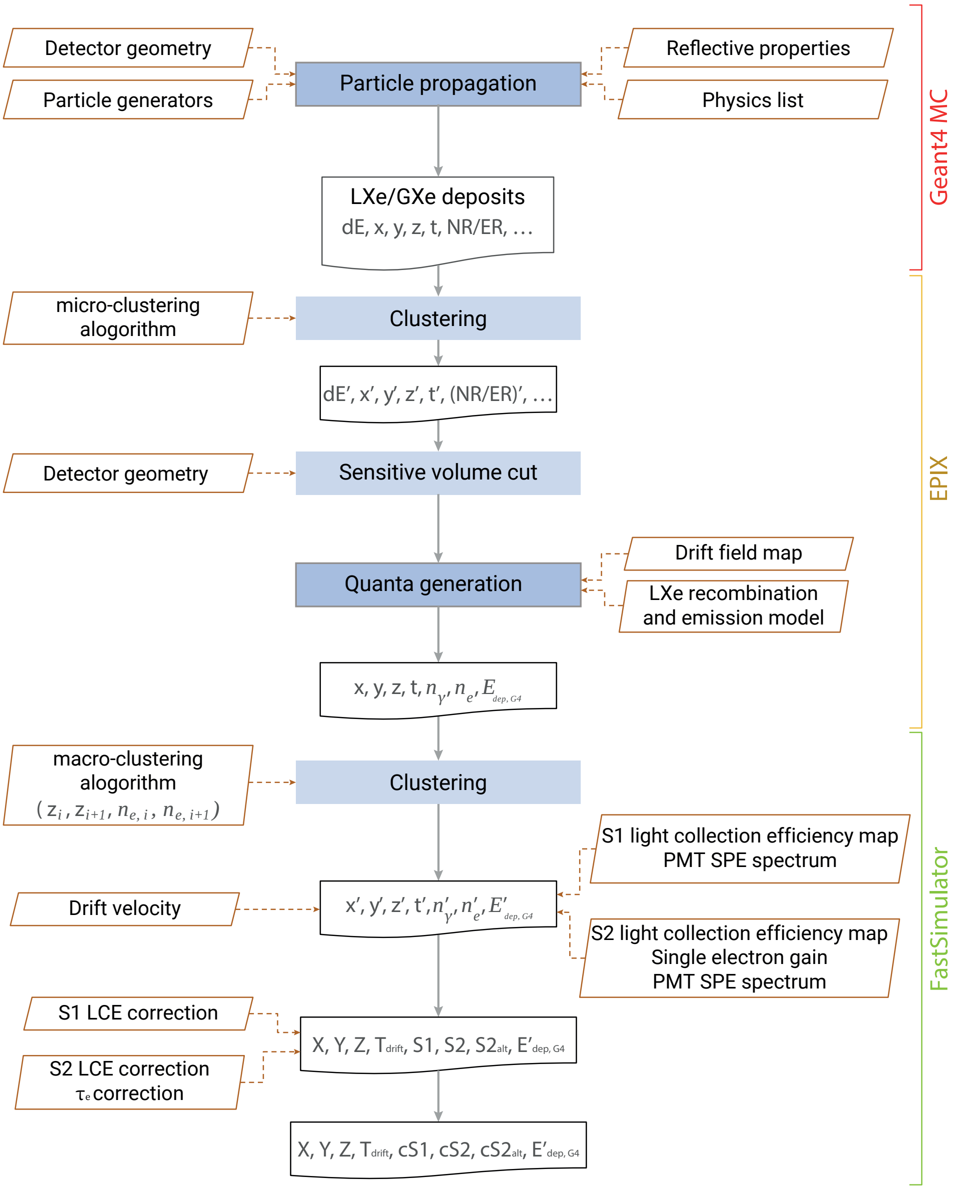

Figure 7.6: The XENONnT effective simulator workflow used in the nucleon disappearance analysis. Via the Geant4 toolkit, the simulated particles are propagated in the detector geometry, and their interactions are simulated. The energy released and particle tracking information are given as input to EPIX software which applies a clustering based on xenon micro-physics and generates the number of photons and electrons. Eventually, FastSimulator software process the EPIX output by applying a clustering that simulates the single- and multi-site detector reconstruction properties and generates the S1s and the S2s based on n_γs and n_{e^-}s and the effective detector response maps. The diagram has been inspired by from [225].

efficiency was used in this analysis than what was discussed in section 6.3.4. Unlike the low-energy ER analysis and the WIMP search, where the selection efficiency was derived by applying the N-1 method to calibration data, in this study, it was derived using the full chain simulation. The N-1 procedure was applied to ^{212}Pb full chain simulation data to obtain the acceptance of each cut (see section 7.1.1), except for the S1 AFT cut for which the data-driven acceptance was used. The selection efficiency of the S2 SS cut was omitted in the total efficiency since it is applied on top of the FastSimulator output. Then, the cumulative cut acceptance as a function of the energy was convolved with the detection efficiency. The solid red line in Fig.7.7 shows the total selection efficiency, and the colored region represents its uncertainty. The multi-step decays of ^{212}Pb are often reconstructed together, leading to larger S2 width than the pure β decay. As a result, approaching energies of 200 keV, the S2 width selection has worse acceptance, producing a decrease in the efficiency. The efficiency drop at a few keV instead is due to the detection efficiency. Moving from $\sim$ 5 kev to $\sim$ 1 keV, the ability to detect events drops rapidly from $\sim$ 100 % to $\sim$ 10 %. The efficiency returns to 1 above $\sim$ 569 keV, the ^{212}Pb spectrum endpoint, where no ^{212}Pb events occur. A more in-depth discussion is present in section 7.2.3.

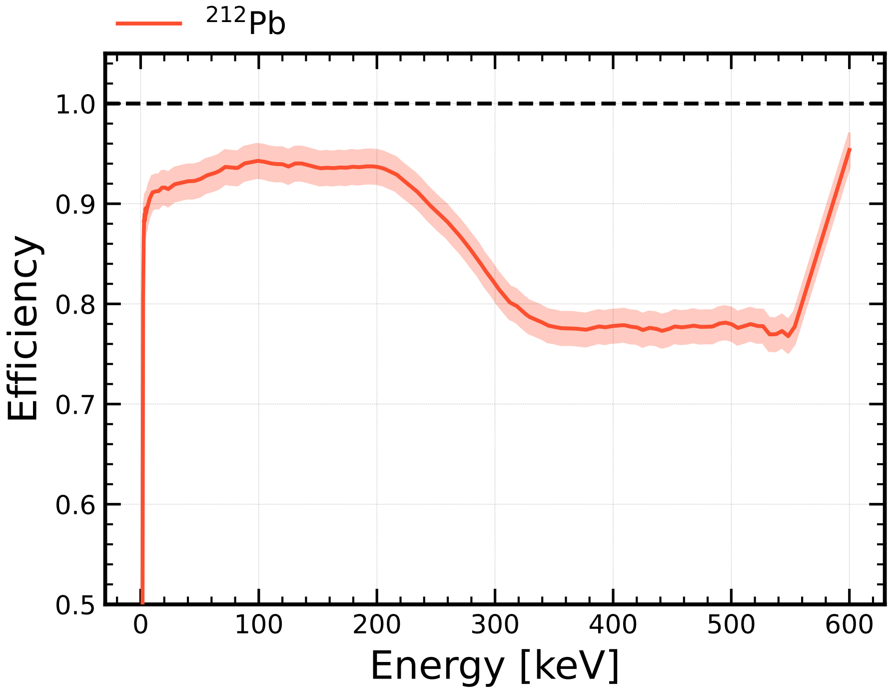

Figure 7.7: ^{212}Pb simulated-driven selection efficiency as a function of the energy. The colored region represents the selection efficiency uncertainty. A more in-depth discussion is present in section 7.2.3.

Once the total selection efficiency was accounted for in the FastSimulator output, the SS energy spectra were compared. In the top panel of Fig.7.8, the ^{212}Pb energy spectra are shown, normalized such that their area is equal to 1. The red markers represent the full chain simulation, whereas the dark purple ones show the FastSimualtor spectrum. The error bars include the statistical uncertainty and the MS-SS ratio systematic uncertainty. The bottom panel shows the residual in units of $\sigma = \sqrt{\delta^2_{FCS} + \delta^2_{FS}}$, where δ are the uncertainty mentioned earlier. Here *FCS* stands for full chain simulation and *FS* for FastSimulator. The residuals are well contained in the 1σ (green) and 2σ (yellow) bands, ensuring the shape's similarity. Therefore, the FastSimulator replicates the results of full chain simulation in energy space and can be used as an alternative tool in combination with simulation-driven efficiency to construct signal and background expectations.

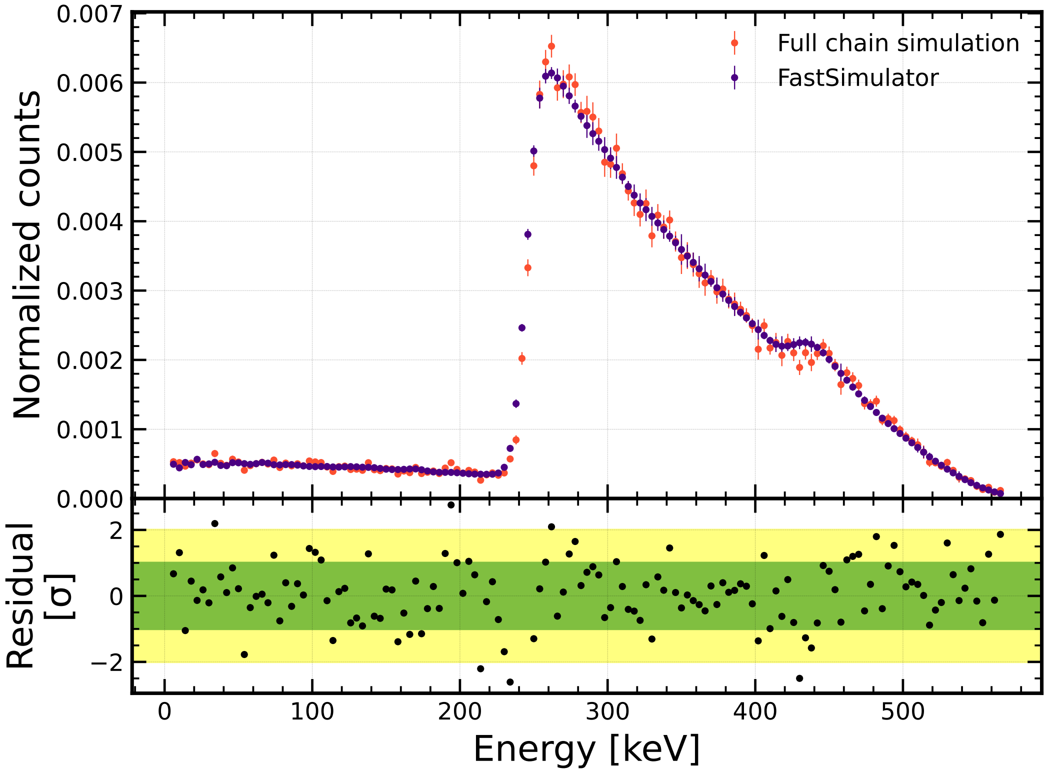

Figure 7.8: ^{212}Pb SS spectra from full chain simulation (red) and FastSimulator (dark purple) are shown in the top panel. The spectra are normalized such that their area is equal to 1. The error bars include the statistical uncertainty and the MS-SS ratio systematic uncertainty. The bottom panel shows the residual as a function of the energy. The green and yellow horizontal bands show the 1σ and 2σ regions.

7.1.3 Updates on the radiogenic background from detector materials

Section 7.1.3 showed the expectation of radiogenic background from detector materials used in the low-energy ER analysis. That expectation was derived using nSort software, which utilized an SS-MS spatial resolution inherited from XENON1T based on different electric drift field conditions [151, 215]. This section will present the expectation derived with FastSimulator in the fiducial volume of the low-energy ER analysis and the comparison with the previous result.

The material background simulations were processed using FastSimulator. The SS events occurring in the low-energy ER analysis fiducial volume were selected, normalized following Eq.6.17, and smeared according to the energy resolution discussed in section 6.1. As examples, in Fig.7.9, the expected SS energy spectra of ^{60}Co and ^{226}Ra before and after updating the SS-MS spatial resolution are shown. Besides the SS selection and the low-energy ER analysis fiducialization, no selections were applied to the datasets. The wiggles at low energies are due to the statistical uncertainty of events that reach the inner part of the TPC volume. These are due to the not optimal number of primaries Geant4 simulated events. Ideally, a higher number of Geant4 events is preferable; however, it was not possible during this analysis due to storage constraints. As shown in Fig.7.4, the MS-SS ratio implies that events below a few hundred of keV are reconstructed as a single site. This was also true for the previous simulation. Indeed, the two methods present no significant difference at low energy. Approaching the MeV scale, the spectra start to deviate from each other. The difference is expected since the outdated SS-MS spatial resolution was based on a higher drift field and, therefore, on a better spatial resolution.

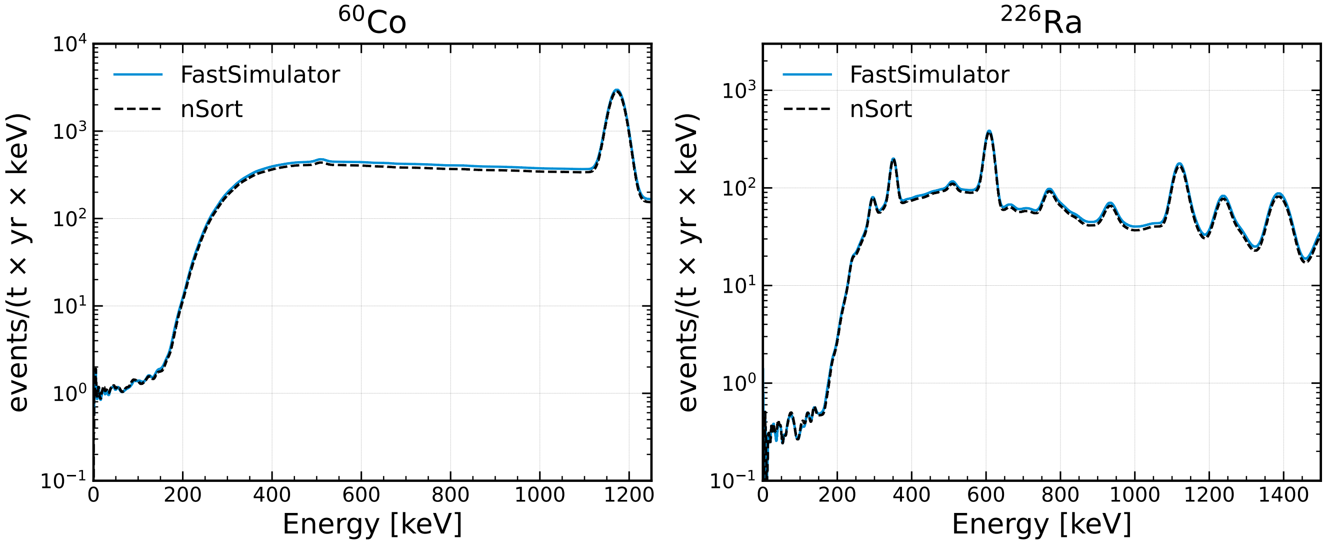

Figure 7.9: Comparison of ^{60}Co and ^{226}Ra single-site energy spectrum before (dashed black) and after (solid blue) having updated the SS-MS spatial resolution.

Fig.7.10 shows the total radiogenic background expectation from materials of the detector in the low-energy ER analysis fiducial volume. The expected rate below 140 keV, namely the low-energy ER analysis region of interest, is equal to (2.5 ± 0.5) events/(t × yr × keV), where the uncertainty is derived as described in section 7.1.3. The updated expectation is consistent with the one derived using nSort based on the XENON1T experience [215, 151, 297], equal to (2.4 ± 0.5) events/(t × yr × keV) (see section 7.1.3).

7.2 Analysis of nucleon disappearance in XENONnT

In this section, the analysis details are discussed. First, the expected signals are presented, then the data used for analysis are outlined. Next, the background model and the statistical framework utilized in the analysis are delineated. The results of a binned likelihood fit performed in the energy space are presented at the end of the section.

7.2.1 Expected signals

The signal models consist of the SS energy spectrum of the radioactive decay of daughter nuclei originating after the disappearance of the nucleon or di-nucleon in ^{129}Xe. Similar to the DAMA/LXe search [143], the channels investigated are p, nn, and pp correspondent to search for the decays of ^{128}I, ^{127}Xe, and ^{127}Te, respectively.

The signal models were generated using 10^8 Geant4 events processed with FastSimulator. From the FastSimulator output, it is possible to retrieve the MS to SS ratio, which is important for correctly interpreting the number of events attributed to the investigated process. The 3 $\%$ offset observed between

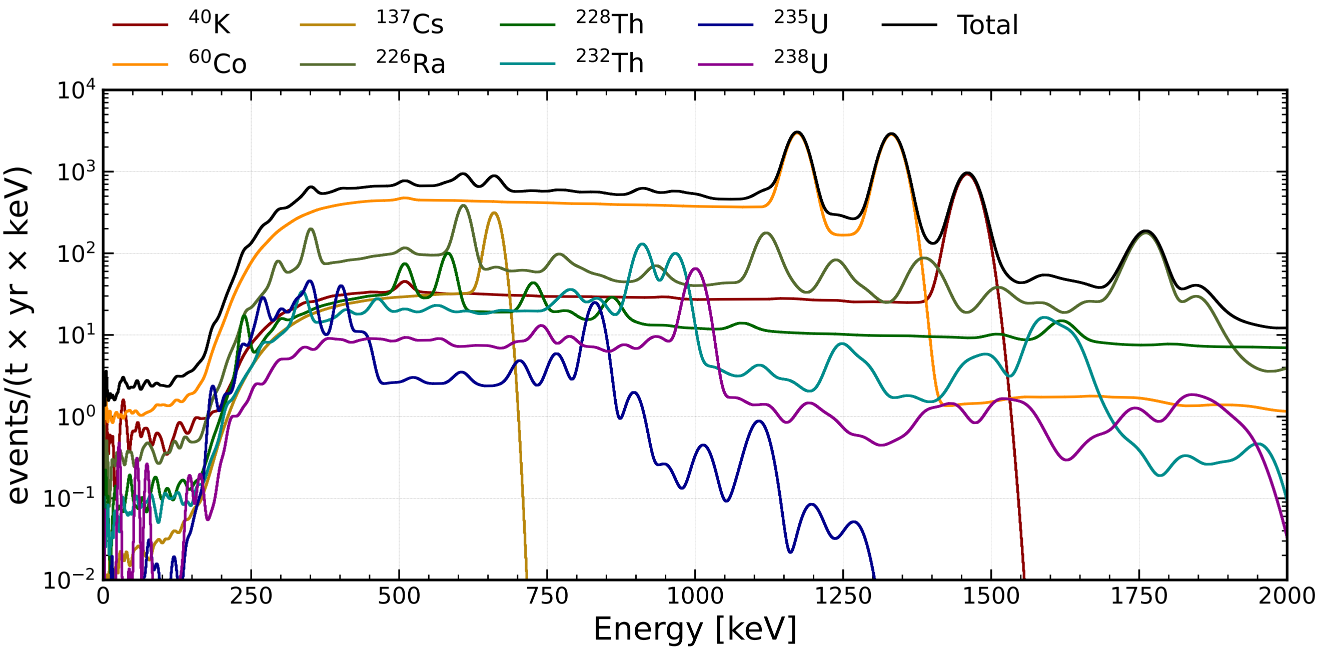

Figure 7.10: The solid black line shows the expected SS material spectrum in the low-energy ER analysis fiducial volume (~ 4.37 t), equal to the sum of the contribution of the isotopes listed in the legend. The expectations are derived using FastSimulator, normalized using the method described in section 7.1.3, and smeared according to the energy resolution discussed in section 6.4. The wiggles at low energies are due to the statistical uncertainty of events that reach the inner part of the TPC volume.

the data- and simulation-driven MS-SS ratio was used here as a systematic uncertainty. The simulated SS energy spectrum was smeared using the skew-Gaussian energy resolution given in section 6.4, which is described by the skewness α - dimensionless - and scale w - dimension of energy - parameters as a function of the reconstructed energy as follow:

$$\frac{w}{E} = \frac{a}{E} + b \qquad \alpha = c \times E^{(d+1)} \tag{7.1}$$

where the parameters a, b, c, and d are $(37.2 \pm 0.4) \times 10^{-2}$ keV, $(4.36 \pm 0.06) \times 10^{-3}$, (1.999 ± 0.006) keV$^{-(d+1)}$, and (-1.256 ± 0.002), respectively. Moreover, the simulated SS energy spectrum was scaled accordingly to the selection efficiency (see section 7.2.3), and convolved with the energy bias (see section 7.2.2).

The spectra were normalized using the approach described in section 7.2.4. These normalizations were used as initialization in the fit. To calculate the T_{eff} in Eq.6.16, the specific activity A_{c} is required. This is computed from the DAMA/LXe lifetime τ upper limit at 90% C.L. [143]. Lifetimes are for nucleon or di-nucleon decays, while normalization is required per nucleus. Therefore, A_{c} needs to be multiplied by the effective number of nucleons $N_{\mathrm{eff}} = N_{\mathrm{obj}} \times \lambda_{\mathrm{obj}}$ whose decays lead to the searched nuclei (see section 2.2.2). The values of τ and N_{eff} are listed in Tab.2.3. Then A_{c} is computed as follows:

$$A_{\mathrm{c}} = \frac{N_{\mathrm{A}} \times \eta}{\mathrm{M}_{\mathrm{Xe}}} \times \frac{1}{\tau} \times N_{\mathrm{eff}} \tag{7.2}$$

where N_{A} is the Avogadro number $(6.02214076 \times 10^{23}$ mol^{-1} [318]), η is the isotopic concentration of ^{129}Xe (26.4 % ($^{\mathrm{mol}}/_{\mathrm{mol}}$) [156]), and M_{Xe} is the xenon molar mass (131.293 g mol^{-1}) [154].

^{128}I

As a result of p disappearance, ^{129}Xe is converted to ^{128}I. With a half-life of 24.99 minutes, ^{128}I decays to ^{128}Xe 93.1(8) % of the time via β decay, with an end point of 2123.4 MeV. The remaining 6.9(8) % of the time, the decay occurs via electron capture (EC) to ^{128}Te [319]. The β^+ decay is allowed but strongly suppressed (total β^+ intensity: 0.0026(4) % [319]). The subsequent X-ray cascade or Auger electrons following the EC lead to peaks in the measured energy spectrum: the K-shell EC is responsible for the peak at 31.82 keV, and the L-shell EC produces a peak at 4.9 keV [320]. Fig.7.11 shows the expected energy spectrum of ^{128}I. The spectrum consists of SS events, corresponding to (90 ± 3) % of the total events. The MeV region, where MS events are easier to reconstruct, contains the discarded multiple scattering events.

^{127}Xe

The nn disappearance in ^{129}Xe produces ^{127}Xe. It decays 100 % of the time via EC to ^{127}I, with a half-life of 36.4 days [321]. The ^{127}I is produced 53 % of the time in a 203 keV excited state, while the remaining 47 % of the time the decay populates a 375 keV isomeric state of ^{127}I [321]. Another excited state exists at 618.4 keV, but it is populated with a sub-percent probability [321]. Subsequent nuclear de-excitation occurs mainly by single or multiple γ-rays and secondarily by internal conversion. The α_T, namely the probability that the transition takes place by ejecting any orbital electron, is 11 % and 2 % for 203 keV and 375 keV isomeric states, respectively [321]. Following the EC, a cascade of X-rays or Auger electrons is emitted. The combination of the latter processes with the nuclear de-excitations generates several peak features in the energy spectrum up to the Q-value of 662.3 keV [321]. These multi-step decays are such that the portion of MS events is significant. The SS events correspond to (80 ± 3) % of the total events. The expected ^{127}Xe SS energy spectrum is shown in Fig.7.11.

^{127}Te

The pp disappearance in ^{129}Xe would produce ^{127}Te. With a half-life of 9.35 hours, it decays via β emission 100 % of the time to ^{127}I. The ^{127}I can be produced in 4 different existing states, followed by single or multiple γ-rays. The preferred mode of decay is to the ground state, with a branching ratio of 98.79 %. Only one decay mode to the 417 keV isomeric state of ^{127}I state has a branching fraction larger than 1 %. Therefore, its energy spectrum resembles a simple featureless β spectrum with an endpoint of 703 keV [321]. Being almost a pure β process ensures that most events are SS. Indeed, only (1 ± 3) % of the decays are reconstructed as MS. The expected ^{127}Te SS energy spectrum is shown in Fig.7.11.

7.2.2 Data selection

The data used for the nucleon disappearance analysis includes the low-energy ER analysis data (97.1 days) and the data acquired with a different xenon recirculation mode (14.3 days). Referring to Fig.6.1, the additional physics search data considered are in the region labeled as *Getter bypass mode*. A threshold for light and charge signals was applied to minimize AC contamination: Similar to the low-energy ER analysis,

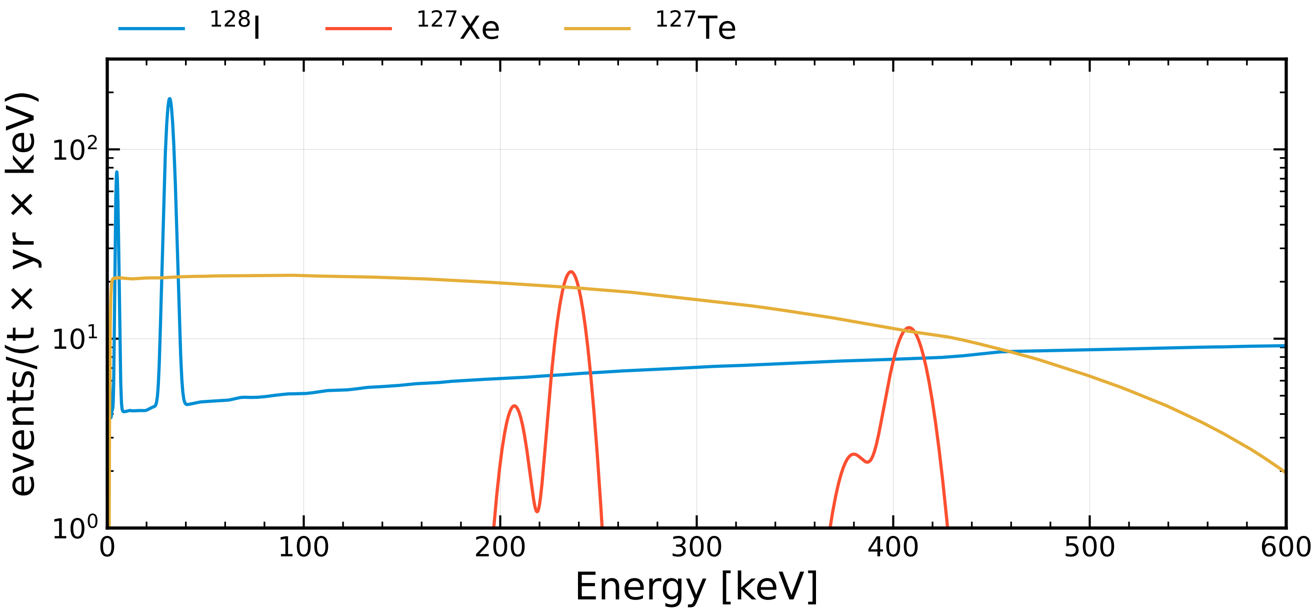

Figure 7.11: Expected SS energy spectra of ^{128}I, ^{127}Xe, and ^{127}Te decays in XENONnT, expressed as events/(t × yr × keV). The spectra are derived using FastSimulator and convolved with energy resolution, bias, and selection efficiency. The normalization is computed from the DAMA/LXe lifetime limits of p ($\tau_{\text{p, lim}} > 1.9 \times 10^{24}$ yr), nn ($\tau_{\text{nn, lim}} > 1.2 \times 10^{25}$ yr), and pp ($\tau_{\text{pp, lim}} > 5.5 \times 10^{23}$ yr) disappearance in ^{129}Xe, respectively [143].

events with at least 3 PMTs contributing to S1, and S2 $\geq$ 500 PE were considered. The energy of each event was reconstructed using the same g_1 and g_2 detector parameters adopted in the low-energy ER analysis. Similarly, the energy resolution, based on the skew Gaussian model (see Eq.7.1), was used in this analysis.

As discussed in section 6.1, an energy bias ($\Delta E/E$) exists due to the extracted g_1 and g_2 parameters. The bias was estimated by fitting the known mono-energetic lines in the reconstructed energy space and assuming a linear background. The fit is performed using skew Gaussians for the low energy ^{37}Ar and ^{83m}Kr lines, while a normal Gaussian distribution is considered for the remaining peaks. This choice is consistent with the skewness trend observed in the energy resolution study ($\alpha < 0.6$ in Eq.7.1 for energy $>$ 150 keV). As an example, the fit performed for the full absorption peaks of ^{214}Bi (1120.3 keV [211]), ^{60}Co (1173.2 keV and 1331.5 keV [277]), and ^{40}K (1460.8 keV [278]) is shown in Fig.7.12. Since another contribution from ^{214}Po nuclear de-excitation at 1377.6 keV [211] was not considered, the energy bias extracted from the second ^{60}Co peak was not used to derive the empirical model.

The empirical model ($F(E_{\text{true}}) = A \times arctan(E_{\text{true}} \times k)$), extracted through a χ^2 fit, is shown with the dashed black line in Fig.7.13. The fitted values are reported in the legend. The white region indicates the region of interest for the nucleon disappearance analysis. The events within the low-energy ER analysis fiducial volume ($\sim$ 4.37 t) were used such that the full absorption peaks of the high energy γ-lines from the detector materials were more pronounced, e.g., ^{208}Tl from ^{232}Th decay chain or ^{214}Bi from ^{238}U decay chain. This model is propagated into the background and signal spectra to account for the energy bias. In particular, the expected energy spectra are derived as a function of the true energy. This is then translated into reconstructed energy by adding the bias predicted by the empirical model to each energy bin. Next, the spectrum is interpolated and evaluated in the original energy binning.

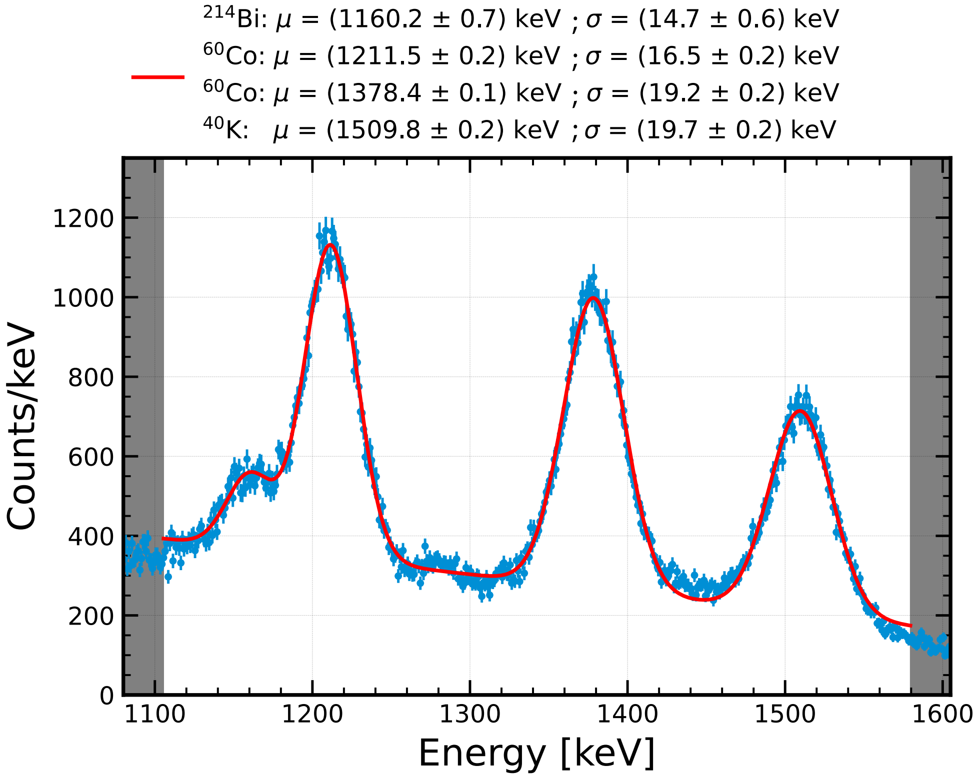

Figure 7.12: Example of the fit performed for the full absorption peaks of ^{214}Bi (1120.3 keV), ^{60}Co (1173.2 keV, 1331.5 keV), and ^{40}K (1460.8 keV). The fit, indicated by a solid red line, was performed with the data, shown in blue, contained in the white region. The data uncertainties were derived from the per energy bin Poisson fluctuation. The best-fit energies, shown in the legend, were used to calculate the energy bias.

The energy range of interest goes from 1 keV to 600 keV. The energy threshold at 1 keV is fixed by the S1 detection efficiency. At this energy, the efficiency is 10 %, and it increases steeply, reaching 100 % above 5 keV. The impact of S2 reconstruction efficiency is negligible. It is expected to be ~ 100 % in the energy range considered [208]. The upper bound at 600 keV was chosen from the β spectrum endpoint of ^{212}Pb. As discussed in section 7.1.1, this nuclide was used to validate the full chain simulation. The signal outside the energy range of interest is less than 1 % for ^{127}Xe and ^{127}Te and 62 % for ^{128}I.

The fiducial volumes in the previous analyses cannot be used in this energy range. Any spectrum features above ~ 160 keV would be obscured by Compton scatters of the high energy γ-rays from detector materials. The selection of the fiducial volume for the nucleon disappearance analysis was informed by the pseudo-significance $Z = \frac{S}{\sqrt{B}}$, where S is the expected number of signals and B is the expected number of background events in the range of interest. The expected signal is proportional to the number of ^{129}Xe nuclei and, therefore, to the fiducial mass M_{fv}. Then, the pseudo-significance can be expressed as $Z \propto M_{\text{fv}}/\sqrt{B}$ [322].

The predicted spatial distribution of the background, consisting of the contributions of the simulated materials plus the intrinsic backgrounds within the low-energy ER fiducial volume, is shown in Fig.7.14. In the central regions of the TPC, where only the intrinsic backgrounds contribute to B, Z reaches the maximum. With the fiducial volume increasing, more and more background events from detector materials are included in B, and Z decreases. The pseudo-significance Z was studied as a function of r^2 and z given

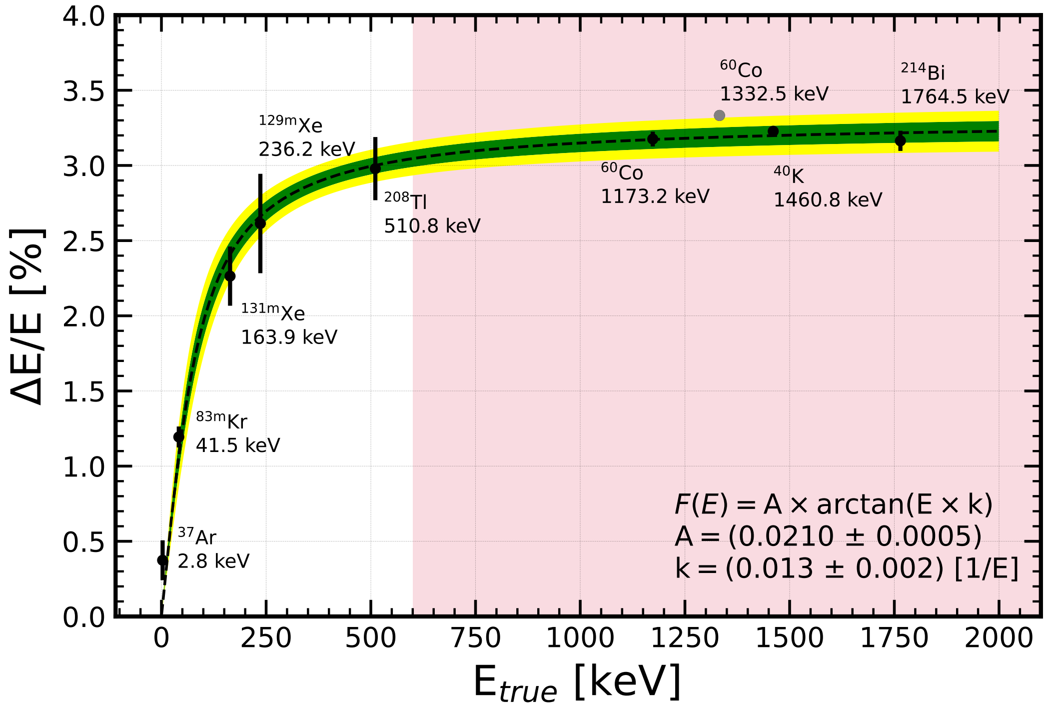

Figure 7.13: The measured energy bias $\Delta E/E$ as a function of true energy using low energy mono-energetic lines and full absorption peaks from detector materials. The energy bias extracted from the 1331.5 keV γ-line of ^{60}Co was not used (see the discussion in the text). The bias model is shown with a black dashed line. The green (yellow) region represents the model's 1σ (2σ) uncertainty. The white region indicates the range of interest for the nucleon disappearance analysis.

the simulated spatial distribution of the backgrounds. Starting from a reference cylinder at the center of the TPC, Z was scanned in the two dimensions considered. Three volumes, with masses equal to 1 t, 2 t, and 3 t, were considered as shown in Fig.7.14. At a later stage of this analysis, a discrepancy was noted in the MeV region in the spatial distribution of material backgrounds between the data and the simulation in the outermost region of the TPC, probably due to incorrect normalization. Even though the range of interest of this analysis is not affected by this mismatch, it was chosen to limit the fiducial volume to the low-energy ER analysis fiducial volume to avoid any overestimation of Z.

As shown in Fig.7.15, the 1 t fiducial volume lies in the region with the highest Z, whereas volumes above 3 t have a small pseudo-significance. The scan of Z suggests small volumes where the contributions of the detector materials are negligible. However, considering that most of the expected signals are below 300 keV where backgrounds are less penetrating (see section 7.2.1), the 2 t fiducial volume was chosen. This also ensures high data statistics (total number of events equal to 33969), essential for the binned likelihood fit to be robust. Then, the analysis was performed with events occurring in a cylindrical volume with $r < 47.5$ cm and $z \in [-130, -25]$ cm. Accounting for possible charge-insensitive regions, the mass was estimated to (2.04 ± 0.16) t.

A series of selection criteria are applied to the data to select the SS population, reduce the poorly reconstructed events, reject unwanted topologies or unphysical events, such as AC events, and improve the overall quality of selected S1 and S2 pairs. The XENONnT SR0 selection criteria were developed for low-energy analysis, and most of them showed significant differences in the energy range considered between the full chain simulation and calibration data in the parameter space in which they were defined. Since the efficiency lost due to the selection criteria applied to the data is based on the full chain simulation, a good match between the simulated and real data is necessary. Otherwise, the acceptance based on the simulation may be misestimated. As explained in section 7.1.1, an exception was made for the S1 AFT criterion for which the ^{220}Rn data-driven efficiency was used. In Tab.7.1, the selections used in this analysis are collected with a brief description. The first four selections, listed in the table, act as live time reduction, and they do not enter into the selection efficiency.

7.2.3 Total selection efficiency

The efficiency as a function of the reconstructed energy is required to derive reliable background and signal models. The efficiency acts on the expectation in two ways: the expected counts and the shape of the model. The total efficiency consists of detection efficiency and selection efficiency. The first efficiency is given by the ability to reconstruct light and charge signals given the threshold applied on S1 and S2. As discussed in section 6.3.4, S1 reconstruction efficiency dominates the detection efficiency. The selection efficiency depends on the selection criteria applied, and contrary to what has been done so far in XENONnT, it was derived using the full chain simulation. As described in section 6.3.4, an iterative approach was

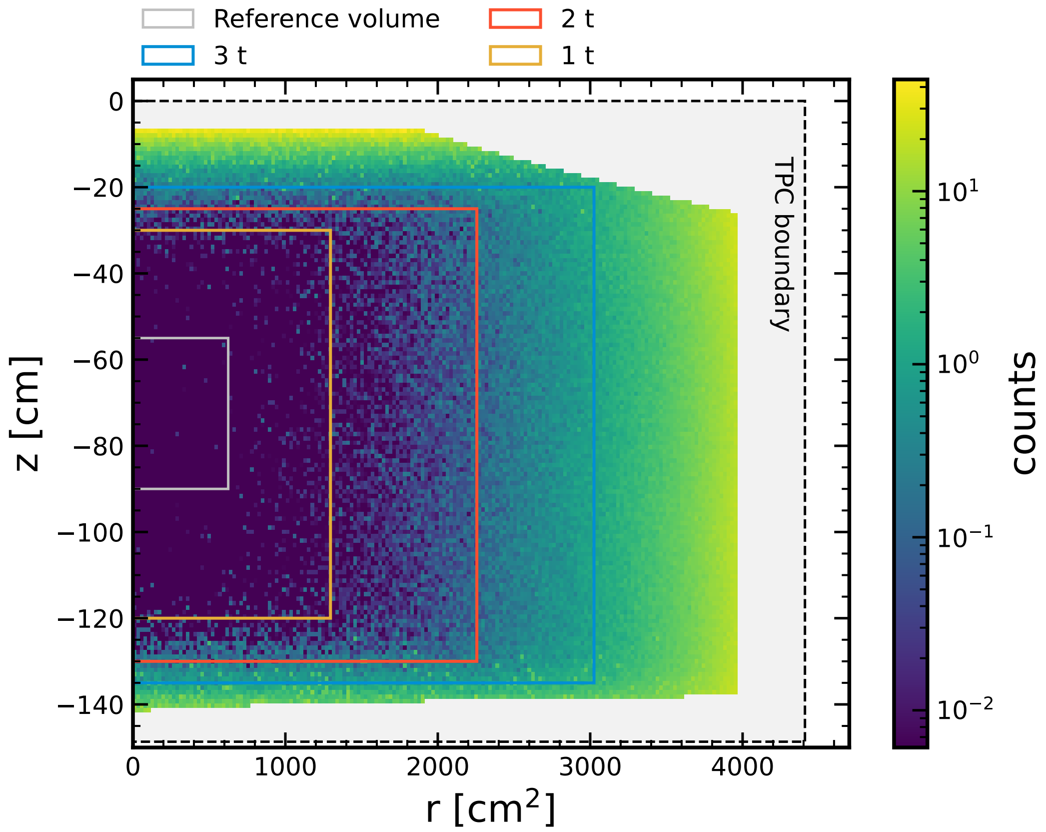

Figure 7.14: Two-dimensional simulated spatial distribution of the SS background as a function of r^2 and z. Only the region inside the low-energy ER fiducial volume was considered: the grey region was excluded in this analysis. The three fiducial volumes considered and the reference volume from which the pseudo-significance scan was performed are shown.

Table 7.1: Data selection adopted in the nucleon disappearance analysis. The table reports the name of the selections and their description.

CUT_DAQ_VETO	Reject events that are too close to a hardware veto start or stop.
CUT_INTERACTION_EXIST	Simple cut to select (S1; S2) events.
CUT_VALID_TRIGGER	Selection which ensures that at least either the main S1 or main S2 is considered a triggering peak. Otherwise, this is most likely an accidental coincidence. Note that the full name is *cut main is valid trigger peak*
CUT_RUN_BOUNDARIES	Removes events that are too close to the boundaries of a data acquisition period (a run), for which some event information could be lost.
CUT_S1_MAX_PMT	Reject events in which a PMT contributes most of the entire S1 area, mainly due to spurious PMT light emission or PMT after-pulses. It effectively rejects AC events. The selection threshold varies with the depth of the TPC: Towards the bottom of the TPC, events are more localized, and the threshold is less rigid.
CUT_S1_SINGLE_SCATTER	This selection checks if an alternative S1 in an event waveform exist to form a valid S1 and S2 pair. If so, the event is removed. The selection rejects mis-reconstructed events and MS.
CUT_S1_NAIVE_BAYES	This selection is based on the probability that a reconstructed S1 is a true S1. The probability is assigned by a Naive Bayes Classifier, a supervised machine learning algorithm trained on WFsim, which classifies peaks as S1-like or S2-like. It targets mis-reconstructed events and rejects AC events at low S1 areas.
CUT_S1_AFT	Reject mis-reconstructed events comparing the observed fraction of light collected by the top PMT array, given the (x;y;z) position, with the expected one derived by a data-driven map. Particularly effective in reducing the AC population. The criterion has been developed in the scope of this thesis (section 6.3.2).
CUT_S2_SINGLE_SCATTER	Based on the size of the alternative reconstructed S2, it rejects MS events. This criterion was discussed in section 7.1.1.
CUT_S2_RECON_POS_DIF	Using the three reconstruction algorithms, this selection rejects events when the reconstructed positions are too different. It mainly targets mis-reconstructed events.
CUT_S2_NAIVE_BAYES	Identical to the S1-based cut, but based on S2 features. It rejects events with poorly reconstructed S2s.
CUT_S2_WIDTH	The deeper the event, the larger the S2 width due to the electron cloud diffusion during the drift. This selection rejects events with unusual S2 width for the position where they have been reconstructed. Due to the presence of perpendicular wires, which distorts the electron cloud trajectory, the rejection threshold has two definitions depending on whether the events are reconstructed near or far from the wires. It rejects MS, AC, and unphysical events.

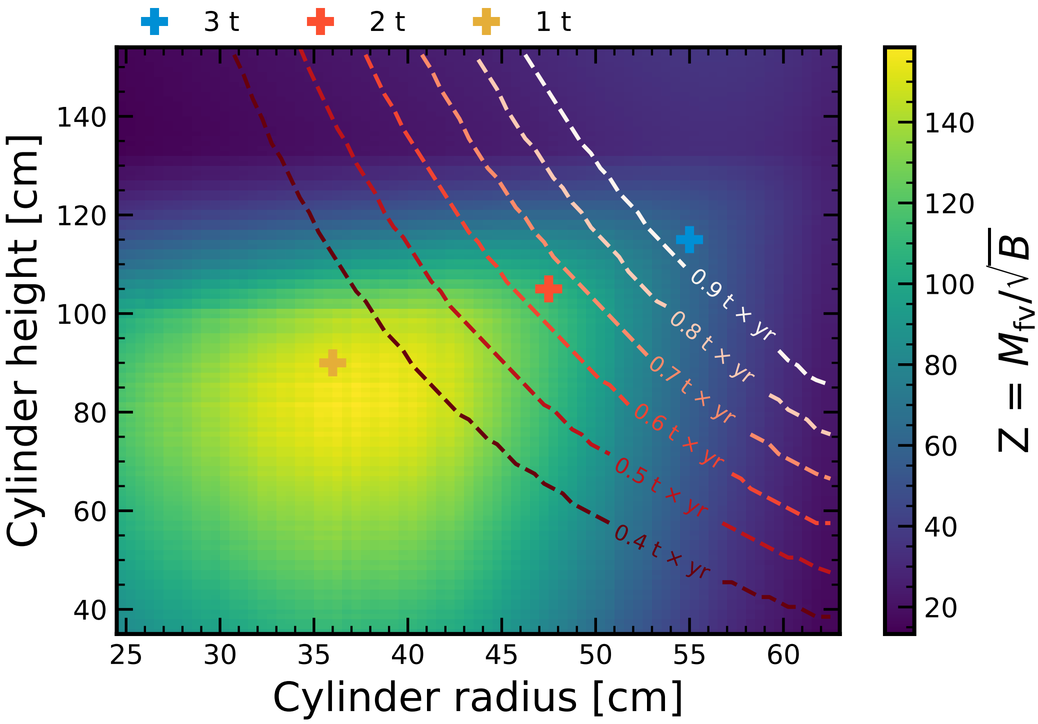

Figure 7.15: Pseudo-significance scan in r and z. The three fiducial volumes considered are shown. The colored lines show the boundary for exposures from 0.4 t × yr to 0.9 t × yr, computed given a 111.4 days livetime.

applied to ^{220}Rn calibration data in the low-energy ER analysis. This cannot be used here since ^{220}Rn calibration provides generalized data only for the low energy region where the naked ^{212}Pb β events occur. Above ~ 200 keV, where the first de-excitation transition starts to occur, these data no longer represent all backgrounds and signals. Then, the acceptance derived using the data-driven method cannot be applied to all spectrum components in the energy range of interest. This is mainly due to the S2 single site and S2 width criteria. The multi-step decay of ^{212}Pb and ^{214}Pb produce a true multi-site population, which can be properly reconstructed from the data processor, resulting in a higher loss from the S2 single site selection. The multi-step decays are often reconstructed together, leading to a substantially large S2 width. Therefore, the S2 width selection applied to ^{212}Pb and ^{214}Pb shows a higher efficiency loss than the remaining background events as well as the purely single-site signal events.

Section 7.1.1 showed that the full chain simulation replicates the single-to-multiple site population well. Similarly, the simulated S2 width was validated with the same data as a function of the event depth [323]. All of which motivates using the full chain simulation to derive the selection efficiency for each background and signal component. Producing enough simulated statistics for each component, however, is not feasible. Then, the simulated selection efficiency was derived for ^{212}Pb (3.8×10^6 events) and ^{214}Pb (6.2×10^7 events), and a dedicated simulated SS dataset for the remaining components, which are expected to produce pure SS events. The latter data consist of 10^7 Geant4 simulated β particles homogeneously distributed in the TPC volume with random energy up to 800 keV. At these energies, the electrons have a mean free path which is smaller, or at most comparable, to the SS-MS spatial resolution, which spans from ~ 0.4 cm at the top of the TPC to ~ 1.4 cm at the bottom. Therefore, these events make an excellent SS-simulated dataset.

The simulated events within the 2 t fiducial volume were selected, then the efficiencies of each cut reported in Tab.7.1 were computed applying the N-1 procedure in the reconstructed energy space, with 5 keV binning, after verifying that no cuts were correlated with any other selection criteria. For the S1 AFT cut, the data-driven efficiency was used. The uncertainties for each selection were computed with the Clopper-Pearson method [271]. This method of calculating uncertainty is based on the binomial distribution and relies only on the number of events per bin. No potential systematic effect due to the full chain simulation was included in the uncertainty derivation. A study in this direction is currently underway within the XENON collaboration and will help better understand the simulation-driven selection efficiency and simulated detector response. Next, the individual selection efficiencies were convolved together, and the uncertainties were summed in quadrature. The cumulative selection efficiency was interpolated with a spline to provide more suitable curves for the analysis, and the average semi-difference between upper and lower uncertainties propagated as curve uncertainties. Lastly, the cumulative selection efficiency was convolved with the detection efficiency to define the total selection efficiency.

The three simulation-driven total efficiencies in the range of interest, with and without S2 SS selection, are shown in Fig.7.16. The colored regions represent the uncertainties. At low energy, the three curves agree with each other, whereas above $\mathcal{O}(200\text{ keV})$ the different decay topology leads to a decrease for ^{212}Pb and ^{214}Pb as expected.

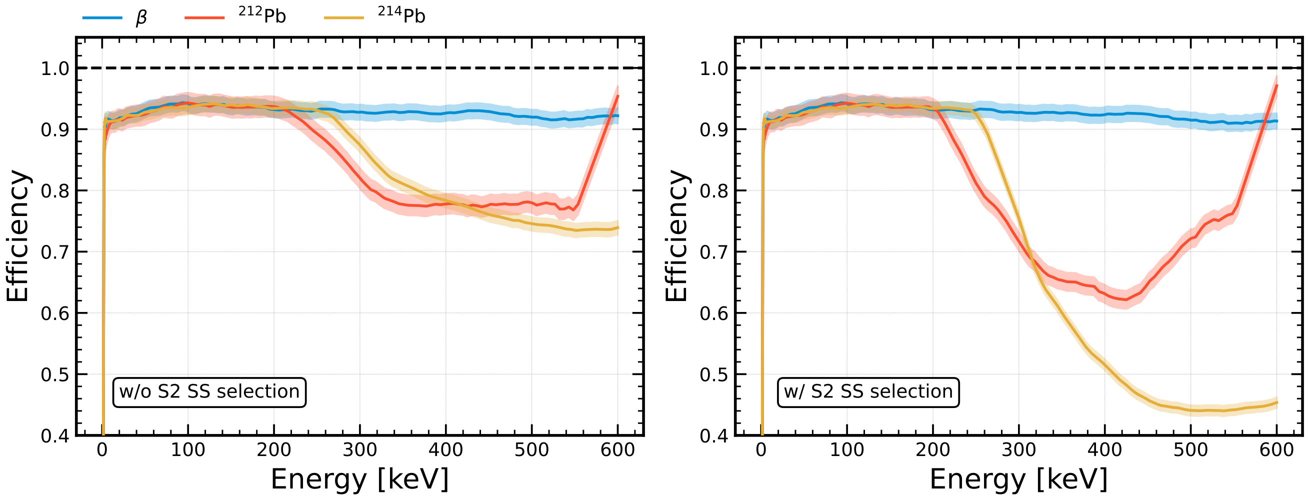

Figure 7.16: Total efficiencies with their uncertainty band for the β, ^{212}Pb, and ^{214}Pb full chain simulations. The efficiencies are shown with (left), and without (right) the S2 SS criterion considered. The decay topology of ^{212}Pb and ^{214}Pb leads to the presence of true MS events, which are responsible for the observed high-energy decrease in the efficiency plot on the left. The detection efficiency is included, and it is responsible for the decrease at low energy.

Since the S2 SS selection is performed directly on the output of FastSimulator, the spectra derived with it were scaled using the simulation-driven efficiency without the effect of this selection criterion. As shown in the next section, this is the case for the ^{212}Pb and ^{214}Pb background models. FastSimulator was also used for the radiogenic background of the detector materials and signals investigated. Therefore, the total β efficiency without the S2 SS criteria was used for them. The remaining background models were derived from theoretical calculations and were scaled with the β total efficiency with the S2 SS cut applied.

7.2.4 Background model

The background model for the nucleon disappearance analysis consists of eleven components, which can be reduced to three groups: elastic scattering of solar neutrinos with the atomic electrons, intrinsic radioactive isotopes (radioactive isotopes dissolved in the xenon itself), and radiogenic background from detector materials. This section presents every component and the expected reconstructed[5] SS energy spectrum in the nucleon disappearance analysis. A summary of the background model is provided at the end of the section.

Radiogenic background from detector materials

As extensively discussed in section 7.2.4 and in section 7.1.3, γ radiation produced by the decay of radionuclides in the detector components such as ^{60}Co, ^{40}K, and ^{137}Cs as well as ^{235}U, ^{238}U, and ^{232}Th, contributes to the total background budget in the energy range of interest via Compton scattering. The ^{238}U and ^{232}Th decay chains were split at ^{226}Ra and ^{228}Th, respectively, to account for possible decay chain disequilibrium. Their contribution was derived using the FastSimulator and normalized using the activities measured during the radioassay campaign after scaling them to account for the exponential decay of nuclei from the time of measurement to the onset of SR0. The scaled activities and their uncertainties have been shown in Tab.6.2. The 90 $\%$ confidence level upper limit was used as the contamination value if no activity above the background was found in the radioassay measurements.

Fig.7.17 shows the radiogenic background from detector materials in the region of interest of this analysis. The summed contribution from each isotope and detector component is shown with a solid black line. Limiting energies below 600 keV, ^{60}Co is the predominant component due to its high concentration, especially in the cryostat. Unphysical features are present in the low-energy region because of low simulation statistics. For energies below $\sim$ 200 keV, the γ-rays have a low probability to reach the inner part of the TPC. Given the tight fiducialization performed, to have a highly populated spectrum in the low-energy region, the Geant4 primaries need to be increased significantly. Since there is no reason not to expect a flat spectrum from Compton scatters at these energies, the total material background below 250 keV, i.e., where the spectra are dominated by statistic uncertainties, was approximated with a constant value equal to the average expected rate. To avoid discontinuity in the spectrum shape, the connection between the flat part and the rest of the spectrum was smoothed with a Savitzky–Golay filter. The approximated spectrum is shown with a dashed black line. The radioassay uncertainties can be propagated into the normalization and used to constrain the spectrum, as described in section 7.1.3. However, given the complications added by smoothing, it was decided to leave the approximate total background of the material free in the inference. These complications can be overcome by increasing the number of Geant4 primaries - currently $O(10^8)$ - to populate the low-energy region with more event. Nevertheless, this was not possible due to storage restrictions at the time of this analysis.

---

[5] Reconstruction should be understood to mean that energy resolution, energy bias, and the effect due to total selection efficiency are convolved in the theoretical energy spectrum, whether or not derived from simulations.

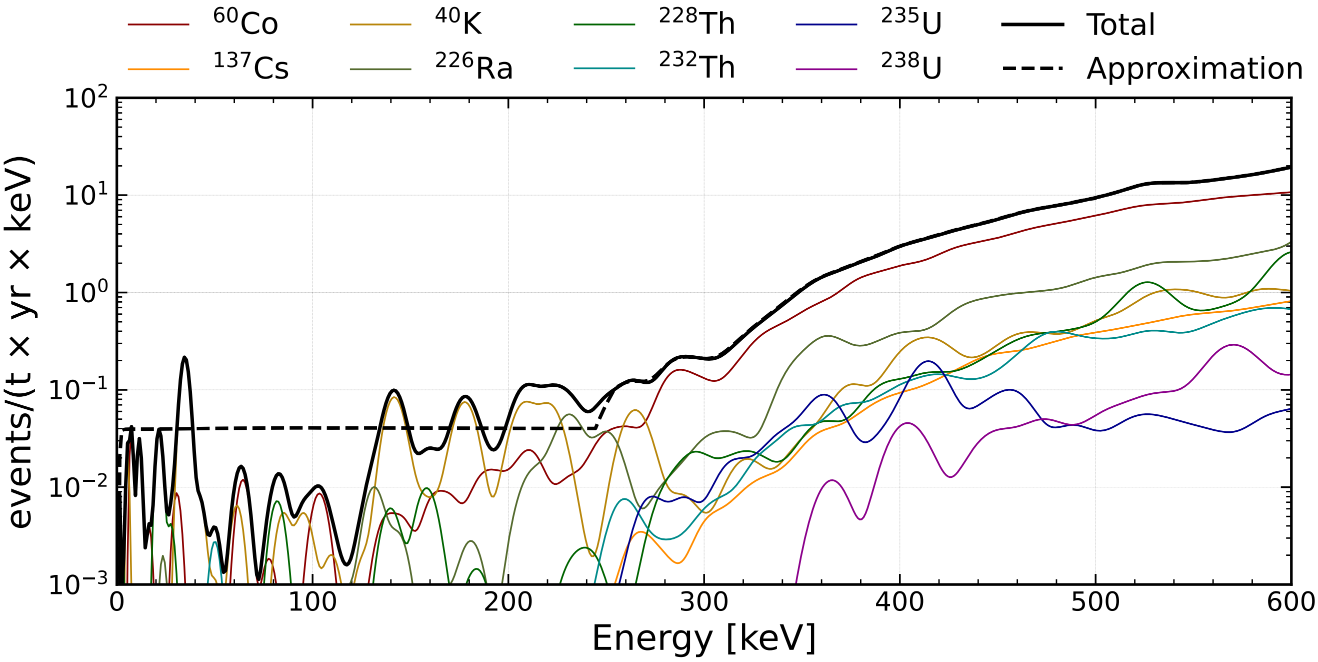

Figure 7.17: Expected SS radiogenic background from detector materials in the nucleon disappearance analysis, expressed as events/(t × yr × keV). The total SS simulated spectrum, equivalent to the sum of the nuclides listed in the legend, is shown with a solid black line. The spectrum is approximated at low energy as a flat contribution, as shown by the dashed black line.

^{214}Pb and ^{212}Pb

The ^{214}Pb is currently the most relevant background in xenon-based dark matter detectors at low electronic recoil energy. Similarly, ^{212}Pb constitutes a source of background, but it has been shown to have a smaller contribution [208, 214]. They both belong to a radon isotope decay chain. Respectively, ^{214}Pb is produced from ^{222}Rn, whereas ^{220}Rn decay leads to the creation of ^{212}Pb. These radon nuclides originally belong to ^{238}U and ^{232}Th decay chains contained in small traces in all materials. Thus, the radon atoms continuously emanate into the xenon target from the detector materials [324].

The decay chains are shown in Fig.7.18. ^{214}Pb (^{212}Pb) is created after two consecutive α decays, starting from ^{222}Rn (^{220}Rn) and passing through ^{218}Po (^{216}Po). Then, they decay via β to ^{214}Bi (^{212}Bi) generating the dangerous events. The bismuth nucleus undergoes β decay to ^{214}Po (^{212}Po) which decays immediately after to ^{210}Pb (^{208}Pb, stable) with a half-life of 164.3 μs (300 ns). The ^{210}Pb slowly disintegrates with 22.3 years half-life via β decay forming ^{210}Bi. The decay chain stops after an α decay to ^{206}Pb. The primary radon α decays have significantly different half-lives: 3.8 days for ^{222}Rn and 55.8 s for ^{220}Rn. A similar time difference is also present in the following α decays. Therefore, ^{214}Pb builds up more in the active target than ^{212}Pb, constituting a more dangerous background source. Several techniques are used to mitigate radon contamination, and they have already been discussed in section 3.3.3. These methods successfully lower the radon concentrations to $\mathcal{O}(\mu\text{Bq/kg})$ level. Thanks to the low concentration and the long half-life, the β decay from ^{210}Pb is not a source of concern. Also, ^{214}Bi is not expected to raise particular concern since its decay is observed in coincidence with the subsequent α decay. This allows for a high rejection efficiency for this type of event. At the time of this analysis, the rejection of ^{214}Bi was not calculated yet. However, previous analyses have shown a rejection larger than 99.8 % [302, 325]. Assuming the same rejection, the ^{214}Bi can be omitted from the background list. The same argument is also assumed for ^{212}Bi. The ^{220}Rn decay chain information have be taken from [326, 327, 314] and from [210, 328, 211, 329] for the ^{222}Rn decay chain.

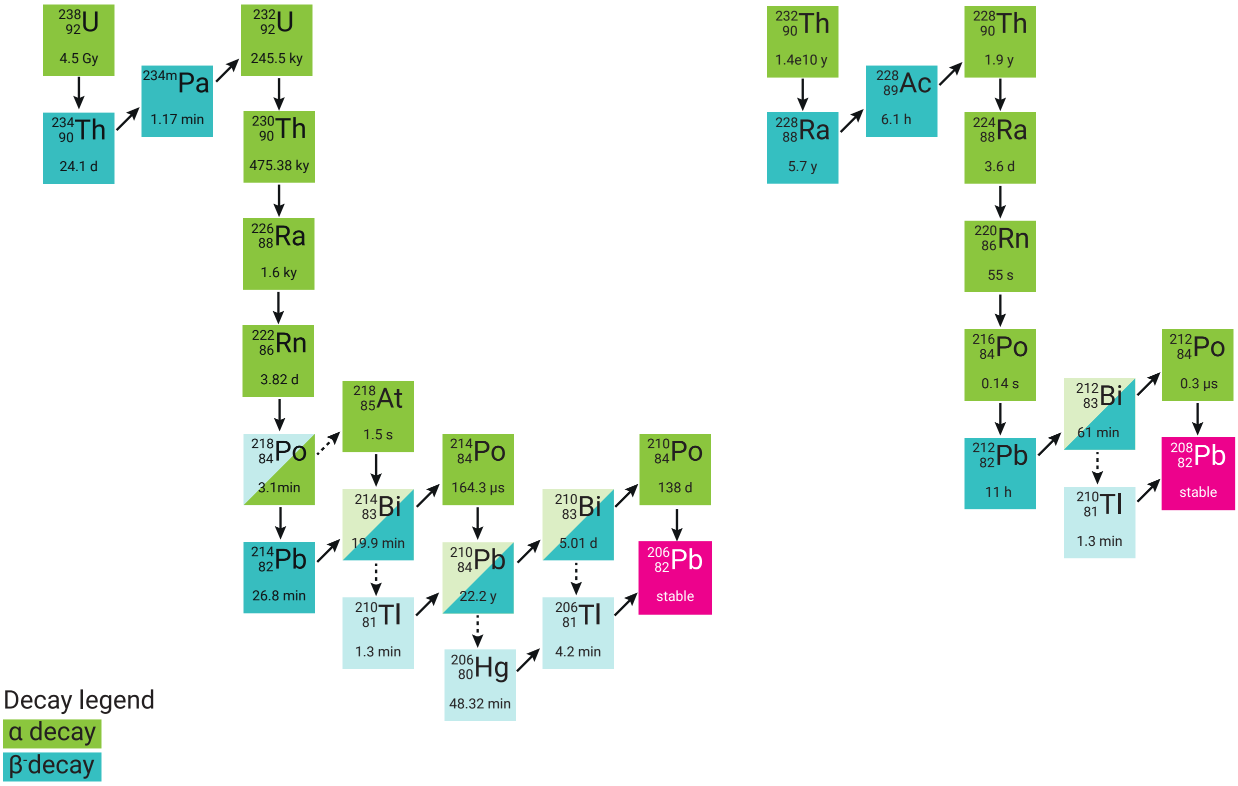

Figure 7.18: Decays chain of ^{238}U and ^{232}Th, progenitors of ^{214}Pb and ^{212}Pb, respectively. Scheme inspired from [324] and data taken from [330].

The characteristics of the decay of ^{212}Pb have already been presented in section 7.1.1. The decay of ^{214}Pb is similar but has excited states with higher energies. With a half-life of 27.06 minutes, ^{214}Pb undergoes a pure β decay only 12.7(9) % of the time. For ~ 87 % of the time, excited states of the daughter ^{214}Bi are populated. The available states are 295.2 keV (39.0(5) %), 351.9 keV (45.5(7) %), 533.68 keV (1.063(18) %), 893.0 keV (2.75(8) %). Another two levels at 258.87 keV and 888.7 keV are allowed, but with negligible probability (0.075(20) % and 0.015(4) %). The spectrum endpoint is at 1019 keV [211].

Contrary to low-energy ER analysis, which considered only the ^{214}Pb β decay to the ground state derived from theoretical calculation [208], the simulated spectrum was used in this analysis for both ^{212}Pb and ^{214}Pb nuclei. The expected SS energy spectra were derived using FastSimulator fed with 3.8×10^6 and $6.2{\times}10^7$ Geant4 primaries homogeneously distributed in the TPC volume for ^{212}Pb and ^{214}Pb, respectively. As mentioned in section 7.1.1, it was realized at a late stage of the analysis that Geant4 uses a different branching ratio (BR) for the ^{212}Pb decay compared to the one suggested in the literature. The spectrum utilized was simulated considering BR of 11.89 % for the ground state, while 83.034 % and 5.0759 % for the excited states of 238.6 keV ad 415.3 keV, respectively. Currently, the corrected BRs are being implemented in the XENONnT Geant4 simulation framework, and a new ^{212}Pb expected energy spectrum will be produced. The analysis will be performed again, however, as it will be explained in the following paragraphs, this is not expected to have a significant impact on inference since ^{212}Pb is a subdominant background, given its low concentration in the xenon volume.

The spectra were normalized following the prescription in section 7.1.3. The activity of ^{214}Pb can be constrained by measuring the α-activities from ^{218}Po and ^{214}Po α-decays, parent and daughter of ^{214}Pb in the decay chain, respectively. Similarly, the upper bound on the concentration of ^{212}Pb can be derived from the α-activities of previous α-decays from ^{220}Rn and ^{216}Po. The subsequent α-decay from ^{212}Po can be used as a lower bound. However, no measurements were available at the stage of this analysis. In conclusion, in SR0, the activity bounds were estimated to be [331]:

- $A_{^{218}\mathrm{Po}} = (1.69 \pm 0.07)$ µBq/kg;
- $A_{^{214}\mathrm{Po}} = (0.78 \pm 0.03)$ µBq/kg;
- $A_{^{220}\mathrm{Rn}} = (0.080 \pm 0.002)$ µBq/kg;
- $A_{^{216}\mathrm{Po}} = (0.078 \pm 0.002)$ µBq/kg.

The reason why the measured activity of ^{218}Po is roughly half that of ^{214}Po lies in the fact that ^{214}Pb has a sufficiently long half-life to migrate to the outer region of the detector, plating out on the PTFE walls so that part of the decay signal is lost. The ^{214}Pb activity in the fiducial volume is expected to lie between the two measured activities, therefore $A_{^{214}\mathrm{Pb}}$ was constrained within $A_{^{216}\mathrm{Po}} + \delta A_{^{216}\mathrm{Po}}$ and $A_{^{214}\mathrm{Po}} - \delta A_{^{214}\mathrm{Po}}$, and the average between $A_{^{216}\mathrm{Po}}$ and $A_{^{214}\mathrm{Po}}$ was used as initial value in the fitting. In contrast, the ^{212}Pb activity cannot be limited within a range. So, it was left free in the inference and initialized with the average value of $A_{^{220}\mathrm{Rn}}$ and $A_{^{216}\mathrm{Po}}$.

In Fig.7.19 the expected energy spectra of ^{214}Pb and ^{212}Pb in the nucleon disappearance analysis range of interest are shown. The wiggles at low energy in the ^{212}Pb spectrum are due to the low simulated statistics. The spectrum was linearly interpolated to avoid nonphysical features that might invalidate the fit.

^{85}Kr and solar ν

Natural Kr ($^{\mathrm{nat}}$Kr), present in the air, contaminates the xenon during the air liquefaction process utilized to obtain it. As a result, the xenon inventory contains the fission product ^{85}Kr, which is present in atmospheric krypton as a result of human-made nuclear activities [332]. It decays via β-emission to the ground state of ^{85}Rb 99.463(10) % of the time with 10.73 years half-life and an endpoint of 687.0 keV. It can also decay to an excited state of ^{85}Rb, at the energy of 514.0 keV, but the probability is low (0.434(10) %) [209]. The same theoretical spectrum as the low-energy ER analysis was used.

Even though it is a subdominant background thanks to the cryogenic distillation deployed in XENONnT [206], the expected activity over time was constrained by combining the measured isotopic abundance of ^{85}Kr/$^{\mathrm{nat}}$Kr (2×10^{-11} (mol/mol)), based on seasonal measurements of ^{85}Kr activity in the LNGS air of 1.4 Bq/m^3 [208], with three dedicated RGMS measurements [207] of xenon samples taken during SR0. In Fig.7.20 are shown the RGMS measurements (black points) and the linear time evolution model (dashed black line), together with 1σ (green) and 2σ (yellow) uncertainty bands derived from the covariance matrix of the fitted

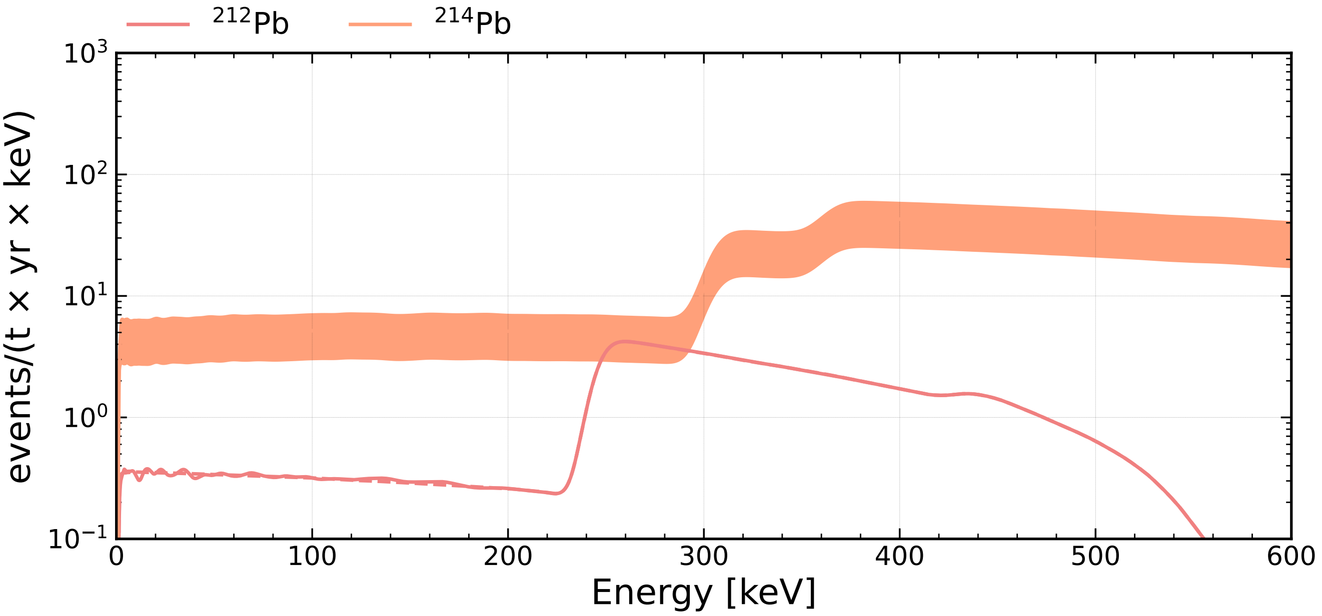

Figure 7.19: Expected background from ^{212}Pb (coral) and ^{214}Pb (salmon) in the nucleon disappearance analysis. The ^{214}Pb is shown as a band with the edges representing the limits imposed on the activity. On the contrary, ^{212}Pb is displayed as a continuous line since it was not constrained. The wiggles present at low energy, due to statistical uncertainties, are removed by interpolating the spectrum below 200 keV.

model [333]. A slight concentration increase was observed. The increase can be due to a small air leak $((4.30 \pm 3.26) \times 10^{-6}$ mbar l/s) or due to PTFE outgassing [333]. The average concentration over the period considered (red point) was used to normalize the spectrum, and the error propagated into the inference as a constraint. The estimated value is (59 ± 15) ppq, where ppq is 1×10^{-15} $(\mathrm{mol}/\mathrm{mol})$. The low concentration value makes the contribution of ^{85}Kr subdominant in the range of interest.

The elastic scattering of solar neutrinos with atomic electrons of the xenon target produces a continuous ER background. The spectrum in energy space is taken from the low-energy ER analysis. The standard neutrino flux in the Large Mixing Angle Mikheyev-Smirnov-Wolfenstein (LMA-MSW) model, to account for the neutrino oscillation both in the vacuum between the Earth and the surface of the Sun and in the medium between the solar surface and core [303, 304], is convolved with the SM cross-section considering electrons bound to nuclei instead of the free electron approximation [305]. The predominant contribution arises from *pp* neutrinos, followed by ^{7}Be neutrinos. Together they contribute 98 % of the neutrino-ER induced events [151]. The former has a continuous spectrum ended at 420 keV, whereas ^{7}Be neutrinos have two discrete energies: 862 keV (89.6 %) and 384 keV (10.4 %) [334]. A 10 % uncertainty is assigned to solar neutrino flux based on the Borexino measurement [306]. Due to the small cross-section, the events are expected to be only single-site. This background contribution is subdominant over the energy range of interest.

The expected ^{85}Kr and solar ν energy spectra are shown in Fig.7.21. The effect of the atomic binding of electrons is responsible of the stepping features at low energies in the solar neutrinos spectrum, whereas the drastic change in slope at $\sim$ 260 keV indicates the energy endpoint of *pp* neutrinos contribution [335].

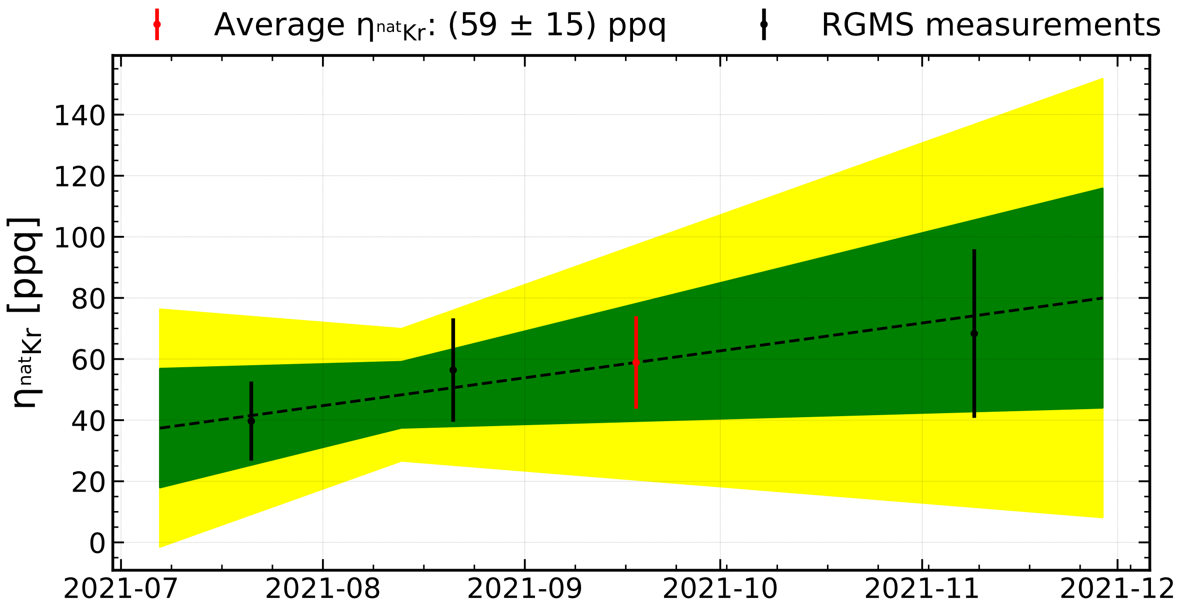

Figure 7.20: Time evolution of ^{nat}Kr concentration (η in ppq = 1×10^{-15} (mol/mol)) during SR0. The black points are the RGMS measurements, while the dashed black line shows the concentration model over time, with 1σ (green) and 2σ (yellow) uncertainty bands. The average concentration over the period considered is shown in red.

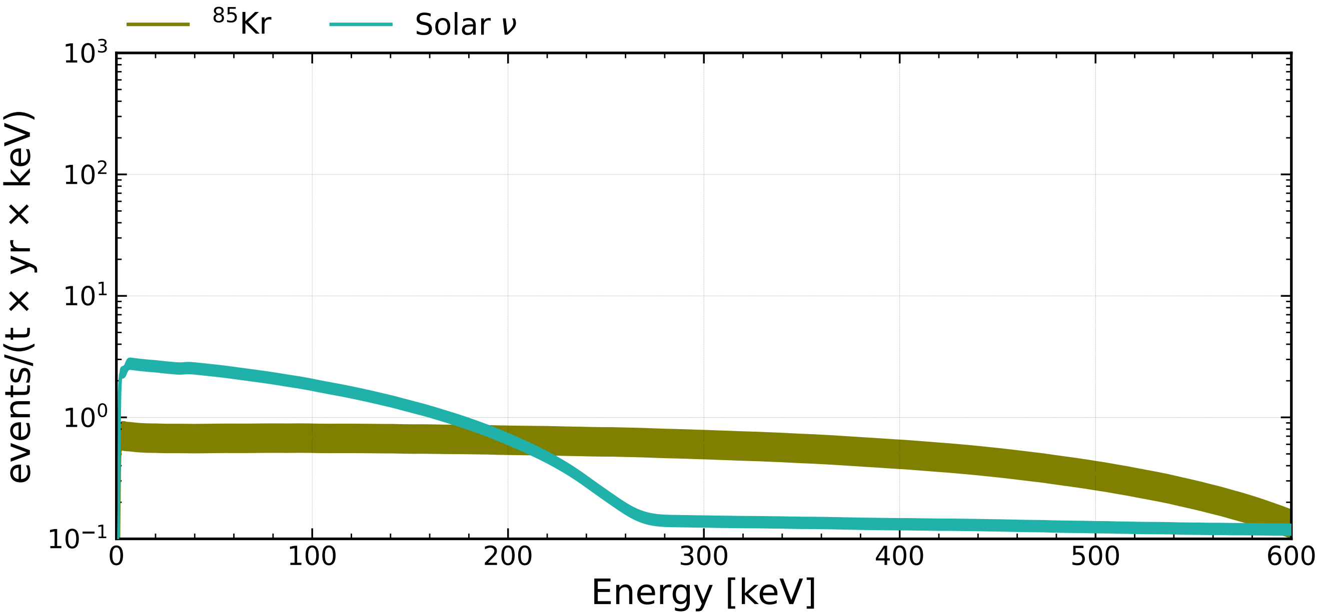

Figure 7.21: Expected background from ^{85}Kr (olive) and solar ν (seagreen) in the nucleon disappearance analysis. They are displayed as bands whose edges represent the size of relative uncertainties discussed in the text.

^{136}Xe and ^{124}Xe

Having successfully reduced ^{222}Rn concentration, the shape of background models within (40; 140) keV is governed by two second-order weak processes: the 2$\nu\beta\beta$ of ^{136}Xe and 2νECEC of ^{124}Xe [208]. Both can be constrained by using xenon isotopic abundance measurements performed in situ with a residual gas analyzer [336] and the half-lives published in literature. The measured ^{136}Xe abundance is (8.97 ± 0.16) % (mol/mol), while an abundance of (0.101 ± 0.006) % (mol/mol) was measured for ^{124}Xe. The half-life adopted for 2νββ of ^{136}Xe from EXO-200 is $(2.165 \pm 0.016_{\text{stat}} \pm 0.059_{\text{sys}}) \times 10^{21}$ years [302]. The most recent half-life estimate for 2νECEC of ^{124}Xe from XENON1T is $(1.1 \pm 0.2_{\text{stat}} \pm 0.1_{\text{sys}}) \times 10^{22}$ years [215]. Contrary to the low-energy ER analysis, the 2νECEC of ^{124}Xe was constrained in the fit.

The two electrons emitted by 2νββ decay are expected to scatter almost immediately in the decay's proximity, leading to a continuous SS population with the sum of the electron energies. As in the low-energy ER analysis, the average spectrum between the higher-state dominated (HSD) model [337] and the single-state dominated (SSD) model [338] was used. The total relative uncertainty in the expected spectrum is 3.7 %, which includes a 1.5 % relative uncertainty for the different theoretical shapes of the HSD and SSD models, a 2.8 % relative uncertainty in the EXO-200 half-life, and a 1.8 % relative uncertainty in the measured abundance [208].

In 2νECEC decay, two inner-shell electrons are captured simultaneously when two protons in the nucleus are converted into neutrons, producing two undetected neutrinos. A characteristic cascade of X-rays and Auger electrons follows the filling of the shell vacancies by outer orbital electrons. The most probable transition of the KK-capture leads to a 64.3 keV characteristic line, whereas the peaks at 37.29 keV and 10.01 keV are due to the KL-capture and LL-capture, respectively [215]. Given the low energy involved, the events are reconstructed as SS. The total relative uncertainty in the 2νECEC decay rate is given by the sum in quadrature of the XENON1T half-life relative uncertainty (18 %) and the measured abundance relative uncertainty (5 %). The energy spectrum adopted is discussed in [215]. The expected signals from ^{136}Xe and ^{124}Xe in the energy range considered are shown in Fig.7.22.

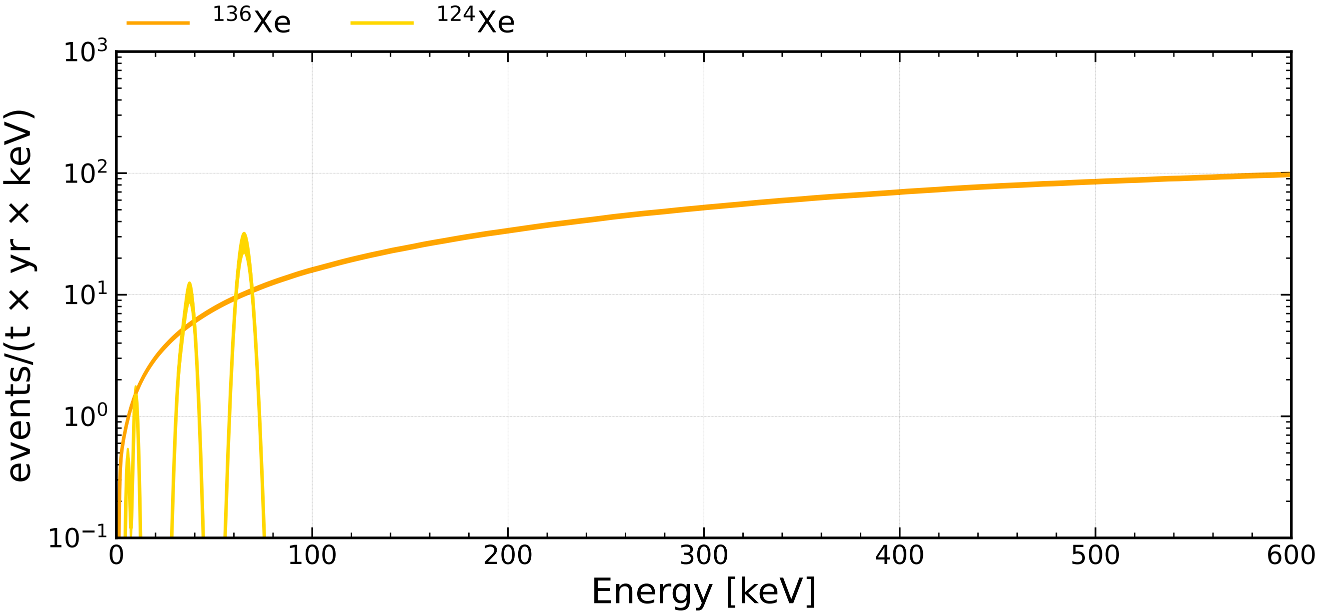

Figure 7.22: Background expected from 2νββ decay and 2νECEC decay of ^{136}Xe (orange) and ^{124}Xe (yellow), respectively, in the nucleon disappearance analysis. They are displayed as bands whose edges represent the size of relative uncertainties discussed in the text.

Neutron activation backgrounds and ^{83m}Kr

Three background components considered were produced during neutron calibration. ^{131m}Xe and ^{129m}Xe are activated by inelastic neutron scattering, whereas ^{133}Xe is produced by thermal neutron capture on ^{132}Xe. The metastable states decay via internal conversion (IC).These decays induce two mono-energetic backgrounds at 163.9 keV and 236.1 keV for ^{131m}Xe [339] and ^{129m}Xe [340], respectively. While ^{131m}Xe de-excites in one step, ^{129m}Xe has an intermediate energy level of 39.6 keV. However, this level has a half-life of $\sim$ 0.97 ns, so the two transitions are resolved together. Given the energy considered, the events are expected to be mostly SS. ^{133}Xe undergoes a β-decay to an excited state of ^{133}Cs, whose de-excitation leads to an 81 keV prompt γ-ray. The de-excitation occurs within a few ns. Therefore, the two decays are reconstructed together, resulting in a continuous SS spectrum starting at 81 keV [341].

These xenon isotopes have sufficient half-lives to appear in the physics search data. Respectively, the half-lives are: 11.8(4) days for ^{131m}Xe [339], 8.88(2) days for ^{129m}Xe [340], and 5.2475(5) days for ^{133}Xe [341]. A time-dependence study was performed in a 4 t cylindrical fiducial volume [151], combining calibration and physics search data. The rate evolution over time in specific energy windows was modeled to infer the presence of neutron-induced backgrounds. The windows are given by the energy of the peak $\pm 2\sigma_E$, where σ_E is given by the energy resolution (see Eq.6.12). For ^{133}Xe, which has no peak, the region within (80, 120) keV was used. By modeling the rate evolution as an exponential decay plus a linear background, it was possible to prove their presence in the physics search data. The ^{241}AmBe source was moved around the outer cryostat during the calibration. Therefore, the neutron flux entering the TPC was not constant. In particular, the source was placed outside the neutron veto calibration in the center part of the calibration. As a result, no activation was observed. Afterward, the source was moved closer to the cryostat, and the number of events in the three energy regions investigated increased again. These two activation periods were accounted for in the models. In Fig.7.23 are shown the models derived with their uncertainty bands. The fitted half-lives (χ^2/degrees of freedom) for ^{129m}Xe, ^{131m}Xe, and ^{133}Xe were (7.2 ± 0.5) days (1.57), (11.3 ± 0.8) days (2.2), and (5.4 ± 0.5) days (1.1), respectively. The half-lives of ^{131m}Xe and ^{133}Xe agree with the literature values. Instead, the value derived for ^{129m}Xe has some tension with the commonly adopted (8.88 ± 0.02) days [340]. The reason is not yet understood; the hypothesis is that it is due to a wrong assumption of linear background below the exponential decay. Studies are ongoing to improve the modeling. Since the descriptions are not sufficiently accurate (see χ^2/degrees of freedom), the neutron-activated background activities were left unconstrained in the inference.

Other xenon isotopes are activated during neutron calibration. However, given the short half-lives and the lack of evidence in the rate evolution modeling approach, they were not considered. Specifically, reference is being made to ^{125}Xe and ^{137}Xe. One of the searched signals, ^{127}Xe, can be produced by thermal neutron capture on ^{126}Xe. As shown in section 7.2.1, ^{127}Xe has a prominent line at 234.2 keV which should lie below the ^{129m}Xe peak. No evidence was found using the rate evolution modeling approach if two exponential decays were used to fit the same data utilized for the ^{129m}Xe study. However, this study was performed with data before mid-august. Additional studies have to be performed, including the remaining period.

Two other approaches can be used to estimate the production of ^{127}Xe during neutron calibration. Comparing the abundance of ^{132}Xe (26.9 % ($^{mol}/_{mol}$)) and ^{126}Xe (0.09 % ($^{mol}/_{mol}$)) and the thermal neutron capture cross-sections, equivalent to 0.4 barn [342] and 3.8 barn [343], a factor $\sim$ 31 less ^{127}Xe nuclei were

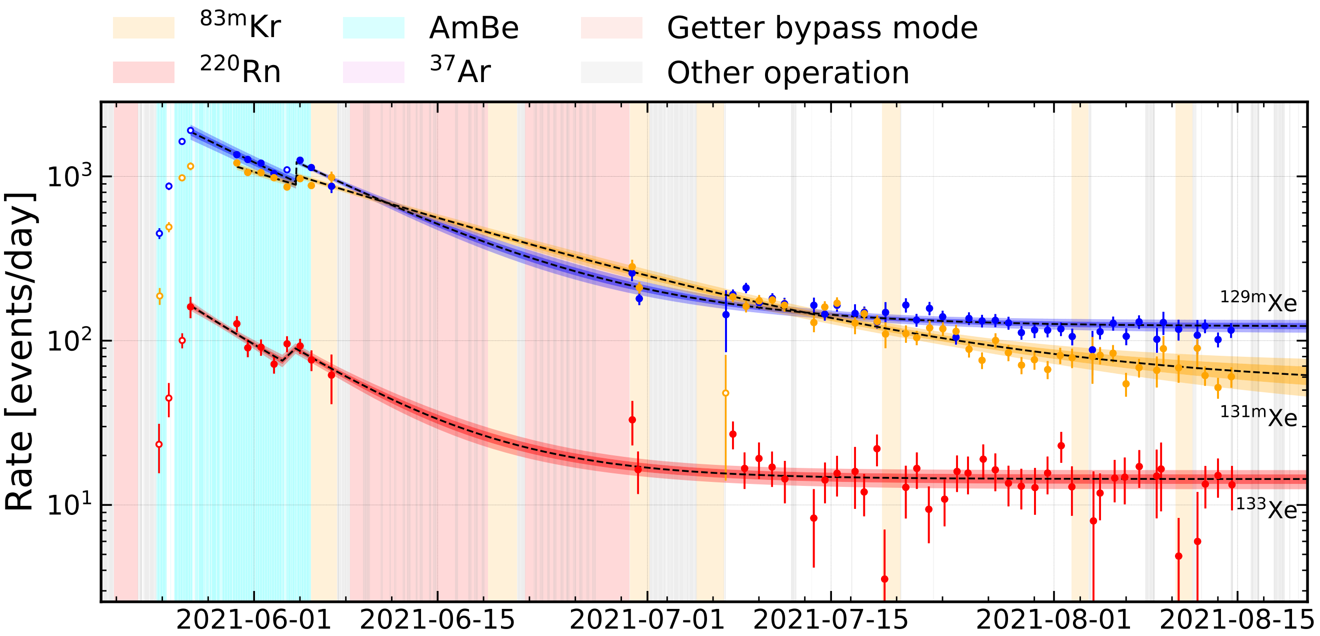

Figure 7.23: Temporal evolution model with 1 and 2 σ band uncertainties of neutron-induced background rate based on an exponential plus linear background fit of ^{129m}Xe (blue), ^{131m}Xe (orange), and ^{133}Xe (red). The rate was extracted in specific energy windows given by the energy of the peak $\pm 2\sigma_E$, where σ_E is given by the energy resolution (see Eq.6.12). For ^{133}Xe, which has no peak, the region within (80, 120) keV was used. The Poisson standard deviations were used as errors for the extracted rate. The calibration periods, e.g., ^{241}AmBe, are shown as reported in the legend.

produced compared to ^{133}Xe during the neutron calibration. Considering the ^{133}Xe activity inferred from the rate evolution model at the end of ^{241}AmBe calibration, equal to (196 ± 11) nBq/kg, the expected ^{127}Xe activity is (3.8 ± 0.2) nBq/kg. Despite the low value, this activity implies $\mathcal{O}(100$ events$)$ in the nucleon disappearance data. In the context of low-energy ER analysis, the production of ^{127}Xe was estimated via Geant4 simulation. This study assessed a conservative activity at the end of ^{241}AmBe calibration equal to (15 ± 2) nBq/kg which implies $\mathcal{O}(300$ events$)$ in the nucleon disappearance data [344]. These estimates are conservative because they do not include nuclei decayed during calibration. Both point towards a presence of ^{127}Xe, even though no clear evidence was observed in the rate evolution model approach.

The last component of the background originates from the leftovers of ^{83m}Kr calibrations, whose tails in rate appear in the physics search data. This source was used every two weeks during SR0 to monitor the detector performance, derive detector parameters, and develop selection criteria. Knowing the period when the source was introduced into the detector and its half-life, a time-based cut could be used to further suppress this background, without any significant impact on exposure. However, this component is not dangerous for any of the sought signals. Therefore, no dedicated cuts were used. The associated background was modeled as a monoenergetic peak at 41.5 keV.

The expected signatures in the energy space from these decays are shown in Fig.7.24. The spectra are normalized with the following activities: 15 nBq/kg (^{129m}Xe), 59 nBq/kg (^{131m}Xe) and 0.35 nBq/kg (^{133}Xe).

These activities, equal to the average activities in SR0 derived from the temporal evolution models, are used as initialization in the inference. No temporal evolution model was derived for ^{83m}Kr. Therefore, a conservative activity of 1 nBq/kg was used as initialization. No constraints were derived for these components; therefore, they were left free to vary in the inference.

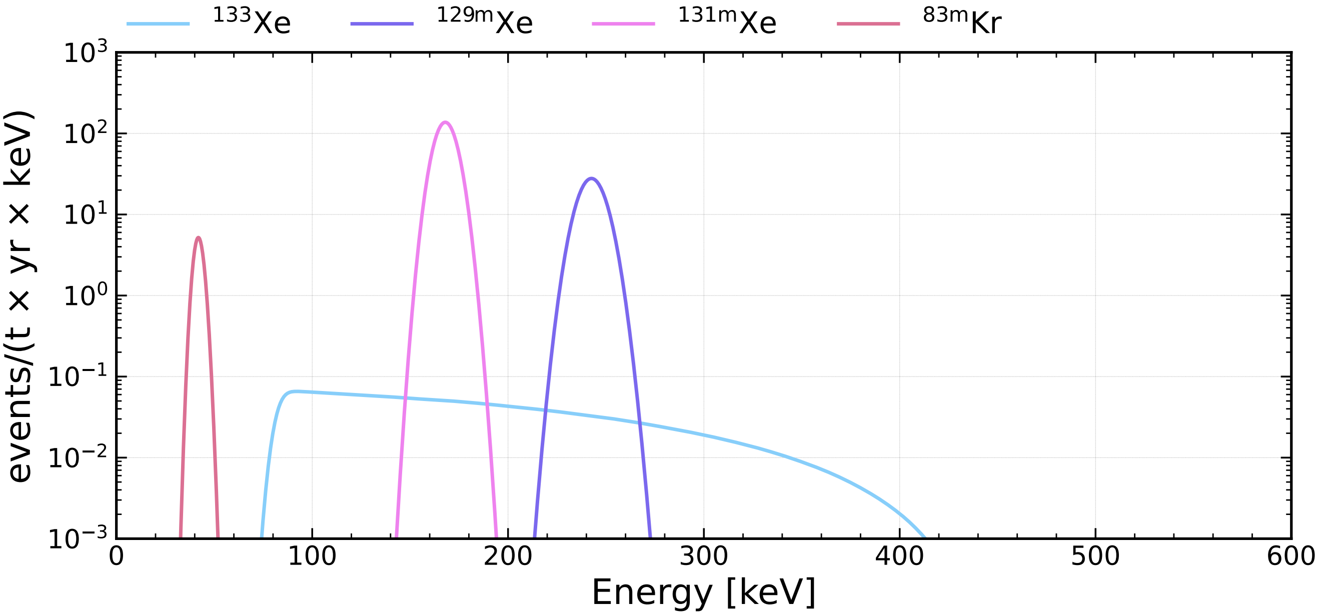

Figure 7.24: Expected background in the energy space from ^{133}Xe, ^{129m}Xe, ^{131m}Xe, and ^{83m}Kr. The normalization of xenon isotope is informed by the temporal evolution models, whereas a conservative activity of 1 nBq/kg was used for ^{83m}Kr.

Other not-considered backgrounds

As in the low-energy ER analysis, ^{125}I was not considered. This isotope is produced from ^{125}Xe decay [345]. In the context of the low-energy ER analysis, the presence of ^{125}I (59.4 days half-life) was tested in the TED data, and the result was consistent with zero. Likely, the reason lies in the updated cryogenic recirculation where the xenon is purified faster than before and ^{125}I is removed efficiently before it can decay, as already observed in XENON1T. If the ^{125}I is removed by the purification, so is ^{128}I. However, assuming a reasonable purification speed of 1 day[6] (notice that the entire liquid xenon mass is exchanged every 2 days), possible ^{128}I nuclei (24.99 minutes half-life) have several half-lives available for decaying before getting removed from the purification. Therefore, no reduction has been assumed for this nuclide.

Moreover, ^{37}Ar and ^{3}H were not part of the background model. ^{37}Ar is found in small quantities in the atmosphere, and then it can be mixed with the xenon during the distillation process. It is generated by the cosmic bombardment of atmospheric argon, mainly via the spallation process ^{40}Ar(n, 4n)^{37}Ar but also via neutron capture on ^{36}Ar. Atmospheric ^{37}Ar can also be produced from cosmic rays starting from calcium via ^{40}Ca(n, α)^{37}Ar [346]. No significant traces are expected to be present in the xenon inventory due to the extensive distillation of krypton, which also removed argon, performed during the commissioning phase [347]. Furthermore, all the xenon inventory has been underground for years, so no cosmogenic

---

[6] In XENON1T it was estimated to be of $\mathcal{O}$(10 days) [264].

activation is expected. The remaining possibility for ^{37}Ar to enter the xenon volume is detector air leakage. This was estimated to be negligible from the Kr concentration evolution. In the same way, ^{3}H can be cosmogenically produced in many materials by several production channels [348]. Owed to its long half-life of 12.32 years [349], it can enter the xenon volume through material outgassing. In addition, ^{3}H is naturally present in H_2O and H_2, which are outgassed continuously from the detector materials into the xenon volume. To mitigate outgassing, the XENONnT detector was under a long evacuation before filling with xenon. Similar to ^{125}I, in the context of low-energy ER analysis, no traces of ^{3}H and ^{37}Ar were found in the SR0 physics search data [208].

Background model summary

The background model has been discussed thoroughly in the previous paragraphs. The independent measurements and the knowledge gained from other analyses were used to derive the normalization for each component and the constraints for some of them. In Tab.7.2 the backgrounds considered, their origin, and the information used for their normalization are reported. If available, the constraints are listed as well.

Components	Origin	Normalization	Constraints
Materials	Radioactive nuclei in detector materials	Activities from radioassay scaled from the day of the measurement till the beginning of SR0	
^{212}Pb	^{220}Rn, emanated from detector materials	0.078 μBq/kg, average α-activities of ^{220}Rn and ^{216}Po	
^{214}Pb	^{222}Rn emanated from detector materials	1.286 μBq/kg, average α-activities of ^{218}Po and ^{214}Po	Flat constraint $[0.747, 1.761]$ μBq/kg, lower (upper) limit from α-activity of ^{214}Po (^{218}Po) minus (plus) its uncertainty
^{85}Kr	By-product of human-made nuclear activities, present in xenon from air	RGMS measurements, average concentration of 59×10^{-15} (mol/mol)	25 % relative uncertainty in the concentration
Solar ν	*pp* and ^{7}Be (98 %), other (2 %)	Standard neutrino flux in the LMA-MSW model convolved with SM cross-section, accounting for atomic electron binding energy	10 % relative uncertainty in the neutrino flux
^{136}Xe	Intrinsic isotope in the xenon inventory	EXO-200 $T_{1/2} = 2.165 \times 10^{21}$ yr, measured concentration in XENONnT of 8.97 % (mol/mol)	3.7 % relative uncertainty from theoretical shapes (1.5 %), half-life (2.8 %) and abundance (1.8 %)
^{124}Xe	Intrinsic isotope in the xenon inventory	XENON1T $T_{1/2} = 1.1 \times 10^{22}$ yr, measured concentration in XENONnT of 0.101 % (mol/mol)	18.7 % relative uncertainty from half-life (18 %) and abundance (5 %)
^{131m}Xe	Inelastic neutron scattering	59 nBq/kg, average activity in SR0 derived from the temporal evolution model	
^{129m}Xe	Inelastic neutron scattering	15 nBq/kg, average activity in SR0 derived from the temporal evolution model	
^{133}Xe	Thermal neutron capture	0.35 nBq/kg, average activity in SR0 derived from the temporal evolution model	
^{83m}Kr	Leftovers of ^{83m}Kr calibrations	1 nBq/kg	

Table 7.2: Background sources considered in the nucleon disappearance of ^{129}Xe analysis. The references are reported in the text.

7.2.5 Statistical framework

The observed energy spectrum was fitted using the maximum likelihood method considering the number of events per bin according to the Poisson distribution. The relevant likelihood function $\mathcal{L}$ for a histogram having b bins labeled by the index i running from 1 to b is:

$$\mathcal{L}(\vec{y};\vec{n}) = \prod_{i=1}^{b} \frac{e^{-y_i}\, {y_i}^{n_i}}{n_i!}, \tag{7.3}$$

where y_i and n_i are the numbers of expected and observed events after applying detector and selection effects, $\vec{y} = (y_1, y_2, ..., y_b)$, and $\vec{n} = (n_1, n_2, ..., n_b)$. Following [350], another statistic can be constructed from Eq.7.3 using the likelihood ratio test for the goodness-of-fit theorem. Since the first derivative of $\mathcal{L}$, used to estimate the parameter of interest, would not be affected by any multiplicative factor, Eq.7.3 can be divided by the constant term $\mathcal{L}(\vec{n};\vec{n})$, where y_i is replaced by its model-independent maximum likelihood estimation n_i:

$$\lambda = \frac{\mathcal{L}(\vec{y};\vec{n})}{\mathcal{L}(\vec{n};\vec{n})} \tag{7.4}$$

Taking the natural logarithm converts λ into the form of a general χ^2 statistic [351]:

$$\chi^2_\lambda = -2\ln\lambda = -2\ln\mathcal{L}(\vec{y};\vec{n}) + 2\ln\mathcal{L}(\vec{n};\vec{n}) = -2\sum_i \left(y_i - n_i + n_i \ln\left(\frac{n_i}{y_i}\right)\right) \tag{7.5}$$

The "Poisson likelihood χ^2" asymptotically obeys a χ^2 distribution for large data samples. Therefore, the minimization of χ^2_λ can be used for point estimation, as well as interval estimation and goodness-of-fit [352].

Each component of the background and signal searched f contributes to the number of events predicted by the model. A scaling parameter r_j is assigned to each component j such that the expectation in the ith bin can be written as:

$$y_i = \sum_{j}^{\text{components}} r_j \times f_{i,j}\,, \tag{7.6}$$

where $f_{i,j}$ is the expected event rate per bin of the j component of the model, either signal (s) or backgrounds (b) normalized to a specific activity, and $\vec{r} = (r_{b,1}, r_{b,2}, ..., r_s, ..., r_j)$ are the scaling parameters derived from the χ^2_λ minimization. In this context, the parameter of interest is r_s, whereas the remaining $\vec{r}_b = (r_{b,1}, r_{b,2,..,r_{j\text{-}1}})$ are the nuisance parameters. Ancillary terms are considered in χ^2_λ to constrain the nuisance parameters whenever a constraint is available. Section 7.2.4 presented the independent measurements $(c_k \pm \delta c_k)$ available to restrict some parameters r_k. These are introduced in the minimization routine as Gaussian penalty terms as follows:

$$\sum_{k}^{\text{constraints}} \left(\frac{r_k - c_k}{\delta c_k}\right)^2 \tag{7.7}$$

an exception is made for ^{214}Pb which instead is constrained within an interval. For a summary of the constraints c_k and their uncertainties δc_k refers to Tab.7.2. Summing all the ingredients, the χ^2_λ object to minimize is:

$$\chi^2_\lambda = -2\sum_{\mathrm{i}} \Big(\sum_{\mathrm{j}} (f_{\mathrm{i,j}} \times r_{\mathrm{j}}) - n_{\mathrm{i}} + n_{\mathrm{i}} \ln\Big(\frac{n_{\mathrm{i}}}{\sum_{\mathrm{j}} (f_{\mathrm{i,j}} \times r_{\mathrm{j}})}\Big)\Big) + \sum_{\mathrm{k}} \Big(\frac{r_{\mathrm{k}} - c_{\mathrm{k}}}{\delta c_{\mathrm{k}}}\Big)^2 , \tag{7.8}$$

where the index i runs over the bins, the index j represents the background and signal components, and the index k is for the constraint terms.

The search for new phenomena - in this case, the baryon violation process - follows the description provided by [353]. The test statistic for the discovery of positive signal q_0 is used to quantify the level of agreement with data of the signal hypothesis H_1, compared to the background-only hypothesis H_0. The test statistic q_0 is computed as follows:

$$q_0 = \begin{cases} -2\ln\lambda(0) & \hat{r}_{\mathrm{s}} \geq 0 \\ 0 & \hat{r}_{\mathrm{s}} < 0 \end{cases} \tag{7.9}$$

where $\hat{r}_{\mathrm{s}}$ is the best fit of the parameter of interest, whereas $\lambda(0)$ is the likelihood ratio defined as:

$$\lambda(0) = \frac{\ln\mathcal{L}(r_{\mathrm{s}} = 0, \hat{\hat{\vec{r}}}_{\mathrm{b}}; \vec{n})}{\ln\mathcal{L}(\hat{r}_{\mathrm{s}}, \hat{\vec{r}}_{\mathrm{b}}; \vec{n})} , \tag{7.10}$$

here $\hat{\hat{\vec{r}}}_{\mathrm{b}}$ are the conditional best-fit results of the nuisance parameters where the parameter of interest is fixed to zero (H_0 hypothesis), while $(\hat{r}_{\mathrm{s}}, \hat{\vec{r}}_{\mathrm{b}})$ are the unconditional best-fit results (H_1 hypothesis). The Eq.7.10 can be manipulated similarly to Eq.7.5, and the numerator and denominator can be divided by constant term $\ln\mathcal{L}(\vec{n};\vec{n})$, to define $\chi^2_{\lambda,\mathrm{H}_0} = \ln\mathcal{L}(r_{\mathrm{s}} = 0, \hat{\hat{\vec{r}}}_{\mathrm{b}}; \vec{n})/\ln\mathcal{L}(\vec{n};\vec{n})$ and $\chi^2_{\lambda,\mathrm{H}_1} = \ln\mathcal{L}(\hat{r}_{\mathrm{s}}, \hat{\vec{r}}_{\mathrm{b}}; \vec{n})/\ln\mathcal{L}(\vec{n};\vec{n})$. Thus, the test statistic q_0 can be written as:

$$q_0 = \begin{cases} \chi^2_{\lambda,\mathrm{H}_0} - \chi^2_{\lambda,\mathrm{H}_1} & \hat{\mu} \geq 0 \\ 0 & \hat{\mu} < 0 \end{cases} \tag{7.11}$$

The terms $\chi^2_{\lambda,\mathrm{H}_0}$ and $\chi^2_{\lambda,\mathrm{H}_1}$ are the Poisson likelihood χ_λ minima for the H_0 and H_1 hypothesis. Given large data samples, the asymptotic relations can be used, and the signal significance Z and the hypothesis p-value can be computed from q_0 as follows [353]:

$$\text{p-value}_{\mu=0} = 1 - \Phi(\sqrt{q_0}); \quad Z_0 = \Phi^{-1}(1 - \text{p-value}_{\mu=0}) = \sqrt{q_0}, \tag{7.12}$$

where Φ is the Gaussian cumulative distribution function (CDF) and Φ^{-1} is the inverse Gaussian CDF. Low Z_0 or high p-value$_{\mu=0}$ indicate that H_0 is favoured over H_1. Using the same procedure applied in the WIMP search, only the upper edge of the confidence interval would be reported unless signal evidence above 3σ is present in the data.

If Z_0, or the p-value$_{\mu=0}$, is consistent with the background-only hypothesis, a two-sided 90 % CL limit is derived using the asymptotic test statistic $\tilde{q}_\mu$ for upper limits [353]. The limit is set using the χ^2_λ as a function of the parameter of interest r_{s}. For convenience, the minimum of the likelihood function χ^2_λ is subtracted during the scan. Like this, the $\Delta\chi^2_\lambda(r_{\mathrm{s}})$ is defined. The 90 % CL is given by the x-projection of the interception of $\Delta\chi^2_\lambda = 2.70$ with the $\Delta\chi^2_\lambda(r_{\mathrm{s}})$ scan. The square root of this value represents the number of σ of a Gaussian distribution centered in 0 and with unity standard deviation such that the area above that is 5 %. Then, $\pm 1.64\sigma$ gives two-sided a 90 % confidence interval[7]. Since the total number of events for this analysis is 33969, the high statistics condition is satisfied so that the asymptotic approach can be used. The procedure for extracting the limit from the scan of $\Delta\chi^2_\lambda(r_s)$ is shown in Fig.7.25.

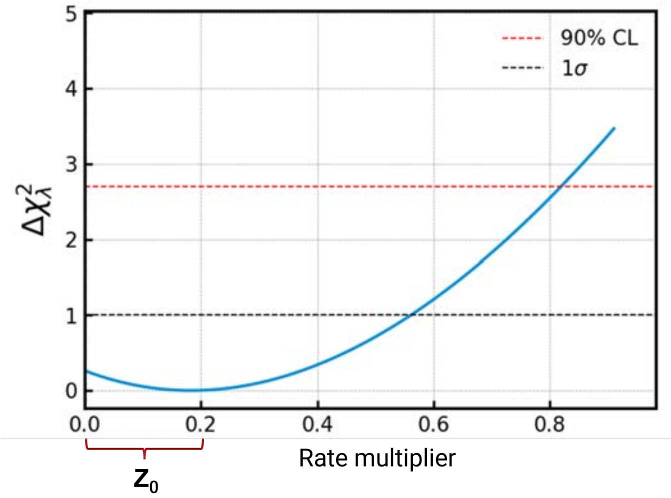

Figure 7.25: Example of $\Delta\chi^2_\lambda$ scan as a function of the parameter of interest. In the case of high statistics and a best-fit value greater than zero, the confidence intervals can be derived from the scan. The two horizontal lines represent the 1σ (black) and 90 % CL (red) of the best-fit value. The distance on the x-axis of the best-fit value with the null result represents the significance Z_0.

7.2.6 Results

In summary, the Poisson binned likelihood χ^2_λ was used to interpret the 111.4 days of XENONnT SR0 data in the (2.04 ± 0.16) t, equivalent to 0.62 t × yr exposure. The fit was performed in the reconstructed energy space considering SS spectrum within (1, 600) keV and 1 keV binning. The expected energy spectrum of the background considered and the signals sought were derived from simulation or theoretical calculations. After including the detector and selection effects, every component was normalized, given the information provided in section 7.2.1 and section 7.2.4. Therefore, a unitary scaling parameter was associated with each component, and when available, the relative uncertainty on the normalization was used as a constraint. The state of the inference presented here is not the final one. The energy bias and the total selection efficiency are fixed before the minimization of χ^2_λ, which will be updated for a future publication.

The scheme in Fig.7.26 summarises the inference pipeline. The background-only H_0 and three signal hypothesis H_1 fits will be shown and discussed in the following section.

Background-only hypothesis

The best-fit H_0 and the corresponding residual are shown in Fig.7.27. The fit converged to a minima with $\chi^2_{\lambda,H_0} = 665.8093$. The distribution of the residual is consistent with a Gaussian distribution centered in

---

[7] In the asymptotic regime: $Z[\sigma] = \sqrt{\tilde{q}_\mu}$, then $\sqrt{2.70} = 1.64\sigma$

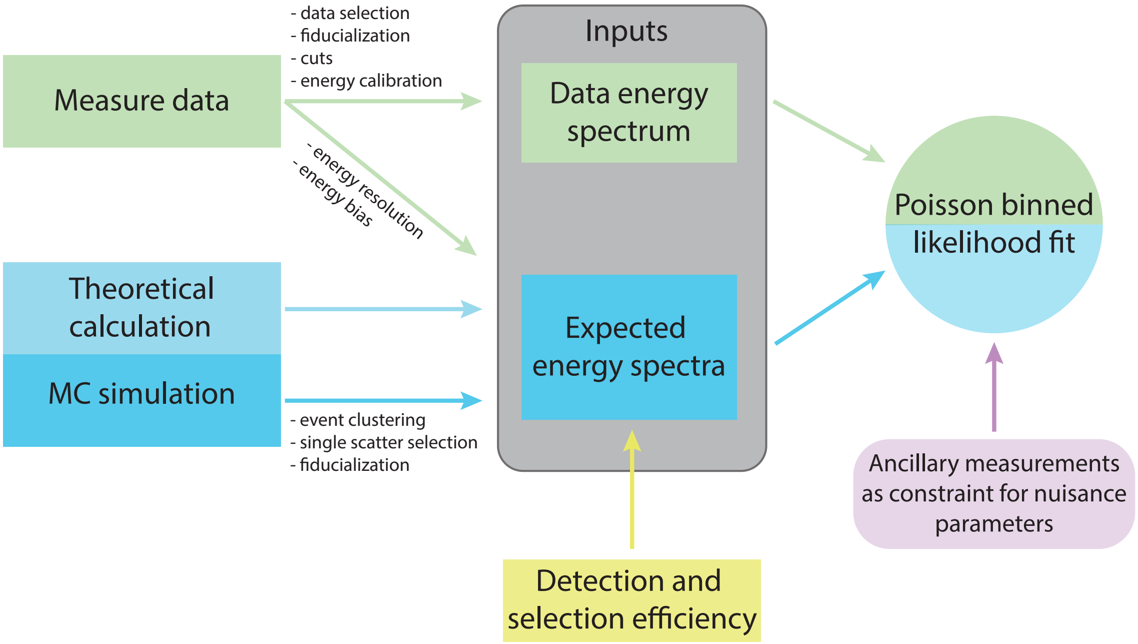

Figure 7.26: The inference pipeline can be summarized as follows: the energy spectrum of selected single scatter XENONnT SR0 data was provided to the Poisson binned likelihood fit after the detector characterization, together with the expected backgrounds and signal, derived either from simulations or from the theoretical calculations. The detection and selection efficiency, as well as the energy resolution and energy bias, were propagated into the expected spectra. The fit was performed considering the ancillary measurements, when available, as constraints for the nuisance parameters. Scheme inspired by [264].

$\mu = (0.07 \pm 0.04)$ and with a standard deviation $\sigma = (1.00 \pm 0.03)$ as shown in Fig.7.28. A slight positive displacement for the ^{129m}Xe peak is present, most likely due to an overestimation in the energy bias. This partially affects the fit quality as shown by the $\chi^2_{\lambda,H_0}/\mathrm{ndf} \approx 1.12$, where ndf is the number of degrees of freedom equal to the number of bins (599) minus the unconstrained scaling parameters (6).

The pre-fit initialization and the post-fit results are collected in Tab.7.3, together with the χ^2_{λ,H_0} value, which will be used later for the comparison with the hypotheses H_1. The pulls for the Gaussian constrained nuisance scaling parameters, defined as the $(\hat{r}_b - c_{r_b})/\delta c_{r_b}$, where $\hat{r}_b$ is the best-fit value whereas c_{r_b} and δc_{r_b} are the pre-fit value and its uncertainty [354], are shown as well. For ^{214}Pb, for which a uniform constraint was used, the pull was computed using as δc_{r_b} the half difference of the two boundaries (equal to 0.39). No anomalous pull above pre-fit uncertainty was observed. Therefore, it is unlikely that the fit result is impacted by one of these being incorrectly modeled.

The correlation among the scaling parameters is investigated, as shown in Fig.7.29. ^{136}Xe is the dominant background above $\sim$ 40 keV, and a negative pull of its scaling parameter is counterbalanced with positive pulls of the other continuous spectra, in particular for ^{212}Pb, ^{214}Pb as well as ^{133}Xe and Material. Indeed an anti-correlation is observed between ^{136}Xe and these background sources. A modest positive correlation is also observed among the material and ^{212}Pb, as well as ^{133}Xe. If the materials are positively pulled in the minimization, they will obscure the features in the spectrum due to the γ-decay from ^{133} Xe at 81 keV as well as the edge in the ^{212}Pb spectrum due to the nuclear de-excitation. Therefore, these

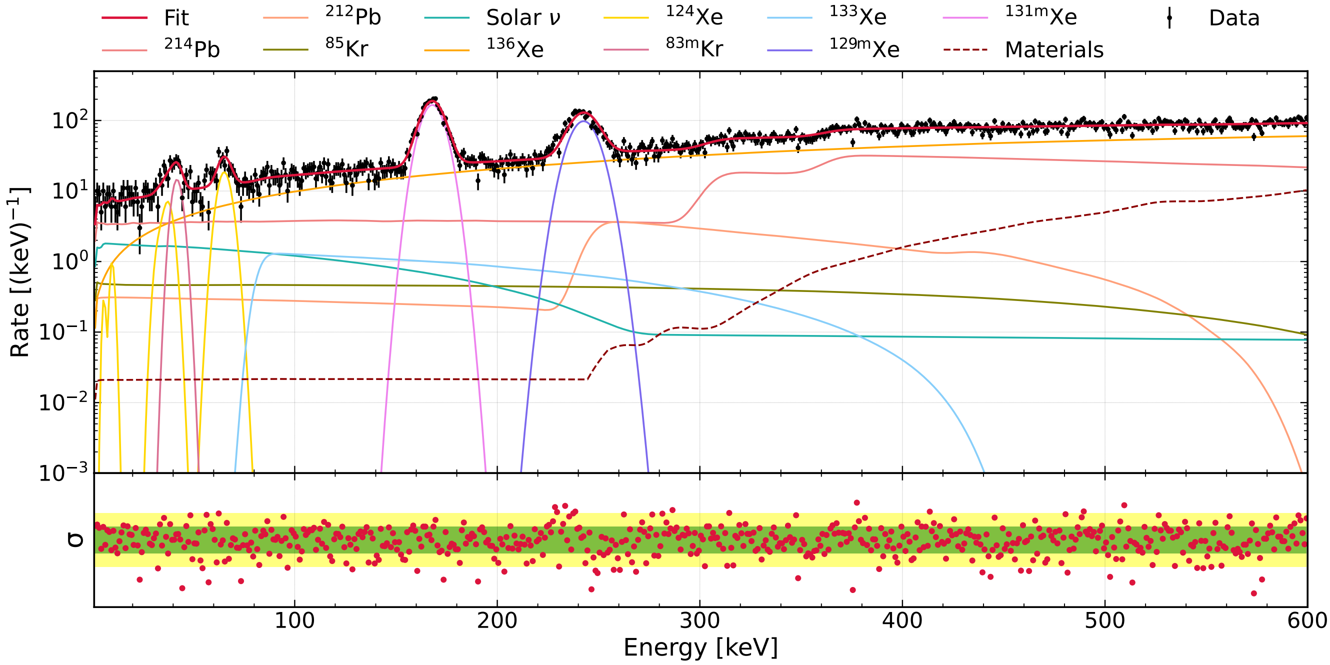

Figure 7.27: Results of background-only H_0 fit. The data are shown in the top panel with black points, while the fit result with a solid red line. For the background components, one must refer to the legend. The bottom panel shows the residual, in units of σ, between the data and the best H_0 model.

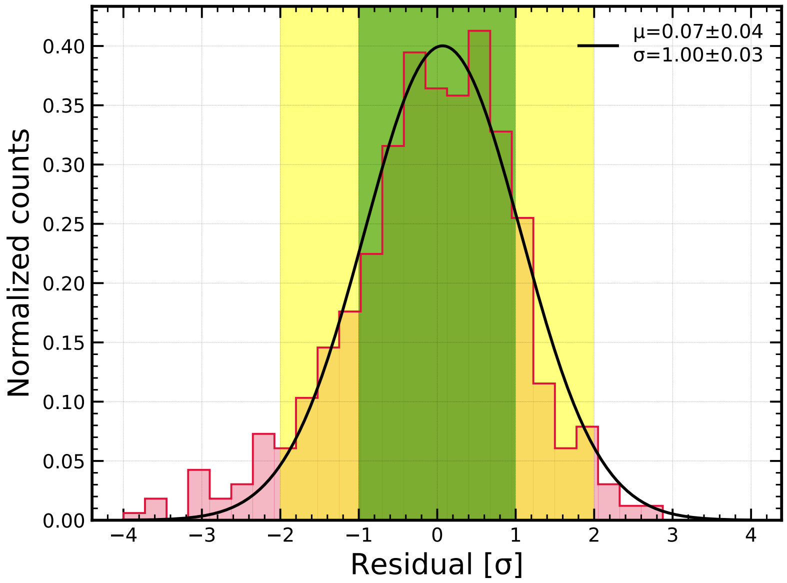

Figure 7.28: Residuals, in units of σ, for the results of background-only H_0 fit. The distribution is well-consisted with a Gaussian distribution centered in zero with unity standard deviation.

components need to be pulled up as well. These correlations would be reduced if constraints for the free parameters were available. The fit uncertainties are modest overall, besides ^{133} Xe, which has $\sim$ 50 $\%$ relative uncertainty. The fit is not very sensitive to it; therefore, if a different data selection was used, namely removing more data near the neutron calibration, this component could have been omitted in the background model.

	Pre-fit	Post-fit	Pull [δc]
Materials	1	0.8 ± 0.2	
^{212}Pb	1	1.4 ± 0.5	
^{214}Pb	$[0.53, 1.37]$	1.17 ± 0.05	0.43
^{85}Kr	1.0 ± 0.3	1.1 ± 0.2	0.28
Solar ν	1.0 ± 0.1	1.04 ± 0.09	0.42
^{136}Xe	1.00 ± 0.04	0.98 ± 0.03	-0.40
^{124}Xe	1.0 ± 0.2	1.1 ± 0.1	0.50
^{83m}Kr	1	4.6 ± 0.8	
^{133}Xe	1	32 ± 15	
^{129m}Xe	1	5.7 ± 0.2	
^{131m}Xe	1	1.95 ± 0.05	

$\chi^2_{\lambda,H_0} = 665.8093$

Table 7.3: Pre-fit values and post-fit results for background-only H_0, together with the minimized χ^2_{λ,H_0} value.

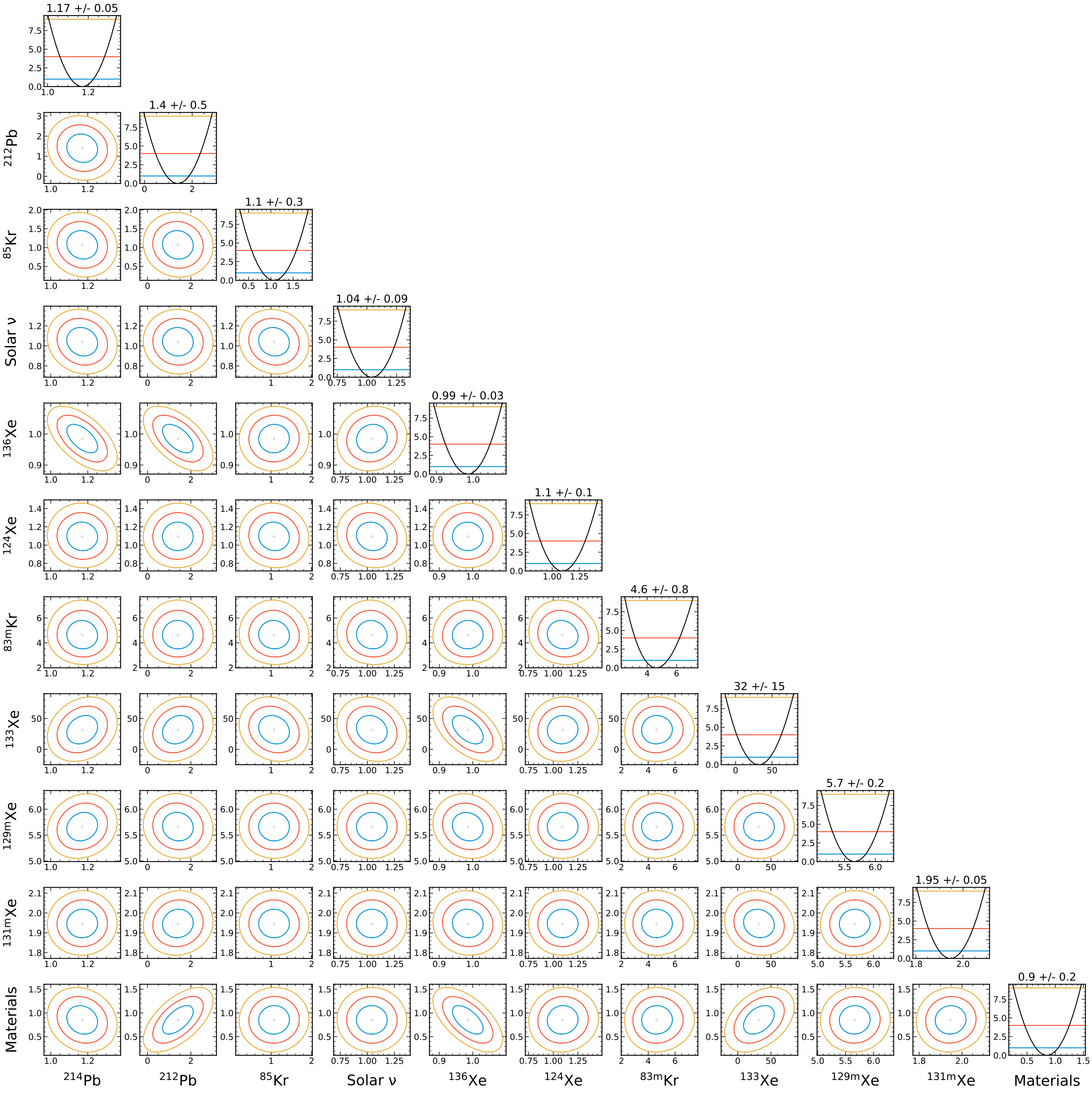

Figure 7.29: So called corner plot for the H$_0$ fit. The $\Delta\chi^2_\lambda$ scans are shown for each pair of scaling parameters. In addition, one-dimensional scans of which minima correspond to best-fit values are shown. The blue, red, and yellow solid lines represent the 1σ, 2σ, and 3σ fit uncertainty. A positive tilt of the two dimensions $\Delta\chi^2_\lambda$ scan corresponds to a positive correlation, while a negative tilt to a negative correlation.

A scaling parameter bigger than 1 translates into more events linked to that source. Therefore, the equivalent activity (half-life) is higher (smaller) than the initialization. The fit results for the constrained parameters are within the expectation. For instance, translating the best fit $\hat{r}_{^{214}\mathrm{Pb}}$ and $\hat{r}_{^{124}\mathrm{Xe}}$ to activity and half-life respectively, one obtains $A_{^{214}\mathrm{Pb}} = (1.50 \pm 0.07_{\mathrm{stats}})$ µBq/kg and $T_{1/2,\,^{124}\mathrm{Xe}} = (1.01 \pm 0.09_{\mathrm{stats}}) \times 10^{22}$ yr. The best fit for ^{212}Pb, which was free of constraints in the minimization, leads to an activity of (0.11 ± 0.04) µBq/kg consistent within the statistical error with the α-decay activities of ^{220}Rn and ^{216}Po.

Signal hypothesis: ^{128}I

The expected ^{128}I energy spectrum, initialized as described in section 7.2.1, was included in the model. The parameter of interest was free to vary in the minimization. The minimum value of the likelihood is $\chi^2_{\lambda,H_1^{128\mathrm{I}}} = 665.7859$. The $H_1^{128\mathrm{I}}$ fit result is shown in Fig.7.30. The best fit of the scaling parameter $\hat{r}_{^{128}\mathrm{I}}$ is equal to 0.002 ± 0.015. As reported by the $\chi^2_{\lambda,H_1^{128\mathrm{I}}}/\mathrm{ndf} \approx 1.12$, no improvement in the quality of the fit was observed. The results of post-fit scaling parameters are consistent with H_0, and they are collected in appendix A. The significance of $\hat{r}_{^{128}\mathrm{I}}$ ($Z_0 = 0.15\sigma$) and the p-value $= 0.44$ ensure that the best fit is consistent with zero and suggest that H_0 is favored over $H_1^{128\mathrm{I}}$. Therefore, the upper limit $r_{^{128}\mathrm{I},\,\mathrm{lim}} < 0.029$ at 90 % CL was extracted from the $\Delta\chi^2_\lambda$ scan as shown in Fig.7.31. The statistical parameters are collected in Tab.7.4.

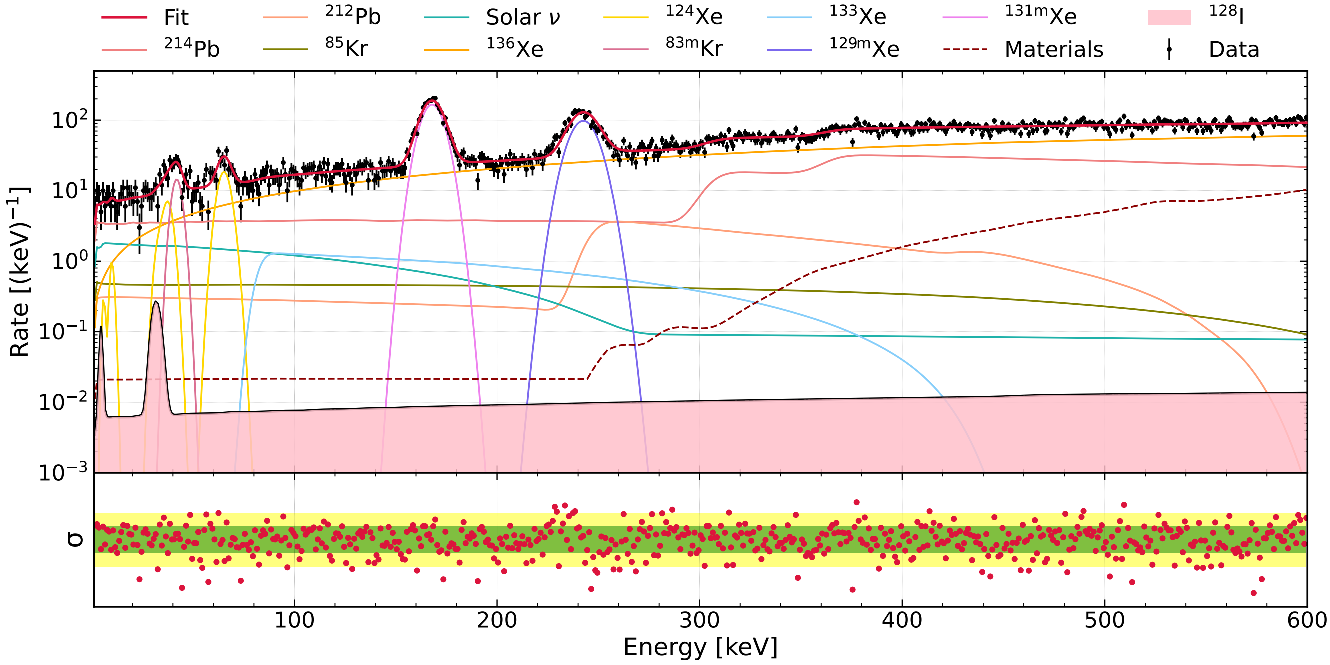

Figure 7.30: Results of $H_1^{128\mathrm{I}}$ fit. The data are shown in the top panel with black points, while the fit result is shown with a solid red line. The searched signal from ^{128}I is shown in pink, and the best fit of the scaling parameter is $\hat{r}_{^{128}\mathrm{I}} = 0.002 \pm 0.015$. All background components are shown in the styles given in the legend. The bottom panel shows the residual, in units of σ, between the data and the fitted model.

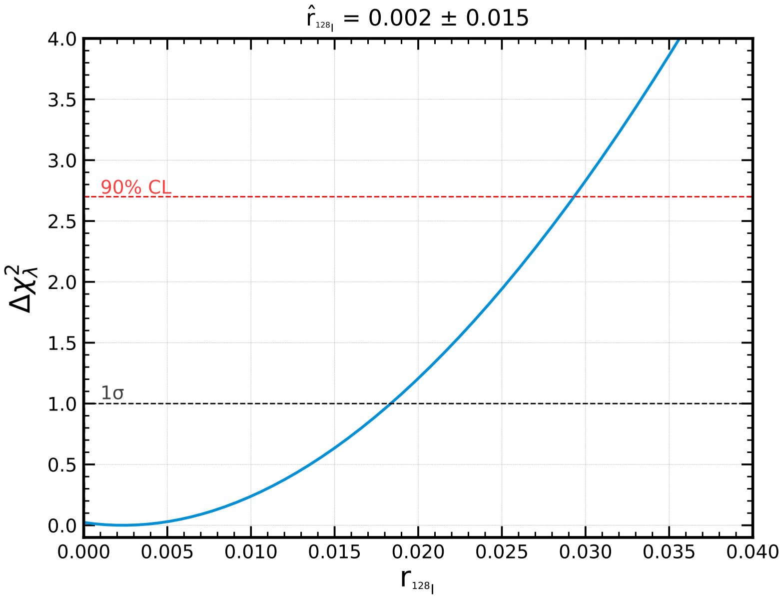

Figure 7.31: $\Delta\chi^2_\lambda$ scan for ^{128}I hypothesis fit as a function of the parameter of interest $r_{^{128}\mathrm{I}}$. The 1σ line and 1.64σ - corresponding to 90 % CL - are shown with black and red dashed lines.

	^{128}I hypothesis
$\chi^2_{\lambda,H_1^{128}\mathrm{I}}$	665.7859
$\hat{r}_{^{128}\mathrm{I}}$	0.002 ± 0.015
q_0	0.023
p-value	0.44
Z_0	0.15σ
$r_{^{128}\mathrm{I},\,\mathrm{lim}}$	0.029

Table 7.4: Summary of $\chi^2_{\lambda,H_1^{128}\mathrm{I}}$ fit.

Signal hypothesis: ^{127}Xe

The expected ^{127}Xe energy spectrum, initialized as described in section 7.2.1, was included in the model. The parameter of interest $r_{^{127}\mathrm{Xe}}$ was free to vary without any limit. The The $H_1^{^{127}\mathrm{Xe}}$ fit result is shown in Fig.7.32. The likelihood minimum is $\chi^2_{\lambda,H_1^{127}\mathrm{Xe}} = 665.7514$. The best fit of the scaling parameter $\hat{r}_{^{127}\mathrm{Xe}}$ is equal to 0.07 ± 0.31. The $\chi^2_{\lambda,H_1^{127}\mathrm{Xe}}/\mathrm{ndf} \approx 1.12$ confirms that with or without the additional signal, the fit quality is identical to H_0. The $\hat{r}_{^{127}\mathrm{Xe}}$ has a substantial relative error, and the reason is to be found in the correlation with $r_{^{129m}\mathrm{Xe}}$, as shown in Fig.7.33. The plot was derived by the two-dimensional scan of $\Delta\chi^2_\lambda$ with respect to the two scaling parameters considered. The shape suggests a negative correlation between the two components.

The results of post-fit scaling parameters are consistent with H_0, and they are collected in appendix A. Given $\chi^2_{\lambda,H_1^{127}\mathrm{Xe}}$, the significance of $\hat{r}_{^{127}\mathrm{Xe}}$ is 0.24σ and the p-value is 0.40. Therefore, H_0 is favored over $H_1^{^{127}\mathrm{Xe}}$. As discussed in section 7.2.4, the expected ^{127}Xe produced during ^{241}AmBe calibration leads to a $\mathcal{O}(100\ \mathrm{events})$ in the science data. From the minimum of $\chi^2_{\lambda,H_1^{127}\mathrm{Xe}}$, the number of events (activity) are 44 ± 182 ((2 ± 9) nBq/kg). Given the consistency with the null hypothesis, it is impossible to claim the presence of ^{127}Xe nuclei in the data. Nevertheless, the physics interpretation of this statement is weak due to the degeneracy of the investigated signal with ^{129m}Xe. This search should be performed again, removing more data in proximity of the ^{241}AmBe calibration, and at the same time, the neutron-activated background must be understood better and constrained.

In conclusion, given that H_0 is favored over $H_1^{^{127}\mathrm{Xe}}$, the 90 % CL upper limit on the scaling parameter of

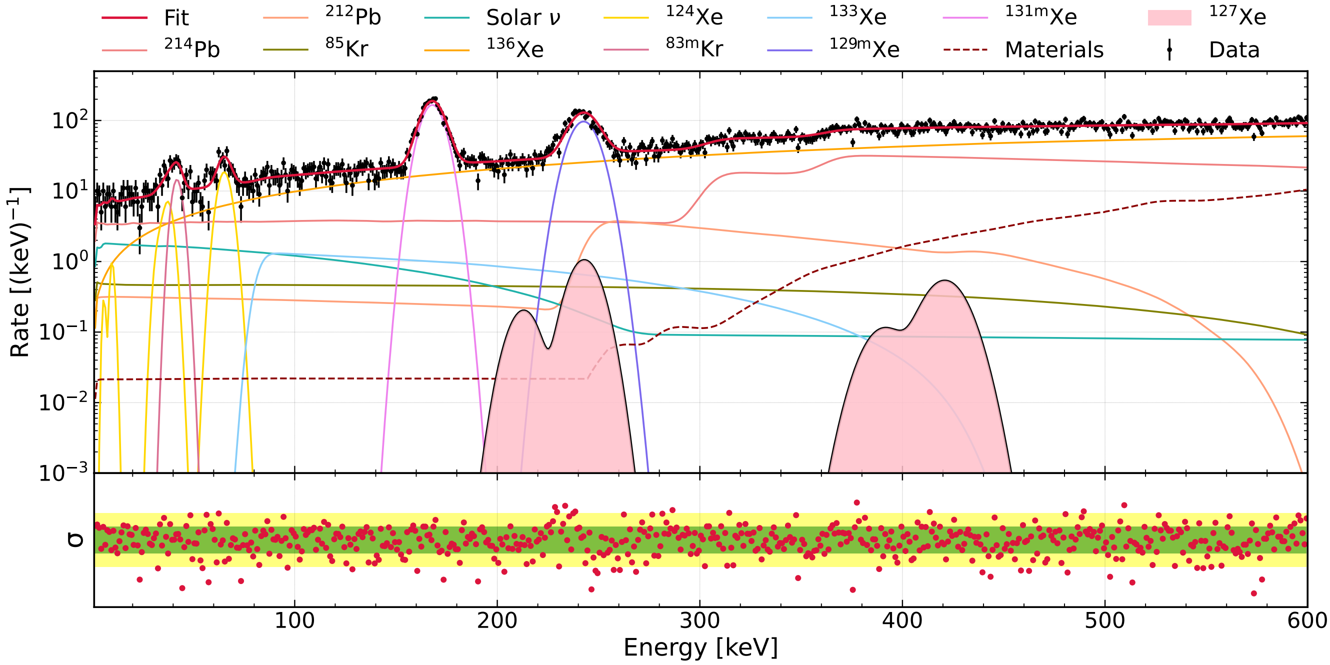

Figure 7.32: Results of $H_1^{^{127}\mathrm{Xe}}$ fit. The data are shown in the top panel with black points, while the fit result is shown with a solid red line. The searched signal from ^{127}Xe is shown in pink, and the best fit of the scaling parameter is $\hat{r}_{^{127}\mathrm{Xe}} = 0.07 \pm 0.31$. All background components are shown in the styles given in the legend. The bottom panel shows the residual, in units of σ, between the data and the fitted model.

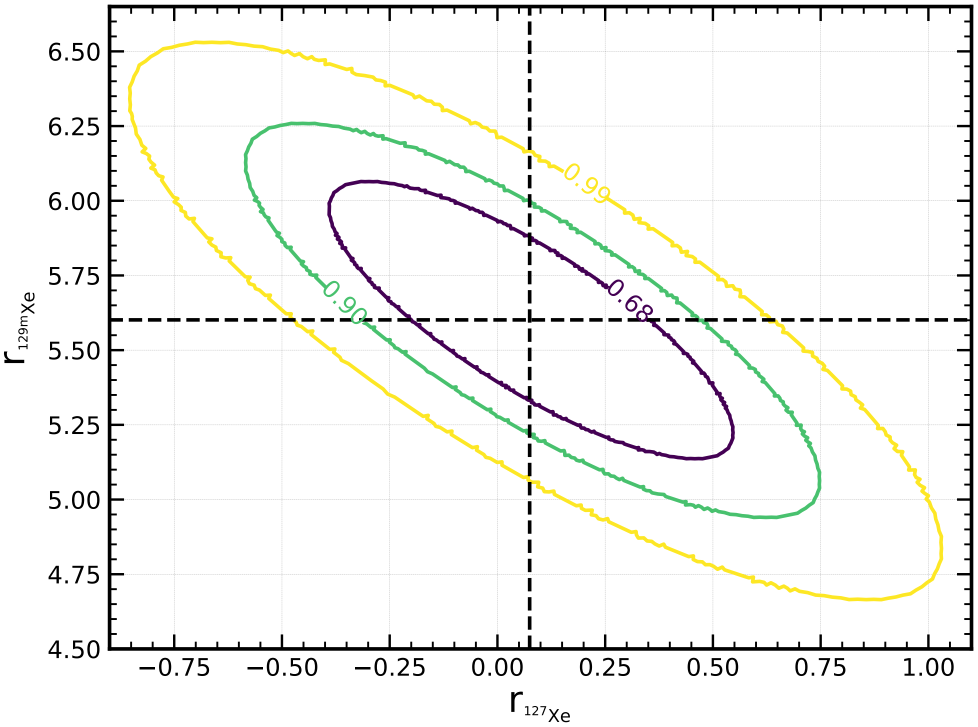

Figure 7.33: Correlation between the scaling parameters associated with ^{127}Xe and ^{129m}Xe. Derived by the two-dimensional scan of $\Delta\chi^2_\lambda$ to the two scaling parameters considered. The 68 %, 90 %, and 99 % percentile lines are shown.

^{127}Xe was derived and used to set a limit on nn disappearance lifetime assuming that no ^{127}Xe nuclei were produced during the ^{241}AmBe calibration, implying that the limit is conservative. The upper limit $r_{^{127}\mathrm{Xe,\,lim}}$ at 90 % CL was estimated to be 0.59 from the $\Delta\chi^2_\lambda$ scan, as shown in Fig.7.34. The statistical parameters are collected in Tab.7.5.

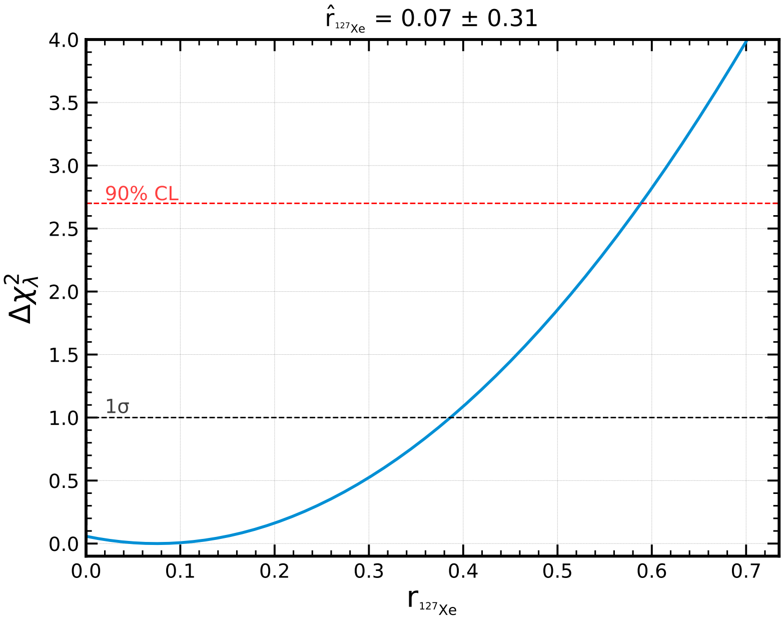

Figure 7.34: $\Delta\chi^2_\lambda$ scan for ^{127}Xe hypothesis fit as a function of the parameter of interest $r_{^{127}\mathrm{Xe}}$. The 1σ line and 1.64σ - corresponding to 90 % CL - are shown with black and red dashed lines.

	^{127}Xe hypothesis
$\chi^2_{\lambda,H_1^{127}\mathrm{Xe}}$	665.7514
$\hat{r}_{^{127}\mathrm{Xe}}$	0.07 ± 0.31
q_0	0.058
p-value	0.40
Z_0	0.24σ
$r_{^{127}\mathrm{Xe,\,lim}}$	0.59

Table 7.5: Summary of $\chi^2_{\lambda,H_1^{127}\mathrm{Xe}}$ fit.

Signal hypothesis: ^{127}Te

The result of $H_1^{^{127}\mathrm{Te}}$ fit, where the expected ^{127}Te energy spectrum was included in the model and initialized as described in section 7.2.1, is shown in Fig.7.35. Being the signal of interest, the scaling parameter $r_{^{127}\mathrm{Xe}}$ was left unconstrained. The minimum of the likelihood is $\chi^2_{\lambda,H_1^{127}\mathrm{Te}} = 664.4797$, corresponding to a $\hat{r}_{^{127}\mathrm{Xe}}$ is equal to 0.04 ± 0.04. The quality of the fit, indicated by the $\chi^2_{\lambda,H_1^{127}\mathrm{Te}}/\mathrm{ndf} \approx 1.12$, is unchanged with respect to H_0. Similarly to the other signal investigated, the results of the post-fit scaling parameters are consistent with H_0. For more information, see appendix A. Given the significance of $\hat{r}_{^{127}\mathrm{Te}}$, equal to 1.15σ, or equivalently the p-value = 0.12, the result is not significant. The 90 % CL was extracted from the $\Delta\chi^2_\lambda$ scan as shown in Fig.7.36. The statistical parameters for interpreting the result are collected in Tab.7.6. The $r_{^{127}\mathrm{Te,\,lim}}$ is 0.11.

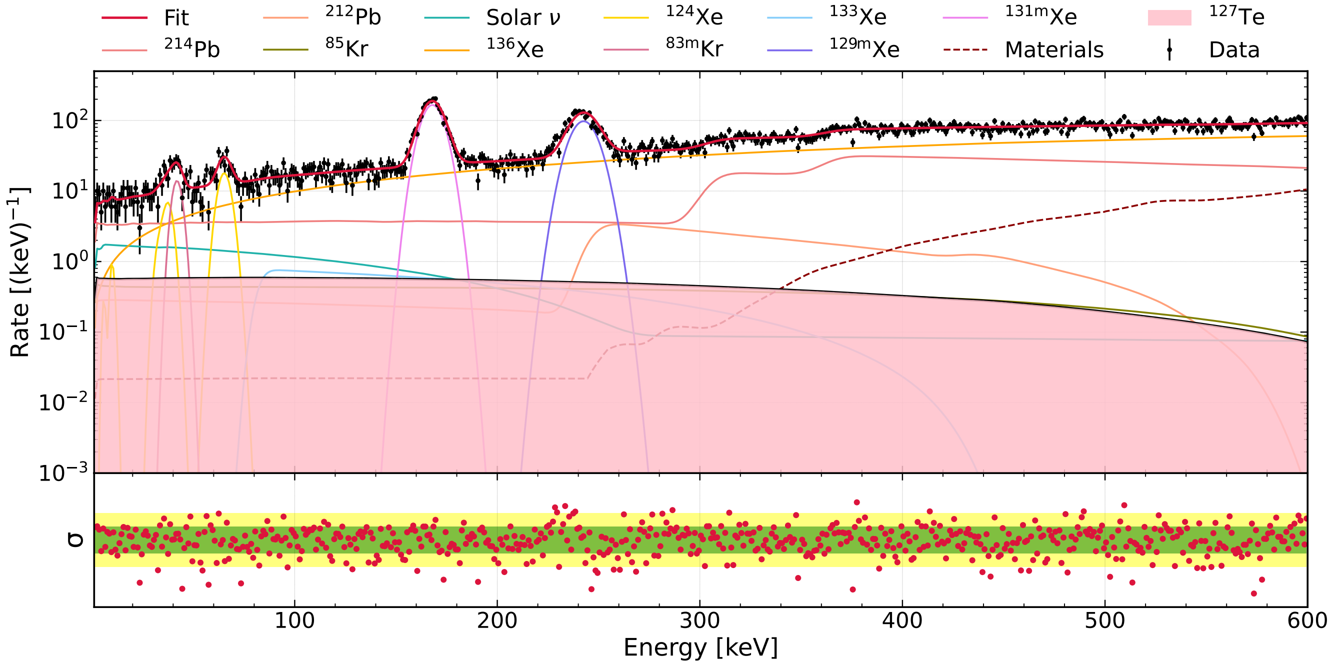

Figure 7.35: Results of $H_1^{^{127}\mathrm{Te}}$ fit. The data are shown in the top panel with black points, while the fit result is shown with a solid red line. The searched signal from ^{127}Xe is shown in pink, and the best fit of the scaling parameter is $\hat{r}_{^{127}\mathrm{Te}} = 0.04 \pm 0.04$. All background components are shown in the styles given in the legend. The bottom panel shows the residual, in units of σ, between the data and the fitted model.

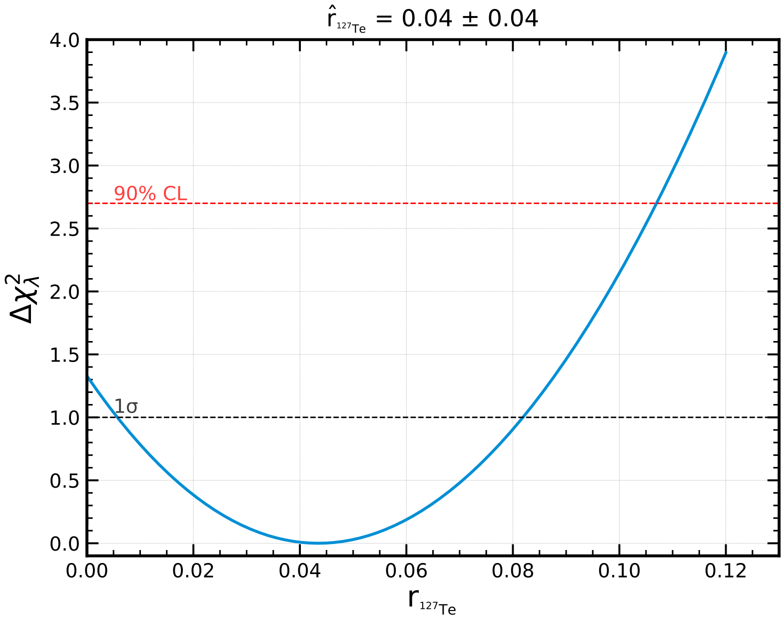

Figure 7.36: $\Delta\chi^2_\lambda$ scan for ^{127}Te hypothesis fit as a function of the parameter of interest $r_{^{127}\mathrm{Te}}$. The 1σ line and 1.64σ - corresponding to 90 % CL - are shown with black and red dashed lines.

	^{127}Te hypothesis
$\chi^2_{\lambda,H_1^{^{127}\mathrm{Te}}}$	664.4797
$\hat{r}_{^{127}\mathrm{Te}}$	0.04 ± 0.04
q_0	1.329
p-value	0.12
Z_0	1.15σ
$r_{^{127}\mathrm{Te, lim}}$	0.11

Table 7.6: Summary of $\chi^2_{\lambda,H_1^{^{127}\mathrm{Te}}}$ fit.

7.2.7 Conclusion

No evidence of the searched signals has been observed in the XENONnT SR0 data. Therefore a lower limit at 90 % CL on the lifetime is derived for the three decays as follows:

$$\tau_{\mathrm{lim}} = \frac{\varepsilon \times N_{\mathrm{eff}} \times \mathrm{T}}{\mathrm{S}_{90\ \%\ \mathrm{CL}}}, \tag{7.13}$$

where ε contains the efficiency lost due to detector effects and data selection, as well as the chosen energy window (see section 7.2.4), N_{eff} is the effective number of nucleons that can undergo the decay investigated, T is the XENONnT SR0 livetime (111.4 days) and $\mathrm{S}_{90\ \%\ \mathrm{CL}}$ is the number of events from the investigated channels which can be excluded at 90 % CL based on the results of the Poisson binned likelihood fits.

N_{eff} consists of the number of ^{129}Xe atoms (N_{nucl}) within the fiducial volume multiplied by the number of protons or neutrons (N_{obj}), whose decay would lead to the investigated signal, and for their decay probability (λ_{obj}). The values of N_{obj} and λ_{obj} were taken from the DAMA/LXe analysis [143] (see Tab.2.3).

The $\mathrm{S}_{90\ \%\ \mathrm{CL}}$ was computed from the upper limits of the scaling parameters at 90 % CL discussed in the previous section. The upper limit of the scaling parameter was used as a normalization factor for the energy spectrum of the signal searched. Then, the $\mathrm{S}_{90\ \%\ \mathrm{CL}}$ was determined as the area subtended by the spectrum. The information to compute the lifetime lower limits for the p, nn, and pp disappearance in ^{129}Xe obtained from the XENONnT SR0 data are collected in Tab.7.7. The limits derived from this analysis are $\mathcal{O}(10)$ times higher than the previous limits on nucleon and di-nucleon disappearance in ^{129}Xe from DAMA/LXe [143].

N_{nucl} of $^{129}_{54}$Xe	decay mode	daughter nucleus	$N_{\mathrm{obj}} \times \lambda_{\mathrm{obj}}$	ε	$\mathrm{S}_{90\ \%\ CL}$	τ_{lim} [yr]
$\sim 2.47 \times 10^{27}$	p	$^{128}_{53}$I	24	31.45 %	93.83	$> 6.09 \times 10^{25}$
	nn	$^{127}_{54}$Xe	9	80.07 %	276.78	$> 1.96 \times 10^{25}$
	pp	$^{127}_{52}$Te	4	93.23 %	593.07	$> 4.76 \times 10^{24}$

Table 7.7: Lifetime lower limits at 90 % CL for the p, nn, and pp disappearance in ^{129}Xe from XENONnT SR0 data, consisting of 111.4 days, in 2 t fiducial volume. The limits were derived with Eq.7.13.

Compared to γ de-excitation searches performed by SNO+ [137] or KamLAND [138], XENONnT is not competitive due to the different detector sizes. However, a future large-scale xenon experiment with a fiducial mass of $\mathcal{O}(10\ \mathrm{t})$, like DARWIN [101], will improve the sensitivity to these baryon violations processes. The XENONnT limits are shown in Fig.7.7 together with the limits from DAMA/LXe [143] limits and γ de-excitation searches.

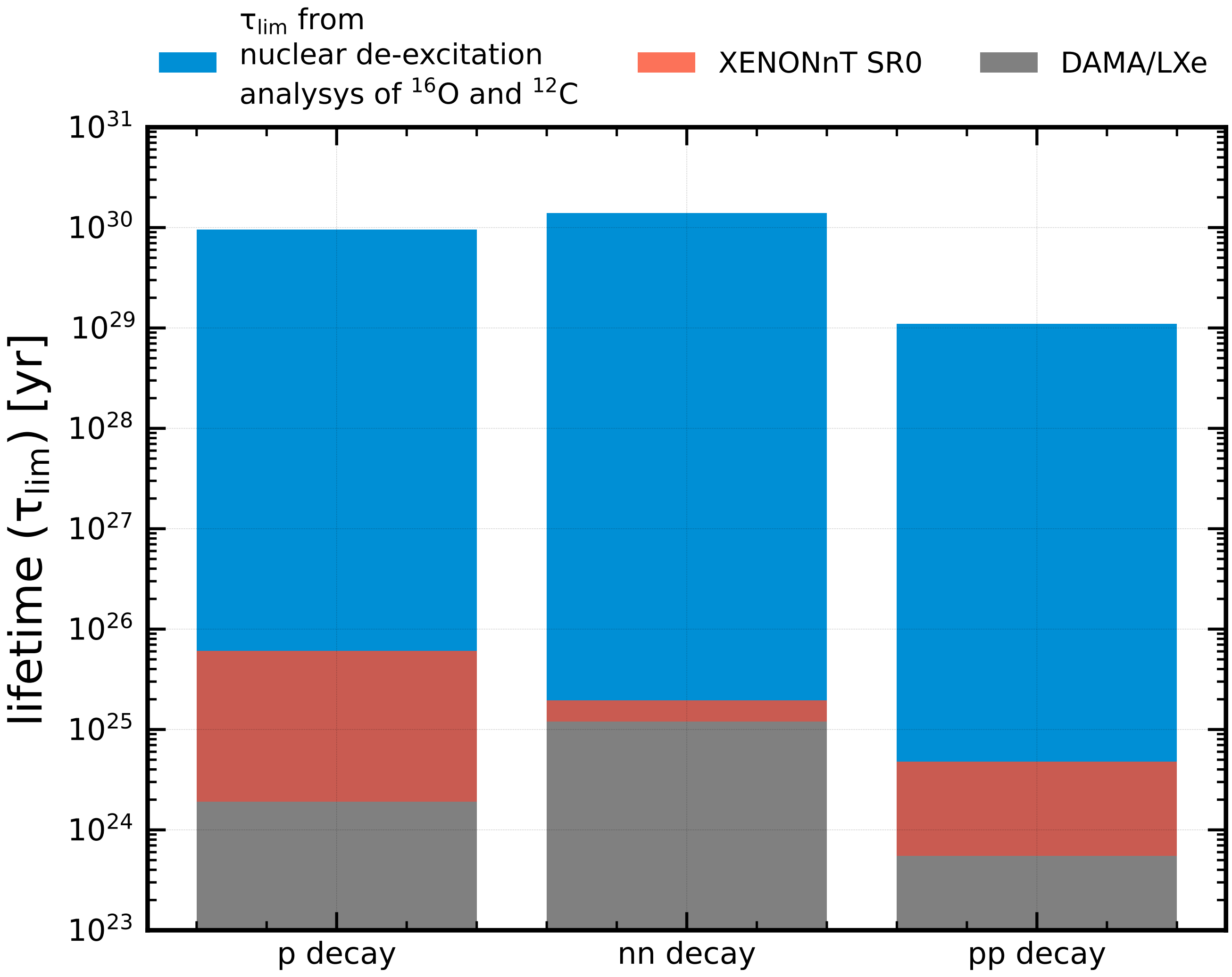

Figure 7.37: Lifetime upper limits at 90 % CL for p, nn, and pp nucleons disappearance. The colored regions represent the lifetime excluded. The radiogenic analysis with XENONnT SR0 data improved the current limits from DAMA/LXe [143] for the nucleon and di-nucleon invisible decays in ^{129}Xe. The most stringent limits have been set with γ-ray de-excitation searches performed by SNO+ [137] or KamLAND [138].

8

Conclusion

A wide range of astrophysical and cosmological observations indicate a Universe in which ordinary baryonic matter is a secondary component, and the total mass content is dominated by a new, yet unknown, form of non-luminous matter: *dark matter*. Evidence suggests that dark matter consists of new particles not contained in the Standard Model of particle physics. Several candidate particles can solve the dark matter problem, and one of the most intriguing is the WIMP. In recent years, axions and bosonic dark matter, such as the dark photon, have gathered a lot of attention in the scientific community. Nevertheless, WIMPs are still one of the main search candidates. In the context of direct detection of dark matter, dual-phase xenon TPCs lead the efforts in the GeV-TeV WIMP mass range; among these, the XENON project is one of the leading players. It is an international collaboration aiming to detect DM particles with an ultra-sensitive and low background dual-phase time projection chamber with 5.9 t of instrumented liquid xenon. The work presented in this manuscript focuses on the preparation for, commissioning, and results of the first science run data of the XENONnT experiment, which operates at the underground Laboratori Nazionali del Gran Sasso in Italy.

Dark matter is not the only problem arising from astrophysical and cosmological observations. The day-to-day experience and cosmological calculations confirm that baryonic antimatter is essentially absent in the observable Universe. The matter-antimatter asymmetry can be explained if baryon and/or lepton quantum numbers are not exact conserved quantities in nature. This has motivated an extensive research program on nucleon decays in recent decades. Among various experimental techniques, the radiogenic approach is one of the main methods for invisible searches, where the products of nucleon decay leave no trace in the detector. This technique relies on the search for the radioactive decay of the daughter nucleus originating after the disappearance of one or more nucleons in some favorable and abundant isotope within the detector. The first search for the nucleon and di-nucleon disappearance in ^{129}Xe using the first XENONnT science data is one of the topics of this manuscript.

The XENONnT TPC is equipped with 494 photomultiplier tubes arranged in two arrays at the top and bottom of the TPC volume, which constantly monitor the 5.9 t of liquid xenon and allow for the reconstruction of the energy deposited by the interacting particles in the active volume. The model used in XENONnT (R11410-21) has been inherited from its predecessor XENON1T. This 3" model was developed by Hamamatsu in collaboration with the XENON collaboration, specifically for use in liquid xenon dark matter experiments: it uses extremely low radioactivity materials and is designed to optimize the performances at xenon cryogenic temperature. Out of the 494 XENONnT PMTs, 153 XENON1T photosensors were reused, and the remaining were newly produced. All of these went through a meticulous testing campaign, where their performance was evaluated for at least one week in both liquid and gas xenon, performed by the University of Zurich, Stockholm University, and Max-Plank-Institut für Kernphysik. At the beginning of my doctoral project, I partly contributed to the last stages of the PMT testing campaign conducted at the University of Zurich, testing 40 out of 105 PMTs. As it has been shown, the meticulous testing campaign had a direct impact on the quality of the XENONnT PMTs. Out of the 368 tested PMTs, 13 PMTs were excluded because of the problem of vacuum leakage, 11 light emitting sensors were rejected, and other 2 PMTs which could not be turned on were not considered for XENONnT. In the first XENONnT science run, only 3 $\%$ were excluded, corresponding to a failure rate that is lower by a factor of $\sim$ 5 than in XENON1T.

Together with the PMTs, the voltage divider circuit, or base, has been discussed in-depth. The same XENON1T design was used for the XENONnT base, but all of them were newly produced after identifying the materials which minimized their radioactive content. Then they were tested, verifying that the voltage drop across each resistor in the circuit was correct, to discard problematic bases. Each PMT has its own base from which Kapton-insulated wires supply the high voltage, while PTFE-insulated RG196 coaxial cables carry the signal. The XENONnT PMT cabling plan has been presented in detail. The distance between the PMTs, and the signal amplifier or the high voltage power supply is $\sim$ 17 m. Therefore, a detailed cabling plan was essential. The installation of the cables was optimized by splitting the cabling plan into three sections and using custom low-radioactivity connectors to join them together.

Next, the PMT array assembly and the TPC assembly were presented. Given the low background requirement, the assembly operations were performed in a clean room at LNGS following a careful cleaning protocol. First, the PMT arrays were assembled after cleaning the cables, the base, and the PMT itself. Once an array of PMTs was completed, each sensor was tested in a black box by ramping up the high voltage to −1.3 kV and checking the signal with an oscilloscope. All PMTs were fully functional, reflecting the careful assembly operation. The TPC assembly lasted for 10 days. The timing was essential to minimize radon progeny plate-out on inner surfaces. Eventually, the TPC was brought to the underground laboratory, installed at the center of the XENON water tank, and sealed into the cryostats. Once the cryostats were closed, the detector commissioning began.

The commissioning lasted for almost one year. This manuscript focuses on the characterization of PMTs performed at various stages of detector commissioning. Two PMT features were monitored closely in the context of this work: the signal amplification, or gain, and the single PE acceptances (SPE). It has been shown how the PMT working conditions were set to optimize the SPE and achieve a uniform gain distribution. At the beginning of SR0, the SPE acceptance was on average above 90 $\%$, while the gain was around 2×10^6. These values remained stable throughout SR0, further demonstrating the reliability of XENONnT PMTs at cryogenic temperature and ensuring high data quality, which was essential for a competitive physics research program.

SR0 started in May 2021, and it lasted until December 2021. The XENONnT data processing pipeline was discussed, from event construction to the correction applied to remove known distortions in event properties. Afterwards, a general overview of data quality criteria, or cuts, was presented to reject unphysical events and unwanted event topology. In the context of the Ph.D. project presented in this manuscript, two cuts based on S1 features were developed. The first, S1 area fraction top, aims to reject events with an improbable relative fraction of light observed from the top array. The second one, S1 pattern likelihood, is based on a statistical interpretation of the S1 light pattern and aims to reject events reconstructed as single S1 and single S2, but which are genuinely multiple scatter events. Both cuts, designed to have $\sim$ 99 $\%$ signal acceptance, were included in the main XENONnT analysis. Then, the XENONnT simulation framework was presented after the energy calibration discussion. In particular, it was shown how the optical settings for the XENONnT TPC Geant4 model were derived based on an MC-data matching analysis, which effectively described the light collection efficiency properties of the XENONnT detector.

Once the events have been corrected, the selection criteria have been developed, the energy calibration has been defined, and the simulation framework has been validated, the SR0 data could be analyzed. In this thesis, the XENONnT results of the low energy ER analysis and the search for spin-independent elastic scattering of WIMPs were shown. A contribution to the background model has been made in the work of this thesis by providing the radiogenic electronic recoil material background prediction for energies below 140 keV, equivalent to (2.4 ± 0.4) events$/(\mathrm{t} \times \mathrm{yr} \times \mathrm{keV})$ in a 4.37 t fiducial mass.

The search for new physics in the low-energy ER region shows no excess above the background. Consequently, 90 $\%$ confidence level upper limits on solar axions, bosonic dark matter models, and solar neutrinos with an enhanced magnetic moment were set. However, an unprecedented background level was achieved. The average measured ER background rate in the 4.37 t fiducial mass, within $(1; 30)$ keV, was (15.8 ± 1.3) events$/(\mathrm{t} \times \mathrm{yr} \times \mathrm{keV})$, a factor $\sim$ 5 lower than the predecessor XENON1T. Similarly, for the WIMP search, the best fit to the SR0 data was compatible with the background-only hypothesis. Therefore, limits were placed on the spin-independent WIMP-nucleon scattering cross-section at 90 $\%$ confidence level for a wide range of WIMP masses. The lowest limit achieved with SR0 is 2.37×10^{-47} cm^2 at 28 GeV/c^2.

Although the XENONnT performance was optimized for the low energy region, the unprecedented background level achieved during SR0 allows the investigation of additional physics channels at energies previously unattainable in XENON experiments, such as the invisible nucleon and di-nucleon decay in ^{129}Xe. Similar to the search performed by DAMA/LXe experiment, a pioneer for these searches in the context of xenon-based detectors, the n, nn, pp disappearances in ^{129}Xe were investigated by searching the radioactive decays of the ^{128}I, ^{127}Xe, and ^{127}Te produced as a result of the decay of the nucleons. The analysis technique resembled the low-energy ER analysis but in a wider energy region up to 600 keV. In order to extend the energy region of interest, several studies had to be performed and new tools had to be developed. In particular, the validation of the XENONnT simulation framework used to derive the signal and background models, as well as the efficiency loss due to data selection, was shown. The simulated detector response was already sufficiently good: The single- and multi-site reconstruction performances were captured well from the simulation framework, as shown by SS-MS spatial resolution (the minimum vertical separation required between consecutive energy depositions to reconstruct them individually) studies. However, further studies must be performed to validate the XENONnT simulation framework fully. The studies carried out with ^{212}Pb data will be performed again after implementing the recommended decay branching ratio in the XENONnT Geant4 model.

The analysis details were discussed in-depth and the expected energy spectra of the instigated signal were shown. The data utilized in the analysis were detailed as well as the independent measurements utilized to develop the background model. A Poisson binned likelihood χ^2_λ was used to interpret the reconstructed energy spectrum within $(1, 600)$ keV and 1 keV binning, from 111.4 days of XENONnT SR0 data in the $\sim$ 2.0 t fiducial volume. This is the first analysis performed in the XENON experiment in this energy range. The background-only hypothesis well described the data, and the best-fit results were within expectations. This suggests the robustness of the methods used, such as the simulation-driven efficiency loss. No significant evidence of the sought signals was observed. A lower limit on the lifetimes of the n, nn, and pp invisible decays at 90 $\%$ CL were derived: $\tau_{\text{n, lim}} > 6.09 \times 10^{25}$ yr, $\tau_{\text{nn, lim}} > 1.96 \times 10^{25}$ yr, and $\tau_{\text{pp, lim}} > 4.76 \times 10^{24}$ yr. Given the fact that it was not possible to quantify the number of ^{127}Xe nuclei produced during the ^{241}AmBe calibration, the limit on nn decay is conservative. The limits derived from this analysis are $O(10)$ times higher than the previous limits on nucleon and di-nucleon disappearance in ^{129}Xe from DAMA/LXe. These results will be summarized for publication.

XENONnT continues to collect data at LNGS. Since the conclusion of SR0, several upgrades have been made to XENON's infrastructure. The radon removal system, which previously operated only in gas mode, is now operating by combining liquid and gas modes, from which further reduction in ^{222}Rn activity is expected. The preliminary operations before doping the XENONnT water tank with gadolinium salt are almost completed. Data collection with the neutron veto operating as designed is planned in the near future. A detector calibration with an external source of ^{232}Th has been performed, and data analysis is underway. Combining this calibration with a dedicated calibration of ^{222}Rn will help to further validate the XENONnT simulation framework. XENONnT started its second physics run in May 2022. The data analysis is ongoing, and new exciting physics results are expected in the near future.

A

H1 hypothesis fitting results

The following table collects the fit results of the nuisance scaling parameters for the three H_1 hypotheses investigated. The scaling parameters derived for the three hypotheses agreed with the background-only hypothesis H_0 (see Tab.7.3), and with each other.

	Pre-fit	$\chi^2_{\lambda,H_1^{^{128}\mathrm{I}}}$	$\chi^2_{\lambda,H_1^{^{127}\mathrm{Xe}}}$	$\chi^2_{\lambda,H_1^{^{127}\mathrm{Te}}}$
Materials	1	0.8 ± 0.2	0.9 ± 0.2	0.9 ± 0.2
^{212}Pb	1	1.4 ± 0.5	1.4 ± 0.5	1.3 ± 0.5
^{214}Pb	$[0.53, 1.37]$	1.17 ± 0.05	1.17 ± 0.06	1.15 ± 0.05
^{85}Kr	1.0 ± 0.3	1.1 ± 0.3	1.1 ± 0.3	1.0 ± 0.3
Solar ν	1.0 ± 0.1	1.04 ± 0.09	1.04 ± 0.09	1.0 ± 0.1
^{136}Xe	1.00 ± 0.04	0.98 ± 0.03	0.98 ± 0.03	0.99 ± 0.03
^{124}Xe	1.0 ± 0.2	1.1 ± 0.1	1.1 ± 0.1	1.1 ± 0.1
^{83m}Kr	1	4.6 ± 0.7	4.6 ± 0.7	4.4 ± 0.8
^{133}Xe	1	32 ± 15	32 ± 15	18 ± 19
^{129m}Xe	1	5.7 ± 0.2	5.6 ± 0.3	5.6 ± 0.2
^{131m}Xe	1	1.95 ± 0.05	1.95 ± 0.05	1.95 ± 0.05

Table A.1: Pre-fit values and post-fit results of nuisance scaling parameters for the three hypotheses.

The following figures are shown the so-called corner plot for the fit. It consists of two dimensions $\Delta\chi^2_\lambda$ scans for each scaling parameters pair and the one dimension scan for each individual fitted parameter. The blue, red, and yellow solid lines represent the 1σ, 2σ, and 3σ fit uncertainty. A positive tilt in the two dimensions $\Delta\chi^2_\lambda$ scans is equivalent to a positive correlation among the parameters. In contrast, a negative tilt reflects a negative correlation. No new correlations were observed among the nuisance parameters compared to H_0 fit corner plot shown in Fig.7.29. As already discussed in section 7.2.6, a strong anti-correlation is present among ^{127}Xe and ^{129m}Xe. Another anti-correlation is present between ^{127}Te and ^{133}Xe due to the similar shape and the absence of any constraint for ^{133}Xe. Current studies on neutron activation background will help in the future to reduce these negative correlations and reduce the fit uncertainty.

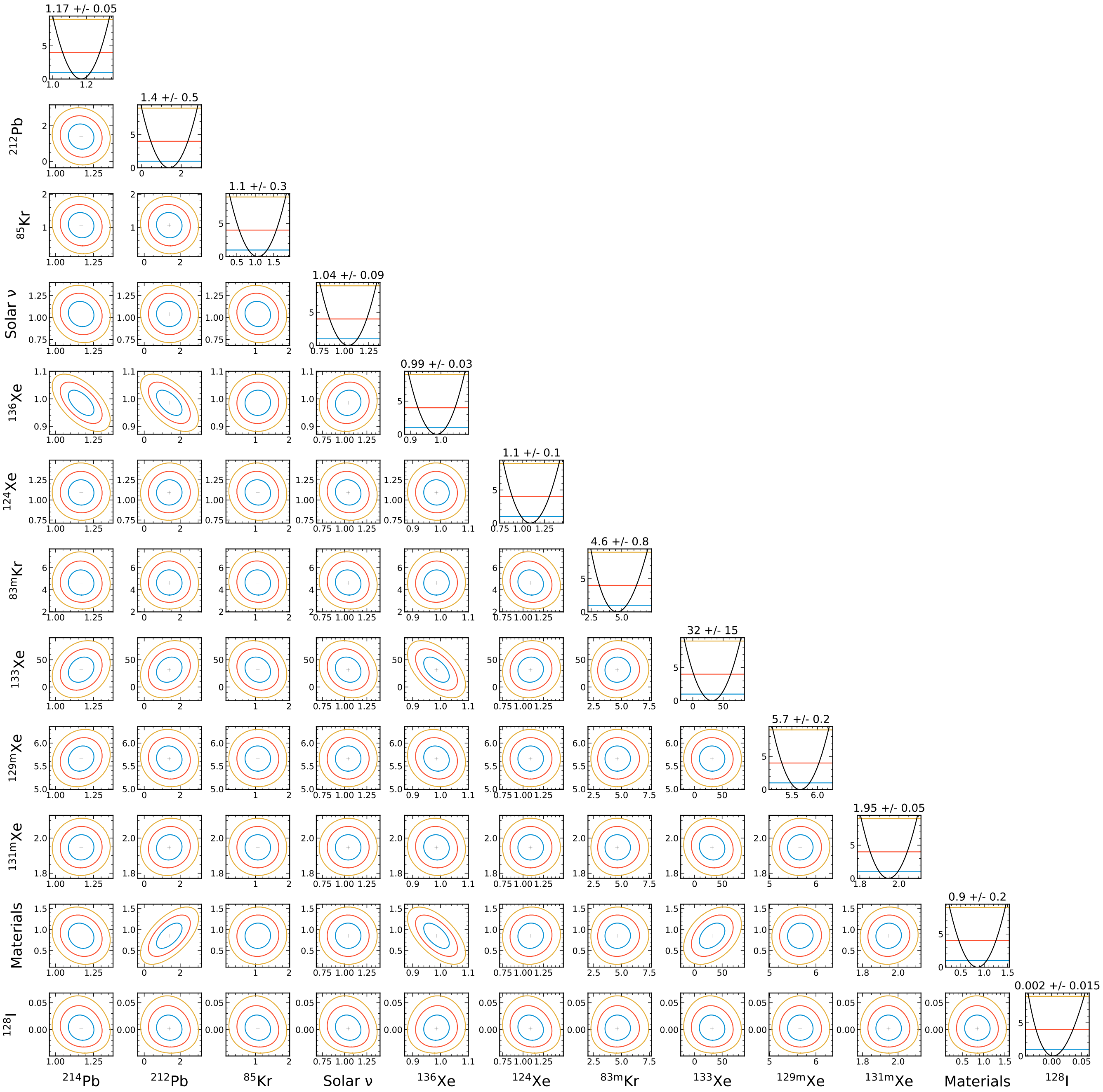

Figure A.1: So called corner plot for the $\mathrm{H}_1^{^{128}\mathrm{I}}$ fit. The $\Delta\chi^2_\lambda$ scans are shown for each pair of scaling parameters. In addition, one-dimensional scans of which minima correspond to best-fit values are shown. The blue, red, and yellow solid lines represent the 1σ, 2σ, and 3σ fit uncertainty. A positive tilt of the two dimensions $\Delta\chi^2_\lambda$ scan corresponds to a positive correlation, while a negative tilt to a negative correlation.

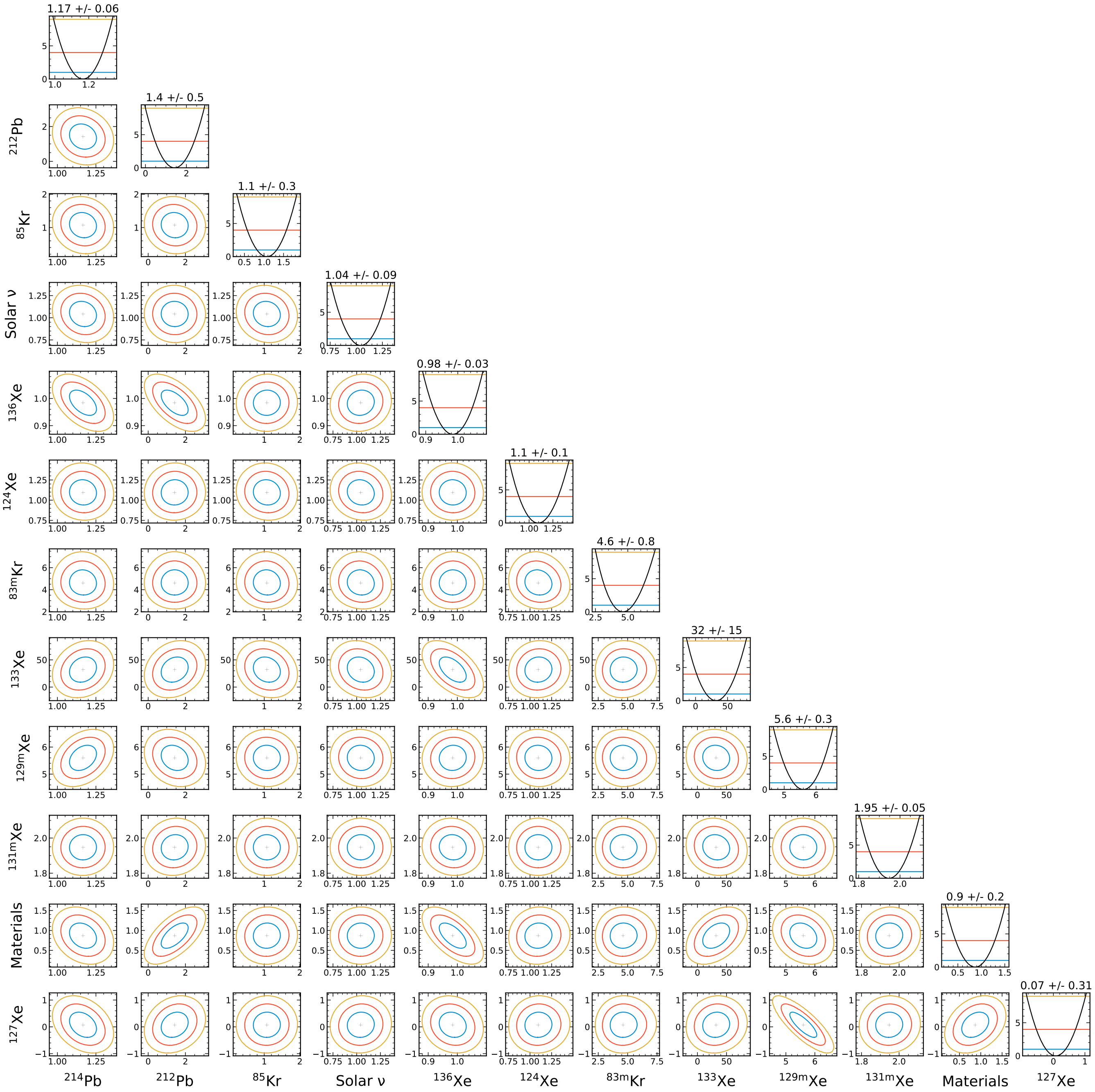

Figure A.2: So called corner plot for the $H_1^{127\text{Xe}}$ fit. The $\Delta\chi^2_\lambda$ scans are shown for each pair of scaling parameters. In addition, one-dimensional scans of which minima correspond to best-fit values are shown. The blue, red, and yellow solid lines represent the 1σ, 2σ, and 3σ fit uncertainty. A positive tilt of the two dimensions $\Delta\chi^2_\lambda$ scan corresponds to a positive correlation, while a negative tilt to a negative correlation.

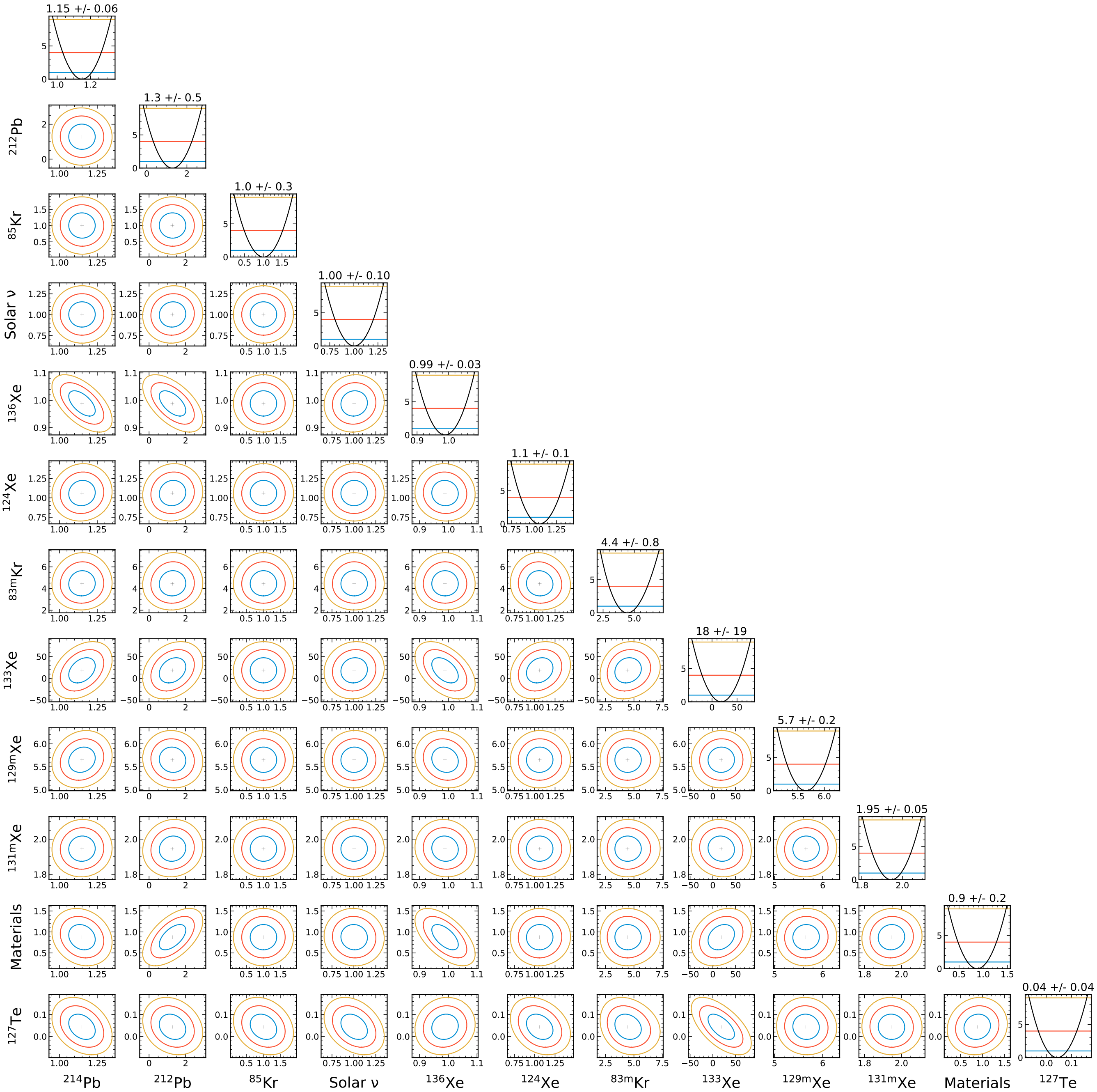

Figure A.3: So called corner plot for the $H_1^{^{127}\mathrm{Te}}$ fit. The $\Delta\chi^2_\lambda$ scans are shown for each pair of scaling parameters. In addition, one-dimensional scans of which minima correspond to best-fit values are shown. The blue, red, and yellow solid lines represent the 1σ, 2σ, and 3σ fit uncertainty. A positive tilt of the two dimensions $\Delta\chi^2_\lambda$ scan corresponds to a positive correlation, while a negative tilt to a negative correlation.

References

[1] S. Dodelson and F. Schmidt. *Modern Cosmology*. Elsevier Science, 2020. ISBN: 9780128159484. URL: https://books.google.ch/books?id=GGjfywEACAAJ.

[2] F. Zwicky. "Die Rotverschiebung von extragalaktischen Nebeln". In: *General Relativity and Gravitation* (1933). DOI: 10.1007/s10714-008-0706-5. URL: https://link.springer.com/article/10.1007/s10714-008-0707-4.

[3] Vera C. Rubin and Jr. Ford W. Kent. "Rotation of the Andromeda Nebula from a Spectroscopic Survey of Emission Regions". In: 159 (Feb. 1970), p. 379. DOI: 10.1086/150317.

[4] Yoshiaki Sofue. "Mass Distribution and Rotation Curve in the Galaxy". In: *Planets, Stars and Stellar Systems. Volume 5: Galactic Structure and Stellar Populations*. Ed. by Terry D. Oswalt and Gerard Gilmore. Vol. 5. 2013, p. 985. DOI: 10.1007/978-94-007-5612-0_1910.48550/arXiv.1307.8215.

[5] M. Milgrom. "The MOND paradigm of modified dynamics". In: *Scholarpedia* 9.6 (2014). revision #197883, p. 31410. DOI: 10.4249/scholarpedia.31410.

[6] Benoît Famaey and Stacy S. McGaugh. "Modified Newtonian Dynamics (MOND): Observational Phenomenology and Relativistic Extensions". In: *Living Reviews in Relativity* 15.1 (Sept. 2012). DOI: 10.12942/lrr-2012-10. URL: https://doi.org/10.12942%5C%2Flrr-2012-10.

[7] Malcolm Fairbairn. "Galactic Anomalies and Particle Dark Matter". In: *Symmetry* 14.4 (2022). ISSN: 2073-8994. DOI: 10.3390/sym14040812. URL: https://www.mdpi.com/2073-8994/14/4/812.

[8] Yoshiaki Sofue. "Dark halos of M 31 and the Milky Way". In: *Publications of the Astronomical Society of Japan* 67.4 (May 2015), p. 75. DOI: 10.1093/pasj/psv042. URL: https://doi.org/10.1093%5C%2Fpasj%5C%2Fpsv042.

[9] De-Chang Dai, Glenn Starkman, and Dejan Stojkovic. "Milky Way and M31 rotation curves: ΛCDM vs. MOND". In: *Physical Review D* 105.10 (May 2022). DOI: 10.1103/physrevd.105.104067. URL: https://doi.org/10.1103%5C%2Fphysrevd.105.104067.

[10] David Harvey et al. "The nongravitational interactions of dark matter in colliding galaxy clusters". In: *Science* 347.6229 (2015), pp. 1462–1465. DOI: 10.1126/science.1261381. eprint: https://www.science.org/doi/pdf/10.1126/science.1261381. URL: https://www.science.org/doi/abs/10.1126/science.1261381.

[11] *Dark matter even darker than once thought - Hubble explores the dark side of cosmic collisions*. https://sci.esa.int/web/hubble/-/55662-dark-matter-even-darker-than-once-thought-heic1506l. Accessed: 13/10/2022.

[12] Richard Massey, Thomas Kitching, and Johan Richard. "The dark matter of gravitational lensing". In: *Reports on Progress in Physics* 73.8 (July 2010), p. 086901. DOI: 10.1088/0034-4885/73/8/086901. URL: https://doi.org/10.1088/0034-4885/73/8/086901.

[13] H. Katayama and K. Hayashida. “X-ray measurements of the dark matter distribution in clusters of galaxies with Chandra”. In: *Advances in Space Research* 34.12 (2004). New X-Ray Results, the Next Generation of X-Ray Observatories and Gamma Ray Burst Afterglow Physics, pp. 2519–2524. ISSN: 0273-1177. DOI: `https://doi.org/10.1016/j.asr.2003.06.045`. URL: `https://www.sciencedirect.com/science/article/pii/S0273117704006817`.

[14] Wayne Hu and Scott Dodelson. “Cosmic Microwave Background Anisotropies”. In: *Annual Review of Astronomy and Astrophysics* 40.1 (Sept. 2002), pp. 171–216. DOI: `10.1146/annurev.astro.40.060401.093926`. URL: `https://doi.org/10.1146%5C%2Fannurev.astro.40.060401.093926`.

[15] Planck Collaboration et al. “Planck 2018 results. I. Overview and the cosmological legacy of Planck”. In: 641, A1 (Sept. 2020), A1. DOI: `10.1051/0004-6361/201833880`. arXiv: `1807.06205 [astro-ph.CO]`.

[16] Planck Collaboration et al. “Planck 2018 results. VI. Cosmological parameters”. In: 641, A6 (Sept. 2020), A6. DOI: `10.1051/0004-6361/201833910`. arXiv: `1807.06209 [astro-ph.CO]`.

[17] Anthony Challinor Antony Lewis. *Code for Anisotropies in the Microwave Background*. `https://camb.info/`. Accessed: 01/08/2022.

[18] *Planck Public Data Release 3 Maps*. `https://irsa.ipac.caltech.edu/data/Planck/release_3/all-sky-maps/index.html`. Accessed: 01/08/2022.

[19] Ryan J. Cooke, Max Pettini, and Charles C. Steidel. “One Percent Determination of the Primordial Deuterium Abundance”. In: 855.2, 102 (Mar. 2018), p. 102. DOI: `10.3847/1538-4357/aaab53`. arXiv: `1710.11129 [astro-ph.CO]`.

[20] Richard H. Cyburt et al. “Big bang nucleosynthesis: Present status”. In: *Rev. Mod. Phys.* 88 (1 Feb. 2016), p. 015004. DOI: `10.1103/RevModPhys.88.015004`. URL: `https://link.aps.org/doi/10.1103/RevModPhys.88.015004`.

[21] Yoshiaki Sofue. “Rotation Curve of the Milky Way and the Dark Matter Density”. In: *Galaxies* 8.2 (2020). ISSN: 2075-4434. DOI: `10.3390/galaxies8020037`. URL: `https://www.mdpi.com/2075-4434/8/2/37`.

[22] Michel Fich and Scott Tremaine. “The mass of the Galaxy.” In: 29 (Jan. 1991), pp. 409–445. DOI: `10.1146/annurev.aa.29.090191.002205`.

[23] Yoshiaki Sofue. “Rotation and mass in the Milky Way and spiral galaxies”. In: *Publications of the Astronomical Society of Japan* 69.1 (Dec. 2016). R1. ISSN: 0004-6264. DOI: `10.1093/pasj/psw103`. eprint: `https://academic.oup.com/pasj/article-pdf/69/1/R1/9937207/psw103.pdf`. URL: `https://doi.org/10.1093/pasj/psw103`.

[24] James Binney and Scott Tremaine. *Galactic Dynamics: Second Edition*. 2008.

[25] Julio F. Navarro, Carlos S. Frenk, and Simon D. M. White. “The Structure of Cold Dark Matter Halos”. In: 462 (May 1996), p. 563. DOI: `10.1086/177173`. arXiv: `astro-ph/9508025 [astro-ph]`.

[26] S. Chandrasekhar. *An Introduction To The Study Of Stellar Structure*. `https://archive.org/details/in.ernet.dli.2015.212456/page/n3/mode/1up`. University Of Chicago Press, 1939.

[27] D. Baxter et al. “Recommended conventions for reporting results from direct dark matter searches”. In: *European Physical Journal C* 81.10, 907 (Oct. 2021), p. 907. DOI: `10.1140/epjc/s10052-021-09655-y`. arXiv: `2105.00599 [hep-ex]`.

[28] Stefano Magni. “Astrophysical aspects of dark matter direct detection”. Theses. Université Montpellier, Nov. 2015. URL: `https://tel.archives-ouvertes.fr/tel-01986333`.

[29] Del Nobile Eugenion. *The Theory of Direct Dark Matter Detection*. Springer Cham, 2022. ISBN: 978-3-030-95227-3. URL: `https://link.springer.com/book/10.1007/978-3-030-95228-0`.

[30] Katherine Freese, Mariangela Lisanti, and Christopher Savage. “Colloquium: Annual modulation of dark matter”. In: *Rev. Mod. Phys.* 85 (4 Nov. 2013), pp. 1561–1581. DOI: `10.1103/RevModPhys.85.1561`. URL: `https://link.aps.org/doi/10.1103/RevModPhys.85.1561`.

[31] J. Diemand et al. “Clumps and streams in the local dark matter distribution”. In: *Nature* 454 (2008), pp. 735–738. DOI: `10.1038/nature07153`. arXiv: `0805.1244 [astro-ph]`.

[32] Annalisa Pillepich et al. “THE DISTRIBUTION OF DARK MATTER IN THE MILKY WAY’S DISK”. In: *The Astrophysical Journal* 784.2 (Mar. 2014), p. 161. DOI: `10.1088/0004-637X/784/2/161`. URL: `https://dx.doi.org/10.1088/0004-637X/784/2/161`.

[33] Lina Necib et al. “Under the Firelight: Stellar Tracers of the Local Dark Matter Velocity Distribution in the Milky Way”. In: (Oct. 2018). DOI: `10.3847/1538-4357/ab3afc`. arXiv: `1810.12301 [astro-ph.GA]`.

[34] Jelle Aalbers et al. *JelleAalbers/wimprates: v0.4.1*. Version v0.4.1. Sept. 2022. DOI: `10.5281/zenodo.7041453`. URL: `https://doi.org/10.5281/zenodo.7041453`.

[35] Michael Kuhlen et al. “Dark Matter Direct Detection with Non-Maxwellian Velocity Structure”. In: *JCAP* 02 (2010), p. 030. DOI: `10.1088/1475-7516/2010/02/030`. arXiv: `0912.2358 [astro-ph.GA]`.

[36] Lina Necib. *DARK MATTER IN DISEQUILIBRIUM: THE LOCAL VELOCITY DISTRIBUTION FROM SDSS-GAIA*. `https://github.com/linoush/DM_Velocity_Distribution`. Accessed: 01/08/2022.

[37] Tongyan Lin. “Dark matter models and direct detection”. In: *PoS* 333 (2019), p. 009. DOI: `10.22323/1.333.0009`. arXiv: `1904.07915 [hep-ph]`.

[38] Chiara Di Paolo, Fabrizio Nesti, and Francesco L. Villante. “Phase space mass bound for fermionic dark matter from dwarf spheroidal galaxies”. In: *Mon. Not. Roy. Astron. Soc.* 475.4 (2018), pp. 5385–5397. DOI: `10.1093/mnras/sty091`. arXiv: `1704.06644 [astro-ph.GA]`.

[39] Edward A. Baltz. “Dark matter candidates”. In: *eConf* C040802 (2004). Ed. by Joanne Hewett et al., p. L002. arXiv: `astro-ph/0412170`.

[40] Jihn E. Kim and Gianpaolo Carosi. “Axions and the Strong CP Problem”. In: *Rev. Mod. Phys.* 82 (2010). [Erratum: Rev.Mod.Phys. 91, 049902 (2019)], pp. 557–602. DOI: `10.1103/RevModPhys.82.557`. arXiv: `0807.3125 [hep-ph]`.

[41] C. Alcock et al. “The MACHO project: Microlensing results from 5.7 years of LMC observations”. In: *Astrophys. J.* 542 (2000), pp. 281–307. DOI: `10.1086/309512`. arXiv: `astro-ph/0001272`.

[42] Bernard Carr, Florian Kuhnel, and Marit Sandstad. “Primordial Black Holes as Dark Matter”. In: *Phys. Rev. D* 94.8 (2016), p. 083504. DOI: `10.1103/PhysRevD.94.083504`. arXiv: `1607.06077 [astro-ph.CO]`.

[43] Jim Alexander et al. “Dark Sectors 2016 Workshop: Community Report”. In: Aug. 2016. arXiv: `1608.08632 [hep-ph]`.

[44] Marco Battaglieri et al. “US Cosmic Visions: New Ideas in Dark Matter 2017: Community Report”. In: *U.S. Cosmic Visions: New Ideas in Dark Matter*. July 2017. arXiv: `1707.04591 [hep-ph]`.

[45] Gianfranco Bertone, Dan Hooper, and Joseph Silk. “Particle dark matter: Evidence, candidates and constraints”. In: *Phys. Rept.* 405 (2005), pp. 279–390. DOI: `10.1016/j.physrep.2004.08.031`. arXiv: `hep-ph/0404175`.

[46] Martin Bauer and Tilman Plehn. *Yet Another Introduction to Dark Matter: The Particle Physics Approach*. Vol. 959. Lecture Notes in Physics. Springer, 2019. DOI: `10.1007/978-3-030-16234-4`. arXiv: `1705.01987 [hep-ph]`.

[47] Dan Hooper and Stefano Profumo. “Dark Matter and Collider Phenomenology of Universal Extra Dimensions”. In: *Phys. Rept.* 453 (2007), pp. 29–115. DOI: `10.1016/j.physrep.2007.09.003`. arXiv: `hep-ph/0701197`.

[48] M. Drewes et al. “A White Paper on keV Sterile Neutrino Dark Matter”. In: *JCAP* 01 (2017), p. 025. DOI: 10.1088/1475-7516/2017/01/025. arXiv: 1602.04816 [hep-ph].

[49] Lawrence J. Hall et al. “Freeze-In Production of FIMP Dark Matter”. In: *JHEP* 03 (2010), p. 080. DOI: 10.1007/JHEP03(2010)080. arXiv: 0911.1120 [hep-ph].

[50] Kim Griest and Marc Kamionkowski. “Unitarity limits on the mass and radius of dark-matter particles”. In: *Phys. Rev. Lett.* 64 (6 Feb. 1990), pp. 615–618. DOI: 10.1103/PhysRevLett.64.615. URL: https://link.aps.org/doi/10.1103/PhysRevLett.64.615.

[51] Daniel J. H. Chung et al. “On the Gravitational Production of Superheavy Dark Matter”. In: *Phys. Rev. D* 64 (2001), p. 043503. DOI: 10.1103/PhysRevD.64.043503. arXiv: hep-ph/0104100.

[52] Stefano Profumo, Leonardo Giani, and Oliver F. Piattella. “An Introduction to Particle Dark Matter”. In: *Universe* 5.10 (2019), p. 213. DOI: 10.3390/universe5100213. arXiv: 1910.05610 [hep-ph].

[53] M. Aker et al. “Direct neutrino-mass measurement with sub-electronvolt sensitivity”. In: *Nature Phys.* 18.2 (2022), pp. 160–166. DOI: 10.1038/s41567-021-01463-1. arXiv: 2105.08533 [hep-ex].

[54] Scott Dodelson and Lawrence M. Widrow. “Sterile neutrinos as dark matter”. In: *Phys. Rev. Lett.* 72 (1 Jan. 1994), pp. 17–20. DOI: 10.1103/PhysRevLett.72.17. URL: https://link.aps.org/doi/10.1103/PhysRevLett.72.17.

[55] Laurent Canetti, Marco Drewes, and Mikhail Shaposhnikov. “Sterile Neutrinos as the Origin of Dark and Baryonic Matter”. In: *Phys. Rev. Lett.* 110.6 (2013), p. 061801. DOI: 10.1103/PhysRevLett.110.061801. arXiv: 1204.3902 [hep-ph].

[56] R. D. Peccei and Helen R. Quinn. “CP Conservation in the Presence of Pseudoparticles”. In: *Phys. Rev. Lett.* 38 (25 June 1977), pp. 1440–1443. DOI: 10.1103/PhysRevLett.38.1440. URL: https://link.aps.org/doi/10.1103/PhysRevLett.38.1440.

[57] Steven Weinberg. “A New Light Boson?” In: *Phys. Rev. Lett.* 40 (4 Jan. 1978), pp. 223–226. DOI: 10.1103/PhysRevLett.40.223. URL: https://link.aps.org/doi/10.1103/PhysRevLett.40.223.

[58] David J. E. Marsh. “Axion cosmology”. In: 643 (July 2016), pp. 1–79. DOI: 10.1016/j.physrep.2016.06.005. arXiv: 1510.07633 [astro-ph.CO].

[59] David G. Cerdeno. “WIMPs: A brief bestiary”. In: *4th Patras Workshop on Axions, WIMPs and WISPs*. July 2009, pp. 9–12. DOI: 10.3204/DESY-PROC-2008-02/cerdeno_david.

[60] Leszek Roszkowski, Enrico Maria Sessolo, and Sebastian Trojanowski. “WIMP dark matter candidates and searches—current status and future prospects”. In: *Rept. Prog. Phys.* 81.6 (2018), p. 066201. DOI: 10.1088/1361-6633/aab913. arXiv: 1707.06277 [hep-ph].

[61] Stefano Profumo. “Astrophysical Probes of Dark Matter”. In: *Theoretical Advanced Study Institute in Elementary Particle Physics: Searching for New Physics at Small and Large Scales*. 2013, pp. 143–189. DOI: 10.1142/9789814525220_0004. arXiv: 1301.0952 [hep-ph].

[62] Torsten Bringmann and Stefan Hofmann. “Thermal decoupling of WIMPs from first principles”. In: *JCAP* 04 (2007). [Erratum: JCAP 03, E02 (2016)], p. 016. DOI: 10.1088/1475-7516/2007/04/016. arXiv: hep-ph/0612238.

[63] Particle Data Group et al. “Review of Particle Physics”. In: *Progress of Theoretical and Experimental Physics* 2020.8 (Aug. 2020). 083C01. ISSN: 2050-3911. DOI: 10.1093/ptep/ptaa104. eprint: https://academic.oup.com/ptep/article-pdf/2020/8/083C01/34673722/ptaa104.pdf. URL: https://doi.org/10.1093/ptep/ptaa104.

[64] Tobias Binder. “Refining the chemical and kinetic decoupling description of thermally produced dark matter”. PhD thesis. Georg-August University School of Science (GAUSS), 2019. URL: %7Bhttps://s3.cern.ch/inspire-prod-files-3/3101c194a1fb79a13f4c485d67e38e55%7D.

[65] Gary Steigman, Basudeb Dasgupta, and John F. Beacom. “Precise Relic WIMP Abundance and its Impact on Searches for Dark Matter Annihilation”. In: *Phys. Rev. D* 86 (2012), p. 023506. DOI: 10.1103/PhysRevD.86.023506. arXiv: 1204.3622 [hep-ph].

[66] Takeshi Nihei, Leszek Roszkowski, and Roberto Ruiz de Austri. “Towards an accurate calculation of the neutralino relic density”. In: *JHEP* 05 (2001), p. 063. DOI: 10.1088/1126-6708/2001/05/063. arXiv: hep-ph/0102308.

[67] Maira Dutra. “Origins for dark matter particles : from the ”WIMP miracle” to the ”FIMP wonder””. PhD thesis. Orsay, LPT, 2019.

[68] Nicolò Trevisani. “Collider Searches for Dark Matter (ATLAS + CMS)”. In: *Universe* 4.11 (2018). ISSN: 2218-1997. DOI: 10.3390/universe4110131. URL: https://www.mdpi.com/2218-1997/4/11/131.

[69] Antonio Boveia and Caterina Doglioni. “Dark Matter Searches at Colliders”. In: *Annual Review of Nuclear and Particle Science* 68.1 (2018), pp. 429–459. DOI: 10.1146/annurev-nucl-101917-021008. eprint: https://doi.org/10.1146/annurev-nucl-101917-021008. URL: https://doi.org/10.1146/annurev-nucl-101917-021008.

[70] Matthew Walker. “Dark Matter in the Galactic Dwarf Spheroidal Satellites”. In: *Planets, Stars and Stellar Systems. Volume 5: Galactic Structure and Stellar Populations*. Ed. by Terry D. Oswalt and Gerard Gilmore. Vol. 5. 2013, p. 1039. DOI: 10.1007/978-94-007-5612-0_20.

[71] Carlos Pérez de los Heros. “Status, Challenges and Directions in Indirect Dark Matter Searches”. In: *Symmetry* 12.10 (2020). ISSN: 2073-8994. DOI: 10.3390/sym12101648. URL: https://www.mdpi.com/2073-8994/12/10/1648.

[72] Marc Schumann. “Direct detection of WIMP dark matter: concepts and status”. In: *Journal of Physics G: Nuclear and Particle Physics* 46.10 (Aug. 2019), p. 103003. DOI: 10.1088/1361-6471/ab2ea5. URL: https://doi.org/10.1088/1361-6471/ab2ea5.

[73] M. T. Ressell and D. J. Dean. “Spin-dependent neutralino-nucleus scattering for $A \sim 127$ nuclei”. In: *Phys. Rev. C* 56 (1 July 1997), pp. 535–546. DOI: 10.1103/PhysRevC.56.535. URL: https://link.aps.org/doi/10.1103/PhysRevC.56.535.

[74] P. Toivanen et al. “Large-scale shell-model calculations of elastic and inelastic scattering rates of lightest supersymmetric particles (LSP) on $^{127}\mathrm{I}$, $^{129}\mathrm{Xe}$, $^{131}\mathrm{Xe}$, and $^{133}\mathrm{Cs}$ nuclei”. In: *Phys. Rev. C* 79 (4 Apr. 2009), p. 044302. DOI: 10.1103/PhysRevC.79.044302. URL: https://link.aps.org/doi/10.1103/PhysRevC.79.044302.

[75] Richard H. Helm. “Inelastic and Elastic Scattering of 187-Mev Electrons from Selected Even-Even Nuclei”. In: *Phys. Rev.* 104 (5 Dec. 1956), pp. 1466–1475. DOI: 10.1103/PhysRev.104.1466. URL: https://link.aps.org/doi/10.1103/PhysRev.104.1466.

[76] David G. Cerdeno and Anne M. Green. “Direct detection of WIMPs”. In: (Feb. 2010), pp. 347–369. DOI: 10.1017/CBO9780511770739.018. arXiv: 1002.1912 [astro-ph.CO].

[77] Chung-Lin Shan. “Determining Ratios of WIMP-Nucleon Cross Sections from Direct Dark Matter Detection Data”. In: *JCAP* 07 (2011), p. 005. DOI: 10.1088/1475-7516/2011/07/005. arXiv: 1103.0482 [hep-ph].

[78] A. Liam Fitzpatrick et al. “The Effective Field Theory of Dark Matter Direct Detection”. In: *JCAP* 02 (2013), p. 004. DOI: 10.1088/1475-7516/2013/02/004. arXiv: 1203.3542 [hep-ph].

[79] Julien Billard et al. “Direct detection of dark matter—APPEC committee report*”. In: *Reports on Progress in Physics* 85.5 (Apr. 2022), p. 056201. DOI: 10.1088/1361-6633/ac5754. URL: https://doi.org/10.1088/1361-6633/ac5754.

[80] A. H. Abdelhameed et al. “First results from the CRESST-III low-mass dark matter program”. In: *Phys. Rev. D* 100.10 (2019), p. 102002. DOI: 10.1103/PhysRevD.100.102002. arXiv: 1904.00498 [astro-ph.CO].

[81] R. Agnese et al. “Search for Low-Mass Weakly Interacting Massive Particles with SuperCDMS”. In: *Phys. Rev. Lett.* 112.24 (2014), p. 241302. DOI: 10.1103/PhysRevLett.112.241302. arXiv: 1402.7137 [hep-ex].

[82] R. Agnese et al. “Search for Low-Mass Dark Matter with CDMSlite Using a Profile Likelihood Fit”. In: *Phys. Rev. D* 99.6 (2019), p. 062001. DOI: 10.1103/PhysRevD.99.062001. arXiv: 1808.09098 [astro-ph.CO].

[83] R. Ajaj et al. “Search for dark matter with a 231-day exposure of liquid argon using DEAP-3600 at SNOLAB”. In: *Phys. Rev. D* 100 (2 July 2019), p. 022004. DOI: 10.1103/PhysRevD.100.022004. URL: https://link.aps.org/doi/10.1103/PhysRevD.100.022004.

[84] P. Agnes et al. “DarkSide-50 532-day Dark Matter Search with Low-Radioactivity Argon”. In: *Phys. Rev. D* 98.10 (2018), p. 102006. DOI: 10.1103/PhysRevD.98.102006. arXiv: 1802.07198 [astro-ph.CO].

[85] P. Agnes et al. “Low-Mass Dark Matter Search with the DarkSide-50 Experiment”. In: *Phys. Rev. Lett.* 121.8 (2018), p. 081307. DOI: 10.1103/PhysRevLett.121.081307. arXiv: 1802.06994 [astro-ph.HE].

[86] P. Agnes et al. “Constraints on Sub-GeV Dark-Matter–Electron Scattering from the DarkSide-50 Experiment”. In: *Phys. Rev. Lett.* 121 (11 Sept. 2018), p. 111303. DOI: 10.1103/PhysRevLett.121.111303. URL: https://link.aps.org/doi/10.1103/PhysRevLett.121.111303.

[87] D. S. Akerib et al. “Results from a search for dark matter in the complete LUX exposure”. In: *Phys. Rev. Lett.* 118.2 (2017), p. 021303. DOI: 10.1103/PhysRevLett.118.021303. arXiv: 1608.07648 [astro-ph.CO].

[88] D. S. Akerib et al. “Results of a Search for Sub-GeV Dark Matter Using 2013 LUX Data”. In: *Phys. Rev. Lett.* 122.13 (2019), p. 131301. DOI: 10.1103/PhysRevLett.122.131301. arXiv: 1811.11241 [astro-ph.CO].

[89] D. S. Akerib et al. “The LUX-ZEPLIN (LZ) Experiment”. In: *Nucl. Instrum. Meth. A* 953 (2020), p. 163047. DOI: 10.1016/j.nima.2019.163047. arXiv: 1910.09124 [physics.ins-det].

[90] J. Aalbers et al. “First Dark Matter Search Results from the LUX-ZEPLIN (LZ) Experiment”. In: (July 2022). arXiv: 2207.03764 [hep-ex].

[91] Qiuhong Wang et al. “Results of dark matter search using the full PandaX-II exposure”. In: *Chin. Phys. C* 44.12 (2020), p. 125001. DOI: 10.1088/1674-1137/abb658. arXiv: 2007.15469 [astro-ph.CO].

[92] Yue Meng et al. “Dark Matter Search Results from the PandaX-4T Commissioning Run”. In: *Phys. Rev. Lett.* 127.26 (2021), p. 261802. DOI: 10.1103/PhysRevLett.127.261802. arXiv: 2107.13438 [hep-ex].

[93] E. Aprile et al. “Dark Matter Search Results from a One Ton-Year Exposure of XENON1T”. In: *Phys. Rev. Lett.* 121.11 (2018), p. 111302. DOI: 10.1103/PhysRevLett.121.111302. arXiv: 1805.12562 [astro-ph.CO].

[94] E. Aprile et al. “Search for Light Dark Matter Interactions Enhanced by the Migdal Effect or Bremsstrahlung in XENON1T”. In: *Phys. Rev. Lett.* 123.24 (2019), p. 241803. DOI: 10.1103/PhysRevLett.123.241803. arXiv: 1907.12771 [hep-ex].

[95] E. Aprile et al. “Light Dark Matter Search with Ionization Signals in XENON1T”. In: *Phys. Rev. Lett.* 123.25 (2019), p. 251801. DOI: 10.1103/PhysRevLett.123.251801. arXiv: 1907.11485 [hep-ex].

[96] E. Aprile et al. “Search for Coherent Elastic Scattering of Solar ^{8}B Neutrinos in the XENON1T Dark Matter Experiment”. In: *Phys. Rev. Lett.* 126 (2021), p. 091301. DOI: 10.1103/PhysRevLett.126.091301. arXiv: 2012.02846 [hep-ex].

[97] R. Bernabei et al. "The DAMA/LIBRA apparatus". In: *Nucl. Instrum. Meth. A* 592 (2008), pp. 297–315. DOI: 10.1016/j.nima.2008.04.082. arXiv: 0804.2738 [astro-ph].

[98] C. Savage et al. "Compatibility of DAMA/LIBRA dark matter detection with other searches". In: *JCAP* 04 (2009), p. 010. DOI: 10.1088/1475-7516/2009/04/010. arXiv: 0808.3607 [astro-ph].

[99] R. Bernabei et al. "First results from DAMA/LIBRA and the combined results with DAMA/NaI". In: *Eur. Phys. J. C* 56 (2008), pp. 333–355. DOI: 10.1140/epjc/s10052-008-0662-y. arXiv: 0804.2741 [astro-ph].

[100] Ciaran A. J. O'Hare. "New Definition of the Neutrino Floor for Direct Dark Matter Searches". In: *Phys. Rev. Lett.* 127.25 (2021), p. 251802. DOI: 10.1103/PhysRevLett.127.251802. arXiv: 2109.03116 [hep-ph].

[101] J. Aalbers et al. "DARWIN: towards the ultimate dark matter detector". In: *JCAP* 11 (2016), p. 017. DOI: 10.1088/1475-7516/2016/11/017. arXiv: 1606.07001 [astro-ph.IM].

[102] Cristiano Galbiati. "Future Dark Matter Searches with Low-Radioactivity Argon". In: Dec. 2017. URL: https://indico.cern.ch/event/765096/contributions/3295671/attachments/1785196/2906164/DarkSide-Argo_ESPP_Dec_17_2017.pdf.

[103] Daniel Z. Freedman. "Coherent Neutrino Nucleus Scattering as a Probe of the Weak Neutral Current". In: *Phys. Rev. D* 9 (1974), pp. 1389–1392. DOI: 10.1103/PhysRevD.9.1389.

[104] J. A. Formaggio and G. P. Zeller. "From eV to EeV: Neutrino cross sections across energy scales". In: *Rev. Mod. Phys.* 84 (3 Sept. 2012), pp. 1307–1341. DOI: 10.1103/RevModPhys.84.1307. URL: https://link.aps.org/doi/10.1103/RevModPhys.84.1307.

[105] Paul Adrien Maurice Dirac and Ralph Howard Fowler. "The quantum theory of the electron". In: *Proceedings of the Royal Society of London. Series A, Containing Papers of a Mathematical and Physical Character* 117.778 (1928), pp. 610–624. DOI: 10.1098/rspa.1928.0023. eprint: https://royalsocietypublishing.org/doi/pdf/10.1098/rspa.1928.0023. URL: https://royalsocietypublishing.org/doi/abs/10.1098/rspa.1928.0023.

[106] Carl D. Anderson. "The Apparent Existence of Easily Deflectable Positives". In: *Science* 76.1967 (1932), pp. 238–239. DOI: 10.1126/science.76.1967.238. eprint: https://www.science.org/doi/pdf/10.1126/science.76.1967.238. URL: https://www.science.org/doi/abs/10.1126/science.76.1967.238.

[107] Carl D. Anderson. "The Positive Electron". In: *Phys. Rev.* 43 (6 Mar. 1933), pp. 491–494. DOI: 10.1103/PhysRev.43.491. URL: https://link.aps.org/doi/10.1103/PhysRev.43.491.

[108] Helen Quinn. "The Asymmetry Between Matter and Antimatter". In: *Physics Today - PHYS TODAY* 56 (Feb. 2003). DOI: 10.1063/1.1564346.

[109] Laurent Canetti, Marco Drewes, and Mikhail Shaposhnikov. "Matter and Antimatter in the Universe". In: *New J. Phys.* 14 (2012), p. 095012. DOI: 10.1088/1367-2630/14/9/095012. arXiv: 1204.4186 [hep-ph].

[110] A. D. Sakharov. "Violation of CP Invariance, C asymmetry, and baryon asymmetry of the universe". In: *Pisma Zh. Eksp. Teor. Fiz.* 5 (1967), pp. 32–35. DOI: 10.1070/PU1991v034n05ABEH002497.

[111] Graham White. *Electroweak Baryogenesis (Second Edition)*. 2053-2563. IOP Publishing, 2022. ISBN: 978-0-7503-3571-3. DOI: 10.1088/978-0-7503-3571-3. URL: https://dx.doi.org/10.1088/978-0-7503-3571-3.

[112] V. A. Rubakov and M. E. Shaposhnikov. "Electroweak baryon number nonconservation in the early universe and in high-energy collisions". In: *Usp. Fiz. Nauk* 166 (1996), pp. 493–537. DOI: 10.1070/PU1996v039n05ABEH000145. arXiv: hep-ph/9603208.

[113] V.A. Kuzmin, V.A. Rubakov, and M.E. Shaposhnikov. “On anomalous electroweak baryon-number non-conservation in the early universe”. In: *Physics Letters B* 155.1 (1985), pp. 36–42. ISSN: 0370-2693. DOI: https://doi.org/10.1016/0370-2693(85)91028-7. URL: https://www.sciencedirect.com/science/article/pii/0370269385910287.

[114] G. ’t Hooft. “Symmetry Breaking through Bell-Jackiw Anomalies”. In: *Phys. Rev. Lett.* 37 (1 July 1976), pp. 8–11. DOI: 10.1103/PhysRevLett.37.8. URL: https://link.aps.org/doi/10.1103/PhysRevLett.37.8.

[115] Makoto Kobayashi and Toshihide Maskawa. “CP-Violation in the Renormalizable Theory of Weak Interaction”. In: *Progress of Theoretical Physics* 49.2 (Feb. 1973), pp. 652–657. ISSN: 0033-068X. DOI: 10.1143/PTP.49.652. eprint: https://academic.oup.com/ptp/article-pdf/49/2/652/5257692/49-2-652.pdf. URL: https://doi.org/10.1143/PTP.49.652.

[116] M.D. Schwartz. *Quantum Field Theory and the Standard Model*. illustrated. Quantum Field Theory and the Standard Model. Cambridge University Press, 2013. ISBN: 9781107034730; 1107034736.

[117] Michael S. Chanowitz, John R. Ellis, and Mary K. Gaillard. “The Price of Natural Flavor Conservation in Neutral Weak Interactions”. In: *Nucl. Phys. B* 128 (1977), pp. 506–536. DOI: 10.1016/0550-3213(77)90057-8.

[118] Howard Georgi and S. L. Glashow. “Unity of All Elementary-Particle Forces”. In: *Phys. Rev. Lett.* 32 (8 Feb. 1974), pp. 438–441. DOI: 10.1103/PhysRevLett.32.438. URL: https://link.aps.org/doi/10.1103/PhysRevLett.32.438.

[119] S.M. Barr. “A new symmetry breaking pattern for SO(10) and proton decay”. In: *Physics Letters B* 112.3 (1982), pp. 219–222. ISSN: 0370-2693. DOI: https://doi.org/10.1016/0370-2693(82)90966-2. URL: https://www.sciencedirect.com/science/article/pii/0370269382909662.

[120] Julian Heeck and Volodymyr Takhistov. “Inclusive Nucleon Decay Searches as a Frontier of Baryon Number Violation”. In: *Phys. Rev. D* 101.1 (2020), p. 015005. DOI: 10.1103/PhysRevD.101.015005. arXiv: 1910.07647 [hep-ph].

[121] Carl E. Carlson and Christopher D. Carone. “Low scale quantum gravity and double nucleon decay”. In: *Phys. Lett. B* 512 (2001), pp. 121–126. DOI: 10.1016/S0370-2693(01)00705-5. arXiv: hep-ph/0103180.

[122] K. S. Babu, Ilia Gogoladze, and Kai Wang. “Gauged baryon parity and nucleon stability”. In: *Phys. Lett. B* 570 (2003), pp. 32–38. DOI: 10.1016/j.physletb.2003.07.036. arXiv: hep-ph/0306003.

[123] S. L. Dubovsky, V. A. Rubakov, and P. G. Tinyakov. “Brane world: Disappearing massive matter”. In: *Phys. Rev. D* 62 (10 Oct. 2000), p. 105011. DOI: 10.1103/PhysRevD.62.105011. URL: https://link.aps.org/doi/10.1103/PhysRevD.62.105011.

[124] Sudhakantha Girmohanta and Robert Shrock. “Baryon-number-violating nucleon and dinucleon decays in a model with large extra dimensions”. In: *Phys. Rev. D* 101 (1 Jan. 2020), p. 015017. DOI: 10.1103/PhysRevD.101.015017. URL: https://link.aps.org/doi/10.1103/PhysRevD.101.015017.

[125] Jogesh C. Pati. “Nucleon decays into lepton + lepton + antilepton + mesons within SU(4) of color”. In: *Phys. Rev. D* 29 (7 Apr. 1984), pp. 1549–1552. DOI: 10.1103/PhysRevD.29.1549. URL: https://link.aps.org/doi/10.1103/PhysRevD.29.1549.

[126] Jogesh C. Pati and Abdus Salam. “Is Baryon Number Conserved?” In: *Phys. Rev. Lett.* 31 (10 Sept. 1973), pp. 661–664. DOI: 10.1103/PhysRevLett.31.661. URL: https://link.aps.org/doi/10.1103/PhysRevLett.31.661.

[127] R. N. Mohapatra, Abdel Perez-Lorenzana, and C. A. de S Pires. “Neutrino mass, bulk Majoron and neutrinoless double beta decay”. In: *Phys. Lett. B* 491 (2000), pp. 143–147. DOI: 10.1016/S0370-2693(00)01031-5. arXiv: hep-ph/0008158.

[128] Julian Heeck. “Phenomenology of Majorons”. In: *13th Patras Workshop on Axions, WIMPs and WISPs*. 2018, pp. 212–215. DOI: 10.3204/DESY-PROC-2017-02/heeck_julian. arXiv: 1709.07670 [hep-ph].

[129] Yoichiro Suzuki. “The Super-Kamiokande experiment”. In: *The European Physical Journal C* 79 (Apr. 2019). DOI: 10.1140/epjc/s10052-019-6796-2.

[130] K. Abe et al. “Search for proton decay via $p \to e^+\pi^0$ and $p \to \mu^+\pi^0$ in 0.31 megaton·years exposure of the Super-Kamiokande water Cherenkov detector”. In: *Phys. Rev. D* 95.1 (2017), p. 012004. DOI: 10.1103/PhysRevD.95.012004. arXiv: 1610.03597 [hep-ex].

[131] R. Matsumoto et al. “Search for proton decay via $p \to \mu^+K^0$ in 0.37 megaton-years exposure of Super-Kamiokande”. In: *Phys. Rev. D* 106 (7 Oct. 2022), p. 072003. DOI: 10.1103/PhysRevD.106.072003. URL: https://link.aps.org/doi/10.1103/PhysRevD.106.072003.

[132] H. Ejiri. “Nuclear deexcitations of nucleon holes associated with nucleon decays in nuclei”. In: *Phys. Rev. C* 48 (3 Sept. 1993), pp. 1442–1444. DOI: 10.1103/PhysRevC.48.1442. URL: https://link.aps.org/doi/10.1103/PhysRevC.48.1442.

[133] K Hagino and M Nirkko. “Branching ratios for de-excitation processes of daughter nuclei following invisible dinucleon decays in 16O”. In: *Journal of Physics G: Nuclear and Particle Physics* 45.10 (Sept. 2018), p. 105105. DOI: 10.1088/1361-6471/aadeb1. URL: https://dx.doi.org/10.1088/1361-6471/aadeb1.

[134] V. Albanese et al. “The SNO+ experiment”. In: *JINST* 16.08 (2021), P08059. DOI: 10.1088/1748-0221/16/08/P08059. arXiv: 2104.11687 [physics.ins-det].

[135] K. Eguchi et al. “First Results from KamLAND: Evidence for Reactor Antineutrino Disappearance”. In: *Phys. Rev. Lett.* 90 (2 Jan. 2003), p. 021802. DOI: 10.1103/PhysRevLett.90.021802. URL: https://link.aps.org/doi/10.1103/PhysRevLett.90.021802.

[136] T. Araki et al. “Measurement of Neutrino Oscillation with KamLAND: Evidence of Spectral Distortion”. In: *Phys. Rev. Lett.* 94 (8 Mar. 2005), p. 081801. DOI: 10.1103/PhysRevLett.94.081801. URL: https://link.aps.org/doi/10.1103/PhysRevLett.94.081801.

[137] A. Allega et al. “Improved search for invisible modes of nucleon decay in water with the SNO+detector”. In: *Phys. Rev. D* 105.11 (2022), p. 112012. DOI: 10.1103/PhysRevD.105.112012. arXiv: 2205.06400 [hep-ex].

[138] T. Araki et al. “Search for the invisible decay of neutrons with KamLAND”. In: *Phys. Rev. Lett.* 96 (2006), p. 101802. DOI: 10.1103/PhysRevLett.96.101802. arXiv: hep-ex/0512059.

[139] S. I. Alvis et al. “Search for trinucleon decay in the Majorana Demonstrator”. In: *Phys. Rev. D* 99 (7 Apr. 2019), p. 072004. DOI: 10.1103/PhysRevD.99.072004. URL: https://link.aps.org/doi/10.1103/PhysRevD.99.072004.

[140] Fabio Cappella. “Ricerca di processi rari con rivelatore a Xenon liquido”. PhD thesis. Università degli studi di Roma Tor Vergata, 2005. URL: %7Bhttps://art.torvergata.it/handle/2108/236#%7D.

[141] P. Belli et al. “Search for WIMPs with enriched xenon at Gran Sasso”. In: *Nuovo Cim. C* 19 (1996), pp. 537–544. DOI: 10.1007/BF02523769.

[142] M Auger et al. “The EXO-200 detector, part I: detector design and construction”. In: *Journal of Instrumentation* 7.05 (May 2012), P05010. DOI: 10.1088/1748-0221/7/05/P05010. URL: https://dx.doi.org/10.1088/1748-0221/7/05/P05010.

[143] R. Bernabei et al. “Search for the nucleon and di-nucleon decay into invisible channels”. In: *Phys. Lett. B* 493 (2000), pp. 12–18. DOI: 10.1016/S0370-2693(00)01112-6.

[144] Bernabei, R. et al. “Search for rare processes with DAMA/LXe experiment at Gran Sasso”. In: *Eur. Phys. J. A* 27 (2006), pp. 35–41. DOI: 10.1140/epja/i2006-08-004-y. URL: https://doi.org/10.1140/epja/i2006-08-004-y.

[145] J. B. Albert et al. “Search for nucleon decays with EXO-200”. In: *Phys. Rev. D* 97.7 (2018), p. 072007. DOI: 10.1103/PhysRevD.97.072007. arXiv: 1710.07670 [hep-ex].

[146] *The Lund/LBNL Nuclear Data Search*. http://nucleardata.nuclear.lu.se/toi/index.asp. Accessed: 06/01/2022.

[147] John C. Evans Jr. and Richard I. Steinberg. “Nucleon Stability: A Geochemical Test Independent of Decay Mode”. In: *Science* 197 (1977), pp. 989–991. DOI: 10.1126/science.197.4307.989.

[148] E. Aprile et al. “Design and performance of the XENON10 dark matter experiment”. In: *Astroparticle Physics* 34.9 (Apr. 2011), pp. 679–698. DOI: 10.1016/j.astropartphys.2011.01.006. URL: https://doi.org/10.1016%5C%2Fj.astropartphys.2011.01.006.

[149] E. Aprile et al. “The XENON100 dark matter experiment”. In: *Astroparticle Physics* 35.9 (Apr. 2012), pp. 573–590. DOI: 10.1016/j.astropartphys.2012.01.003. URL: https://doi.org/10.1016%5C%2Fj.astropartphys.2012.01.003.

[150] E. Aprile et al. “The XENON1T Dark Matter Experiment”. In: *Eur. Phys. J. C* 77.12 (2017), p. 881. DOI: 10.1140/epjc/s10052-017-5326-3. arXiv: 1708.07051 [astro-ph.IM].

[151] E. Aprile et al. “Projected WIMP sensitivity of the XENONnT dark matter experiment”. In: *Journal of Cosmology and Astroparticle Physics* 2020.11 (Nov. 2020), pp. 031–031. DOI: 10.1088/1475-7516/2020/11/031. URL: https://doi.org/10.1088/1475-7516/2020/11/031.

[152] *NIST: National Institute of Standards and Technology*. https://www.nist.gov/pml/stopping-power-range-tables-electrons-protons-and-helium-ions. Accessed: 01/09/2022.

[153] I. T. Steinberger and U. Asaf. “Band-Structure Parameters of Solid and Liquid Xenon”. In: *Phys. Rev. B* 8 (2 July 1973), pp. 914–918. DOI: 10.1103/PhysRevB.8.914. URL: https://link.aps.org/doi/10.1103/PhysRevB.8.914.

[154] Juris Meija et al. In: *Pure and Applied Chemistry* 88.3 (2016), pp. 265–291. DOI: doi:10.1515/pac-2015-0305. URL: https://doi.org/10.1515/pac-2015-0305.

[155] Ian H. Bell et al. “Pure and Pseudo-pure Fluid Thermophysical Property Evaluation and the Open-Source Thermophysical Property Library CoolProp”. In: *Industrial & Engineering Chemistry Research* 53.6 (2014), pp. 2498–2508. DOI: 10.1021/ie4033999. eprint: http://pubs.acs.org/doi/pdf/10.1021/ie4033999. URL: http://pubs.acs.org/doi/abs/10.1021/ie4033999.

[156] Sujoy Mukhopadhyay. “Xenon Isotopes”. In: *Encyclopedia of Geochemistry: A Comprehensive Reference Source on the Chemistry of the Earth*. Ed. by William M. White. Cham: Springer International Publishing, 2018, pp. 1500–1508. ISBN: 978-3-319-39312-4. DOI: 10.1007/978-3-319-39312-4_203. URL: https://doi.org/10.1007/978-3-319-39312-4_203.

[157] Glenn F. Knoll. *Radiation detection and measurement / Glenn F. Knoll*. English. 2nd ed. Wiley New York, 1989, xix, 754 p. : ISBN: 0471815047.

[158] D.-M. Mei et al. “A model of nuclear recoil scintillation efficiency in noble liquids”. In: *Astroparticle Physics* 30.1 (2008), pp. 12–17. ISSN: 0927-6505. DOI: https://doi.org/10.1016/j.astropartphys.2008.06.001. URL: https://www.sciencedirect.com/science/article/pii/S0927650508000765.

[159] R. Sahu et al. “Elastic and inelastic scattering of neutrinos and weakly interacting massive particles on nuclei”. In: *Phys. Rev. C* 102.3 (2020), p. 035501. DOI: 10.1103/PhysRevC.102.035501. arXiv: 2004.04055 [nucl-th].

[160] Guillaume Plante. “The XENON100 Dark Matter Experiment: Design, Construction, Calibration and 2010 Search Results with Improved Measurement of the Scintillation Response of Liquid Xenon to Low-Energy Nuclear Recoils”. PhD thesis. Columbia University, New York, Jan. 2012.

[161] Md. Mamunur Rashid et al. “Evaluation of neutron nuclear data on xenon isotopes”. In: *Journal of Nuclear Science and Technology* 53.9 (2016), pp. 1310–1320. DOI: `10.1080/00223131.2015.1105164`. eprint: `https://doi.org/10.1080/00223131.2015.1105164`. URL: `https://doi.org/10.1080/00223131.2015.1105164`.

[162] E. Aprile and T. Doke. “Liquid xenon detectors for particle physics and astrophysics”. In: *Rev. Mod. Phys.* 82 (3 July 2010), pp. 2053–2097. DOI: `10.1103/RevModPhys.82.2053`. URL: `https://link.aps.org/doi/10.1103/RevModPhys.82.2053`.

[163] Keiko Fujii et al. “High-accuracy measurement of the emission spectrum of liquid xenon in the vacuum ultraviolet region”. In: *Nuclear Instruments and Methods in Physics Research Section A: Accelerators, Spectrometers, Detectors and Associated Equipment* 795 (2015), pp. 293–297. ISSN: 0168-9002. DOI: `https://doi.org/10.1016/j.nima.2015.05.065`. URL: `https://www.sciencedirect.com/science/article/pii/S016890021500724X`.

[164] Akira Hitachi et al. “Effect of ionization density on the time dependence of luminescence from liquid argon and xenon”. In: *Phys. Rev. B* 27 (9 May 1983), pp. 5279–5285. DOI: `10.1103/PhysRevB.27.5279`. URL: `https://link.aps.org/doi/10.1103/PhysRevB.27.5279`.

[165] K. Ueshima et al. “Scintillation-only based pulse shape discrimination for nuclear and electron recoils in liquid xenon”. In: *Nuclear Instruments and Methods in Physics Research Section A: Accelerators, Spectrometers, Detectors and Associated Equipment* 659.1 (2011), pp. 161–168. ISSN: 0168-9002. DOI: `https://doi.org/10.1016/j.nima.2011.09.011`. URL: `https://www.sciencedirect.com/science/article/pii/S0168900211017566`.

[166] Carl Eric Dahl. “The physics of background discrimination in liquid xenon, and first results from Xenon10 in the hunt for WIMP dark matter”. PhD thesis. Princeton U., 2009.

[167] Akira Hitachi. “Exciton kinetics in condensed rare gases”. In: *The Journal of Chemical Physics* 80.2 (1984), pp. 745–748. DOI: `10.1063/1.446781`. eprint: `https://doi.org/10.1063/1.446781`. URL: `https://doi.org/10.1063/1.446781`.

[168] J Lindhard et al. “INTEGRAL EQUATIONS GOVERNING RADIATION EFFECTS. (NOTES ON ATOMIC COLLISIONS, III)”. In: *Kgl. Danske Videnskab., Selskab. Mat. Fys. Medd.* (Jan. 1963). URL: `https://www.osti.gov/biblio/4701226`.

[169] Peter Sorensen and Carl Eric Dahl. “Nuclear recoil energy scale in liquid xenon with application to the direct detection of dark matter”. In: *Phys. Rev. D* 83 (2011), p. 063501. DOI: `10.1103/PhysRevD.83.063501`. arXiv: `1101.6080 [astro-ph.IM]`.

[170] Tadayoshi Doke et al. “Let dependence of scintillation yields in liquid argon”. In: *Nuclear Instruments and Methods in Physics Research Section A: Accelerators, Spectrometers, Detectors and Associated Equipment* 269.1 (1988), pp. 291–296. ISSN: 0168-9002. DOI: `https://doi.org/10.1016/0168-9002(88)90892-3`. URL: `https://www.sciencedirect.com/science/article/pii/0168900288908923`.

[171] Werner F. Schmidt et al. “The mobility of positive and negative ions in liquid xenon”. In: *Radiation Physics and Chemistry* 74.3 (2005). Professor Robert Schiller’s 70th Birthday, pp. 152–159. ISSN: 0969-806X. DOI: `https://doi.org/10.1016/j.radphyschem.2005.04.008`. URL: `https://www.sciencedirect.com/science/article/pii/S0969806X05000861`.

[172] M Szydagis et al. “NEST: a comprehensive model for scintillation yield in liquid xenon”. In: *Journal of Instrumentation* 6.10 (Oct. 2011), P10002–P10002. DOI: `10.1088/1748-0221/6/10/p10002`. URL: `https://doi.org/10.1088/1748-0221/6/10/p10002`.

[173] V Chepel and H Araújo. “Liquid noble gas detectors for low energy particle physics”. In: *Journal of Instrumentation* 8.04 (Apr. 2013), R04001–R04001. DOI: 10.1088/1748-0221/8/04/r04001. URL: https://doi.org/10.1088/1748-0221/8/04/r04001.

[174] M. Szydagis et al. *Noble Element Simulation Technique v2.0*. Version v2.0.0. July 2018. DOI: 10.5281/zenodo.1314669. URL: https://doi.org/10.5281/zenodo.1314669.

[175] Tadayoshi Doke et al. “Absolute Scintillation Yields in Liquid Argon and Xenon for Various Particles”. In: *Japanese Journal of Applied Physics* 41.3A (Mar. 2002), p. 1538. DOI: 10.1143/JJAP.41.1538.

[176] T. Takahashi et al. “Average energy expended per ion pair in liquid xenon”. In: *Phys. Rev. A* 12 (1975), pp. 1771–1775. DOI: 10.1103/PhysRevA.12.1771.

[177] G. Anton et al. “Measurement of the scintillation and ionization response of liquid xenon at MeV energies in the EXO-200 experiment”. In: *Phys. Rev. C* 101.6 (2020), p. 065501. DOI: 10.1103/PhysRevC.101.065501. arXiv: 1908.04128 [physics.ins-det].

[178] Laura Baudis, Patricia Sanchez-Lucas, and Kevin Thieme. “A measurement of the mean electronic excitation energy of liquid xenon”. In: *Eur. Phys. J. C* 81.12 (2021), p. 1060. DOI: 10.1140/epjc/s10052-021-09834-x. arXiv: 2109.07151 [physics.ins-det].

[179] E. Aprile et al. “Observation of anticorrelation between scintillation and ionization for MeV gamma rays in liquid xenon”. In: *Phys. Rev. B* 76 (1 July 2007), p. 014115. DOI: 10.1103/PhysRevB.76.014115. URL: https://link.aps.org/doi/10.1103/PhysRevB.76.014115.

[180] Brian Lenardo et al. “A Global Analysis of Light and Charge Yields in Liquid Xenon”. In: *IEEE Trans. Nucl. Sci.* 62.6 (2015), pp. 3387–3396. DOI: 10.1109/TNS.2015.2481322. arXiv: 1412.4417 [astro-ph.IM].

[181] “CERN Courier Volume 50, Number 10, December 2010”. In: (2010). URL: https://cds.cern.ch/record/1734479.

[182] Alexey Buzulutskov. “Electroluminescence and Electron Avalanching in Two-Phase Detectors”. In: *Instruments* 4.2 (2020). ISSN: 2410-390X. DOI: 10.3390/instruments4020016. URL: https://www.mdpi.com/2410-390X/4/2/16.

[183] D. S. Akerib et al. “Discrimination of electronic recoils from nuclear recoils in two-phase xenon time projection chambers”. In: *Phys. Rev. D* 102.11 (2020), p. 112002. DOI: 10.1103/PhysRevD.102.112002. arXiv: 2004.06304 [physics.ins-det].

[184] E. Aprile et al. “XENON1T dark matter data analysis: Signal and background models and statistical inference”. In: *Phys. Rev. D* 99.11 (2019), p. 112009. DOI: 10.1103/PhysRevD.99.112009. arXiv: 1902.11297 [physics.ins-det].

[185] E. Aprile et al. “XENON1T Dark Matter Data Analysis: Signal Reconstruction, Calibration and Event Selection”. In: *Phys. Rev. D* 100.5 (2019), p. 052014. DOI: 10.1103/PhysRevD.100.052014. arXiv: 1906.04717 [physics.ins-det].

[186] The XENON Collaboration. *XENONnT Technical Design Report*. Tech. rep. Feb. 2018.

[187] XENON collaboration. “The XENONnT Dark Matter Experiment”. publication ongoing. 2023.

[188] XENON collaboration. “The Neutron Veto of the XENONnT Experiment”. publication ongoing. 2023.

[189] Tomoyuki Tanaka et al. “Gamma-ray spectra from thermal neutron capture on gadolinium-155 and natural gadolinium”. In: *Progress of Theoretical and Experimental Physics* 2020.4 (Apr. 2020). 043D02. ISSN: 2050-3911. DOI: 10.1093/ptep/ptaa015. eprint: https://academic.oup.com/ptep/article-pdf/2020/4/043D02/33040537/ptaa015.pdf. URL: https://doi.org/10.1093/ptep/ptaa015.

[190] E. Aprile et al. “Conceptual design and simulation of a water Cherenkov muon veto for the XENON1T experiment”. In: *JINST* 9 (2014), P11006. DOI: 10.1088/1748-0221/9/11/P11006. arXiv: 1406.2374 [astro-ph.IM].

[191] J. Angle et al. “First Results from the XENON10 Dark Matter Experiment at the Gran Sasso National Laboratory”. In: *Phys. Rev. Lett.* 100 (2 Jan. 2008), p. 021303. DOI: 10.1103/PhysRevLett.100.021303. URL: https://link.aps.org/doi/10.1103/PhysRevLett.100.021303.

[192] E. Aprile et al. “Dark Matter Search Results from a One Ton-Year Exposure of XENON1T”. In: *Phys. Rev. Lett.* 121 (11 Sept. 2018), p. 111302. DOI: 10.1103/PhysRevLett.121.111302. URL: https://link.aps.org/doi/10.1103/PhysRevLett.121.111302.

[193] L. Baudis et al. “Gator: a low-background counting facility at the Gran Sasso Underground Laboratory”. In: *JINST* 6 (2011), P08010. DOI: 10.1088/1748-0221/6/08/P08010. arXiv: 1103.2125 [astro-ph.IM].

[194] Gabriela R. Araujo et al. “The upgraded low-background germanium counting facility Gator for high-sensitivity γ-ray spectrometry”. In: *JINST* 17.08 (2022), P08010. DOI: 10.1088/1748-0221/17/08/P08010. arXiv: 2204.12478 [physics.ins-det].

[195] G. Heusser, M. Laubenstein, and H. Neder. “Low-level germanium gamma-ray spectrometry at the μBq/kg level and future developments towards higher sensitivity”. In: *Radionuclides in the Environment*. Ed. by P.P. Povinec and J.A. Sanchez-Cabeza. Vol. 8. Radioactivity in the Environment. Elsevier, 2006, pp. 495–510. DOI: https://doi.org/10.1016/S1569-4860(05)08039-3. URL: https://www.sciencedirect.com/science/article/pii/S1569486005080393.

[196] M. von Sivers et al. “The GeMSE facility for low-background γ-ray spectrometry”. In: *JINST* 11.12 (2016), P12017. DOI: 10.1088/1748-0221/11/12/P12017. arXiv: 1606.03983 [physics.ins-det].

[197] Diego Ramírez García et al. “GeMSE: a low-background facility for gamma-spectrometry at moderate rock overburden”. In: *JINST* 17.04 (2022), P04005. DOI: 10.1088/1748-0221/17/04/P04005. arXiv: 2202.06540 [physics.ins-det].

[198] Gerd Heusser et al. “GIOVE - A new detector setup for high sensitivity germanium spectroscopy at shallow depth”. In: *Eur. Phys. J. C* 75.11 (2015), p. 531. DOI: 10.1140/epjc/s10052-015-3704-2. arXiv: 1507.03319 [astro-ph.IM].

[199] M. L. di Vacri, S. Nisi, and M. Balata. “Measurement of low radioactivity background in a high voltage cable by high resolution inductively coupled plasma mass spectrometry”. In: *Low Radioactivity Techniques 2013 (LRT 2013)*. Ed. by Lino Miramonti and Luciano Pandola. Vol. 1549. American Institute of Physics Conference Series. Aug. 2013, pp. 66–69. DOI: 10.1063/1.4818077.

[200] E. Aprile et al. “^{222}Rn emanation measurements for the XENON1T experiment”. In: *Eur. Phys. J. C* 81.4 (2021), p. 337. DOI: 10.1140/epjc/s10052-020-08777-z. arXiv: 2009.13981 [physics.ins-det].

[201] E. Aprile et al. “Material radiopurity control in the XENONnT experiment”. In: *The European Physical Journal C* 82.7 (July 2022). DOI: 10.1140/epjc/s10052-022-10345-6. URL: https://doi.org/10.1140%5C%2Fepjc%5C%2Fs10052-022-10345-6.

[202] Kenji Ozone. “Liquid Xenon Scintillation Detector for the New $\mu \to e\gamma$ *Search Experiment*”. PhD thesis. University of Tokyo, 2005. URL: %7Bhttp://meg.icepp.s.u-tokyo.ac.jp/docs/theses/ozoned.pdf%7D.

[203] D. Schulte et al. “Ultra-clean radon-free four cylinder magnetically-coupled piston pump”. In: *JINST* 16.09 (2021), P09011. DOI: 10.1088/1748-0221/16/09/P09011. arXiv: 2107.00755 [physics.ins-det].

[204] G. Plante et al. “Liquid-phase purification for multi-tonne xenon detectors”. In: *The European Physical Journal C* 82.10 (Oct. 2022). DOI: 10.1140/epjc/s10052-022-10832-w. URL: https://doi.org/10.1140%5C%2Fepjc%5C%2Fs10052-022-10832-w.

[205] XENON collaboration. “Novel liquid xenon purification technique for the XENONnT dark matter experiment”. publication ongoing. 2023.

[206] E. Aprile et al. “Removing krypton from xenon by cryogenic distillation to the ppq level”. In: *Eur. Phys. J. C* 77.5 (2017), p. 275. DOI: 10.1140/epjc/s10052-017-4757-1. arXiv: 1612.04284 [physics.ins-det].

[207] Sebastian Lindemann and Hardy Simgen. “Krypton assay in xenon at the ppq level using a gas chromatographic system and mass spectrometer”. In: *Eur. Phys. J. C* 74 (2014), p. 2746. DOI: 10.1140/epjc/s10052-014-2746-1. arXiv: 1308.4806 [physics.ins-det].

[208] E. Aprile et al. “Search for New Physics in Electronic Recoil Data from XENONnT”. In: *Phys. Rev. Lett.* 129.16 (2022), p. 161805. DOI: 10.1103/PhysRevLett.129.161805. arXiv: 2207.11330 [hep-ex].

[209] Balraj Singh and Jun Chen. “Nuclear Data Sheets for A=85”. In: *Nuclear Data Sheets* 116 (2014), pp. 1–162. ISSN: 0090-3752. DOI: https://doi.org/10.1016/j.nds.2014.01.001. URL: https://www.sciencedirect.com/science/article/pii/S0090375214000106.

[210] Sukhjeet Singh, A.K. Jain, and Jagdish K. Tuli. “Nuclear Data Sheets for A = 222”. In: *Nuclear Data Sheets* 112.11 (2011), pp. 2851–2886. ISSN: 0090-3752. DOI: https://doi.org/10.1016/j.nds.2011.10.002. URL: https://www.sciencedirect.com/science/article/pii/S0090375211000962.

[211] Shaofei Zhu and E.A. McCutchan. “Nuclear Data Sheets for A=214”. In: *Nuclear Data Sheets* 175 (2021), pp. 1–149. ISSN: 0090-3752. DOI: https://doi.org/10.1016/j.nds.2021.06.001. URL: https://www.sciencedirect.com/science/article/pii/S009037522100034X.

[212] M. Murra et al. “Design, construction and commissioning of a high-flow radon removal system for XENONnT”. PhD thesis. 2022. DOI: 10.48550/ARXIV.2205.11492. URL: https://arxiv.org/abs/2205.11492.

[213] V.C. Antochi et al. “Improved quality tests of R11410-21 photomultiplier tubes for the XENONnT experiment”. In: *Journal of Instrumentation* 16.08 (Aug. 2021), P08033. DOI: 10.1088/1748-0221/16/08/p08033. URL: https://doi.org/10.1088/1748-0221/16/08/p08033.

[214] E. Aprile et al. “Excess electronic recoil events in XENON1T”. In: *Phys. Rev. D* 102.7 (2020), p. 072004. DOI: 10.1103/PhysRevD.102.072004. arXiv: 2006.09721 [hep-ex].

[215] E. Aprile et al. “Double-Weak Decays of ^{124}Xe and ^{136}Xe in the XENON1T and XENONnT Experiments”. In: *Phys. Rev. C* 106.2 (2022), p. 024328. DOI: 10.1103/PhysRevC.106.024328. arXiv: 2205.04158 [hep-ex].

[216] P. Barrow et al. “Qualification tests of the R11410-21 photomultiplier tubes for the XENON1T detector”. In: *Journal of Instrumentation* 12.01 (Jan. 2017), P01024–P01024. DOI: 10.1088/1748-0221/12/01/p01024. URL: https://doi.org/10.1088/1748-0221/12/01/p01024.

[217] *PHOTOMULTIPLIER TUBES. Basics and Application. FOURTH EDITION*. https://www.hamamatsu.com/content/dam/hamamatsu-photonics/sites/documents/99_SALES_LIBRARY/etd/PMT_handbook_v4E.pdf. Accessed: 15/10/2022.

[218] A. G. Wright. *The Photomultiplier Handbook*. Oxford University Press, June 2017. ISBN: 9780199565092. DOI: 10.1093/oso/9780199565092.001.0001. URL: https://doi.org/10.1093/oso/9780199565092.001.0001.

[219] E. Aprile et al. “Lowering the radioactivity of the photomultiplier tubes for the XENON1T dark matter experiment”. In: *Eur. Phys. J. C* 75.11 (2015), p. 546. DOI: 10.1140/epjc/s10052-015-3657-5. arXiv: 1503.07698 [astro-ph.IM].

[220] B.K Lubsandorzhiev et al. “Studies of prepulses and late pulses in the 8" electron tubes series of photomultipliers”. In: *Nuclear Instruments and Methods in Physics Research Section A: Accelerators, Spectrometers, Detectors and Associated Equipment* 442.1 (2000), pp. 452–458. ISSN: 0168-9002. DOI: https://doi.org/10.1016/S0168-9002(99)01272-3. URL: https://www.sciencedirect.com/science/article/pii/S0168900299012723.

[221] F Kaether and C Langbrandtner. “Transit time and charge correlations of single photoelectron events in R7081 photomultiplier tubes”. In: *Journal of Instrumentation* 7.09 (Sept. 2012), P09002. DOI: 10.1088/1748-0221/7/09/P09002. URL: https://dx.doi.org/10.1088/1748-0221/7/09/P09002.

[222] Alexander Bolozdynya et al. “Peculiarities of the Hamamatsu R11410-20 photomultiplier tubes”. In: *PoS* PhotoDet2015 (2016), p. 025. DOI: 10.22323/1.252.0025.

[223] D.Yu. Akimov et al. “Observation of light emission from Hamamatsu R11410-20 photomultiplier tubes”. In: *Nuclear Instruments and Methods in Physics Research Section A: Accelerators, Spectrometers, Detectors and Associated Equipment* 794 (2015), pp. 1–2. ISSN: 0168-9002. DOI: https://doi.org/10.1016/j.nima.2015.04.066. URL: https://www.sciencedirect.com/science/article/pii/S0168900215005823.

[224] Carlos H. Faham. “Prototype, Surface Commissioning and Photomultiplier Tube Characterization for the Large Underground Xenon (LUX) Direct Dark Matter Search Experiment”. PhD thesis. Brown U., 2014. DOI: 10.7301/Z0QV3JV5.

[225] Diego Ramirez Garcia. “Simulating the XENONnT dark matter experiment: backgrounds and WIMP sensitivity”. PhD thesis. Albert-Ludwigs-Universität Freiburg, 2022. URL: %7Bhttps://freidok.uni-freiburg.de/data/228338%7D.

[226] L. Baudis et al. “Measurements of the position-dependent photo-detection sensitivity of the Hamamatsu R11410 and R8520 photomultiplier tubes”. In: (Sept. 2015). arXiv: 1509.04055 [physics.ins-det]

[227] K. Lung et al. “Characterization of the Hamamatsu R11410-10 3-Inch Photomultiplier Tube for Liquid Xenon Dark Matter Direct Detection Experiments”. In: *Nucl. Instrum. Meth. A* 696 (2012), pp. 32–39. DOI: 10.1016/j.nima.2012.08.052. arXiv: 1202.2628 [physics.ins-det].

[228] C. H. Faham et al. “Measurements of wavelength-dependent double photoelectron emission from single photons in VUV-sensitive photomultiplier tubes”. In: *JINST* 10.09 (2015), P09010. DOI: 10.1088/1748-0221/10/09/P09010. arXiv: 1506.08748 [physics.ins-det].

[229] Annika Behrens. “Light Detectors for the XENON100 and XENON1T Dark Matter Search Experiments”. PhD thesis. University of Zurich, 2014. URL: %7Bhttps://www.physik.uzh.ch/groups/groupbaudis/darkmatter/theses/xenon/thesis_behrens.pdf%7D.

[230] Daniel Mayani Paras. “Photomultiplier Tubes for the XENON1T Dark Matter Experiment and Studies on the XENON100 Electromagnetic Background”. PhD thesis. University of Zurich, 2017. URL: %7Bhttps://www.physik.uzh.ch/groups/groupbaudis/darkmatter/theses/xenon/PhD_thesis_Mayani.pdf%7D.

[231] *Evans Analytical Group (EAG)*. http://www.eaglabs.com/mc/glow-discharge-mass-spectrometry.html.

[232] Adam Michael Brown. “Search for Elastic and Inelastic Dark Matter Interactions in XENON1T and Light Detection for XENONnT”. PhD thesis. University of Zurich, 2020. URL: %7Bhttps://www.physik.uzh.ch/dam/jcr:a9cd6398-58ad-45e9-b87d-85e8f2490d1d/abrown_thesis_final.pdf%7D.

[233] Julien Wulf. “Direct Dark Matter Search with XENON1T and Developments for Multi-Ton Liquid Xenon Detectors”. PhD thesis. University of Zurich, 2018. URL: %7Bhttps://www.physik.uzh.ch/dam/jcr:52522bb9-437b-46d9-976d-fc88be3ceb89/PhD_Thesis_Julien_Wulf.pdf%7D.

[234] R. Saldanha et al. “Model Independent Approach to the Single Photoelectron Calibration of Photomultiplier Tubes”. In: *Nucl. Instrum. Meth. A* 863 (2017). Ed. by Guoqing Xiao, Hao Shen, and Guanghua Du, pp. 35–46. DOI: 10.1016/j.nima.2017.02.086. arXiv: 1602.03150 [physics.ins-det].

[235] E. Glueckauf and G. P. Kitt. “The Krypton and Xenon Contents of Atmospheric Air”. In: *Proceedings of the Royal Society of London. Series A, Mathematical and Physical Sciences* 234.1199 (1956), pp. 557–565. ISSN: 00804630. URL: http://www.jstor.org/stable/100004 (visited on 04/06/2023).

[236] S. Li et al. “Performance of photosensors in the PandaX-I experiment”. In: *Journal of Instrumentation* 11.02 (Feb. 2016), T02005. DOI: 10.1088/1748-0221/11/02/T02005. URL: https://dx.doi.org/10.1088/1748-0221/11/02/T02005.

[237] C. Sutour et al. “Determination of the argon concentration in ambient dry air for the calculation of air density”. In: *Metrologia* 44.6 (Oct. 2007), p. 448. DOI: 10.1088/0026-1394/44/6/003. URL: https://dx.doi.org/10.1088/0026-1394/44/6/003.

[238] Luisa Hoetzsch XENON Collaboration. *XENONnT arrays: PMT categorization and distribution*. Internal note. 2019. URL: https://xe1t-wiki.lngs.infn.it/doku.php?id=xenon:xenonnt:dsg:pmt:categorizationdistribution.

[239] CEAN. *A996, 52 pin cable connector*. https://www.caen.it/download/?filter=A996l. Accessed: 15/03/2023.

[240] E. Aprile et al. “The Triggerless Data Acquisition System of the XENONnT Experiment”. In: (Dec. 2022). arXiv: 2212.11032 [physics.ins-det].

[241] Gaudenz Kessler. “Inelastic WIMP-Nucleus Interactions in XENON100 and Cables and Connectors for XENON1T”. PhD thesis. University of Zurich, 2016. URL: %7Bhttps://www.physik.uzh.ch/groups/groupbaudis/darkmatter/theses/xenon/thesis_kessler.pdf%7D.

[242] E. S. Morrison, T. Frels, E. H. Miller, R. W. Schnee, and J. Street. “Radon daughter plate-out onto Teflon”. In: *AIP Conference Proceedings*. 2018. DOI: doi.org/10.1063/1.5019012.

[243] Chiara Capelli. “Search for Dark Matter and Neutrinoless Double Beta Decay in XENON1T and Calibration of the Photosensors in XENONnT”. PhD thesis. University of Zurich, 2020. URL: %7Bhttps://www.physik.uzh.ch/dam/jcr:71dc084f-baf2-430f-b70c-97a99063f52b/capelli_phd_final.pdf%7D.

[244] Jelle Aalbers. *AxFoundation/strax: v0.11.1*. Version v0.11.1. June 2020. DOI: 10.5281/zenodo.3894675. URL: https://doi.org/10.5281/zenodo.3894675.

[245] Joran R. Angevaare et al. *XENONnT/straxen: v2.0.4*. Version v2.0.4. Jan. 2023. DOI: 10.5281/zenodo.7541292. URL: https://doi.org/10.5281/zenodo.7541292.

[246] The University of Chicago. *Research Computin Center*. https://rcc.uchicago.edu/. Accessed: 15/03/2023.

[247] Evan Shockley. “Study of Excess Electronic Recoil Events in XENON1T”. PhD thesis. University of Chicago, 2021. URL: %7Bhttps://link.springer.com/book/10.1007/978-3-030-87752-1%7D.

[248] Alvaro Loya Villalpando XENON Collaboration. *Overview of notes by Alvaro Loya Villalpando*. Internal note. 2020. URL: https://xe1t-wiki.lngs.infn.it/doku.php?id=xenon:aaloya&s[]=notes&s[]=by&s[]=alvaro.

[249] Milind V. Diwan. “Statistics of the Charge Spectrum of Photo-Multipliers and Methods for Absolute Calibration”. In: *JINST* 15.02 (2020), P02001. DOI: 10.1088/1748-0221/15/02/P02001. arXiv: 1909.05373 [physics.ins-det].

[250] XENON collaboration. “Design and performance of the field cage for XENONnT”. publication ongoing. 2023.

[251] Peter Gaemers et al. *XENONnT/WFSim: v1.0.2*. Version v1.0.2. Oct. 2022. DOI: 10.5281/zenodo.7216324. URL: https://doi.org/10.5281/zenodo.7216324.

[252] A. G. Wright. “603 Light emission by the Cerenkov effect”. In: *The Photomultiplier Handbook*. Oxford University Press, June 2017. ISBN: 9780199565092. DOI: 10.1093/oso/9780199565092.005.0002. eprint: https://academic.oup.com/book/0/chapter/197327116/chapter-pdf/40209190/oso-9780199565092-appendix-2.pdf. URL: https://doi.org/10.1093/oso/9780199565092.005.0002.

[253] E.A. McCutchan. “Nuclear Data Sheets for A = 83”. In: *Nuclear Data Sheets* 125 (2015), pp. 201–394. ISSN: 0090-3752. DOI: https://doi.org/10.1016/j.nds.2015.02.002. URL: https://www.sciencedirect.com/science/article/pii/S0090375215000034.

[254] A Manalaysay et al. “Spatially uniform calibration of a liquid xenon detector at low energies using Kr-83m”. In: *The Review of scientific instruments* 81 (July 2010), p. 073303. DOI: 10.1063/1.3436636.

[255] L. W. Kastens et al. “Calibration of a Liquid Xenon Detector with Kr-83m”. In: *Phys. Rev. C* 80 (2009), p. 045809. DOI: 10.1103/PhysRevC.80.045809. arXiv: 0905.1766 [physics.ins-det].

[256] V. Hannen et al. “Limits on the release of Rb isotopes from a zeolite based 83mKr calibration source for the XENON project”. In: *JINST* 6 (2011), P10013. DOI: 10.1088/1748-0221/6/10/P10013. arXiv: 1109.4270 [astro-ph.IM].

[257] Isao Murata et al. “Neutron and gamma-ray source-term characterization of AmBe sources in Osaka University”. In: *Progress in Nuclear Science and Technology* 4 (Jan. 2014), pp. 345–348. DOI: 10.15669/pnst.4.345.

[258] S.A. Baranov et al. “α-decay of Am241”. In: *Nuclear Physics* 43 (1963), pp. 547–552. ISSN: 0029-5582. DOI: https://doi.org/10.1016/0029-5582(63)90375-4. URL: https://www.sciencedirect.com/science/article/pii/0029558263903754.

[259] J. Scherzinger et al. “Tagging fast neutrons from an 241Am/9Be source”. In: *Applied Radiation and Isotopes* 98 (2015), pp. 74–79. ISSN: 0969-8043. DOI: https://doi.org/10.1016/j.apradiso.2015.01.003. URL: https://www.sciencedirect.com/science/article/pii/S0969804315000044.

[260] Ali Asghar Mowlavi and Rahim Koohi-Fayegh. “Determination of 4.438MeV γ-ray to neutron emission ratio from a 241Am–9Be neutron source”. In: *Applied Radiation and Isotopes* 60.6 (2004), pp. 959–962. ISSN: 0969-8043. DOI: https://doi.org/10.1016/j.apradiso.2004.02.008. URL: https://www.sciencedirect.com/science/article/pii/S0969804304000703.

[261] E. Aprile et al. “Results from a Calibration of XENON100 Using a Source of Dissolved Radon-220”. In: *Phys. Rev. D* 95.7 (2017), p. 072008. DOI: 10.1103/PhysRevD.95.072008. arXiv: 1611.03585 [physics.ins-det].

[262] E. M. Boulton et al. “Calibration of a two-phase xenon time projection chamber with a ^{37}Ar source”. In: *JINST* 12.08 (2017), P08004. DOI: 10.1088/1748-0221/12/08/P08004. arXiv: 1705.08958 [physics.ins-det].

[263] E. Aprile et al. “Energy resolution and linearity of XENON1T in the MeV energy range”. In: *Eur. Phys. J. C* 80.8 (2020), p. 785. DOI: 10.1140/epjc/s10052-020-8284-0. arXiv: 2003.03825 [physics.ins-det].

[264] Christian Wittweg. “Second-Order Weak Decays in XENON1T and Future Xenon Time Projection Chambers”. PhD thesis. Westfälischen Wilhelms-Universität Münster, 2021. URL: https://www.uni-muenster.de/Physik.KP/AGWeinheimer/en/arbeitsgruppe/arbeiten.html.

[265] Shixiao Liang et al. “Domain-Informed Neural Networks for Interaction Localization Within Astroparticle Experiments”. In: *Front. Artif. Intell.* 5 (2022), p. 832909. DOI: 10.3389/frai.2022.832909. arXiv: 2112.07995 [hep-ex].

[266] Francesco Toschi. “Design of the field cage and charge response of the XENONnT dark matter experiment”. PhD thesis. Albert-Ludwigs-Universität Freiburg, 2023.

[267] Jingqiang Ye. “Searches for WIMPs and Axions with the XENON1T Experiment”. PhD thesis. UC, San Diego (main), UC, San Diego (main), 2020.

[268] *COMSOL AB*. https://www.comsol.com/.

[269] Florian Jörg et al. “Characterization of alpha and beta interactions in liquid xenon”. In: *Eur. Phys. J. C* 82.4 (2022), p. 361. DOI: 10.1140/epjc/s10052-022-10259-3. arXiv: 2109.13735 [physics.ins-det].

[270] Marc Paterno. “Calculating efficiencies and their uncertainties”. In: (Dec. 2004). DOI: 10.2172/15017262.

[271] C. J. CLOPPER and E. S. PEARSON. “THE USE OF CONFIDENCE OR FIDUCIAL LIMITS ILLUSTRATED IN THE CASE OF THE BINOMIAL”. In: *Biometrika* 26.4 (Dec. 1934), pp. 404–413. ISSN: 0006-3444. DOI: 10.1093/biomet/26.4.404. eprint: https://academic.oup.com/biomet/article-pdf/26/4/404/823407/26-4-404.pdf. URL: https://doi.org/10.1093/biomet/26.4.404.

[272] Darryl Masson. “Novel Ideas and Techniques for Large Dark Matter Detectors”. PhD thesis. Purdue University, 2018. URL: %7Bhttps://docs.lib.purdue.edu/dissertations/AAI10792046/%7D.

[273] Joanna M. Papakonstantinou and Richard A. Tapia. “Origin and Evolution of the Secant Method in One Dimension”. In: *The American Mathematical Monthly* 120.6 (2013), pp. 500–518. ISSN: 00029890, 19300972. URL: https://www.jstor.org/stable/10.4169/amer.math.monthly.120.06.500 (visited on 02/04/2023).

[274] Pauli Virtanen et al. “SciPy 1.0: Fundamental Algorithms for Scientific Computing in Python”. In: *Nature Methods* 17 (2020), pp. 261–272. DOI: 10.1038/s41592-019-0686-2.

[275] Yuan Mei. “Direct Dark Matter Search with the XENON100 Experiment”. PhD thesis. Rice University, 2011. URL: %7Bhttps://scholarship.rice.edu/handle/1911/70350%7D.

[276] E. Aprile et al. “First Dark Matter Search with Nuclear Recoils from the XENONnT Experiment”. In: (Mar. 2023). arXiv: 2303.14729 [hep-ex].

[277] E. Browne and J.K. Tuli. “Nuclear Data Sheets for A = 60”. In: *Nuclear Data Sheets* 114.12 (2013), pp. 1849–2022. ISSN: 0090-3752. DOI: https://doi.org/10.1016/j.nds.2013.11.002. URL: https://www.sciencedirect.com/science/article/pii/S0090375213000823.

[278] Jun Chen. “Nuclear Data Sheets for A=40”. In: *Nuclear Data Sheets* 140 (2017), pp. 1–376. ISSN: 0090-3752. DOI: https://doi.org/10.1016/j.nds.2017.02.001. URL: https://www.sciencedirect.com/science/article/pii/S0090375217300169.

[279] M. Szydagis et al. “Investigating the XENON1T low-energy electronic recoil excess using NEST”. In: *Phys. Rev. D* 103.1 (2021), p. 012002. DOI: 10.1103/PhysRevD.103.012002. arXiv: 2007.00528 [hep-ex].

[280] J. Allison et al. “Recent developments in Geant4”. In: *Nuclear Instruments and Methods in Physics Research Section A: Accelerators, Spectrometers, Detectors and Associated Equipment* 835 (2016), pp. 186–225. ISSN: 0168-9002. DOI: https://doi.org/10.1016/j.nima.2016.06.125. URL: https://www.sciencedirect.com/science/article/pii/S0168900216306957.

[281] S. Agostinelli et al. “Geant4—a simulation toolkit”. In: *Nuclear Instruments and Methods in Physics Research Section A: Accelerators, Spectrometers, Detectors and Associated Equipment* 506.3 (2003), pp. 250–303. ISSN: 0168-9002. DOI: https://doi.org/10.1016/S0168-9002(03)01368-8. URL: https://www.sciencedirect.com/science/article/pii/S0168900203013688.

[282] Ramirez Diego XENON collaboration. *epix - Electron and Photon Instructions generator for XENON*. URL: https://pypi.org/project/epix/.

[283] Lutz Althüser. “Light collection efficiency simulations of the XENON1T experiment and comparison to data”. MA thesis. Westfälischen Wilhelms-Universität Münster, 2017. URL: https://www.uni-muenster.de/Physik.KP/AGWeinheimer/en/arbeitsgruppe/arbeiten.html.

[284] K. Abe. “XMASS MC simulation”. In: *Journal of Instrumentation* 11.02 (Feb. 2016), p. C02053. DOI: 10.1088/1748-0221/11/02/C02053. URL: https://dx.doi.org/10.1088/1748-0221/11/02/C02053.

[285] A. Lyashenko et al. “Measurement of the absolute Quantum Efficiency of Hamamatsu model R11410-10 photomultiplier tubes at low temperatures down to liquid xenon boiling point”. In: *JINST* 9.11 (2014), P11021. DOI: 10.1088/1748-0221/9/11/P11021. arXiv: 1410.3890 [astro-ph.IM].

[286] Alexey Lyashenko. “Progress in characterization of the Photomultiplier Tubes for XENON1T Dark Matter Experiment”. In: *2014 IEEE Nuclear Science Symposium and Medical Imaging Conference and 21st Symposium on Room-Temperature Semiconductor X-ray and Gamma-ray Detectors*. Feb. 2015. arXiv: 1502.01000 [astro-ph.IM].

[287] Rei Kitamura, Laurent Pilon, and Miroslaw Jonasz. “Optical constants of silica glass from extreme ultraviolet to far infrared at near room temperature”. In: *Appl. Opt.* 46.33 (Nov. 2007), pp. 8118–8133. DOI: 10.1364/AO.46.008118. URL: https://opg.optica.org/ao/abstract.cfm?URI=ao-46-33-8118.

[288] L.M Barkov et al. “Measurement of the refractive index of liquid xenon for intrinsic scintillation light”. In: *Nuclear Instruments and Methods in Physics Research Section A: Accelerators, Spectrometers, Detectors and Associated Equipment* 379.3 (1996). Proceedings of the Sixth International Conference on Instrumentation for Experiments at e+ e- Colliders, pp. 482–483. ISSN: 0168-9002. DOI: https://doi.org/10.1016/0168-9002(99)00518-5. URL: https://www.sciencedirect.com/science/article/pii/0168900299005185.

[289] V.N Solovov et al. “Measurement of the refractive index and attenuation length of liquid xenon for its scintillation light”. In: *Nuclear Instruments and Methods in Physics Research Section A: Accelerators, Spectrometers, Detectors and Associated Equipment* 516.2 (2004), pp. 462–474. ISSN: 0168-9002. DOI: https://doi.org/10.1016/j.nima.2003.08.117. URL: https://www.sciencedirect.com/science/article/pii/S0168900203024331.

[290] G. M. Seidel, R. E. Lanou, and W. Yao. “Rayleigh scattering in rare gas liquids”. In: *Nucl. Instrum. Meth. A* 489 (2002), pp. 189–194. DOI: 10.1016/S0168-9002(02)00890-2. arXiv: hep-ex/0111054.

[291] V.Y. Chepel et al. “Purification of liquid xenon and impurity monitoring for a PET detector”. In: *Nuclear Instruments and Methods in Physics Research Section A: Accelerators, Spectrometers, Detectors and Associated Equipment* 349.2 (1994), pp. 500–505. ISSN: 0168-9002. DOI: https://doi.org/10.1016/0168-9002(94)91217-3. URL: https://www.sciencedirect.com/science/article/pii/0168900294912173.

[292] Emily Grace et al. “Index of refraction, Rayleigh scattering length, and Sellmeier coefficients in solid and liquid argon and xenon”. In: *Nuclear Instruments and Methods in Physics Research Section A: Accelerators, Spectrometers, Detectors and Associated Equipment* 867 (2017), pp. 204–208. ISSN: 0168-9002. DOI: https://doi.org/10.1016/j.nima.2017.06.031. URL: https://www.sciencedirect.com/science/article/pii/S0168900217306848.

[293] A. Baldini et al. “Absorption of scintillation light in a 100 l liquid xenon gamma ray detector and expected detector performance”. In: *Nucl. Instrum. Meth. A* 545 (2005), pp. 753–764. DOI: `10.1016/j.nima.2005.02.029`. arXiv: `physics/0407033`.

[294] K. Yoshino et al. “Absorption cross section measurements of water vapor in the wavelength region 120 to 188 nm”. In: *Chemical Physics* 211.1 (1996), pp. 387–391. ISSN: 0301-0104. DOI: `https://doi.org/10.1016/0301-0104(96)00210-8`. URL: `https://www.sciencedirect.com/science/article/pii/0301010496002108`.

[295] L. Althueser et al. “VUV Transmission of PTFE for xenon-based particle detectors”. In: *Journal of Instrumentation* 15.12 (Dec. 2020), P12021. DOI: `10.1088/1748-0221/15/12/P12021`. URL: `https://dx.doi.org/10.1088/1748-0221/15/12/P12021`.

[296] F. Neves et al. “Measurement of the absolute reflectance of polytetrafluoroethylene (PTFE) immersed in liquid xenon”. In: *JINST* 12.01 (2017), P01017. DOI: `10.1088/1748-0221/12/01/P01017`. arXiv: `1612.07965 [physics.ins-det]`.

[297] E. Aprile et al. “Physics reach of the XENON1T dark matter experiment”. In: *JCAP* 04 (2016), p. 027. DOI: `10.1088/1475-7516/2016/04/027`. arXiv: `1512.07501 [physics.ins-det]`.

[298] S. Bricola et al. “Noble-gas liquid detectors: measurement of light diffusion and reflectivity on commonly adopted inner surface materials”. In: *Nuclear Physics B - Proceedings Supplements* 172 (2007). Proceedings of the 10th Topical Seminar on Innovative Particle and Radiation Detectors, pp. 260–262. ISSN: 0920-5632. DOI: `https://doi.org/10.1016/j.nuclphysbps.2007.08.059`. URL: `https://www.sciencedirect.com/science/article/pii/S0920563207006093`.

[299] J. Calcutt et al. “Geant4Reweight: a framework for evaluating and propagating hadronic interaction uncertainties in Geant4”. In: *JINST* 16.08 (2021), P08042. DOI: `10.1088/1748-0221/16/08/P08042`. arXiv: `2105.01744 [physics.data-an]`.

[300] James B. Dent et al. “Inverse Primakoff Scattering as a Probe of Solar Axions at Liquid Xenon Direct Detection Experiments”. In: *Phys. Rev. Lett.* 125.13 (2020), p. 131805. DOI: `10.1103/PhysRevLett.125.131805`. arXiv: `2006.15118 [hep-ph]`.

[301] Andreas Bollhöfer et al. “Half a century of Krypton-85 activity concentration measured in air over Central Europe: Trends and relevance for dating young groundwater”. In: *Journal of Environmental Radioactivity* 205-206 (2019), pp. 7–16. ISSN: 0265-931X. DOI: `https://doi.org/10.1016/j.jenvrad.2019.04.014`. URL: `https://www.sciencedirect.com/science/article/pii/S0265931X19300888`.

[302] J. B. Albert et al. “Improved measurement of the $2\nu\beta\beta$ half-life of ^{136}Xe with the EXO-200 detector”. In: *Phys. Rev. C* 89.1 (2014), p. 015502. DOI: `10.1103/PhysRevC.89.015502`. arXiv: `1306.6106 [nucl-ex]`.

[303] John N. Bahcall and Carlos Pena-Garay. “Solar models and solar neutrino oscillations”. In: *New J. Phys.* 6 (2004), p. 63. DOI: `10.1088/1367-2630/6/1/063`. arXiv: `hep-ph/0404061`.

[304] W. C. Haxton, R. G. Hamish Robertson, and Aldo M. Serenelli. “Solar Neutrinos: Status and Prospects”. In: *Ann. Rev. Astron. Astrophys.* 51 (2013), pp. 21–61. DOI: `10.1146/annurev-astro-081811-125539`. arXiv: `1208.5723 [astro-ph.SR]`.

[305] Jiunn-Wei Chen et al. “Low-energy electronic recoil in xenon detectors by solar neutrinos”. In: *Physics Letters B* 774 (2017), pp. 656–661. ISSN: 0370-2693. DOI: `https://doi.org/10.1016/j.physletb.2017.10.029`. URL: `https://www.sciencedirect.com/science/article/pii/S0370269317308419`.

[306] M. Agostini et al. “Comprehensive measurement of *pp*-chain solar neutrinos”. In: *Nature* 562.7728 (2018), pp. 505–510. DOI: `10.1038/s41586-018-0624-y`.

[307] Arianna Rocchetti. “The XENONnT experiment: assembly, backgrounds and sensitivity to the neutrinoless double beta decay of 136Xe”. PhD thesis. Albert-Ludwigs-Universität Freiburg, 2021. URL: %7Bhttps://freidok.uni-freiburg.de/data/223691%7D.

[308] Harry Bteman. “Solution of a system of differential equations occurring in the theory of radioactive transformations”. In: *Proceedings of the Cambridge Philosophical Society, Mathematical and physical sciences.* (1910). URL: https://archive.org/details/cbarchive_122715_solutionofasystemofdifferentia1843.

[309] Dr. Shingo Kazama XENON Collaboration. *Leakage below NR-mean in XENONnT SR0*. Internal note. 2022. URL: https://xe1t-wiki.lngs.infn.it/doku.php?id=xenon:xenonnt:analysis:ntsciencerun0:er_leakage&s[]=leakage.

[310] Baxter, D. et al. “Recommended conventions for reporting results from direct dark matter searches”. In: *Eur. Phys. J. C* 81.10 (2021), p. 907. DOI: 10.1140/epjc/s10052-021-09655-y. URL: https://doi.org/10.1140/epjc/s10052-021-09655-y.

[311] Gary J. Feldman and Robert D. Cousins. “Unified approach to the classical statistical analysis of small signals”. In: *Phys. Rev. D* 57 (7 Apr. 1998), pp. 3873–3889. DOI: 10.1103/PhysRevD.57.3873. URL: https://link.aps.org/doi/10.1103/PhysRevD.57.3873.

[312] Glen Cowan et al. “Power-Constrained Limits”. In: (May 2011). arXiv: 1105.3166 [physics.data-an].

[313] E. Aprile et al. “Constraining the spin-dependent WIMP-nucleon cross sections with XENON1T”. In: *Phys. Rev. Lett.* 122.14 (2019), p. 141301. DOI: 10.1103/PhysRevLett.122.141301. arXiv: 1902.03234 [astro-ph.CO].

[314] K. Auranen and E.A. McCutchan. “Nuclear Data Sheets for A=212”. In: *Nuclear Data Sheets* 168 (2020), pp. 117–267. ISSN: 0090-3752. DOI: https://doi.org/10.1016/j.nds.2020.09.002. URL: https://www.sciencedirect.com/science/article/pii/S0090375220300351.

[315] Martin Ester et al. “A Density-Based Algorithm for Discovering Clusters in Large Spatial Databases with Noise”. In: *Proceedings of the Second International Conference on Knowledge Discovery and Data Mining*. KDD’96. Portland, Oregon: AAAI Press, 1996, pp. 226–231.

[316] F. Pedregosa et al. “Scikit-learn: Machine Learning in Python”. In: *Journal of Machine Learning Research* 12 (2011), pp. 2825–2830.

[317] Jaron Grigat XENON Collaboration. *XENONnT S2-separation resolution from WFsim*. Internal note. 2022. URL: https://xe1t-wiki.lngs.infn.it/doku.php?id=xenon:xenon1t:jgrigat:s2_separation.

[318] David Newell and Eite Tiesinga. “The international system of units (SI):” in: 2019.

[319] Zoltan Elekes and Janos Timar. “Nuclear Data Sheets for A = 128”. In: *Nuclear Data Sheets* 129 (2015), pp. 191–436. ISSN: 0090-3752. DOI: https://doi.org/10.1016/j.nds.2015.09.002. URL: https://www.sciencedirect.com/science/article/pii/S0090375215000472.

[320] Lawrence Berkeley National Laboratory. *X-RAY DATA BOOKLET*. [Online; accessed 15-Janury-2023]. 2009. URL: https://xdb.lbl.gov/.

[321] “Nuclear data sheets for A = 127”. In: *Nuclear Data Sheets* 35.2 (1982), pp. 181–277. ISSN: 0090-3752. DOI: https://doi.org/10.1016/S0090-3752(82)80014-8. URL: https://www.sciencedirect.com/science/article/pii/S0090375282800148.

[322] Pietro Vischia. “Pseudosignificances as figures of merit: a systematic study and exploration of Bayesian solutions”. In: *PoS* Confinement2018 (2019), p. 249. DOI: 10.22323/1.336.0249.

[323] Shenyang Shi XENON Collaboration. *XENONnT SR0 Neutron Background Prediction*. Internal note. 2022. URL: https://xe1t-wiki.lngs.infn.it/doku.php?id=xenon:xenonnt:neutron_background:prediction#cuts_validation_and_acceptance.

[324] Natascha Margarita Rosa Elisabeth Rupp. "Radon Induced Background in the XENON1T Dark Matter Search Experiment and Studies on Xenon Purity in the HeXe System". PhD thesis. Natural Sciences and Mathematics of the Ruperto-Carola-University of Heidelberg, Germany, 2021. URL: %7Bhttps://archiv.ub.uni-heidelberg.de/volltextserver/29342/%7D.

[325] L. Baudis et al. "Neutrino physics with multi-ton scale liquid xenon detectors". In: *Journal of Cosmology and Astroparticle Physics* 2014.01 (Jan. 2014), p. 044. DOI: 10.1088/1475-7516/2014/01/044. URL: https://dx.doi.org/10.1088/1475-7516/2014/01/044.

[326] E. Browne and J.K. Tuli. "Nuclear Data Sheets for A = 220". In: *Nuclear Data Sheets* 112.4 (2011), pp. 1115–1161. ISSN: 0090-3752. DOI: https://doi.org/10.1016/j.nds.2011.03.002. URL: https://www.sciencedirect.com/science/article/pii/S0090375211000214.

[327] S.-C. Wu. "Nuclear Data Sheets for A = 216". In: *Nuclear Data Sheets* 108.5 (2007), pp. 1057–1092. ISSN: 0090-3752. DOI: https://doi.org/10.1016/j.nds.2007.04.001. URL: https://www.sciencedirect.com/science/article/pii/S0090375207000415.

[328] Balraj Singh et al. "Nuclear Data Sheets for A=218". In: *Nuclear Data Sheets* 160 (2019), pp. 405–471. ISSN: 0090-3752. DOI: https://doi.org/10.1016/j.nds.2019.100524. URL: https://www.sciencedirect.com/science/article/pii/S009037521930050X.

[329] M. Shamsuzzoha Basunia. "Nuclear Data Sheets for A = 210". In: *Nuclear Data Sheets* 121 (2014), pp. 561–694. ISSN: 0090-3752. DOI: https://doi.org/10.1016/j.nds.2014.09.004. URL: https://www.sciencedirect.com/science/article/pii/S0090375214006589.

[330] *Nuclear Data Sheets*. URL: https://www.sciencedirect.com/journal/nuclear-data-sheets.

[331] Carlo Fuselli Dominick Cichon XENON Collaboration. *XENONnT SR0 - Alpha event selection summary*. Internal note. 2022. URL: https://xe1t-wiki.lngs.infn.it/doku.php?id=xenon:xenonnt:sr0:alpha_event_selection_summary.

[332] Jochen Ahlswede et al. "Update and improvement of the global krypton-85 emission inventory". In: *Journal of Environmental Radioactivity* 115 (2013), pp. 34–42. ISSN: 0265-931X. DOI: https://doi.org/10.1016/j.jenvrad.2012.07.006. URL: https://www.sciencedirect.com/science/article/pii/S0265931X12001816.

[333] Dr. Hardy Simgen XENON Collaboration. *SR0 Kr-in-Xe measurements with RGMS*. Internal note. 2022. URL: https://xe1t-wiki.lngs.infn.it/doku.php?id=xenon:xenonnt:dsg:clean:analytics:rgms:rgms_sr08.

[334] Edoardo Vitagliano, Irene Tamborra, and Georg Raffelt. "Grand Unified Neutrino Spectrum at Earth: Sources and Spectral Components". In: *Rev. Mod. Phys.* 92 (2020), p. 45006. DOI: 10.1103/RevModPhys.92.045006. arXiv: 1910.11878 [astro-ph.HE].

[335] Roni Harnik, Joachim Kopp, and Pedro A. N. Machado. "Exploring nu Signals in Dark Matter Detectors". In: *JCAP* 07 (2012), p. 026. DOI: 10.1088/1475-7516/2012/07/026. arXiv: 1202.6073 [hep-ph].

[336] Alexander Fieguth. "Investigations of impurities in xenon gas with a cold-trap-enhanced quadrupole mass spectrometer". MA thesis. Institut für Kernphysik Mathematisch-Naturwissenschaftliche Fakultät Westfälische Wilhelms-Universität Münster, 2014.

[337] J. Kotila and F. Iachello. "Phase space factors for double-β decay". In: *Phys. Rev. C* 85 (2012), p. 034316. DOI: 10.1103/PhysRevC.85.034316. arXiv: 1209.5722 [nucl-th].

[338] Kotila, J. private communication.

[339] "Nuclear Data Sheets for A = 131". In: *Nuclear Data Sheets* 107.11 (2006), pp. 2715–2930. ISSN: 0090-3752. DOI: https://doi.org/10.1016/j.nds.2006.10.001. URL: https://www.sciencedirect.com/science/article/pii/S0090375206000809.

[340] Janos Timar, Zoltan Elekes, and Balraj Singh. "Nuclear Data Sheets for A = 129". In: *Nuclear Data Sheets* 121 (2014), pp. 143–394. ISSN: 0090-3752. DOI: `https://doi.org/10.1016/j.nds.2014.09.002`. URL: `https://www.sciencedirect.com/science/article/pii/S0090375214006565`.

[341] "Nuclear Data Sheets for A = 133". In: *Nuclear Data Sheets* 112.4 (2011), pp. 855–1113. ISSN: 0090-3752. DOI: `https://doi.org/10.1016/j.nds.2011.03.001`. URL: `https://www.sciencedirect.com/science/article/pii/S0090375211000202`.

[342] K. Ni et al. "Preparation of neutron-activated xenon for liquid xenon detector calibration". In: *Nuclear Instruments and Methods in Physics Research Section A: Accelerators, Spectrometers, Detectors and Associated Equipment* 582.2 (2007), pp. 569–574. ISSN: 0168-9002. DOI: `https://doi.org/10.1016/j.nima.2007.08.180`. URL: `https://www.sciencedirect.com/science/article/pii/S0168900207018827`.

[343] A E Shustov et al. "Thermal neutrons registration by xenon gamma-ray detector". In: *Journal of Physics: Conference Series* 675.4 (Jan. 2016), p. 042024. DOI: `10.1088/1742-6596/675/4/042024`. URL: `https://dx.doi.org/10.1088/1742-6596/675/4/042024`.

[344] Pavel Kavrigin XENON Collaboration. *In-situ Xe127 production during AmBe calibration in XENONnT SR0*. Internal note. 2022. URL: `https://xe1t-wiki.lngs.infn.it/doku.php?id=xenon:xenonnt:pkavrigin:mc_ambe_xe127`.

[345] E. Aprile et al. "Observation of two-neutrino double electron capture in ^{124}Xe with XENON1T". In: *Nature* 568.7753 (2019), pp. 532–535. DOI: `10.1038/s41586-019-1124-4`. arXiv: `1904.11002 [nucl-ex]`.

[346] J. Aalbers et al. "Cosmogenic production of Ar37 in the context of the LUX-ZEPLIN experiment". In: *Phys. Rev. D* 105.8 (2022), p. 082004. DOI: `10.1103/PhysRevD.105.082004`. arXiv: `2201.02858 [hep-ex]`.

[347] E. Aprile et al. "Application and modeling of an online distillation method to reduce krypton and argon in XENON1T". In: *PTEP* 2022.5 (2022), 053H01. DOI: `10.1093/ptep/ptac074`. arXiv: `2112.12231 [physics.ins-det]`.

[348] C. Zhang et al. "Cosmogenic Activation of Materials Used in Rare Event Search Experiments". In: *Astropart. Phys.* 84 (2016), pp. 62–69. DOI: `10.1016/j.astropartphys.2016.08.008`. arXiv: `1603.00098 [physics.ins-det]`.

[349] LL. Lucas and Unterweger MP. "Comprehensive Review and Critical Evaluation of the Half-Life of Tritium". In: *J Res Natl Inst Stand Technol.* (2000). DOI: `10.6028/jres.105.043`.

[350] Steve Baker and Robert D. Cousins. "Clarification of the use of CHI-square and likelihood functions in fits to histograms". In: *Nuclear Instruments and Methods in Physics Research* 221.2 (1984), pp. 437–442. ISSN: 0167-5087. DOI: `https://doi.org/10.1016/0167-5087(84)90016-4`. URL: `https://www.sciencedirect.com/science/article/pii/0167508784900164`.

[351] G. Cowan. *Statistical data analysis*. 1998. ISBN: 978-0-19-850156-5.

[352] F. James. "Interpretation of the shape of the likelihood function around its minimum". In: *Computer Physics Communications* 20.1 (1980), pp. 29–35. ISSN: 0010-4655. DOI: `https://doi.org/10.1016/0010-4655(80)90103-4`. URL: `https://www.sciencedirect.com/science/article/pii/0010465580901034`.

[353] Glen Cowan et al. "Asymptotic formulae for likelihood-based tests of new physics". In: *Eur. Phys. J. C* 71 (2011). [Erratum: Eur.Phys.J.C 73, 2501 (2013)], p. 1554. DOI: `10.1140/epjc/s10052-011-1554-0`. arXiv: `1007.1727 [physics.data-an]`.

[354] L. Demortier and L. Lyons. *Everything you always wanted to know about pulls*. `http://physics.rockefeller.edu/luc/technical_reports/cdf5776_pulls.pdf`. Accessed: 24/02/2022.

Acknowledgments

This is the end of this manuscript and my journey to get a Ph.D.. Initially, these acknowledgments were meant to be a video. However, I realized that the writing and the preparation for the defense required all my energy, and nothing was left for additional projects. The writing of this section has been postponed until now (i.e., 11th of June, 2023), allowing me to recover and look at what happened in the last four and a half years without all the stress and fatigue accumulated in the previous months before thanking those without whom this journey would not have been the same. The order in which people appear is unquestionably not a ranking. All the people I got to cross paths with, whether a day or a year, teach something to me. Certainly, there are those who have meant more to me, but I'm sure I don't have to flaunt it to the four winds for them to know. Most likely, I forgot to mention someone, and I apologize. For complaints or comments, feel free to contact me, or not!

Pursuing the Ph.D. project at the University of Zurich has been an honor. A piece of my heart will always be in that University and in that gorgeous city. This would not be possible without Laura. She believed in me, offering me a position in her group, although I was no more than a novice. Thank you for being so patient initially: You gave me the time to learn and feel confident in a highly competitive world. And also, thank you for pushing me once I had the tools and knowledge to achieve high-quality work. I learned valuable human and work-related lessons from you and will always bring them with me. Similarly, I want to thank Michelle, who has followed me through all these years. Sometimes silently and other times loudly, she was there along the path for all the stages. You have always been available for discussion, suggestions, and guidance. I appreciate the time you dedicated to me. I would also like to thank Nicola Serra for being part of my committee and taking an interest in my work. Thank you for all your suggestions and comments over the years.

I am grateful to all of Laura's group members. Despite the punctiliousness of some personalities, I always felt comfortable with all the group members. I learned to be a scientist thanks to them. So thank Adam, Alessandro, Alex, Andrej, Chiara, Chloe, Christian, Diego, Frédéric, Gabriela, Jonathan, Jose, Junting, Kevin, Lars, Livio, Mariana, Marta, Maximinio, Michael, Neil, Paloma, Patricia, Pin-Jung Chiu, Ricardo, Roman, Shayne, Simon, Stefan, Valentino, Vera, Yannick, and Yanina. Beyond the work environment, I have built important relationships with several of them. Thank you, Adam, for supervising me and teaching me everything I need to learn. You were and still are an incredible source of knowledge, good moments, and beer. I must spend a few words for the Italian office members: Chiara and Ale. Besides you being incredible scientists from whom I still have only to learn, you are also a beautiful people: Thank you for being there. With Ricardo, I shared this path. We started together, went through the same phases, and finished together. You are a wonderful guy, an inexhaustible source of inspiration. Thank you for your friendship. Dear Alex, you are one of my favorite Germans ever. Gabriela and Yannick, you are the essence of great Ph.D. students. Still, most importantly, you are fresh and easygoing people, and I appreciate every moment we spent together outside the University. Please bring me a greeting also to Tobi and Chiara, respectively. Lastly, I want to express my deepest gratitude to Diego and Christian. Their guidance, both in terms of work and not, in the final stages of my project was indispensable.

My gratitude goes as well towards the XENON collaboration. I got to know and had the opportunity to work with extraordinary people with whom I shared an unbridled passion for research. There were many stressful moments, but through cooperation and goodwill, together, we managed to raise - albeit slightly - the bar of human knowledge. All these efforts were amply balanced by the good times spent during the collaboration meetings. Among the many, I would like to thank Alfredo, Andrii, Cecilia, Daniel, Danilo, Evan, Francesco, Hagar, Jacques, Jaron, Joaquim, Jörn, Joran, Jungi, Jingqiang, Knut, Lanqing, Luca, Lutz, Maxime, Micheal, Peter, Roberto, Shingo, Tianyu, and Yossi.

Outside the University and the experiment, I met true friends, and I hope our relationship will last despite being spread across Europe right now. Thanks to Andrea, Daniela, Federico, Mara, and Martina. You have been my outlet for all the stress that Ph.D. entails. I have had fantastic adventures with you. You have encouraged me to do things I didn't think I was capable of, one overall, the triathlon. I will miss you very much. Despite the large group of Italian friends, Italy was not the main nationality that kept me company over the past four years, but Sweden. I owe a lot to my flatmates Björn and Helena for the days we spent together, for the sparkling discussions, and for the sharing of the day-to-day routine: you were great traveling companions as well as great friends.

For me, Zurich is a second home, but there is nothing like Ferrara. I am a simple guy with simple values and a deep connection to his land and the people there. So many friends I have left behind by moving first to Zurich and now to Heidelberg, but the bond has not been broken. On the contrary, it has become more intense and truer over the years. This thesis is dedicated to the friends in Ferrara who have held me up and supported me. In particular, my highest appreciation goes to Andrea, Giulio, Matteo, and Edoardo.

When it comes to support, however, no one can compete with Elena. Elena and I met a few weeks before I moved to Zurich. Neither of us believed that a long-distance relationship would survive. However, after more than 4 years, she is still here, pushing me to do my best, helping me to reflect, making me laugh, and comforting me. Clearly, this journey would have been a completely different story without her. That is why I want to dedicate this manuscript to her.

I save my family last: my parents Patrizia e Gigi, and two brothers, Giacomo and Filippo. I want to give you the gratitude you deserve: You were always present and helped me in many different ways. You never backed down when there was something to scold me for, and at the same time, you were one of the first to cheer me on. This work is dedicated to them, without whom it would not be achieved.

Again, thank you all, and see you again!